VRIJE UNIVERSITEIT BRUSSEL

Faculteit Wetenschappen en Bio-ingenieurswetenschappen

Vakgroep Fysica - Interuniversity Institute for High Energies

Solar Flare Neutrinos in the Multi-Messenger Era:

Flux Calculations and a Search with the IceCube Neutrino Observatory

Gwenhaël de Wasseige

Proefschrift ingediend met het oog op het behalen van de academische graad van Doctor in de Wetenschappen.

Promotors: **Prof. Dr. Nick van Eijndhoven**
Prof. Dr. Kael D. Hanson

July 2018

Doctoral Examination Committee

Chair: Prof. Dr. Jorgen D'Hondt (VUB)
Secretary: Prof. Dr. Stijn Buitink (VUB)
Promotor: Prof. Dr. Nick van Eijndhoven (VUB)
Promotor: Prof. Dr. Kael D. Hanson (University of Wisconsin, Madison, USA)
Prof. Dr. Dominique Maes (VUB)
Prof. Dr. Petra Van Mulders (VUB)
Prof. Dr. Markus Ahlers (University of Copenhagen, Denmark)
Prof. Dr. Melissa Pesce-Rollins (INFN Sezione di Pisa, Italy)

Pour Papy, Mamy et Loulou,
j'y suis, grâce à vous.

Mais d'autres, dans les nuits claires de l'été,
lèvent les yeux vers les étoiles.
Jean d'Ormesson

Contents

Preface

This thesis starts with a story. A long and stupendous story that has involved several generations of researchers and experimental devices from all over the World. For ages, the closest star from our planet has been keeping secrets, occasionally revealing some mysteries of nature. While the first scientific observations of the Sun started as early as 800 BC with the Babylonian astronomers [1], we will focus on a more recent chapter, when the neutrinos take the stage. Before telling the story, an introduction of its main characters is required. Chapter 1 will therefore be dedicated to the description of the Sun and the neutrino. The rest of the Chapter will be dedicated to review all possible neutrino production in the solar environment. I personally contributed to the estimate of solar atmospheric and solar flare neutrino fluxes that will be described at the end of Chapter 1.

Chapter 2 introduces solar flares, magnetic phenomena happening in the atmosphere of the Sun. Their potential production of neutrinos is the main subject of this thesis. While electromagnetic, charged particles and neutrons have provided for many years observations allowing to understand particle acceleration, propagation and interaction in the solar flare environment, neutrinos, as it will be detailed in the text, would bring a new insight into the hadronic process and could therefore constrain the characteristics of the accelerated flux. We also note that, once solar flare neutrinos will lead to a significant signal in neutrino telescopes, their detection could be used as an early warning of major solar storms potentially oriented towards the Earth. Combined with existing or future other techniques, these neutrino detections could therefore be used to predict storms, offering the opportunity to protect astronauts, communication satellites, and the electrical system deployed at the ground against high-energy solar energetic particles.

A study of this neutrino production as well as a calculation of the expected flux at Earth is presented in Chapter 3. This Chapter also presents a new approach, inspired by multi-messenger astronomy, that may optimize experimental searches of solar flare neutrinos. This multi-messenger aspect, especially the synergy between gamma rays and neutrinos, will be extensively used throughout the thesis, both for the calculation of the neutrino flux and the experimental search developed in Chapter 5 and 6. In view of establishing this connection, a close collaboration with Fermi-LAT scientists, and especially Dr. Melissa Pesce-Rollins and Dr. Nicola Omodei, has been established.

In Chapter 3, I also demonstrate that solar flare neutrinos could be emitted up to a few GeV and present a science case for large neutrino telescopes.

While several large neutrino telescopes are currently under operation around the globe, the only one that has the capability to detect solar flare neutrinos at the moment is the IceCube Neutrino Observatory. Chapter 4 presents the main characteristics of large neutrino telescopes with a focus on IceCube, before concluding on the main achievements reached in Neutrino Astronomy at the time of writing. As it will be shown, the IceCube Collaboration is continuously pushing the limit of the detector in view of increasing the discovery potential in Astroparticle and Particle physics. Along the same lines, I have developed an innovative analysis that allows a reduction of the energy threshold of IceCube down to the GeV level necessary to carry out a search for solar flare neutrinos.
The combination of the multi-messenger approach previously described and the experimental neutrino search is presented in Chapter 6. The Chapter ends with the constraints set on neutrino emission from solar flares. Chapter 7 concludes by presenting short and long term prospects for the work achieved in this thesis.

—Mais pour le principe, et pour l'exemple aussi,
Je trouve qu'il est bon d'exagérer ainsi.

Cyrano de Bergerac, Deuxième acte, scène VIII,
Edmond Rostand

1

Neutrinos from the Sun

This Chapter aims at presenting relevant characteristics of the Sun and the production of neutrinos related to solar flares. We review all the processes that are potential sources of a solar neutrino flux. For each contribution, we give the main characteristics of the flux at Earth. This review is required in order to identify potential solar backgrounds for the search of solar flare neutrinos presented in this work.

1.1 Once Upon a Time, the Sun and its Neutrinos...

1.1.1 General characteristics of the Sun

The Sun, located 1.5×10^8 km away [1], is the star closest to the Earth. Its mass of $1{,}988{,}500 \times 10^{24}$ kg and its G2V spectral type make it a typical star of the *Main Sequence*, converting Hydrogen to Helium through nuclear fusion. This characteristic is especially interesting for us as the process produces a large amount of neutrinos. The production chain as well as the consequent neutrino yield will be detailed in Section 1.2.

The Sun can be divided into different layers. These layers cover a density profile extending from 10^2 g/cm^3 in the inner region down to 10^{-17} g/cm^3 in the upper layers. One can distinguish, from the center to the outer part [3]:

[1] ... or more accurately, 149, 597, 870 km, which corresponds to 1 astronomical unit (A.U.). This distance varies along the year [2].

- the Core: This is the center of the Sun, which expands up to 20 to 25% of the solar radius with densities as high as 150 g/cm^3. The temperature reaches 10^7 K in the center. We note that the core is the site where nuclear fusion takes place.
- the Radiative zone: A radiative zone develops above the core and up to 70% of the solar radius. The density falls from 20 to 0.2 g/cm^3 while the temperature goes down to 10^6 K.
- the Convective zone: After a transition layer, called the *tachocline*, appears a convection zone where densities go down to 10^{-6} g/cm^3.
- the Photosphere: The photosphere is located around the radius of the Sun (about 696×10^3 km) and is therefore the lowest layer of the atmosphere. It expands over 500 km with temperature around 6000 K. The density falls below 10^{-6} g/cm^3.
- the Chromosphere: The 2000 km thick layer has a density of about 10^{-8} g/cm^3 and a temperature of 20,000 K. This layer will be of great importance for the work presented in this thesis. More details about composition as well as a specific model will be detailed in Chapter 3.
- the Transition region: Between the Chromosphere and the Corona expands a Transition region with a thickness of about 200 km. In this region, the temperature increases from 20,000 to 10^6 K.
- the Corona: Outermost layer of the Sun, the Corona expands above the transition region for thousands of km with no well-defined upper-limit. The temperature can reach values up to 20×10^6 K.
- the Heliosphere: Finally the winds emitted by the Sun create the Heliosphere that expands as far as 50 A.U. with a particle density varying from 0.01 to more than 100 cm^{-3}.

We will especially focus on the Core and the atmosphere, i.e. from the bottom of the Photosphere to the Corona, as they are the relevant areas for neutrino production in the Sun (see Section 1.2, 1.4 and Section 1.5, 1.6 respectively). Although details on the radiative and convective zones might be interesting for their potential role of magnetic field generator through the magnetic dynamo [4], we will not discuss them here. The interested reader can find more information in [4].

As mentioned above, an important feature is the complex magnetic field intrinsically linked to the Sun. This magnetic field is present at different scales around the Sun and exhibits cyclic variations along the years. The most relevant cycle in the framework of this thesis is the 11-year cycle describing the number of sunspots visible on the solar disk. The sunspots, observed as dark areas anchored in the photosphere, reflect high magnetic field concentrations at these locations. While their existence was noticed by Galileo Galilei in the XVIIth century, the cyclic behavior of the sunspot number was

discovered much later, in 1755, by Rudolf Wolf [5]. The current solar cycle is the 24th since Wolf's observations and will leave room for the 25th cycle at the end of 2019. The sunspots are of interest in our study for their role in the phenomenon of solar flares, which are gigantic outbursts due to magnetic field distortions, as detailed in Chapter 2.

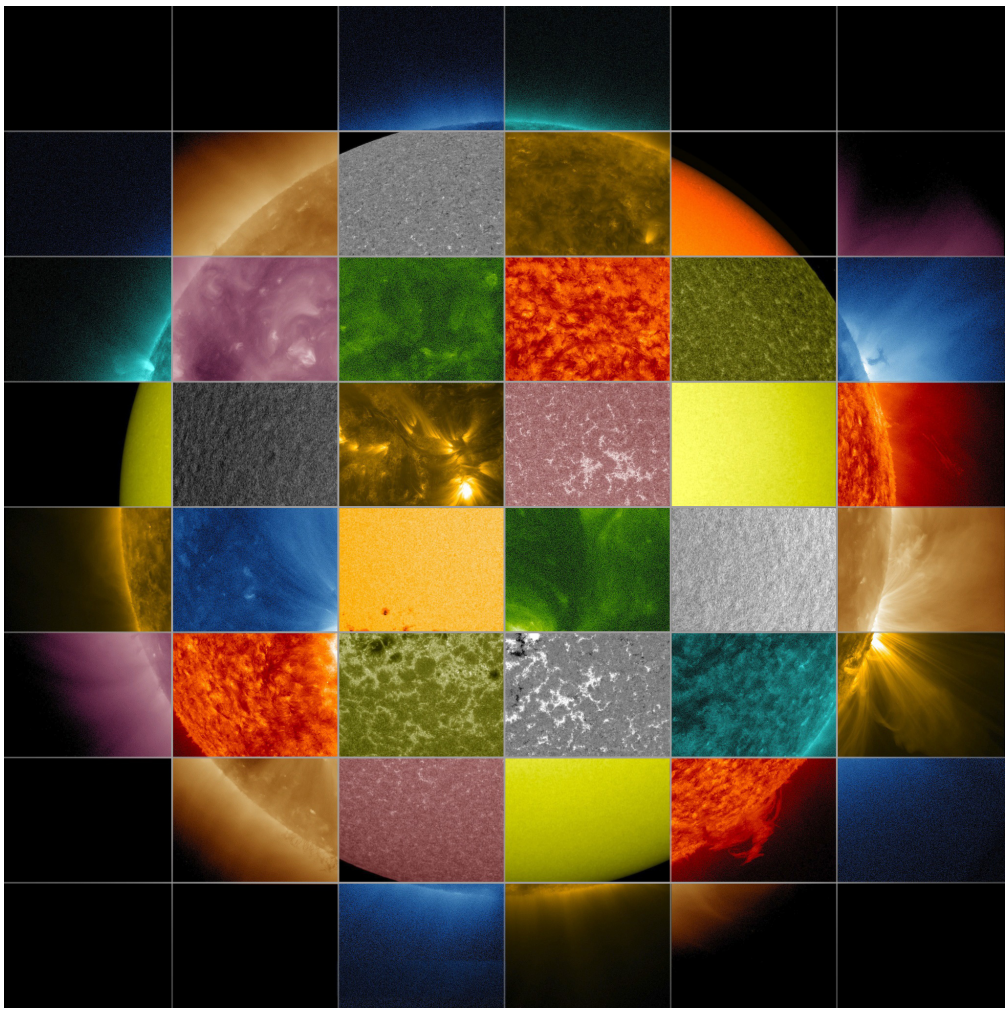

Figure 1.1: Multiwavelength patchwork of the Sun. Each wavelength highlights specific features of the Sun, from magnetic field line concentration to the hottest regions in the Corona. The combination of the different wavelengths allows for a better understanding of the phenomena and features linked with solar activity. Credits: The Solar Dynamic Observatory.

We finish this brief introduction by reminding the reader that the Sun is studied through the whole electromagnetic spectrum as shown in Fig. 1.1. These observations allow for a deep and detailed understanding of the solar features. Moreover, as detailed

in Section 1.2, the Sun was the first multimessenger [2] source ever observed, with the detection of solar neutrinos in the early sixties. As we will see in the course of this thesis, these multimessenger observations enlarge our vision of the Sun and its role in Astroparticle physics. Neutrinos, unlike photons, can travel across large amount of matter without being attenuated. In the case of the Sun, they therefore transport information from the inner layers, i.e. below the photosphere, that could not be probed using only photons. Before sketching this part of the story, we will introduce the main characteristics of its second character: the neutrino.

1.1.2 Introduction of the neutrino as an elementary particle

"I have done a terrible thing, I have invented a particle that cannot be detected" wrote Wolfgang Pauli in 1930 after postulating the existence of a neutral particle [6]. Named *neutron* at that time, this elusive candidate was supposed to solve both the apparent momentum non-conservation of nuclear beta decays and the anomalous spin-statistics of nitrogen and lithium nuclei [6]. Later on James Chadwick could demonstrate that the neutron indeed solves the spin-statistics question [7]. Unfortunately, its mass being close to the proton mass prevented it from playing the third body role in beta decays. In 1932, Enrico Fermi developed the first theory of beta decay including the unknown neutral particle. His origins explain the well-known name: *neutrino* or little neutral one in Italian [8].

The scientific community had to wait 24 years for the first observation of the neutrino [3]. The experiment was carried out by Fred Reines and Clyde Cowan [9]. Their detector, located 11 meters from a nuclear reactor core, consisted of layers of Cadmium-loaded water, sandwiched between layers of liquid scintillator. The former was used as a neutrino target and an array of photomultipliers was used to monitor the liquid scintillator volumes to look for the characteristic double-flash signature, produced by the positron annihilation and the neutron capture. With the advent of a more sophisticated theoretical description of elementary particle physics, also neutrinos of muon and tau types were predicted. The first observations of these particles happened respectively in 1962 and 2000 [10, 11].

Once discovered, the (anti-)neutrinos joined the family of the observed elementary particles. The Standard Model of particle physics being a Lorentz invariant quantum field theory with a gauge symmetry $SU(3) \times SU(2)_L \times U(1)$, which is spontaneously broken via the Higgs mechanism, is the most accurate model describing particle interactions developed to date. This model is able to describe the properties of all known elementary particles and their interactions. It includes 12 fermions, their antiparticles and 4 bosons, i.e. 3 gauge bosons and the scalar boson, as illustrated in Fig. 1.2. The interactions

[2] Multimessenger astronomy aims at studying a specific object using the observations through different messengers such as photons, neutrinos or cosmic rays.

[3] More precisely: an electron antineutrino interaction was observed.

between these particles happen through the exchange of the gauge bosons of three of the fundamental forces : the photon, Z and $W^{\pm}$, and gluons for the electromagnetic, weak and strong nuclear interactions respectively.

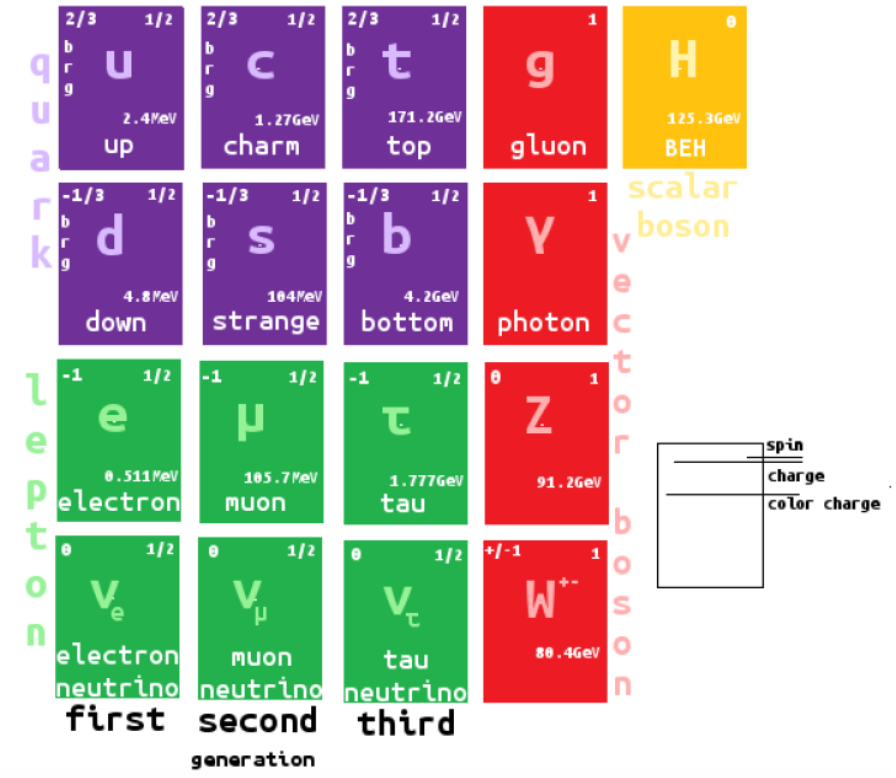

Figure 1.2: The Standard Model of particle physics.

Being neutral with a spin 1/2, the neutrino only interacts weakly, through the exchange of a boson Z or $W^{\pm}$ [4]. The cross-section of neutrino interactions with matter is therefore of the order of 10^{-38} cm^2 at 1 GeV, i.e. orders of magnitude below what is expected for strong or electromagnetic interactions. These properties explain its elusive character and thus the inventive technicalities required to detect it. However, as we will detail hereafter, astronomers were able to take advantage of its properties and turn it into one of the most promising messengers to study the inner engines of the energetic astrophysical objects populating our Universe.

There is much more to say on the properties of the neutrino as many of them still hold clues to solve open questions in particle physics [13, 14]. Some of them will be outlined in the next sections as they were discovered through the study of solar neutrinos and are relevant for the research described in this thesis.

[4] The measurements of the width of the Z-boson at LEP experiments confirmed the existence of only 3 light neutrinos as described in the Standard Model [12].

1.1.3 Neutrinos as astrophysical messengers

Neutrinos are profusely produced in astrophysical objects making them next to photons the most abundant known elementary particles in the Universe. While photons have helped us to unravel the mysteries of the cosmos for centuries, neutrinos came late into the game. As mentioned earlier, their small cross-sections and their electromagnetic neutrality make their detection difficult and, consequently, also the decryption of the message they carry.

However, their ghostly character guarantees an almost unhindered travel between the source and the observer. Unlike photons that can be scattered or absorbed by interstellar dust, and cosmic rays that are deflected by (inter)galactic magnetic fields due to their electric charge, neutrinos are able to travel through our Universe basically without being affected by matter or magnetic fields. Fig. 1.3 shows an illustration of this idea. The first high-energy neutrinos with an astrophysical origin were detected in 2012 by the IceCube Neutrino Observatory [15]. Even though scientists are still working towards the identification of their sources, these first detections signed the beginning of a new era, where the high energy phenomena in the Universe can be observed and understood not only by means of photons and cosmic rays but also via neutrinos [5].

Despite the size of our Universe and the numerous potential sources of astrophysical neutrinos, we will focus on the closest extraterrestrial source : the Sun. We review below the different processes that can produce solar neutrinos. We will start from the core of the Sun before moving towards external layers up to the atmosphere. Even though this thesis focuses on solar flare neutrinos, it is relevant to compare the flux expected from this phenomenon with the other processes that may lead to a neutrino detection at Earth.

1.2 Solar Neutrinos

1.2.1 Production and flux in the core of the Sun

As previously mentioned, the core of the Sun is the location of nuclear reactions turning Hydrogen to Helium and producing a large flux of neutrinos. We describe here the reaction chain and evaluate the subsequent neutrino flux. The derivation presented here is inspired by [16]. The complete fusion process can be written as

$$4p \rightarrow^4 \mathrm{He} + 2\mathrm{e}^- + 2\nu_e + 26.73 \text{ MeV} \tag{1.1}$$

[5] In 2016, the LIGO collaboration announced the first direct observation of gravitational waves, enlarging again the view of the astronomers on our Universe.

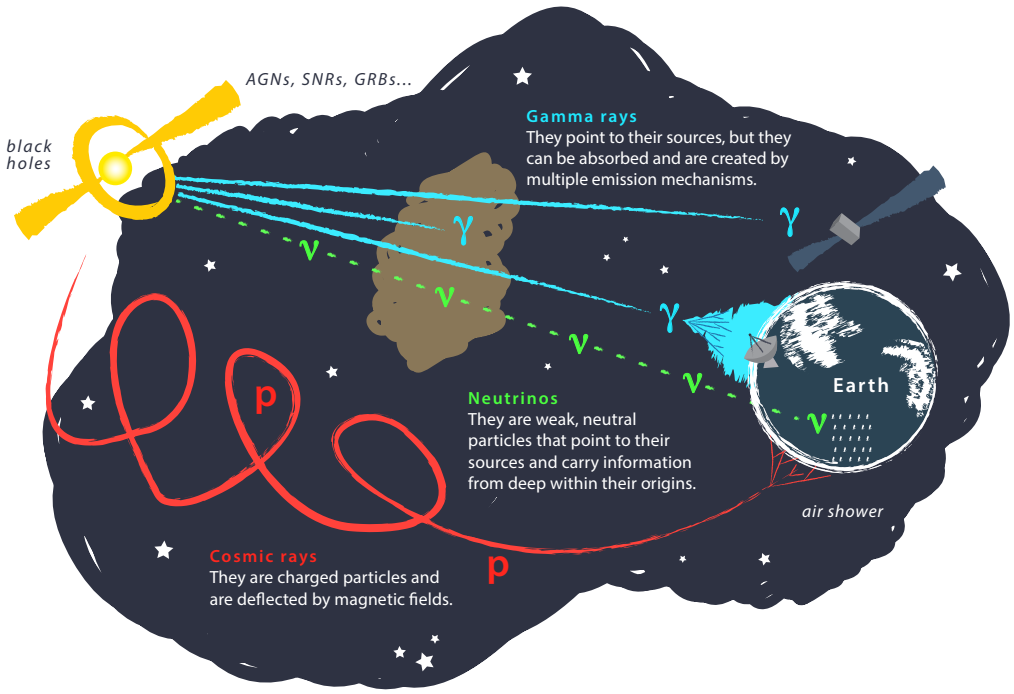

Figure 1.3: Properties of the different messengers in Astroparticle physics. As mentioned in the text, the neutrino has the advantage of traveling from the source to the observer basically without being affected by matter or magnetic fields present in the Universe, unlike photons and cosmic rays. Credits: The IceCube Collaboration.

Several stages are needed to go from one side of the arrow to the other one. The first step is the fusion of two protons to form a deuteron through a weak interaction:

$$2p \rightarrow d + \mathrm{e}^{+} + \nu_e \tag{1.2}$$

The neutrino production through this process will be called *pp*. Another reaction producing a deuteron includes an electron:

$$p + e^{-} + p \rightarrow d + \nu_e \tag{1.3}$$

This reaction, named *pep*, however contributes only at the level of 0.4%.
Once formed, the deuteron can interact with a proton, producing a photon and a Helium-3 nucleus:

$$p + d \rightarrow {}^{3}\mathrm{He} + \gamma \tag{1.4}$$

Finally, several processes produce the Helium-4 via strong interactions. The contributions of each of them to the total production rate of Helium-4 is indicated between brackets.
One can differentiate a direct production of Helium-4:

$${}^{3}\mathrm{He} + {}^{3}\mathrm{He} \rightarrow {}^{4}\mathrm{He} + 2p \quad (85\%) \tag{1.5}$$

with the production of heavier elements that generate the helium as a side product:

$${}^{3}\mathrm{He} + {}^{4}\mathrm{He} \rightarrow {}^{7}\mathrm{Be} + \gamma \tag{1.6}$$

$$e^{-} + {}^{7}\mathrm{Be} \rightarrow {}^{7}\mathrm{Li} + \nu_e; \quad p + {}^{7}\mathrm{Li} \rightarrow 2\,{}^{4}\mathrm{He} \quad (15\%) \tag{1.7}$$

$$p + {}^{7}\mathrm{Be} \rightarrow {}^{8}\mathrm{B} + \gamma; {}^{8}\mathrm{B} \rightarrow {}^{8}\mathrm{B}^{*} + e^{+} + \nu_e; \tag{1.8}$$

$${}^{8}\mathrm{Be}^{*} \rightarrow 2\,{}^{4}\mathrm{He} \quad (0.02\%) \tag{1.9}$$

1.2.2 Characteristics of the solar neutrino flux at Earth

From the reaction chain we have just described, it is possible to estimate the resulting neutrino fluxes at Earth. The different contributions to the total solar flux are illustrated in Fig. 1.4.

The first attempts to detect this solar neutrino flux were performed in the sixties with the pioneer experiments from Davis in the Homestake mine of South Dakota [17]. Using a 615-ton tank filled of C_2Cl_4, Davis was aiming at detecting the reaction

$$\nu_e + {}^{37}\mathrm{Cl} \rightarrow e^{-} + {}^{37}\mathrm{Ar} \tag{1.10}$$

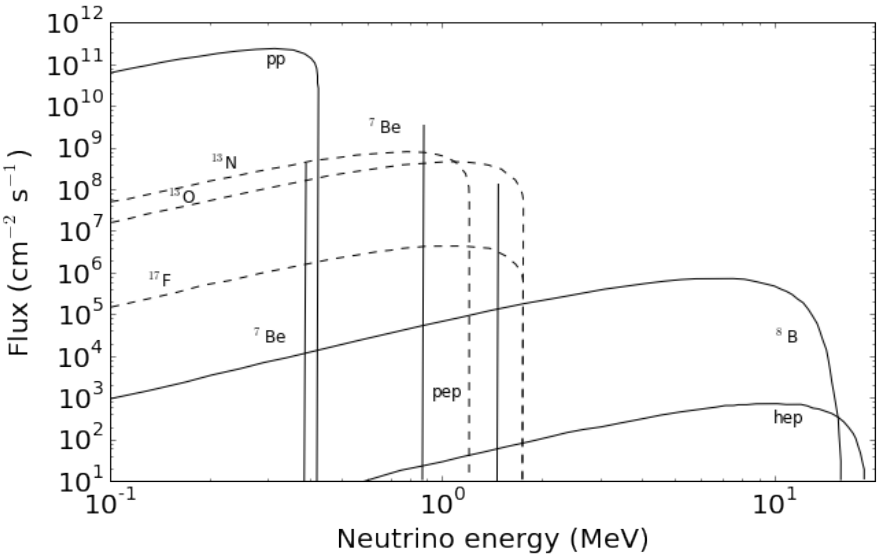

Figure 1.4: Predicted solar neutrino flux at the Earth decomposed in the different reactions as estimated by John Bahcall in 1989. Data from [16].

with an expected rate of about one Argon atom per day [16]. While the *pp* reaction is the main producer of neutrinos, with a peak below 0.5 MeV, the cross-section for the reaction presented in Eq. 1.10 varies approximatively like E_ν^3 [18]. This implies a better detector sensitivity in the energy range of Boron-8 neutrinos.

Davis and collaborators managed to detect solar neutrinos, but surprisingly the number of observed solar events was a only third of the expectations. Two possibilities could explain this discrepancy:

1 The Standard Solar model used to predict the different contributions to the solar neutrino flux was wrong

2 The nature of the neutrinos, described as massless in the Standard Model of particles, was different from the predictions

It appeared that the second hypothesis was the correct one. Discrepancies between the predicted and the observed neutrino flux have also been reported in other scenarios such as in the measured number of muon neutrinos from cosmic ray interactions in the upper atmosphere [19] or the number of electron neutrinos observed from nuclear reactors [20, 21]. Solar neutrinos therefore helped to discover an important characteristic

of the neutrino nature: it is massive [6]. This nonzero mass indeed allows the neutrino to oscillate from one flavor eigenstate to another, because they can be described as a mixing of the mass eigenstates.

Neutrino oscillation Let us call the neutrino mass eigenstates, which are the fundamental particles, ν_1, ν_2 and ν_3. As just mentioned, these mass eigenstates are different from the weak eigenstates, ν_e, ν_μ and ν_τ, which are produced in weak interactions [23].

One can write the relation between the flavor and mass eigenstates as:

$$\nu_\alpha = \sum_{k=1,2,3} U^*_{\alpha k}\, \nu_k \tag{1.11}$$

where $U^*_{\alpha k}$ are elements of the Pontecorvo-Maka-Nakagawa-Sakata, or PMNS, matrix. ν_α represents the flavor eigenstates, with α running over e, μ and τ and the mass eigenstates are represented by ν_k, where k =1, 2, 3. It is practical to rewrite the PMNS matrix using sine and cosine functions, as written in Eq. 1.12. This parametrization allows to introduce three mixing angles θ_{ij} that define the mixing composition of each flavor eigenstate. The U matrix can therefore be expressed as:

$$U = \begin{pmatrix} 1 & 0 & 0 \\ 0 & c_{23} & s_{23} \\ 0 & -s_{23} & c_{23} \end{pmatrix} \begin{pmatrix} c_{13} & 0 & s_{13}\, e^{i\delta} \\ 0 & 1 & 0 \\ -s_{13}\, e^{-i\delta} & 0 & c_{13} \end{pmatrix} \begin{pmatrix} c_{12} & s_{12} & 0 \\ -s_{12} & c_{12} & 0 \\ 0 & 0 & 1 \end{pmatrix} \begin{pmatrix} e^{i\rho_1} & 0 & 0 \\ 0 & e^{i\rho_2} & 0 \\ 0 & 0 & 1 \end{pmatrix} \tag{1.12}$$

where c_{ij} and s_{ij} represent the sine and cosine functions of the mixing angles, respectively. We note that the unitarity condition $UU^\dagger = I$ gives nine relations between the elements of the PMNS matrix, such as e.g.,

$$U_{e1}U^*_{e1} + U_{e2}U^*_{e2} + U_{e3}U^*_{e3} = 1 \tag{1.13}$$

and

$$U_{e1}U^*_{\mu 1} + U_{e2}U^*_{\mu 2} + U_{e3}U^*_{\mu 3} = 0. \tag{1.14}$$

Three complex phases δ, ρ_1 and ρ_2 are added as illustrated in Eq. 1.12. These phases violate the CP symmetry as they introduce an imaginary part that creates a different oscillation probability for neutrinos and anti-neutrinos [22]. The observation (or not) of the phases ρ_1 and ρ_2 will determine whether the neutrino is a Majorana-(Dirac-)like particle. The two additional phases for the Majorana case however do not affect the oscillation pattern. The interested reader can find more details in [24].

Let us consider the neutrino state produced in the charged-current interaction along with an electron. This state can be seen as a coherent linear superposition of mass eigenstates with a wavefunction at time $t = 0$ of

$$|\psi(0)\rangle = |\nu_e\rangle = U^*_{e1}\,|\nu_1\rangle + U^*_{e2}\,|\nu_2\rangle + U^*_{e3}\,|\nu_3\rangle \tag{1.15}$$

[6] Even though the neutrino mass is estimated to be very small, i.e. smaller than 2 eV from Tritium decay measurements [22].

More interesting is the time evolution of this state, which is determined by the evolution of the mass eigenstates, and it can be written as:

$$|\psi(\mathbf{x},t))\rangle = U^*_{e1}\,|\nu_1\rangle\,e^{-i\phi_1} + U^*_{e2}\,|\nu_2\rangle\,e^{-i\phi_2} + U^*_{e3}\,|\nu_3\rangle\,e^{-i\phi_3}, \tag{1.16}$$

with $\phi_i = (E_i t - \mathbf{p}_i.\mathbf{x})$. Replacing the mass eigenstates by the weak eigenstates and rearranging the terms for each weak eigenstate, Eq. 1.16 becomes:

$$\begin{aligned}|\psi(\mathbf{x},t))\rangle = &\left(U^*_{e1}U_{e1}e^{-i\phi_1} + U^*_{e2}U_{e2}e^{-i\phi_2} + U^*_{e3}U_{e3}e^{-i\phi_3}\right)|\nu_e\rangle \\ &+ \left(U^*_{e1}U_{\mu1}e^{-i\phi_1} + U^*_{e2}U_{\mu2}e^{-i\phi_2} + U^*_{e3}U_{\mu3}e^{-i\phi_3}\right)|\nu_\mu\rangle \\ &+ \left(U^*_{e1}U_{\tau1}e^{-i\phi_1} + U^*_{e2}U_{\tau2}e^{-i\phi_2} + U^*_{e3}U_{\tau3}e^{-i\phi_3}\right)|\nu_\tau\rangle\,. \end{aligned} \tag{1.17}$$

It is now possible to calculate the oscillation probability of this neutrino state into, e.g., a muon neutrino state

$$P(\nu_e \to \nu_\mu) = |\langle\nu_\mu|\psi(\mathbf{x},t)\rangle|^2 = \left|U^*_{e1}U_{\mu1}e^{-i\phi1} + U^*_{e2}U_{\mu2}e^{-i\phi2} + U^*_{e3}U_{\mu3}e^{-i\phi3}\right|^2. \tag{1.18}$$

From Eq. 1.18, we see that if all phases were the same, the unitarity conditions written out in Eq. 1.14 would lead to $P(\nu_e \to \nu_\mu) = 0$. To understand how to avoid phases cancellation, let us derive the phase difference between, e.g., ϕ_1 and ϕ_2 [23]:

$$\Delta\phi_{12} = \phi_1 - \phi_2 = (E_1 - E_2)\,t - (p_1 - p_2)\,x. \tag{1.19}$$

If we assume that the momenta of the mass eigenstates are equal, i.e. $p_1 = p_2 = p$ and using relation between energy, momentum and mass, Eq. 1.14 becomes

$$\Delta\phi_{12} = (E_1 - E_2)\,t = \left[\left(1 + \frac{m_1^2}{p^2}\right)^{1/2} - \left(1 + \frac{m_2^2}{p^2}\right)^{1/2}\right] t. \tag{1.20}$$

This relation directly implies that, in view of explaining oscillation, neutrinos need to be massive and the masses should not be all the same [23]. However, the masses are expected to be very small, and therefore we can assume $m << E$ and using the following approximation

$$\left(1 + \frac{m^2}{p^2}\right)^{1/2} \approx 1 + \frac{m^2}{2p^2}. \tag{1.21}$$

The phase difference in Eq. 1.19 can thus be written as:

$$\Delta\phi_{12} \approx \frac{m_1^2 - m_2^2}{2p}\,x, \tag{1.22}$$

where we assume $t \approx x$ in natural units, which follows since neutrinos are traveling at $\beta \approx 1$[7]. We note that the same result is indifferently obtained when changing the

[7]This simplified treatment does not take into account that different mass eigenstates will travel to different speed. We point the interested reader to [23] for a more accurate derivation.

assumption $p_1 = p_2 = p$ to $E_1 = E_2 = E$. The probability of oscillation presented in Eq. 1.18, generalized to three flavor oscillations, becomes

$$P(\nu_\alpha \to \nu_\beta) = \sum_{k,j} U^*_{\alpha k} U_{\beta k} U_{\alpha j} U^*_{\beta j} e^{-i\frac{\Delta m^2_{kj}}{2E}L} \tag{1.23}$$

which represents the probability of a neutrino in a flavor eigenstate α with an energy E to oscillate to a flavor eigenstate β after traveling a distance L in the vacuum.

The neutrino masses, intrinsically linked to their oscillations as mentioned earlier, appear in the relation 1.23 in the form of $\Delta m^2_{kj} = m^2_k - m^2_j$. The oscillation probability therefore depends on the mass difference rather than the masses themselves. The most up-to-date experimental limits of the involved parameters are presented in Table 1.1. These values have been obtained by studying oscillations from atmospheric neutrinos, accelerator-based experiments and the neutrino flux produced in nuclear reactors, in addition to the solar flux we described [25].

It has to be noted that neutrino oscillation measurements are one of the main priorities of the (astro)particle physics community and several experiments have been proposed, as Pingu [26], or are under construction like KM3NeT-Orca [27], DUNE [28] or JUNO [29] in view of a further understanding of this phenomenon. These future devices aim at precise measurements of the parameters presented in Table 1.1 as well as the determination of the mass hierarchy, i.e. whether ν_3 has a larger mass than ν_2 or the opposite.

Neutrino oscillation in matter We note that the presence of matter distorts the oscillation patterns described above. The neutrinos can indeed be subject to interactions when propagating through matter. As mentioned earlier, neutrinos can suffer both neutral current and charged current interactions.
The neutral current interactions have no effect on oscillation since these interactions are identical for all flavors. However, the charge current interactions mediated by the $W^\pm$ gauge boson change the oscillation pattern presented earlier. In the energy range of the solar neutrinos (a few MeV), ν_μ and ν_τ lack the energy to generate the corresponding charged lepton. The ν_e therefore gains an extra weak potential [8] compared to the other flavors. This extra potential has to be added to the mass matrix in the Dirac equation of a neutrino state, since in addition to oscillate, a ν_e can now also interact. This extra potential can be written as:

$$V_e = G_F \sqrt{2} N_e, \tag{1.24}$$

where N_e represents the electron density and G_F is the Fermi constant [16]. In particular, one can determine the electron density leading to a resonance, i.e. a maximal mixing

[8] To obtain the expression for antineutrinos, one would simply reverse the sign of the potential V_e.

Table 1.1: Current values of the neutrino oscillation parameters. These values are reported in the 2017 update of the Particle Data Group [25]. Values between rectangular brackets correspond to the inverted hierarchy case, i.e. the case where Δm^2_{32} is negative. If not mentioned, the values for the inverted hierarchy case are similar to the normal hierarchy ones within the current measurements uncertainties.

$\sin^2\theta_{12}$	$0.307\,^{+0.013}_{-0.012}$
$\sin^2\theta_{23}$	$0.538\,^{+0.03}_{-0.069}$ $[0.554\,^{+0.023}_{-0.033}]$
$\sin^2\theta_{13}$	$(2.206\,\pm 0.075\,)\times 10^{-2}$
Δm^2_{12}	$(7.40\,^{+0.021}_{-0.020})\times 10^{-5}\mathrm{eV}^2$
$\lvert\Delta m^2_{32}\rvert$	$(2.494\,^{+0.021}_{-0.020})\times 10^{-3}\,\mathrm{eV}^2$ $[(2.465\,^{+0.032}_{-0.031})\times 10^{-3}\,\mathrm{eV}^2]$

angle between the mass eigenstates:

$$N_e(res) = \frac{\Delta m^2_{1,j}\cos(2\theta_{1,j})}{2E}, \tag{1.25}$$

with j = 2, 3. The solar core matches this resonant electron density, explaining the large suppression of the solar ν_e flux and thus the deficit observed in experimental devices at the Earth.

The solar neutrino flux has therefore contributed to increase our understanding of the intrinsic nature of the neutrino. The detection of this flux allowed the Sun to be the first source observed from a multimessenger point of view, adding the neutrino signal, as illustrated in Fig. 1.5, to the electromagnetic observations.

1.3 Thermal Neutrinos

1.3.1 Neutrino production and flux in the solar plasma

This solar neutrino flux, far less known than the neutrino yield from nuclear reactions described in the previous section, is expected to be the dominant component in the keV

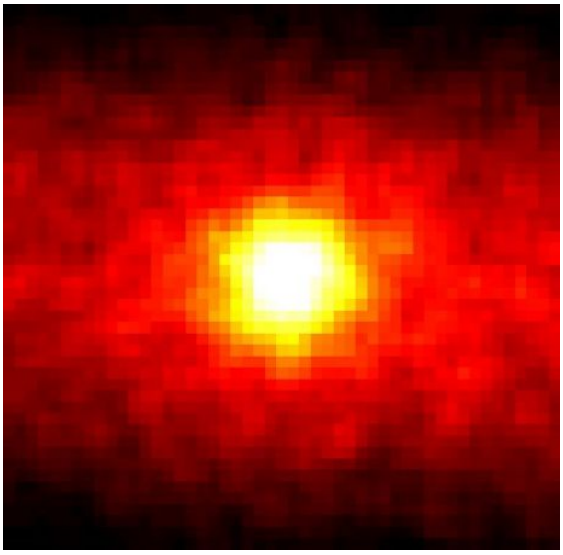

Figure 1.5: The Sun as seen in Super-Kamiokande. The figure shows the number of events in the direction of the Sun during 500 days of data. Centered on the Sun's position, the picture covers a significant fraction of the sky (90x90 degrees in right ascension and declination). Brighter colors represent a larger flux of neutrinos. Nasa Astronomy Picture of the Day, June 5, 1998.

energy range [30].
Neutrino pairs are produced by non relativistic electrons coupling to the ambient electromagnetic fields. The following processes, depicted in Fig. 1.6, contribute to the resulting thermal neutrino flux:

- Atomic deexcitation, including free-bound (fb, also known as electron capture or recombination) and bound-bound (bb) processes
- Bremsstrahlung, including free-free (ff, atomic bremsstrahlung) and electron-electron (ee) interactions
- Compton scattering
- Plasmon decay, i.e., the decay of a photon, which is kinematically allowed because of its dispersion relation in a medium.

The corresponding neutrino flux can be calculated for both the vector (V) and axial-vector (A) interactions, leading to a different yield for ν_e and the other neutrino flavors since the former can also be produced through a W boson exchange. The neutrino flux from the different types of interactions (V or A) as well as the different processes are shown in Fig. 1.7. As one can see, the flux is maximized around a few keV.

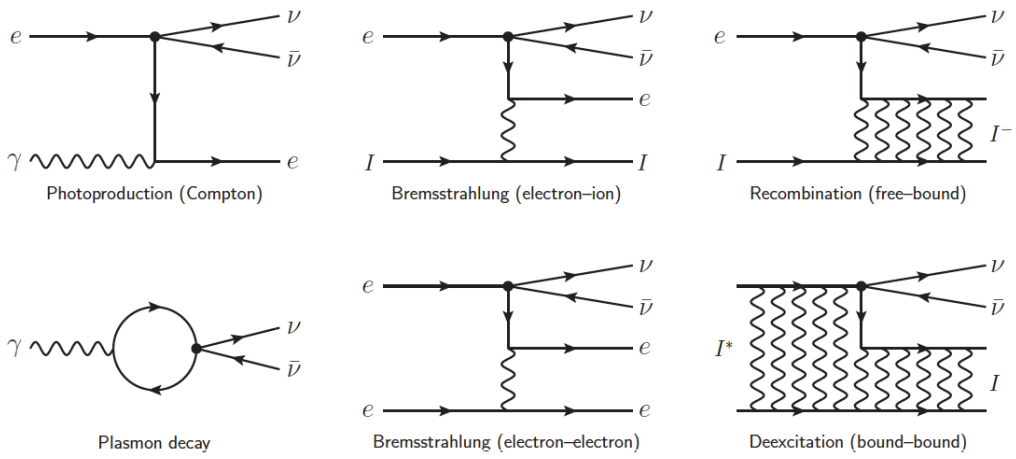

Figure 1.6: Processes contributing to the thermal neutrino flux in the keV energy range [30].

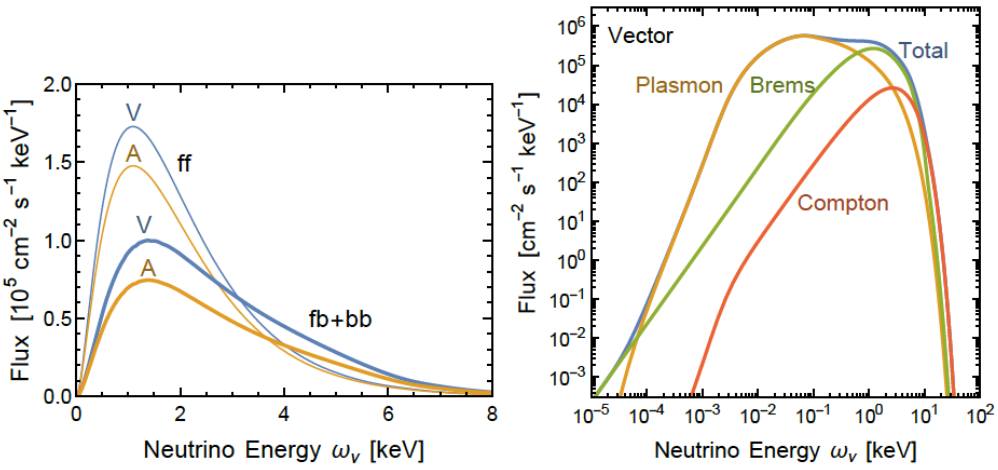

Figure 1.7: Predicted solar neutrino flux at the Earth from free-free (ff), free-bound (fb) and bound-bound (bb) electron-ion transitions for the vector (V) and axial-vector (A) contributions. Right panel: Spectrum at the Sun produced by vector coupling. Figure and caption from [30].

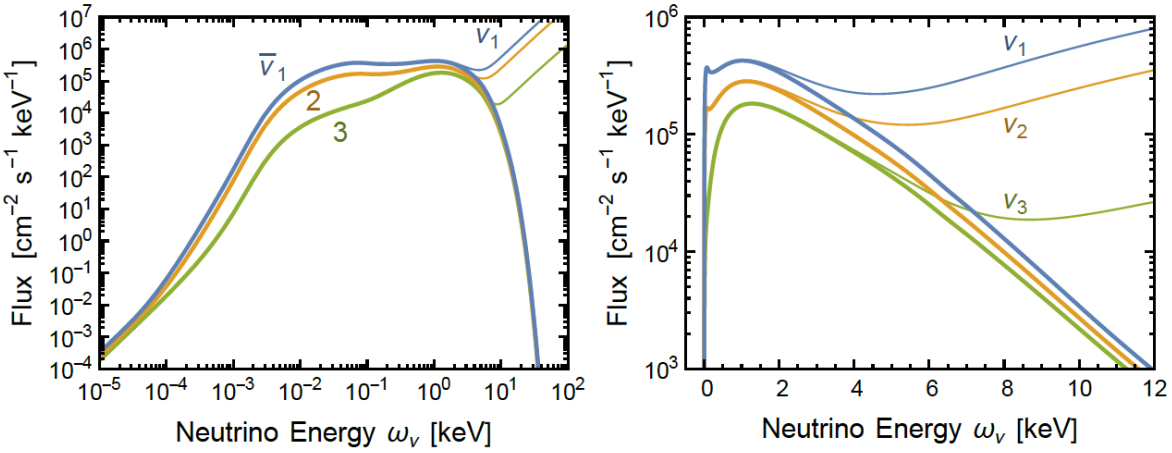

Figure 1.8: Predicted solar neutrino fluxes of different mass eigenstates at the Earth in the keV range. Thick lines are for $\bar{\nu}$, thin lines for ν, which includes a contribution of ν_e from the nuclear pp reaction. The other source channels are thermal processes, which produce both $\bar{\nu}$ and ν. Figure and caption adapted from [30].

1.3.2 Characteristics of the thermal solar neutrino flux at Earth

As outlined in the previous section, one has to account for flavor oscillations both in matter and in vacuum in order to get the solar neutrino flux at Earth. The flux produced through axial-current processes is identical to the mass eigenstate production in the Sun due to the equal production of the three flavors. The vector-current processes, however, produce almost exclusively electron neutrinos, and one has therefore to take into account flavor oscillations. We can assume vacuum oscillations only since the matter effects for keV neutrinos are negligible. Both oscillation length and scale of solar distances are negligible compared to Sun-Earth distance, allowing to consider the spectrum as an incoherent mixture of mass eigenstates. The thermal neutrino flux expected at the Earth can be derived from Fig. 1.8. Unlike the flux produced by nuclear interactions, this contribution has not been detected yet. A neutrino detector sensitive to this flux would be able to yield information about the metallicity of the Sun according to [31, 30]. This neutrino flux is also a potential background for direct searches for a possible keV-mass sterile neutrino, a promising dark matter candidate [30].

1.4 The Potential Emission from Dark Matter

1.4.1 Neutrino production and flux from WIMP annihilation

The final neutrino production mechanism that might take place at the center of the Sun is directly linked with the existence and characteristics of dark matter. We will not describe the motivation for dark matter particles as the topic is different from the scope of this thesis. The interested reader can however find a review of the dark matter evidence, particle candidates and detection techniques in [32].

Considering that a dark matter particle would have to be massive, almost non interacting and unlikely be relativistic, several candidates can be envisaged. Among them are the Weakly Interacting Massive Particles, or the so called WIMPs, which could be, for instance, the lightest of the proposed supersymmetric particles. WIMPs are a leading candidate for Cold Dark Matter and would, according to the models, carry no electric or color charge. Massive and stable, these particles are expected to interact through gravity and a force of approximatively the same strength as the Weak interaction.

Neutrinos can be produced as a result of pair annihilation of WIMPs. The produced neutrino yield is directly proportional to the number of WIMP annihilations, itself proportional to the square of the dark matter density. As outlined hereafter, high-density environments, such as the center of the Sun or the Earth, the Galactic center, or dwarf spheroidal galaxies among others, have therefore more chance to produce a detectable neutrino flux. We will focus on the requirements for a WIMP-based neutrino production scenario in the Sun [33].

WIMPs traveling in our Universe can scatter on nuclei in the Sun. This would cause a loss of energy and consequently a gravitational capture due to a speed v, which falls below the escape velocity v_{esc} needed for the Sun. One can express the total capture rate of WIMPs by the Sun as [34]:

$$C_C = \frac{\rho_{DM}}{m_\chi} \sum_i \sigma_i \int_0^{R_{Sun}} dr 4\pi r^2 n_i(r) \int_0^\infty dv 4\pi v^2 f_{Sun}(v) \frac{v^2 + v_{esc}^2}{v} p_i(v, v_{esc}), \quad (1.26)$$

where the index i varies over the nuclei that compose the Sun, σ_i is the scattering cross-section between the WIMP and the nucleus i and f_{Sun} is the velocity distribution of dark matter particles near the Sun in the rest frame of the Sun and in absence of solar gravity [34]. m_χ and ρ_{DM} are respectively the WIMP mass and the local dark matter density.

The evolution of the total number N of WIMPs inside the Sun is therefore given by:

$$\frac{dN}{dt} = C_C - C_A N^2 - C_E N \quad (1.27)$$

with C_C being the WIMP capture rate, C_A the annihilation rate coefficient and C_E the coefficient of loss due to evaporation. The last term is negligible for WIMP masses above 10 GeV, as demonstrated in [35]. Ignoring C_E, one can therefore solve Eq. 1.27 to obtain the annihilation rate $\Gamma_A = C_A N^2/2$

$$\Gamma_A = \frac{C_C}{2} \tanh^2(t_\odot/\tau) \tag{1.28}$$

where the age of the Sun is written as $t_\odot$ and $\tau = (C_C C_A)^{-1/2}$ is the time scale required to reach an equilibrium between WIMP capture and WIMP annihilation [36]. Once captured, WIMPs can annihilate with each other to form Standard Model particles. Neutrino production is expected in case of b, c and t quark production as annihilation products. A contribution from τ-leptons and gauge bosons is also expected in addition to a direct annihilation into neutrinos.

1.4.2 Characteristics of the neutrino flux at Earth

The differential neutrino fluxes expected from these different annihilation scenarios are presented in Fig. 1.9. These fluxes take into account neutrino oscillation in the Sun and on their way towards the Earth. As shown in Fig. 1.9, the neutrino flux is strongly dependent on the WIMP mass. The same exercise could also be performed using different assumptions on the initial dark matter scenario. Mediators between the dark and the standard model particles, such as dark photon, dark Higgs or many supersymmetric particles [37], may have a long decay lifetime and thus decay outside of the solar core. This delayed decay would have the effect of allowing the corresponding neutrino flux to escape the solar environment without any attenuation. The produced neutrino flux at the Earth would therefore peak at a higher energy.

This potential neutrino contribution has not been detected yet. Several searches have however been performed and allowed to set strong limits on the WIMP-nucleus cross-section as show in Fig. 1.10 [38]. While the neutrino spectrum can a priori extend to arbitrarily low energy, the limits are linked with the sensitivity of the neutrino detectors performing the search. The IceCube Collaboration holds, at the time of writing, the strongest limit on the spin-dependent WIMP-nucleon cross-section in the GeV-TeV range [38].

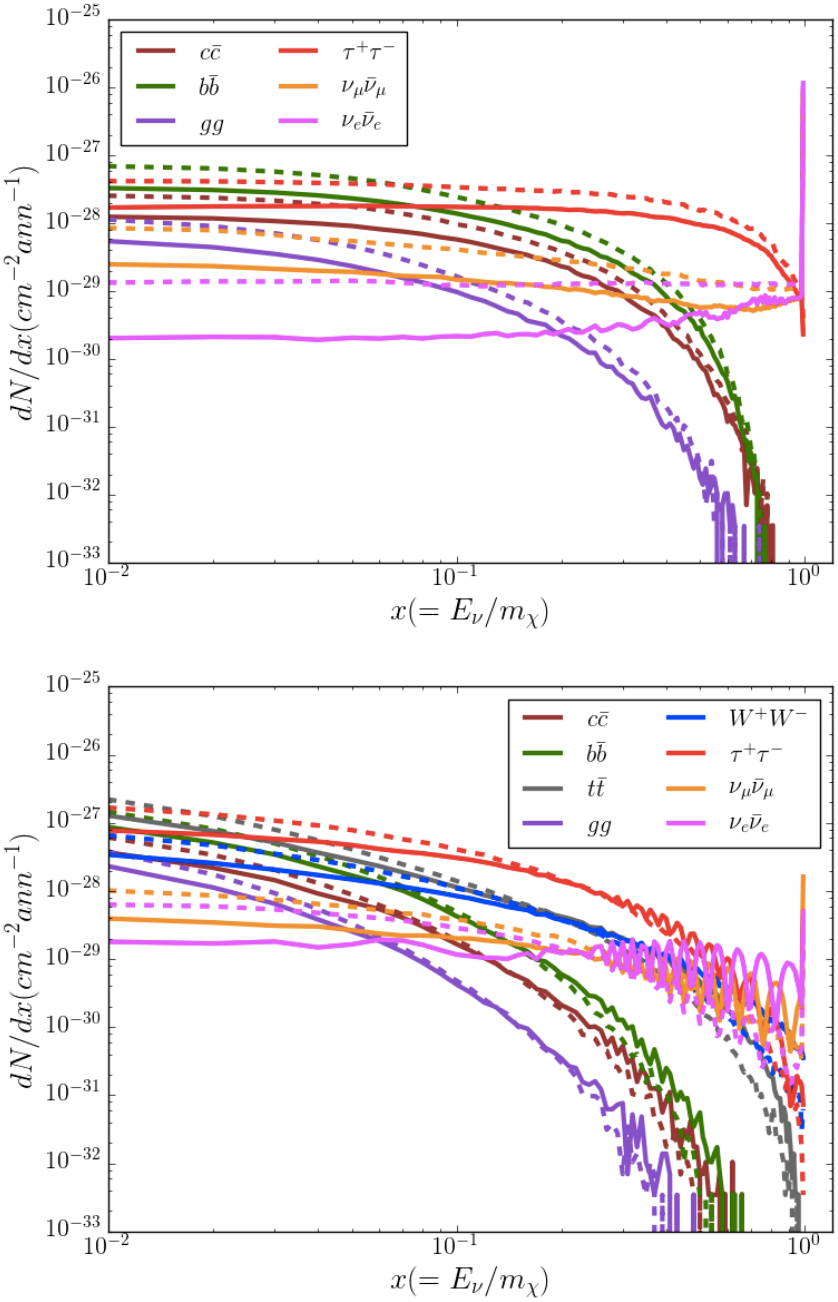

Figure 1.9: ν_μ (solid lines) and $\bar{\nu}_\mu$ (dashed lines) fluxes at the Earth as a function of the ratio of the neutrino energy and WIMP mass, for selected channels. The sharp peaks at $E_\nu/m_\chi = 1$ correspond to the primary neutrinos from the annihilation process. The neutrinos at lower energies from the $\nu_\mu\bar{\nu}_\mu$ and $\nu_e\bar{\nu}_e$ come from the interactions of some of these primary neutrinos for these channels. The top (bottom) plot corresponds to a WIMP mass of 50 GeV (1 TeV). Figure and caption from [33].

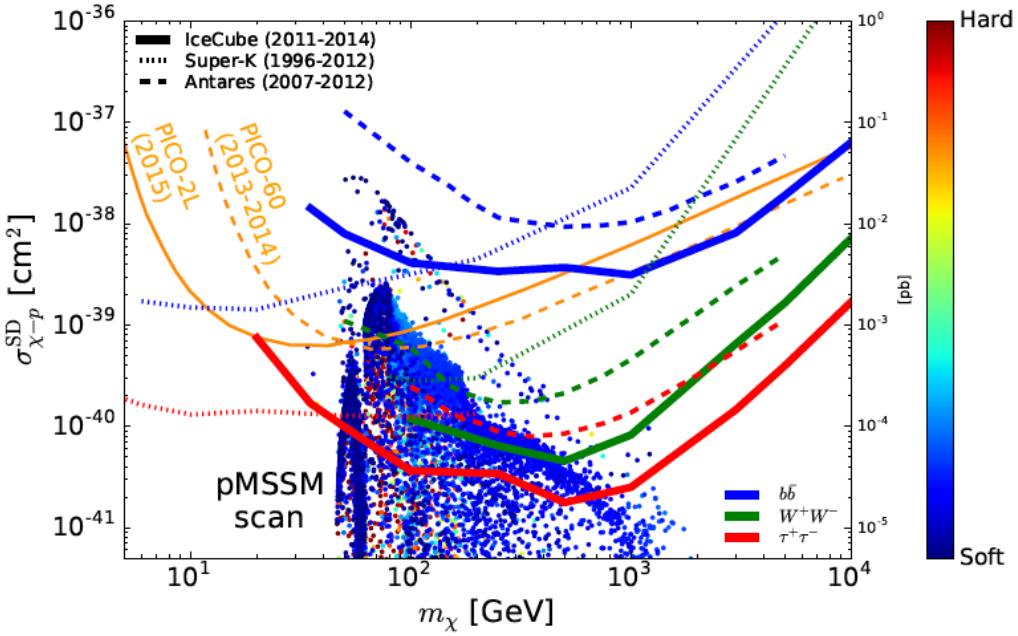

Figure 1.10: Limits on σ_{SD}, compared to the results from other neutrino detectors and direct detection experiments. The colored points correspond to various dark matter model predictions and are shown color coded by the 'hardness' of the resultant neutrino spectrum. Points close to the red end of the spectrum annihilate predominantly into harder channels such as $\tau^+\tau^-$ and can hence be excluded by the IceCube red line. Figure and caption from [38].

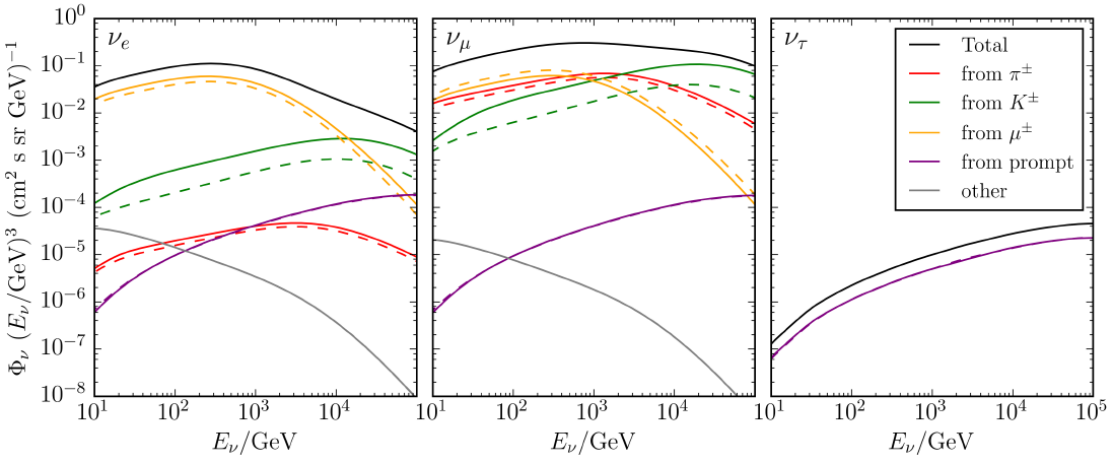

Figure 1.11: Contributions to the solar atmospheric neutrino flux at production for each neutrino flavor for impact parameter b=0. Solid lines show the contribution from neutrinos, dashed lines from antineutrinos. The black line shows the sum of neutrinos and antineutrinos of each flavor. Figure and caption from [39].

1.5 Solar Atmospheric Neutrinos

1.5.1 Neutrino production and flux in the atmosphere of the Sun

Moving towards the upper layers of the Sun, one can expect neutrino production from cosmic-ray interactions with the solar atmosphere. Similar to the interactions happening in the Earth atmosphere, hadronic cosmic rays can hit the solar atmosphere and create showers of particles. The solar atmospheric neutrino flux however distinguishes itself from the Earth atmosphere counterpart in several aspects. The neutrino flux arises from meson decays such as pions and kaons. In the solar atmosphere, most of the interactions happen in a less dense medium and extends into a larger region than its equivalent at Earth. Consequently, the high-energy mesons in the solar atmosphere have a larger chance to decay before being absorbed through inelastic interactions. The resulting high-energy solar atmospheric neutrino flux is therefore larger than the terrestrial one. However, these high-energy neutrinos might be lost through interactions with the solar material when traveling through the core towards Earth. Another difference arises from the mean free path length of high-energy muons. While those are stopped by the Earth's crust, the muons in the solar atmosphere have the chance to decay and produce neutrinos, dominating the low-energy part of the spectrum.
The so-called 'prompt' component, produced by e.g., charmed hadrons, is the only source of ν_τ while being sub-dominant compared to both ν_e and ν_μ. The different contributions to this atmospheric neutrino flux are shown on Fig. 1.11. Considering that the solar atmospheric neutrinos are produced in the atmosphere of the Sun, one expects a higher

flux from cosmic rays hitting the back side of the Sun, i.e. the part of the Sun opposite to the Earth. The neutrinos have therefore to cross the solar medium on their way towards the Earth, which will reduce the observed flux at higher energies.

1.5.2 Characteristics of the solar atmospheric neutrino flux at Earth

In order to obtain the related neutrino flux at Earth as shown in Fig. 1.12, one needs to propagate these neutrinos through the solar material and the distance between the Sun and the Earth. This solar atmospheric neutrino flux has not been detected so far. Recent predictions, see [39, 37, 40], have evaluated the sensitivity of large neutrino detectors such as IceCube or KM3NeT to this flux. It appears that a few events might be detectable per year, leading to the potential detection of a significant signal in the coming years.

Once detectable, this flux will cause an additional background for dark matter searches related to the center of the Sun. Comparable to the neutrino floor for direct detection experiments, which consists of among others the solar neutrinos described in Section 1.2, this solar atmospheric neutrino flux will constrain experimentalists to improve their detector ability to resolve direction and/or energy distribution. Most of the solar atmospheric neutrinos are indeed produced in the atmosphere, i.e. the contour of the disk, while dark matter-produced neutrinos would be arriving from the center of the disk. We also expect a different energy spectrum from these two contributions: one depends on the mass of the WIMP producing the signal while the other is determined by the cosmic-ray spectrum and composition.

Fig. 1.13 reproduces Fig. 1.10 adding the expected contribution from solar atmospheric neutrinos. As seen in Fig. 1.10, this "neutrino floor" is located one order of magnitude below the current detection limits.

1.6 Solar Flare Neutrinos

1.6.1 Neutrino production mechanism

Similarly to the flux outlined in the previous section, solar flare neutrinos are produced in the atmosphere of the Sun. The magnetic reconnection creating the solar flare has the consequence of accelerating electrons and ions constituting the solar material. The acceleration process(es) orients the particles both towards the interplanetary space direction and towards the dense solar atmosphere as shown in Fig. 1.14. Once the accelerated ions reach the Chromosphere, the higher density (10^{-13} to 10^{-7} g/cm^3) forces them to interact. If the proton energy is high enough, the threshold of pion production can be

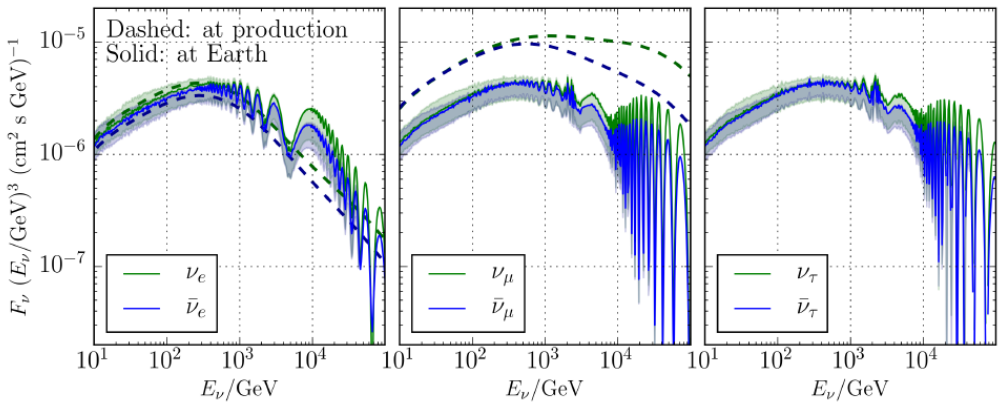

Figure 1.12: The fluxes arriving at Earth (solid) compared with those produced in the solar atmosphere (dashed). The lines show the result for a specific shower model (H4a, SIBYLL-2.3 interaction model and MRS prompt). The bands show the uncertainty region across all models. The three panels show the flux for each neutrino flavor, in both neutrinos and antineutrinos. Figure and caption from [39].

reached, giving rise to neutrino production. Several studies (see e.g., [41, 42, 43]) have demonstrated that this neutrino flux could extend from MeV up to a few GeV, covering the gap between solar neutrinos as described in Section 1.2 and 1.3 and the dark matter and atmospheric contributions of Section 1.4 and 1.5.

Besides the intermediate energy range, this neutrino flux is the only one being discontinuous since the solar flares are transient phenomena. The produced neutrino yield depends on the efficiency of the acceleration process, which varies from one flare to another, as well as the position of the flare on the solar disk. These characteristics create a unique signature for solar flare neutrinos and allow to distinguish them from the previously described neutrinos from solar origin.

1.6.2 Characteristics at Earth

Being produced in the atmosphere of the Sun in the way as indicated in Fig. 1.14, solar flare neutrinos do not suffer from matter effects on their way towards the Earth. The oscillation in vacuum, however, redistributes the flux into the three flavors.

This work aims at studying the production of these neutrinos and attempts to detect them using the IceCube Neutrino Telescope. The following chapters will therefore outline in detail the different aspects of solar flares and their corresponding neutrino flux. The solar flare process will be described in Chapter 2 together with the detected high-energy products such as gamma rays and neutrons. Chapter 3 will be dedicated to solar flare neutrino fluxes and their correlation with gamma rays. An innovative analysis to detect

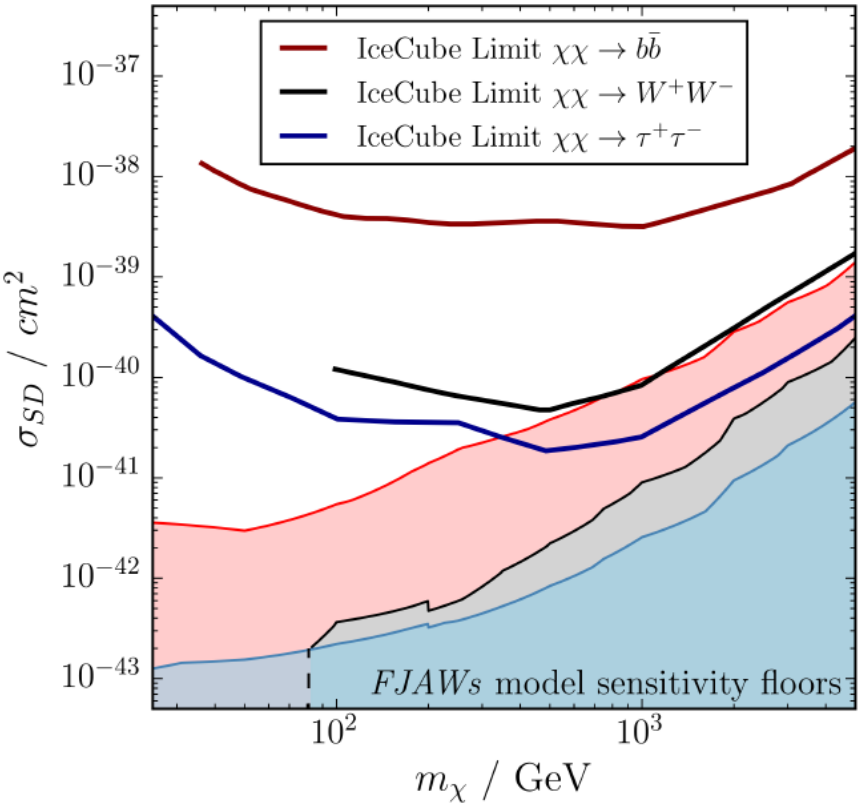

Figure 1.13: The predicted sensitivity floor compared to present experimental limits for three different dark matter annihilation channels. The lines show the 90% CL limits, and the shaded regions show the parts of parameter space which lie below the sensitivity floor imposed by solar atmospheric neutrinos. The colors of the shaded regions match the colors of the corresponding lines. Figure and caption from [39].

the interactions of these neutrinos with the South Pole ice will be presented in Chapter 5.

1.7 Summary of Solar Neutrino Fluxes

In this chapter, we have reviewed the different neutrino fluxes that could be produced in the center or the atmosphere of the Sun. These contributions extend from a few keV for the thermal neutrinos up to several TeV for the atmospheric or dark matter yields. A summary is presented in Table 1.2. While these contributions have all been theoretically studied to different extent, solar neutrinos produced by nuclear reactions as presented in Section 1.2 are the only ones to produce a significant signal in the current generation of neutrino observatories. One can however expect that the next generation of devices will offer a better sensitivity to the fluxes we described and might lead to a detection of one or several of these predicted contributions.

The aim of this chapter was to identify all possible neutrino sources related to the Sun in order to evaluate the potential background for solar flare neutrino searches. We concluded that none of them could be mistaken for a solar flare signal. All the contributions presented are indeed continuous emissions while the solar flares should produce a transient flux. However, the build up of low-energy neutrinos from solar atmospheric and potential dark matter contributions might limit the sensitivity to a transient signal. As will be described in Chapter 5, the selection of neutrino interactions in IceCube has therefore been developed and optimized accordingly.

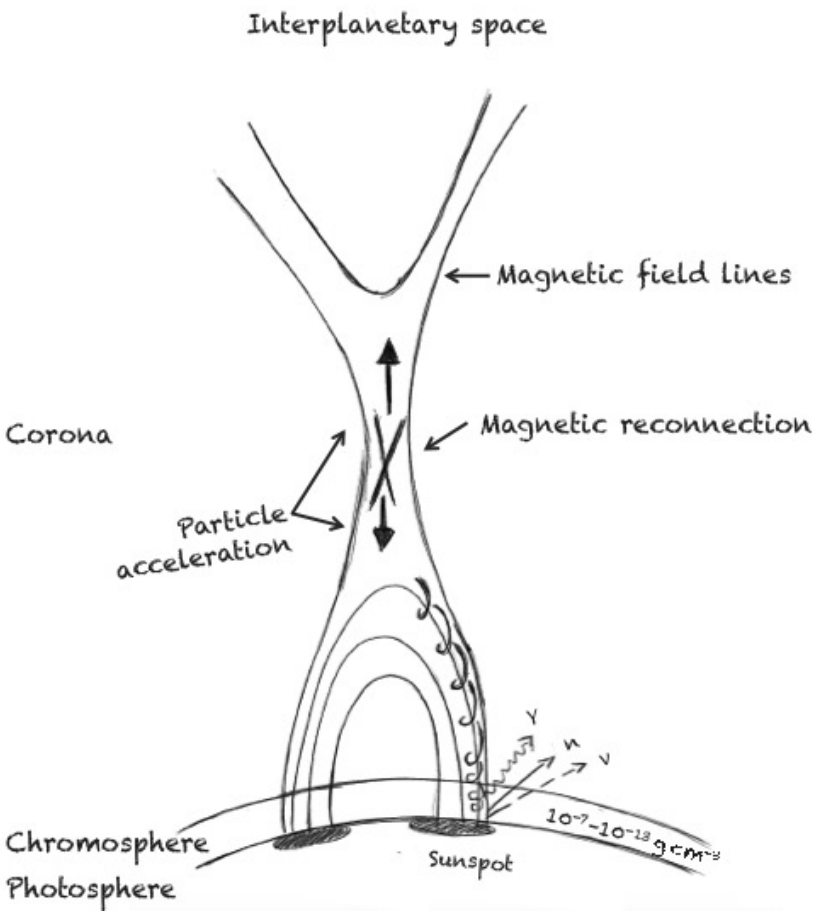

Figure 1.14: Sketch of neutrino production in solar flares. The magnetic reconnection happening during the flare provokes particle acceleration both towards the interplanetary space and the dense layers of the solar atmosphere. When entering the Chromosphere, the accelerated ions interact with the medium to create, among others, gamma rays, neutrons and neutrinos.

Table 1.2: Summary of neutrino production in the Sun. The Table presents the main characteristics of the fluxes introduced in this Chapter, as well as the expected, observed or constrained number of signal events. The neutrino devices that may be sensitive in the corresponding energy range are also mentioned.

	Energy range	Characteristics	Number of events (observed, expected, 90% C.L.)	Examples of relevant detectors
Solar neutrinos (from fusion)	0.1-20 MeV	Continuous emission Observed since 1967 [44]	$92.2^{+10.8}_{-10.6}$ events/year/kton (3.49-3.99 MeV) [45]	SuperKamiokande JUNO
Thermal neutrinos	keV	Continuous emission	To be determined	XENON1T DARWIN
Neutrinos from dark matter annihilation	GeV-TeV	Continuous emission	$<$ 45 events in 532 days (90%C.L.) [38]	IceCube KM3NeT
Solar atmospheric neutrinos	GeV-TeV	Continuous emission	$<$ 3.29 ν_μ events/year (expected) [39]	IceCube KM3NeT
Solar flare neutrinos	MeV- a few GeV	Transient emission	$<$ 18 events above 500 MeV in 40 minutes for March 7th, 2012 event (90%C.L.) (this work)	IceCube KM3NeT SuperKamiokande JUNO

Ah ! non ! c'est un peu court, jeune homme !
On pouvait dire... Oh ! Dieu !... bien des choses en somme

Cyrano de Bergerac, Premier acte, scène IV,
Edmond Rostand

2

Solar Flares: Particle Acceleration and High-Energy Emission

This Chapter introduces solar flare physics. Considering the numerous research fields required in view of developing a complete description of the phenomenon, we have to restrict ourselves to describing only the aspects directly relevant for neutrinos. Along the Chapter, the interested reader will find references containing more details about the different topics. After a short introduction on solar flares, we briefly describe three potential acceleration mechanisms that could take place in solar flares, before presenting the high-energy emissions produced as a consequence of the particle acceleration.

2.1 General Description of Solar Flares

Solar flares are gigantic explosions happening in the atmosphere of the Sun. With a released energy between 10^{28} and 10^{32} erg[1], they are among the most energetic events happening in the solar system [46]. With magnetic structures anchored in the Photosphere through the sunspots, solar flares affect all the atmospheric layers, from the Photosphere to the Corona, and can extend over 10^5 km for the largest events [46]. As will be discussed later, several temporal phases with different durations succeed each other.
Fig. 1.14 gives a schematic representation of a solar flare. Open or closed magnetic

[1] 1 erg being 10^{-7} J or 624.15 GeV.

field lines are attached to the sunspots. Closed field lines form magnetic loops that are connected to the solar surface, while open field lines reach out into the interplanetary space [47]. The existence of open field lines is a direct consequence of the magnetic reconnection process happening in the Corona. This magnetic reconnection creates the required environment for particle acceleration. The magnetic topology of solar flares is discussed in detail in [46, 47].
We first present a classification of solar flares based on X-ray observations. As described in Chapter 3, we extensively use gamma-ray observations in estimating and searching for a solar flare neutrino flux, while we do not make use of X-ray observations for this. However, the main classification of solar flares is based on *GOES* observations [48], given in the X-ray band 1-8 angstrom, and is used when referring to every solar flare happening on the visible side of the Sun. The classification uses the maximal intensity measured by GOES and converts it into a logarithmic scale, where:

- A = 10^{-8} W m^{-2}
- B = 10^{-7} W m^{-2}
- C = 10^{-6} W m^{-2}
- M = 10^{-5} W m^{-2}
- X = 10^{-4} W m^{-2}

A linear scale is used to refine this classification, using numbers between 1 and 9 representing the intensity of the flare. As an example, a C5.9 flare has a X-ray fluence of 5.9×10^{-6} W m^{-2}.

2.2 Acceleration, Propagation and Interaction of Solar Flare Particles

In this section, we will give general facts about particle acceleration, propagation and interaction in solar flares. Based on electromagnetic and neutron observations, one can expect between 10^{31} and 10^{33} protons with an energy of about 30 MeV to be accelerated during the solar flare [49, 50]. For a complete description, we recommend the review on particle acceleration and kinematics prepared by M. Aschwanden [47]. In this review, the author decomposes the flare kinematics into five different physical processes, namely: Acceleration, Injection, Propagation, Trapping and Energy loss of the solar atmospheric matter. These processes occur either in sequential order or near-simultaneously. After describing the context in which flare kinematics take place, we give a general overview of each of the above processes.

Magnetic Reconnection: The magnetic field topology influences most, if not all, of the processes mentioned above. The possibility of a magnetic reconnection, in particular, constitutes the main requirement for a solar flare to happen.
As a consequence of the emergence of a magnetic field at the surface, the pre-solar flare environment starts building up energy. The magnetic energy transported from the interior up to the solar atmosphere is indeed partially stored as field-aligned electric currents, which do not produce a Lorentz force [46]. The highly conductive medium prevents efficient dissipation of this electric current. The central engine allowing the rapid release of this energy is the magnetic reconnection, i.e. the reconfiguration of the magnetic structure into a lower state. Several models, characterized by different reconnection rates, are proposed to explain how magnetic reconnection can occur in a pre-solar flare environment. We refer the interested reader to the review proposed by Kazunari Shibata and Tetsuya Magara for details on the existing models, the two classical treatments of reconnection processes involving long current sheets or short X-points [46].

Acceleration: Three acceleration mechanisms, taking place together or separately, could potentially explain X-ray observations in solar flares[2]: Direct Current (DC) electric field acceleration, Stochastic acceleration and Shock acceleration. The summary we present here on each model is inspired from [47, 51]. Before describing the big picture of each model, let me recall that the accelerating forces acting on a charged particle depend on the time-dependent electric E(t) and magnetic B(t) fields, and can be written for a constant mass as :

$$m\frac{d\mathbf{v}(t)}{dt} = q\left[\mathbf{E}(t) + \frac{1}{c}\mathbf{v}(t)\times\mathbf{B}(t)\right] \tag{2.1}$$

DC Electric Field Acceleration: One of the simplest models to explain particle acceleration is the existence of large-scale quasi-static electric fields [51]. In the framework of solar flares, such fields could be generated in magnetic reconnection regions and charged particles would therefore be accelerated along the X-lines schematized in Fig. 1.14. One can divide the *Direct Current* models with respect to their orientation compared to the magnetic field. Eq. 2.1 could therefore be divided into parallel and perpendicular components, respectively expressed as [47]:

$$m\frac{d\mathbf{v}_{||}}{dt} = qE_{||} \tag{2.2}$$

$$m\frac{d\mathbf{v}_{\perp}}{dt} = q\left[\mathbf{E}_{\perp}(t) + \frac{1}{c}\mathbf{v}_{\perp}(t)\times\mathbf{B}(t)\right] \tag{2.3}$$

[2]It has to be noted that the entire radiative process has been mainly developed using electron-generated radiation. This is due to a poorer photon statistics at higher energy, where one would expect radiative signatures of protons and ions. The observations of Fermi-LAT as well as a potential neutrino detection would therefore help to overcome this discrepancy between electron and proton-based diagnostics.

Weak and strong fields give rise to different models and are differentiated through their magnitude with respect to the critical *Dreicer value*,

$$\epsilon_D = \frac{q_i \ln \Lambda}{4\pi\epsilon_0 \lambda_D^2}, \tag{2.4}$$

where $\ln \Lambda$ is the Coulomb logarithm and λ_D represents the Debye length. Sub-Dreicer electric fields ($E < \epsilon_D$), inevitably aligned to the magnetic field to avoid E×B drift that would disrupt the acceleration, are able to accelerate electrons up to $<$ 100 keV [51]. The model therefore encounters difficulties to explain the high-energy solar flare emissions we describe later in the Chapter. Super-Dreicer fields are more realistic as they require a significantly smaller current sheet than sub-Dreicer DC models. However, the electric field, created by the inflow v of solar material during the reconnection, takes the form $E = v \times B$ and therefore limits the maximum energy an electron could reach to $<$ 100 keV due to the E×B drift previously mentioned [51]. This group of models therefore experiences issues explaining the high-energy emissions we are interested in but the energy gain is sufficient for the bulk of electrons observed in most hard X-ray flares [47].

Stochastic Acceleration Another proposed mechanism for particle acceleration is based on a statistical process of gain and loss of energy in electromagnetic wave-particle interactions on short intervals, with an overall gain on long-time average. Originally proposed by Enrico Fermi, this model is generally referred to as *second order Fermi* process. An illustration is presented in Fig. 2.1. The frequency ω and wave factor k of the waves play an important role in the determination of the energy gain. The process indeed depends on the wave turbulence level, function of the wave factor, the particle velocity distribution and the dispersion relation of the resonant waves.

Let us assume electromagnetic waves, characterized by a dispersion relation $\omega(k)$ and a particle with a speed v, a relativistic Lorentz factor $\gamma = 1/\sqrt{1-(v/c)^2}$, which gyrates in a guiding magnetic field with a gyroperiod $\Omega = eB/m_e c$. The fundamental coupling between the electromagnetic waves and the particle is the *Doppler resonance condition* [47],

$$\omega - s\Omega/\gamma = k_{||}\, v_{||}, \tag{2.5}$$

which specifies when the gyromotion is in phase with the Doppler-shifted wave vector. The maximum efficiency is reached when the above condition is fulfilled. In view of showing the dependence on the wave dispersion relation $\omega(k)$, Eq. 2.5 can be rewritten as:

$$\omega - s\Omega/\gamma = kc\,\beta\, \cos\vartheta\, \cos\alpha, \tag{2.6}$$

where

- s is the harmonic number.

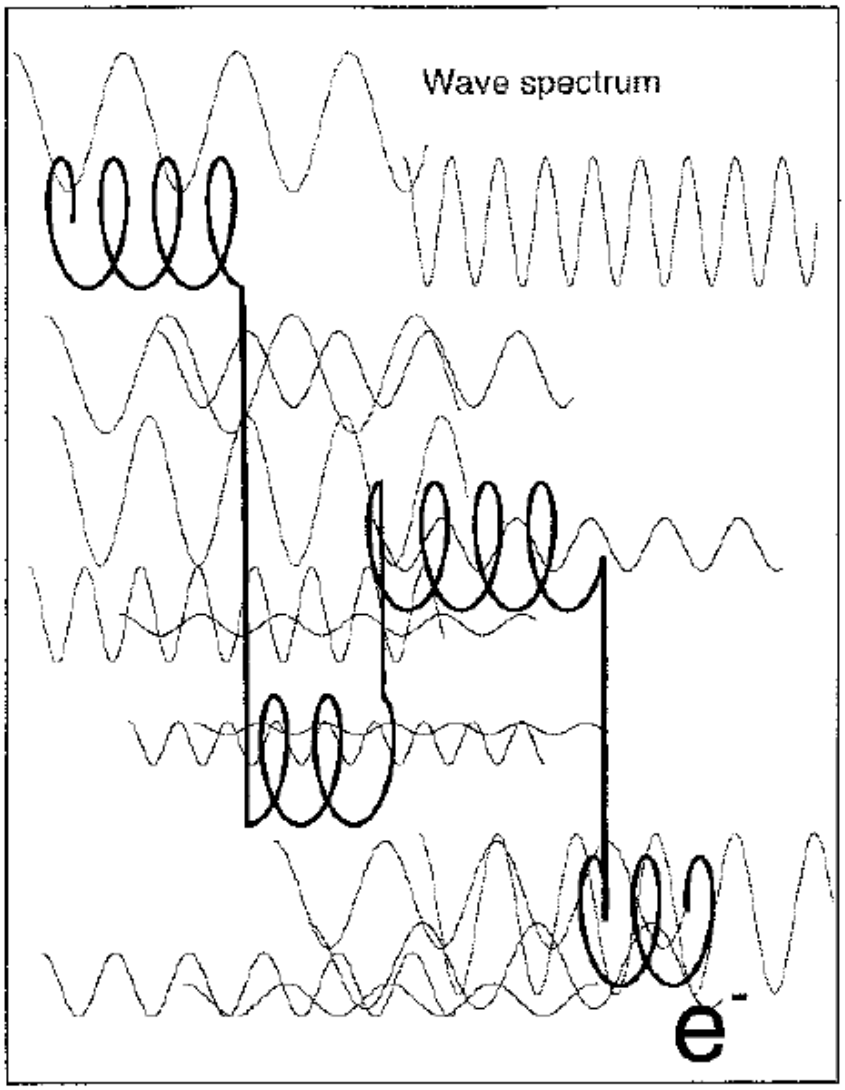

Figure 2.1: Cartoon of a stochastic acceleration process. A charged particle (e.g. an electron here) executes its gyromotion around the guiding magnetic field. If the Doppler-shifted gyrofrequency is in phase with the frequency of waves, the electron experiences the electromagnetic field of the resonant waves and is accelerated until it becomes detuned. If a broad wave spectrum is present, the electron suffers many random acceleration and deceleration episodes, which add up to a net gain in energy for suitable wave spectra. Figure and caption from [47].

- $\beta = v/c$ is the relativistic speed.
- $\alpha = \arccos(v_{||}/v)$ is the pitch angle of the particle. This parameter will be used later in the Chapter.
- $\vartheta = \arccos(k_{||}/k)$ is the angle of the wave vector to the guiding magnetic field.

However, ω values do not generally lead to the Doppler resonance and energy gains and losses succeed each other, as shown in Fig. 2.1. Details about this mechanism can be found in [47, 51]. The spectrum of accelerated protons using this model has the form [52]

$$N(E) = K_2 \left[2 \left(3p/m_p c\alpha T\right)^{1/2}\right], \tag{2.7}$$

where $N(E)$ is the number of particles per unit kinetic energy per nucleon E, p is the momentum per nucleon, m_p is the mass of the proton and K_2 is a modified Bessel function. This spectrum is characterized by αT, with α being the acceleration efficiency and T the time to escape the acceleration site. This combination corresponds to the steepness of the spectrum, meaning that larger values of αT lead to harder spectra (i.e. more high-energy particles) [52]. Stochastic acceleration models have several advantages over the sus-mentioned DC acceleration [47]. Among them, we emphasize that the acceleration volume is potentially much larger than the direct vicinity of the reconnection point in a current sheet.

Shock Acceleration: Generally the most accepted model to describe efficient particle acceleration in astrophysical objects, the acceleration mechanism through shock waves, is also believed to play an important role in solar flares. Known as the *Fermi acceleration of first order*, the model uses shock waves propagating faster than the sound speed in the ambient medium. The particles to-be-accelerated cross the shock back and forth as this one moves along a given direction.
Assume a strong shock wave traveling at a highly supersonic velocity U and consider the frame of reference in which this shock front is at rest. Let us give the following properties to the upstream gas flowing into the shock: (p_1, T_1, ρ_1), with $v_1 = U$ [53]. The downstream gas will then be (p_2, T_2, ρ_2). To ensure the mass conservation through the shock, we use the equation of continuity:

$$\rho_1 v_1 = \rho_2 v_2, \tag{2.8}$$

and consider the case of a strong shock, i.e. $\rho_2/\rho_1 = (\gamma+1)/(\gamma-1)$, where γ the ratio of specific heat capacities of the gas and equals 5/3 in case of a fully ionised gas as it is the case in the solar flare environment. We therefore obtain

$$\rho_2/\rho_1 = 4, \text{ and thus } v_2 = \frac{1}{4} v_1. \tag{2.9}$$

Let us consider the particles ahead of the shock. Their scattering ensures an isotropic distribution in the frame of reference where the ambient medium is at rest. The shock

advances through the medium at velocity U but the gas behind the shock travels at a velocity $3/4U$ with respect to the upstream gas. If we now consider the particles behind the shock, they meet a gas moving towards the shock front, with a similar velocity of $3/4U$ [53]. We then conclude that particles on both sides of the shock encounter the same process, ensuring that each crossing of the shock front will increase the particle energy. Continuing to follow the derivation presented in [53], we can perform a Lorentz transformation, to obtain the energy of the particle when it passes into the downstream gas:

$$E' = \gamma_V (E + p_x V), \tag{2.10}$$

where we have defined $V = 3/4U$, and placing the x-coordinate perpendicular to the shock. Assuming relativistic particles, i.e. $E = pc$ and $p_x = (E/c)\cos\theta$, and a non-relativistic shock $U << c$, we obtain

$$\Delta E = pV\cos\theta, \text{ and thus } \frac{\Delta E}{E} = \frac{V}{c}\cos\theta. \tag{2.11}$$

As explained in [53], the probability for a particle to cross the shock with an angle between θ and $\theta + d\theta$, normalised so that the integral of the probability distribution over all the particles approaching the shock is equal to 1,

$$P(\theta) = 2\sin\theta\cos\theta d\theta, \tag{2.12}$$

Eq. 2.11 therefore becomes

$$\left\langle \frac{\Delta E}{E} \right\rangle = \frac{V}{c}\int_0^{\pi/2} 2\cos^2\theta\sin\theta d\theta = \frac{2}{3}\frac{V}{c}. \tag{2.13}$$

The energy gain after each round trip is therefore

$$\left\langle \frac{\Delta E}{E} \right\rangle = \frac{4}{3}\frac{V}{c}. \tag{2.14}$$

The spectrum of the particle flux accelerated through shocks varies as a power law of the particle energy, $N(E) \propto E^{-s}$, s being called the spectral index, as shown in [53]. For solar flares, this model is considered as a viable mechanism to accelerate ions up to ≈ 100 MeV within ≤ 1 s and simulations confirmed that the proposed mechanism could explain the observed gamma-ray energies. The detailed application to solar flares can be read in [47, 51].

Injection: Once accelerated, the particles need to escape the acceleration regions. In case of DC electric field acceleration, the particles leave the acceleration path directly and continue their propagation, leading to an injection time equals zero [47]. However, for stochastic and shock acceleration, as well as a few DC field models, an injection mechanism is required to deflect the particle out of the trap where it has been accelerated. A macroscopic change of the magnetic structure or miscroscopic modifications, e.g., changes in the pitch angle of the particle in a turbulent region, could be efficient injection models. Details can be found in [51].

Propagation: As mentioned in [51], the plasma surrounding the acceleration region can be considered as collisionless for electrons with energies > 20 keV. This means one can assume a free-streaming particle propagation into the medium, where the particle orbits are defined by their gyromotion around the magnetic field line. The orbits can be calculated by integrating Eq. 2.1 under the considered assumptions. In view of determining the propagation of particles from the acceleration site to the interaction region, one therefore needs to know the velocity of the particle, its initial pitch angle and the magnetic field in which the particle propagates.

Trapping: Particles can be trapped in a magnetic structure. This process happens simultaneously to the propagation. Some particles directly propagate to the energy loss region, i.e. interaction site, whereas others get stored in a magnetic trap and could be mirrored many times before finally losing their energy or interacting [47]. The second option, i.e. the trapping, is expected in case of a broad pitch angle distribution. It also requires a magnetic mirror ratio larger than unity, i.e.

$$R = \frac{B(s = s_M)}{B_0} > 1, \tag{2.15}$$

where B(s=s_M) and B_0 are the magnetic field strength at the mirror point and looptop respectively [51]. We note that B_0 = B(s = 0) represents the (minimum) magnetic field strength at the top of the magnetic loop. The position of the mirror point at s = s_M is given by the interface from the collisionless to the collisional regime. The trapping of accelerated protons in magnetic loops of low density could explain the extended emission of gamma rays detailed at the end of this Chapter. Details about the propagation and trapping processes can be read in [47, 51].

Energy loss: The particle has finally reached the region where it collides with the solar atmosphere and creates, in the case of interest in this thesis, mesons that could later decay into neutrinos. It is possible to localize the interaction region using solar flare observations. One can differentiate thin-target from thick-target interactions [49]. In the thick-target interaction hypothesis, the accelerated particles interact when slowing down in the dense solar atmosphere instead of interacting directly after escaping the acceleration site where the density is much lower. The thick-target interactions have been preferred over thin-target ones mainly because of several observational effects. Among these observations we can cite that:

- As mentioned in [49], rapid slowing down and annihilation of the positrons are observed. This requires a high density medium, allowing to exclude annihilation in the Corona,
- In parallel, observations of high-energy neutrons have been made for limb flares[3].

[3] *Limb* flares are solar flares happening on the edge of the visible solar disk.

This directly gives an upper limit on the density, preventing otherwise the neutrons to escape. Through these observations, the interaction region was estimated to be above the Photosphere.

Combining these two facts, the thick-target interaction region appears to be located in the Chromosphere [49]. The localization of the interaction region is of great importance for the production of neutrinos. As described in Chapter 3, the simulation of proton-ion interactions during solar flares leads to an estimate of the interaction region density similar to what is obtained with observational considerations.

2.3 Observed High-Energy Emissions

We summarize the different emissions related to high-energy proton collisions in the solar flare environment. This brief description will be useful to optimize solar flare neutrino searches using a multi-messenger approach.

X-ray and Gamma ray observations While solar flares emit radiation across the whole electromagnetic spectrum, we focus on the high energy photons because of their intrinsic relationship with neutrinos. Fig. 2.2 shows the photon spectrum between 1 keV and 100 MeV. Several features can be distinguished [54]:

- Continuous emission below 0.5 MeV, due to hot and superhot thermal flare plasmas as well as bremsstrahlung emission from energetic electrons.
- Gamma-ray lines: we can cite in addition to several nuclear de-excitation lines, the neutron capture by Hydrogen at 2.223 MeV and the positron annihilation line at 0.511 MeV. While the study of these lines has provided numerous constraints on the composition, i.e. numbers and energetic ion abundance, accelerated ion spectra and acceleration timescales, we will not detail these features as they are not directly linked with the production of neutrinos. We recommend the interested reader to consult [54, 55] for more details about these lines.
- Gamma-ray continuum: In addition to these lines, interactions of energetic ions with the solar atmosphere can produce pions. These pions decay into gamma rays (π^0) or electrons and positrons ($\pi^{+/-}$) that yield gamma rays via bremsstrahlung. The contribution of each process is illustrated in Fig. 2.3, where one can see that the spectrum extends up to a few GeV.

The first convincing observation of π^0-decay radiation was made during the solar flare of June 3rd, 1982, by the *SMM-GRS* instrument[4] [54]. The pion production was observed

[4] *Solar Maximum Mission Gamma-Ray Spectrometer*, satellite operating in the 1980s.

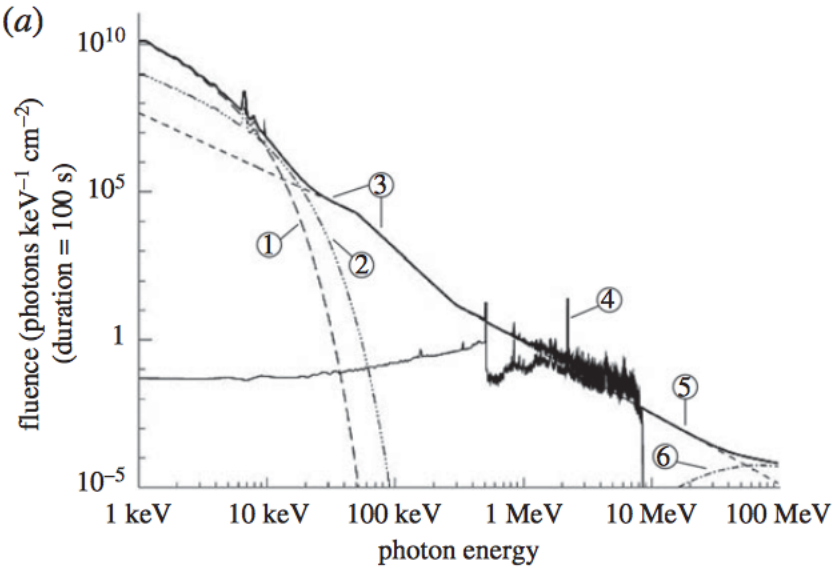

Figure 2.2: Composite X-ray/gamma-ray spectrum from 1 keV to 100 MeV for a large flare. At energies up to ≃10-30 keV, emission from hot (≃10^7 K; curve 1) and superhot (≃3 × 10^7 K; curve 2) thermal flare plasmas. Bremsstrahlung emission from energetic electrons produces the X-ray/ gamma-ray continuum (curves 3 and 5) up to tens of MeV. Broad and narrow gamma-ray lines from nuclear interactions of energetic ions sometimes dominate the spectrum between ≃1 and 7 MeV (curve 4). Above 70 MeV, the photons produced by the decay of neutral pions (curve 6) sometimes dominate. Figure and caption adapted from [55].

during the *impulsive phase*, defined by the onset of hard X-rays near 10 keV, but also in an *extended phase* well after the X-ray peak [54]. The numerous observations made during this first *pion flare* have allowed to put constraints on the accelerated proton spectrum [49]. We therefore used this flare, in addition to more recent ones, as a benchmark for the simulation presented in Chapter 3. Emission of pion-decay products has been confirmed on several flares later on, both in the impulsive and in the long duration phases[5].

The *Fermi* Observatory, launched 10 years ago, in 2008, consists of two instruments: the *Gamma-ray Burst Monitor* (GBM) and the *Large Area Telescope* (LAT). As described in [56, 57], the energy range covered by these instruments, ranges from 8 keV up to 300 GeV, and the sky coverage, not-occulted for GBM and 20 % for the LAT, make Fermi an ideal observatory to study solar flares. Fermi-LAT especially, detecting gamma rays above 100 MeV, will be an asset in the detection of solar flare neutrinos, as described in Chapter 3. Fermi has substantially increased the amount of solar flares detected in the high energy range (> 25 MeV) as illustrated in Fig. 2.4. The spectral

[5]These two different phases will be described in the next Chapter, using Fermi-LAT observations.

analysis of Fermi observations has confirmed that pion-decay was most likely producing the detected gamma rays [50]. Another significant achievement of the LAT in the solar flare area, was to detect solar flares happening behind the limb. Solar flares that happen on the hidden face of the Sun have their interaction region, where most of the hard X-rays and gamma rays are produced, not visible from a terrestrial orbit. X-ray observatories such as *GOES* cannot therefore detect them. Fermi-LAT however managed to detect 3 events, with one of them being among the most significant detected during the 10 years of Fermi operation. These detections suggest the potential existence of a spatially extended component for high-energy gamma-rays [58]. As will be mentioned in the next Chapter, these events are especially promising for neutrino searches. We searched for neutrinos during the most significant of these events, and the results are presented in Chapter 6.

Neutron observations As mentioned in e.g., [47], neutrons can be produced by the interactions of accelerated ions with the ambient solar atmosphere. If the neutron manages to escape the dense environment, it can propagate directly towards us and produce a cascade in our atmosphere that could be detected by ground monitors. We expect the events detected by neutron monitors on the ground to be related to ions accelerated to energies between 0.1 and 10 GeV [47]. Despite the fact that these neutrons are linked with high-energy proton acceleration in solar flares, we will not use them in this work. As described in the next Chapter, we chose to work with gamma rays considering their special link with neutrinos through their common pion production.

SEP observations Some of the accelerated particles can escape the acceleration site and propagate towards interplanetary space instead of down to denser layers of the solar atmosphere. This escape is made possible through the existence of open magnetic field lines formed as a consequence of the magnetic reconnection happening in the Corona. Known as *Solar Energetic Particles* or SEPs, these particles may suffer additional or different acceleration mechanisms than the particles colliding with the solar atmosphere [47]. As stated at the end of Chapter 3, comparing the observations of gamma rays and neutrinos with SEP observations made by, e.g. [59], may help solving the open question of particle acceleration in solar flares. As an illustration, we can take the constraints on the high-energy cutoff: an incompatibility between constraints set using escaping protons, i.e. SEPs, and constraints from joint gamma ray and neutrino observations produced by accelerated protons colliding with the solar atmosphere, would directly point towards the existence of different mechanisms accelerating these two populations. We advise the interested reader the brief review by J. Ryan et al. [60], where a comparison between colliding and escaping particles is presented.

We note that the surface array of IceCube (see Chapter 4 for details), IceTop, has observed, while still under construction, the first extraterrestrial events seen by the

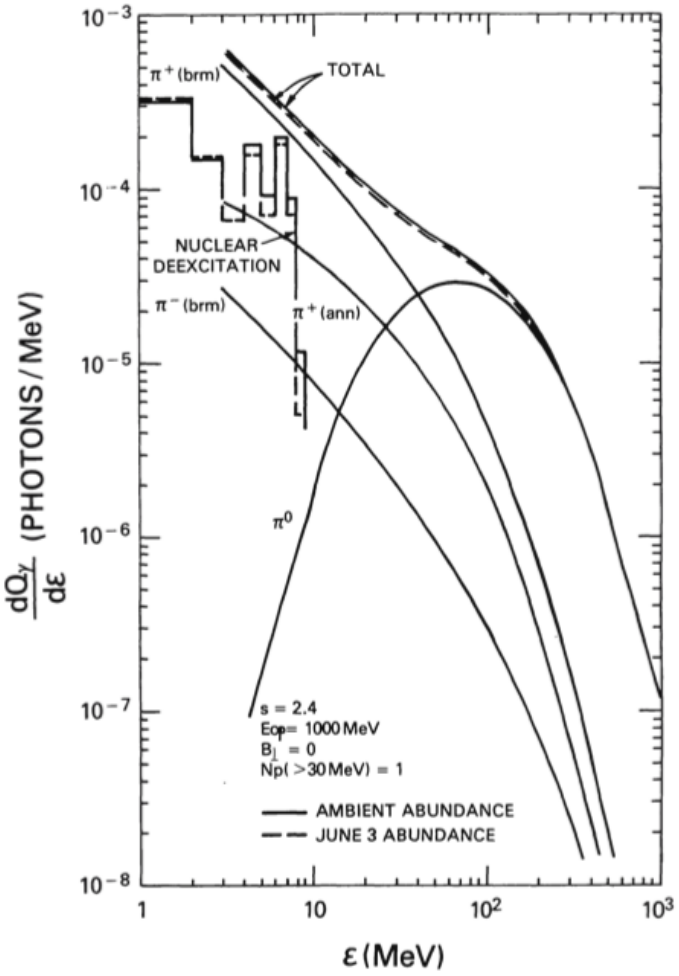

Figure 2.3: Gamma-ray spectrum resulting from pion production and nuclear de-excitation for a primary shock-acceleration spectrum with s = 2.4, E_{max} = 1000 MeV and ambient composition. The total gamma-ray spectrum for a primary composition given by the June 3rd, 1982 flare composition is shown by the dashed curve and the histogram. Figure and caption adapted from [52].

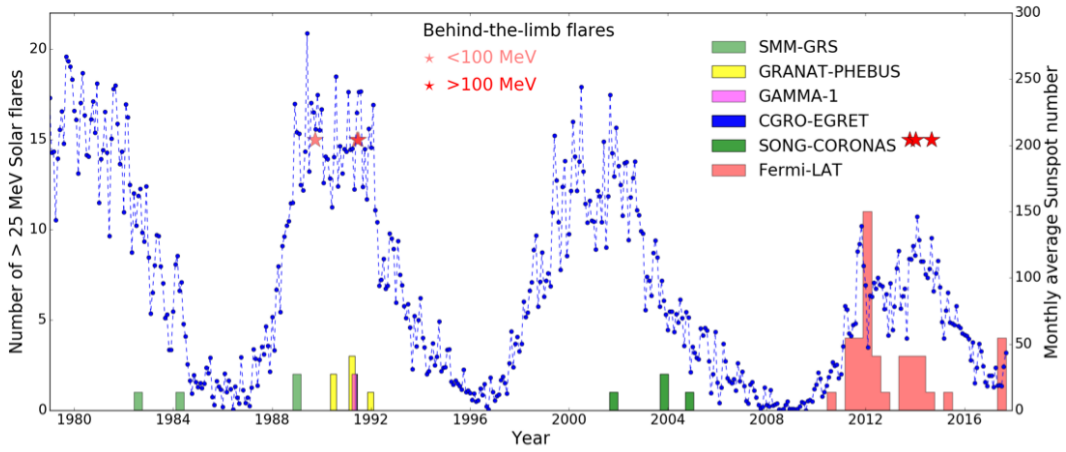

Figure 2.4: Number of solar flares with observed emission >25 MeV (left axis) together with the monthly averaged sunspot numbers (right axis) from 1980 to present. The light red stars represent the behind-the-limb solar flares detected with emission <100 MeV and the dark stars represent the behind-the-limb solar flares detected with emission >100 MeV. Figure and caption from [58].

IceCube observatory. IceTop was indeed able to detect the Ground Level Enhancement (GLE) after a solar flare (X3.4) on December 13th, 2006. Furthermore, the observations allowed to derive a time dependent spectrum of the solar particles [61]. It therefore means that when the in-ice component of IceCube will be sensitive to solar flare neutrinos, the IceCube Collaboration will be able to offer a general view of the high-energy process in solar flares, observing both the escaping and colliding-product particles.

De Guiche: *Qu'un moulinet de leurs grands bras chargés de toiles*
Vous lance dans la boue !...
Cyrano: *ou bien dans les étoiles !*

Cyrano de Bergerac, Deuxième acte, scène VII,
Edmond Rostand

3

Solar Flare Neutrinos and Prospects for Observation in Large Neutrino Telescopes

This Chapter is dedicated to solar flare neutrinos. We first describe the production mechanism before summarizing previous attempts to detect these. We then present an optimization procedure for the selection of every component that would be used in a neutrino search. We present a selection of solar flares as well as a definition of the optimal time window that could be used in neutrino searches. In the second part of the Chapter, we present the results of a Geant4 simulation we have designed in view of estimating the neutrino flux that may be produced in solar flares. We study how the characteristics of the accelerated ion spectrum could influence the resulting neutrino flux. We conclude by describing the potential science case for neutrino detectors in solar flare physics.

3.1 Solar Flare Neutrinos: Context and History

Producing solar flare neutrinos As previously mentioned, solar flare neutrinos are produced through pion decays. These pions are emitted when the ion flux, accelerated during the solar flare, has sufficient energy to exceed the pion production threshold when colliding with the ambient medium. Eq. 3.1 presents the possible production processes,

where the energy thresholds are 280 MeV and 180 MeV for p-p and p-α respectively.

$$p + p \text{ or } p + \alpha \longrightarrow \begin{cases} \pi^+ + X; & \pi^+ \longrightarrow \mu^+ + \nu_\mu;\ \mu^+ \longrightarrow e^+ + \nu_e + \bar{\nu}_\mu \\ \pi^0 + X; & \pi^0 \longrightarrow 2\gamma \\ \pi^- + X; & \pi^- \longrightarrow \mu^- + \bar{\nu}_\mu;\ \mu^- \longrightarrow e^- + \bar{\nu}_e + \nu_\mu \end{cases} \tag{3.1}$$

The gamma rays, produced by the decay of neutral pion as illustrated in Eq. 3.1, are of great interest in neutrino searches as already mentioned in the previous Chapter. The common production process via pion decay, indeed guarantees the joint emission of these gamma-rays and neutrinos. The observed gamma spectrum can therefore serve as a template for neutrino searches. The analysis described in the following chapters makes an extensive use of this special link between gamma rays and neutrinos.

Attempting to detect solar flare neutrinos In the late eighties, the Homestake Collaboration reported an increase in the event rate of their experiment, potentially due to large solar flares [62]. If this increase were indeed due to solar flares, it would lead to large characteristic signals in large neutrino detectors, according to the prediction of J.N. Bahcall [63]. In response, experiments such as Kamiokande [64] and the Sudbury Neutrino Observatory (SNO) [65] performed several searches. Even though different solar flare samples and analyses were used, the experiments were not able to confirm the potential signal seen by Homestake. Constraints have been set on the solar flare neutrino flux between 2 and 35 MeV. Fig. 3.1 shows the limits set by Kamiokande and SNO, as well as the excess seen in Homestake. As will be detailed later in this thesis, this work targets the upper part of the neutrino spectrum, located in the GeV range. We will therefore not be able to directly compare our findings with the limits presented in Fig. 3.1.

3.2 Selecting Solar Flares of Interest

As will be outlined in Chapter 4, the IceCube Neutrino Observatory has a lower threshold of 10 GeV for reconstructible neutrino induced events. Even though we developed a new event selection allowing to lower the threshold down to the GeV level, optimizing the signal over background ratio in IceCube through the selection of favorable solar flares would further help to increase the sensitivity for neutrino searches. The combination of the solar flare and neutrino event selections allowed us to carry out the first search in the upper part of the solar flare neutrino spectrum. As mentioned at the end of this Chapter, probing the upper part of the spectrum enables to probe the characteristics of the accelerated ion spectrum, and especially its high-energy cutoff.

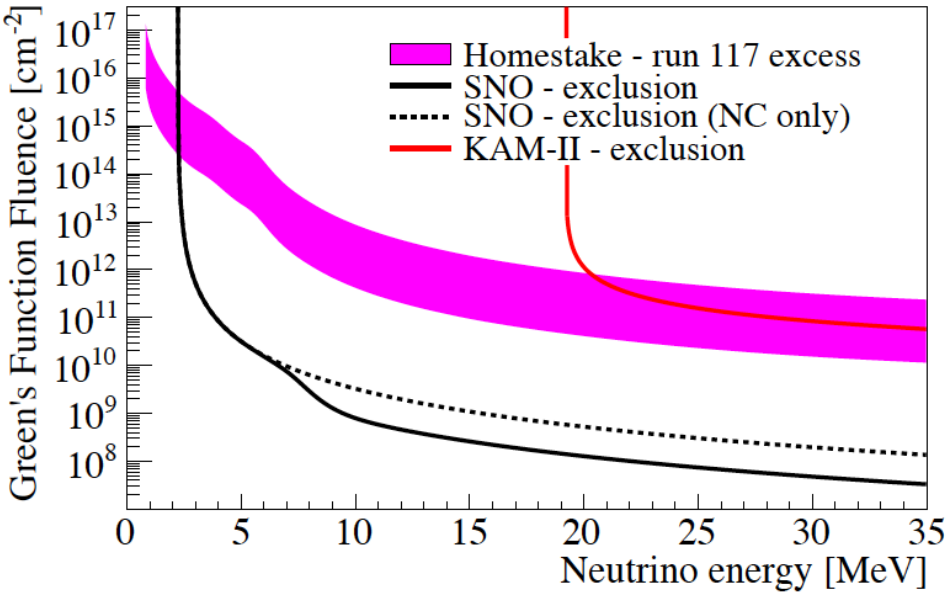

Figure 3.1: Fluence of neutrinos from solar flares versus neutrino energy. The excess shown for Homestake occured during run 117, which corresponded to a large solar flare. The Homestake result is obtained assuming the excess in run 117 is attributed to a large solar flare. The results for all experiments are calculated assuming pure ν_e production in the solar atmosphere and include vacuum oscillations during their journey to Earth. The results for Kam II are recalculated from [64] based on this model and assuming a 100% detection efficiency for scattered electrons above 19 MeV and 0% efficiency below this. Due to the lack of well known spectra, the figure expresses the limits on neutrino fluences at the detector in terms of *Green's function fluence* for mono-energetic neutrinos. Figure and caption adapted from [65].

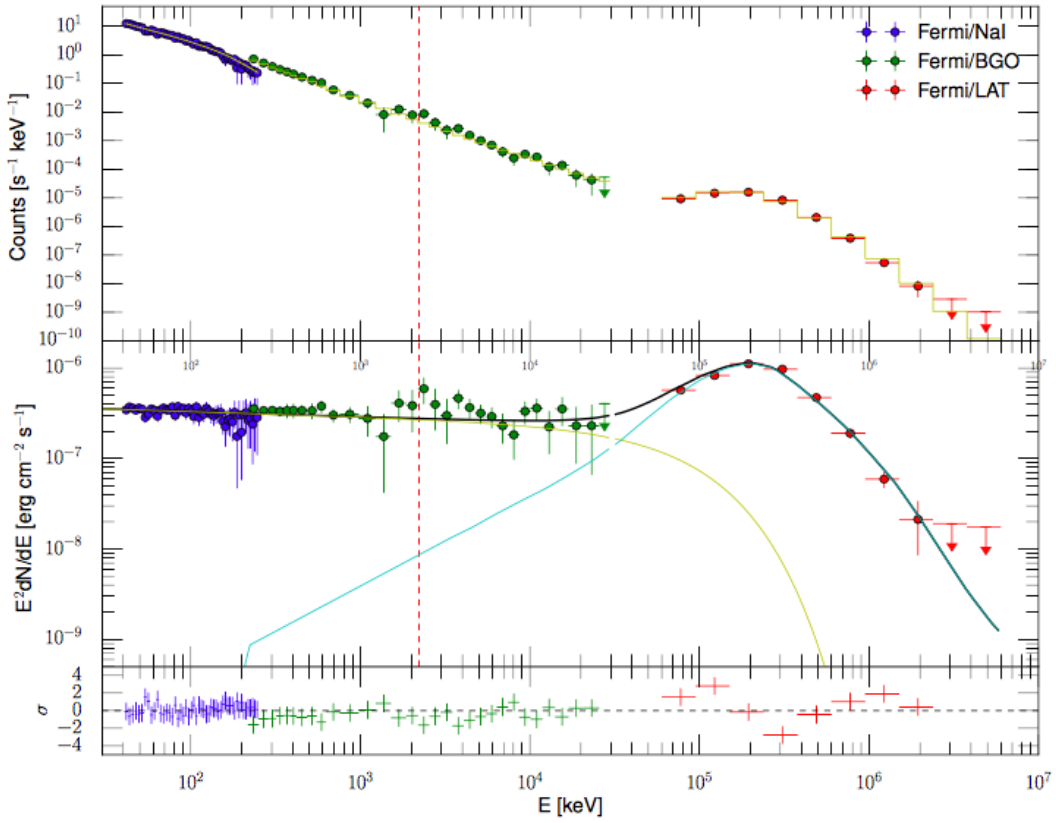

Figure 3.2: Combined Fermi-GBM/LAT count spectra (top panel) and SED (middle panel) for the Sep 1st, 2014 flare integrated between 11:02 and 11:20 UT and the lower panel shows the residuals of the fit. The best-fit model is a power law with exponential decay at high energy to describe the emission from 30 keV to $\simeq$ 10 MeV and a pion-decay model to describe the Fermi-LAT spectrum. The neutron capture line (at 2.223 MeV, highlighted by the red vertical dashed line) is not statistically significant ($\simeq 2\sigma$) and neither is an additional power law at low energy $\simeq 2\sigma$. Figure and caption adapted from [66].

Following Eq. 3.1, we can see that pion production would generate both neutrino and gamma-ray emissions. In order to create a sample containing only solar flares that emit neutrinos, we can therefore use the gamma-ray observations. Fortunately, pion-decay products seem to dominate the gamma-ray spectrum above 100 MeV as seen in Fig. 2.2. Furthermore, as we mentioned in the previous Chapter, Fermi-LAT has the ability to detect gamma rays above 100 MeV coming from the Sun. A spectral analysis allowed to confirm that the major contribution of the LAT observations, illustrated in Fig. 3.2 with the event from Sep 1st, 2014, was indeed consistent with pion decay emissions [66]. The approach we propose is therefore to only search for neutrinos when Fermi-LAT has

detected a significant pion decay signal coming from the solar flare. This yields a significant improvement compared to previous solar flare selections [64, 65] based on the X-ray flux, considering that Fermi-LAT detects in average only 5% of the M- and X-solar flares detected by GOES [1].

We have considered the list of solar flares detected by Fermi since the completion of the IceCube Neutrino Observatory and the start of steady data taking with the full detector in March 2011. Among the about 40 solar flares detected, we have selected the most significant ones. Table 3.1 shows the 4 most significant solar flares detected by the LAT since 2011. We present in this table the corresponding GOES flare classification as well as the location on the solar disk. In addition, we propose to also consider the solar flare from Sep 6th, 2017, which is the brightest detected in X-rays during the 24th solar cycle. This event was emitted by the same active region as the Sep 10th, 2017 considered in our list.

As will be presented in this Chapter and as described in [43], the neutrino emission towards the Earth may depend on orientation of proton beam and location in the Chromosphere. If the pions are produced by ions with a sufficiently high energy, a preferential direction, i.e. along the primary ion direction, can be observed for the pion-decay products. Therefore, the location of the solar flare and the pitch angle of the proton flux may have an influence on the resulting neutrino flux emitted towards Earth. It is actually expected that solar flares happening on the back side of the Sun would lead to an enhanced neutrino flux compared to events happening at the center of the visible solar disk as mentioned in e.g., [43]. The different locations of the solar flares considered in Table 3.1 would allow, in case of a significant detection, to probe and quantify a potential geometrical effect. If the center-to-limb neutrino flux ratio would deviate from one, this could point out an anisotropy of the pitch-angle distribution, as mentioned in [47] for the case of gamma rays.
Fig. 3.3 shows the light curves observed by Fermi-LAT for the selected solar flares.

[1] This number has been obtained averaging the number of solar flares detected by Fermi-LAT between 2011 and 2015 and the number of M and X flares in GOES during the same period. It has to be noted that, since the Sun is not always in the field of view of Fermi-LAT, this number does not directly convert to the fraction of pion flares.

[2] This solar flare was not detected by GOES since it happened far behind the limb. The classification is therefore an estimation [67].

Table 3.1: Selected solar flare events detected by Fermi-LAT. East and West are reversed compared to Earth definition, so that sunspots go from East (which is the left hand side of the solar disk) to West (on the right hand side).

Date	Corresponding GOES flare	Location on the solar disk
March 7th, 2012	X5.4	Centered, North-East quarter
February 25th, 2014	X4.9	Limb, South-East quarter
September 1st, 2014	X2.1[2]	36° behind the East limb
September 6th, 2017	X9.3	Centered, South-West quarter
September 10th, 2017	X8.2	Limb, South-West quarter

3.3 Optimizing the Time Window for Neutrino Searches

3.3.1 Differentiating two phases in the gamma-ray emission

As already highlighted for the first pion flare of 1982, high-energy gamma rays are emitted in two different phases during the solar flare. One can indeed distinguish a short-duration emission, called impulsive phase, almost simultaneous to the hard X-ray emission, and a long duration emission that may last for several hours [52]. Fig. 3.4 illustrates these two components observed by Fermi-LAT during the event of March 7th, 2012. As it can be seen in Fig. 3.4 by the red points, the impulsive emission seems to be provoked by a harder proton spectrum (spectral index between 3 and 4) compared to the long duration - also called *extended* - emission, which is characterized by a proton spectral index between 4 and 6. The impulsive phase also shows a higher gamma ray flux (blue points) compared to the extended emission. Considering these two effects, a solar flare search in large neutrino telescopes would have more chance to be successful when carried out during the impulsive phase. This is explained by two effects:

- Its initial proton spectrum being harder (i.e. having a smaller value of the spectral index), the impulsive phase likely emits more high-energy neutrinos compared to the extended phase. Large neutrino telescopes such as the IceCube Neutrino Observatory, which may be sensitive to the GeV energy range, have therefore a higher potential to detect the impulsive phase.

- As will be detailed in Chapter 5, large neutrino telescopes such as IceCube may be sensitive to solar flare neutrinos when searching for an increase in the overall detector rate compared to the rate in absence of a solar flare. This is different from high-energy astrophysical neutrino searches, where a probability of being of astrophysical origin can be assigned to single events. In this low-energy range, we will have to integrate background and signal events and search for a significant deviation from the observed rate during the absence of solar flares. We thus want to integrate as few background events as possible. This means that the duration

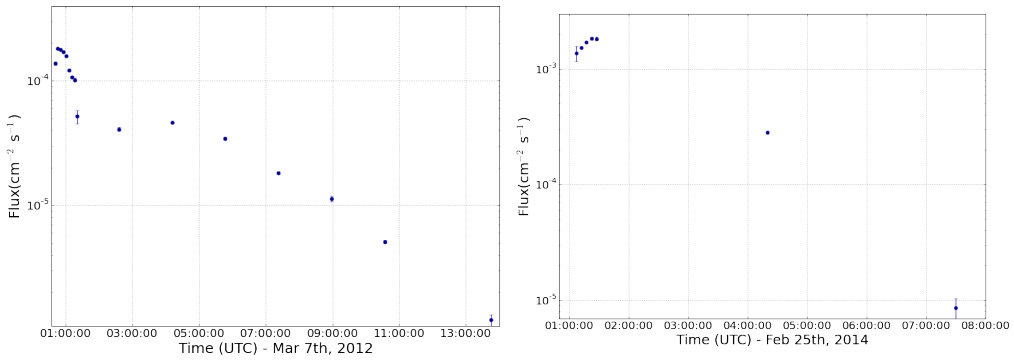

(a) March 7th, 2012

(b) February 25th, 2014

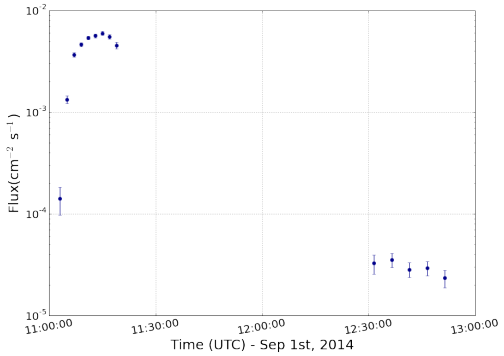

(c) September 1st, 2014

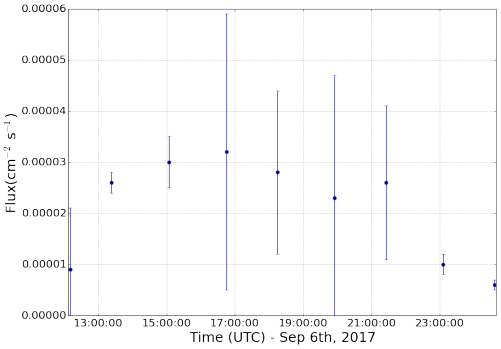

(d) September 6th, 2017

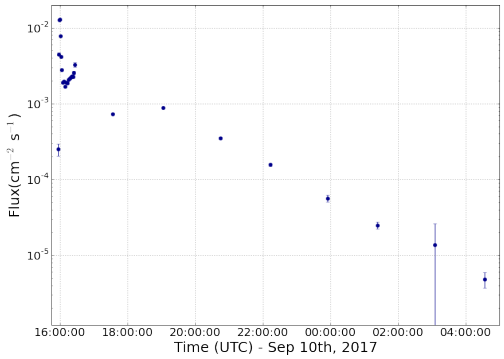

(e) September 10th, 2017

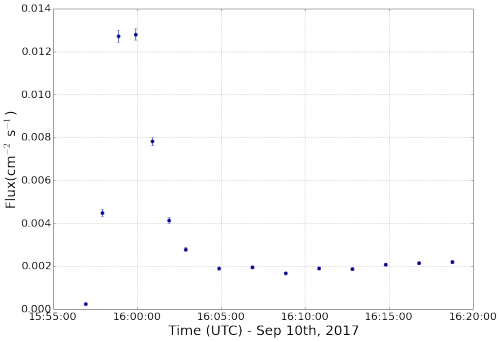

(f) Zoom on the impulsive emission of September 10th, 2017

Figure 3.3: Light curves for the Fermi-LAT events presented in Table 3.1. The light curves show the gamma-ray emission detected above 500 MeV for March 7th, 2012 and >100 MeV for the other events. The data used in these plots have been provided by Melissa Pesce-Rollins and Nicola Omodei via private communication.

of the time window considered in the neutrino search may play an important role in the significance of the observed signal. The impulsive phase being both shorter and having a higher flux represents the ideal candidate for a neutrino search. The

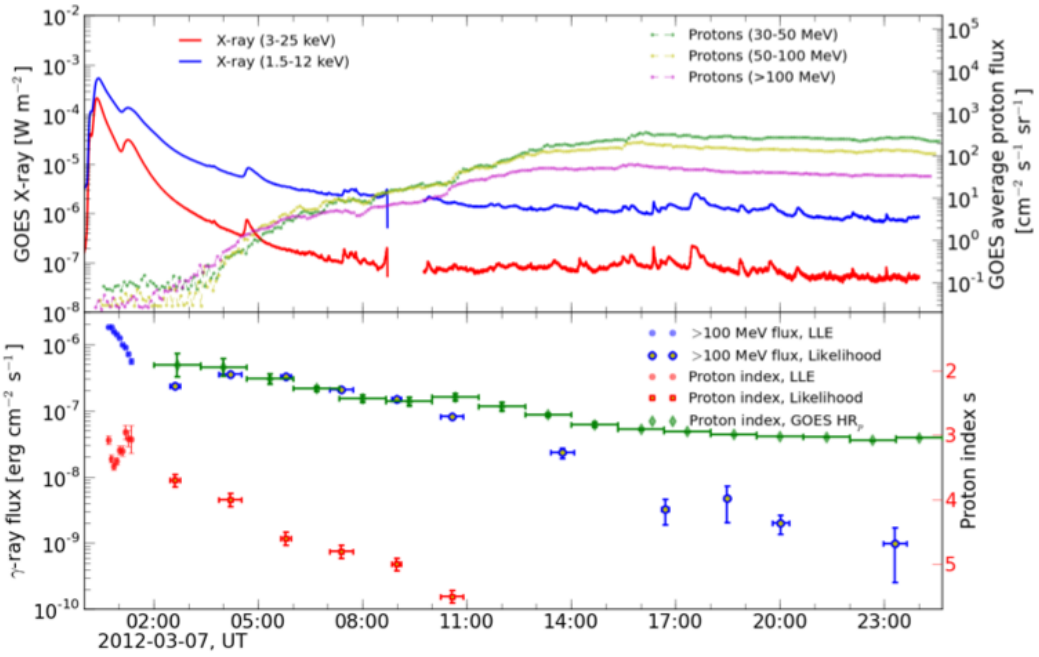

Figure 3.4: Long lasting emission. Top panel: soft X-rays (red: 1.5-12 keV, blue: 3-25 keV) from the GOES 15 satellite. On the right axis, 5-minute averaged proton flux (green: 30-50 MeV, yellow: 50-100 MeV, magenta: >100 MeV). We display the average of detectors A and B. Bottom panel: high energy gamma ray flux above 100 MeV measured by the Fermi LAT. The blue/red circles represent the flux and the derived proton spectral index obtained with the LLE analysis (covering the initial period, when the instrumental performance was affected by pileup of hard-X-rays in the ACD tiles). Blue/red empty circles/squares represent the flux and the derived proton spectral index obtained by standard likelihood analysis. Green diamonds are the GOES proton spectral indexes derived from the hardness ratio. Figure and caption adapted from [68].

following section will present an optimization of the time window, which maximizes the signal-to-background ratio.

3.3.2 Optimizing the time window for neutrino searches

As mentioned before, we want to minimize the time window of the neutrino search while maximizing the ratio of signal to background observed in large neutrino telescopes. We explain our approach for the case of the solar flare of Sep 10th, 2017. An identical approach has been used for each flare. The results for all events are documented in Table 3.2 and the plots are presented in Appendix A. We note that for most of the solar flares, the impulsive phase, or part of it, constitutes the optimal time window. An

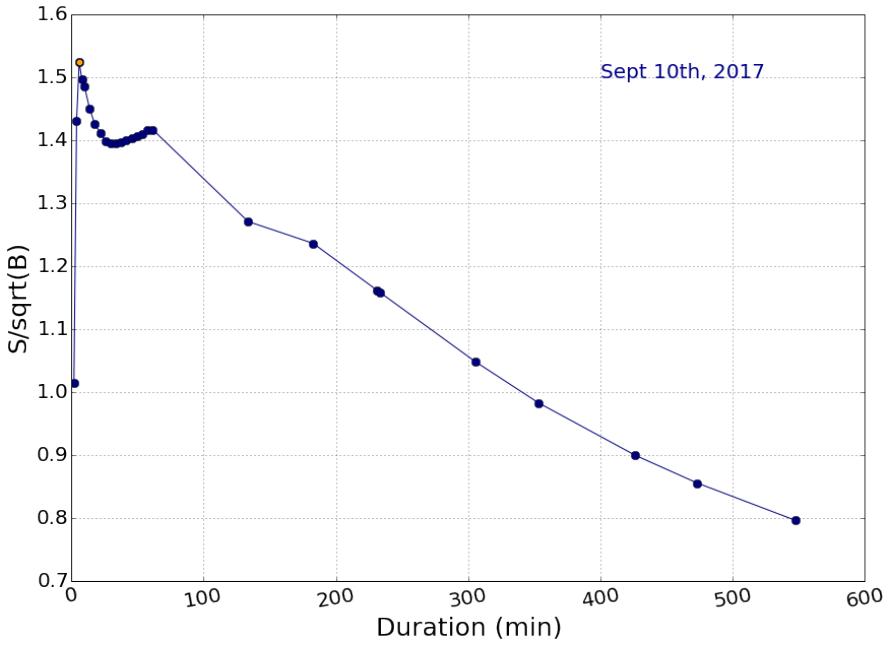

Figure 3.5: Ratio of signal over background for the Sep 10th, 2017 event. This curve has been obtained via the procedure outlined in the text. The maximum of the curve is highlighted with an orange point.

exception is made for the event of Sep 6th, 2017, where several hours, corresponding therefore to a long duration emission, will be studied.
In view of determining the optimal time window, we assume the neutrino signal will follow the detected gamma-ray light curve. This constitutes a reasonable assumption since both gamma rays and neutrinos are expected to be produced through pion decays. We consider an arbitrary level for the background, following a Poisson distribution in the considered time region. As will be detailed in Chapter 5, we expect the rate in large neutrino telescopes to be dominated by pure noise events in the considered energy range; assuming a Poisson distribution constitutes therefore a fair assumption.
We start integrating at the highest-flux points and extend to the lower ones, increasing the considered duration. For each integration step, we compute $\frac{S}{\sqrt{B}}$, where S is the assumed signal, proportional to the detected gamma-ray flux, and B an arbitrary background level following a Poisson distribution. The result of this integration for the Sep 10th, 2017 event can be seen in Fig. 3.5. As illustrated with the orange point, the maximum of the studied ratio appears after three integration steps, which corresponds to a duration of about 6 minutes. Fig. 3.6 shows the resulting time window selection compared to the initial light curve.

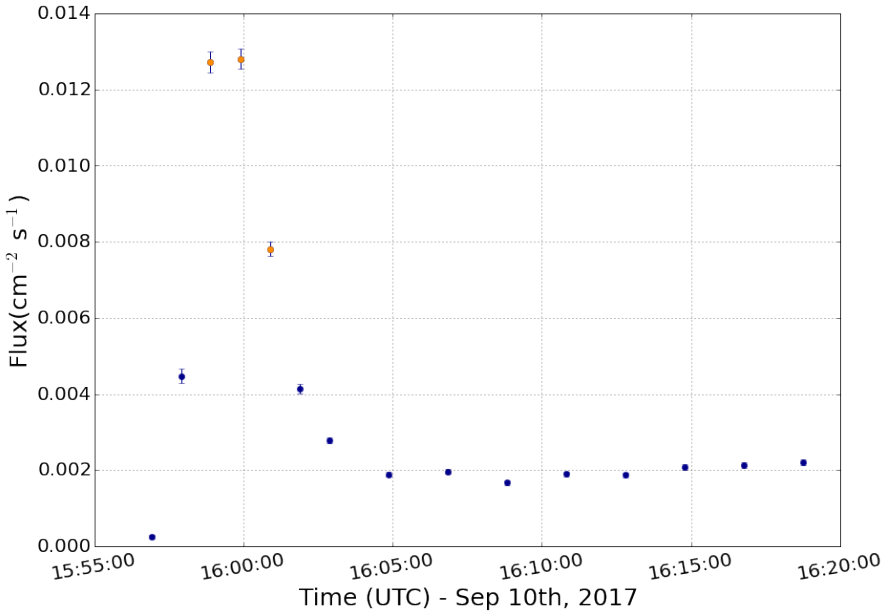

Figure 3.6: Selected time window (orange points) compared to the initial gamma-ray light curve.

Table 3.2: Optimized time window for neutrino searches

Date	Selected time window	Duration (minutes)	Fraction observed
March 7th, 2012	00:41:22 - 01:21:22	40	85%
February 25th, 2014	01:07:30 - 01:32:30	25	97%
September 1st, 2014	11:07:00 - 11:21:00	14	95.5%
September 6th, 2017	13:23:03 - 22:00:37	515	87%
September 10th, 2017	15:58:54 - 16:02:52	5.96	45%

3.4 Predicting the Solar Flare Neutrino Yield

In this section, we describe a simulation carried out in view of establishing the energy range of solar flare neutrinos, their expected spectrum as well as the potential signal in large neutrino observatories.

3.4.1 A Geant4-based Monte Carlo simulation

In order to evaluate the neutrino flux produced by a single solar flare, we have designed a Geant4 simulation [69] of proton-nucleus interactions in the solar atmosphere. What is relevant to estimate the neutrino yield of hadronic interactions is the density of the medium seen by the accelerated protons. As described above, the Chromosphere is believed to be the main interaction region for solar flare particles. Special care has therefore been given to define its density profile. We selected an atmospheric model that attempts to describe the density of the flaring Sun [70]. As indicated in [70], this semiempirical model allows to reproduce both the lines and continuum observed in X-rays. Our atmosphere is therefore made of a discrete number of spherical layers with uniform density inside each layer. We assumed a mass fraction of 75% of Hydrogen and 25% of Helium for the solar atmosphere, which is a standard assumption for the solar surface. The resulting density profile is shown in Fig. 3.7, where the x-axis is expressed as height above the Photosphere. We added to this model containing the upper part of the Photosphere, the Chromosphere and the Transition region, a homogeneous interior as well as a Corona with typical densities mentioned in Chapter 1.
We assume that the accelerated flux consists only of protons. In reality, one would expect a fraction of alpha particles and heavier ions to be accelerated as well. Considering that these heavier particles would decrease the pion production threshold, and therefore increase the neutrino yield for a given energy of the primary particle, our assumption will lead to a conservative estimate of the neutrino flux. Fig. 3.16, presented later in this Chapter, illustrates this statement.
We did not simulate the hadron acceleration nor any other magnetic effects in this work. These non-simulated effects may have a significant impact on the resulting neutrino flux directed towards Earth. In order to overcome the absence of magnetic field, we have therefore simulated two extreme cases and we expect the reality to be somewhere in between. The two cases are:

A. a proton beam tangent to the Chromosphere and directed towards Earth

B. an isotropic distribution of protons injected into the Chromosphere

These two proton distributions are illustrated in Fig. 3.8. The influence of these two distributions on the solar flare neutrino flux emitted towards the Earth will be presented

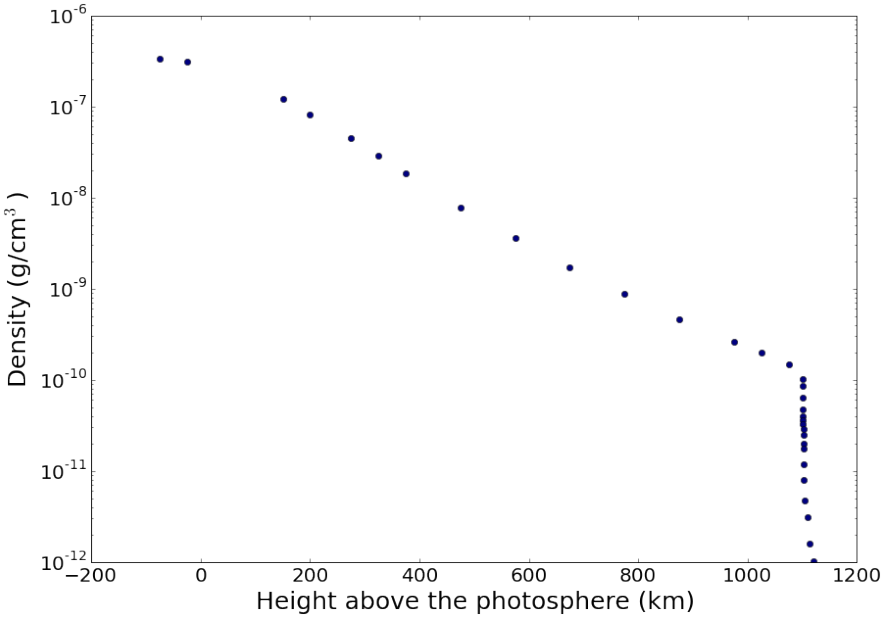

Figure 3.7: Density profile implemented in the Geant4 simulation.

in Fig. 3.15, later in the Chapter.

In addition to the direction of the injected proton spectrum, the simulation has two free parameters and their effects on the resulting neutrino flux are presented in Section 3.4.3. These parameters are the spectral index of the accelerated proton spectrum, and its upper cutoff, i.e. the maximum energy up to which protons can be accelerated in the solar flare. The accelerated proton flux is therefore parametrized as

$$\frac{d\Phi}{dE} = AE^{-\delta}H(E_{max} - E), \tag{3.2}$$

where A is a normalisation constant, δ represents the spectral index and E_{max} is the upper cutoff in a Heaviside function. We assume that no protons are accelerated above the upper cutoff. This assumption is probably conservative since an exponential spectrum may reach beyond this maximum energy, and would lead to extra high-energy protons.

3.4.2 Study of the neutrino production

Before detailing the effect of each of the different parameters of the simulation, we first study the neutrino production in the solar atmosphere. We assumed a spectral index of the accelerated proton spectrum of 3 and an E_{max} of 5 GeV. The accelerated flux has been injected following the tangent to the Chromosphere directed towards Earth.

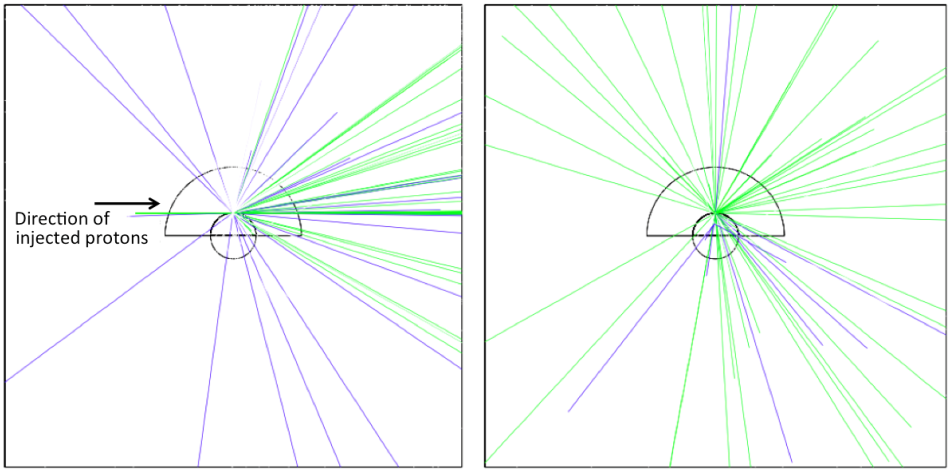

Figure 3.8: The two different proton injection distributions considered in this work: a proton beam tangent to the Chromosphere directed towards Earth (left, labeled A) an an isotropic distribution of protons injected into the Chromosphere (right, labeled B). The small sphere represents the Chromosphere, where most of the proton interactions happen, and the half sphere is the Corona. The green lines represent the protons (injected or scattered) and the blue lines show the produced neutrinos. On the left figure, the injected protons are shown with the thick green line located on the left side of the simulated Sun. The Earth is assumed to be located on the right side of simulated Sun. The figures have been obtained by injecting 100 protons between 0.5 and 5 GeV into the geometry.

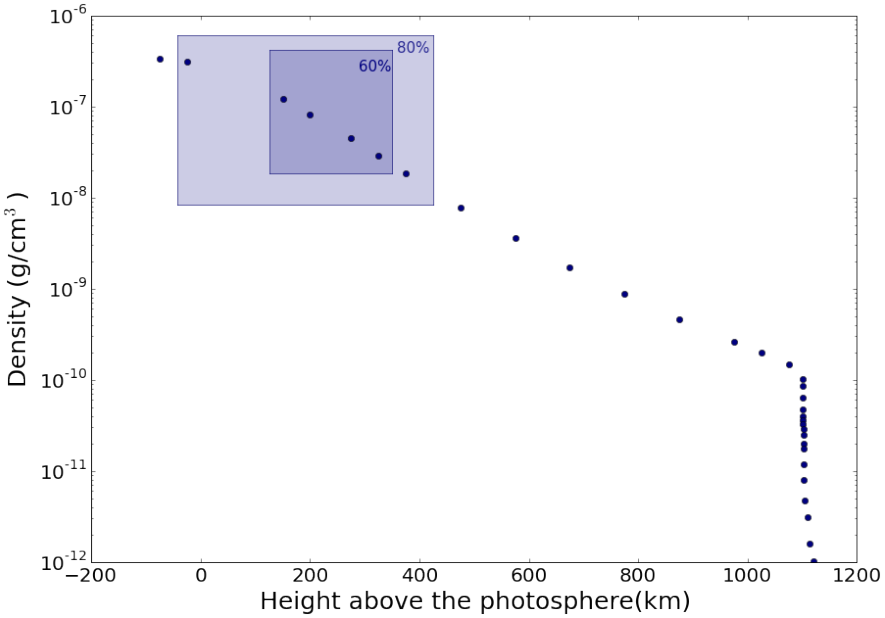

Figure 3.9: Density profile implemented in the Geant4 simulation. The two shaded areas show the density and region of the atmosphere where most (i.e. 60% and 80%) neutrinos are produced according to the simulation. This agrees with observational constraints.

Density dependence of neutrino production in the solar atmosphere: As presented in Fig. 3.9, most of the neutrinos are produced at densities around 10^{-7}-10^{-8} g cm^{-3} in our simulation. This agrees with the statement presented in Chapter 2, which sets limits on the density using observational features from positron and neutron emissions [49] and could locate the interaction region in the Chromosphere.

Energy distribution of the neutrinos: Another interesting feature to study is the neutrino energy distribution as a function of the primary proton producing it. The results can be seen in Fig. 3.10. One can directly see that increasing the high-energy cutoff of the proton spectrum, i.e. the maximum energy protons can be accelerated to, would have the effect of producing high-energy neutrinos, but also to populate more the lowest part of the neutrino spectrum. This feature will be confirmed in the next section, when we will present the influence of the free parameters of our model.

Contribution of each neutrino flavor to the total flux: It is interesting to decompose the total neutrino flux produced in the solar atmosphere into the different neutrino flavors. As noticed in Eq. 3.1, only ν_μ and ν_e and their anti-neutrinos are produced during solar flares. The presence of ν_τ in the solar flare flux would only appear after vacuum oscillations between the Sun and the Earth. Fig. 3.11 shows the contribution of each

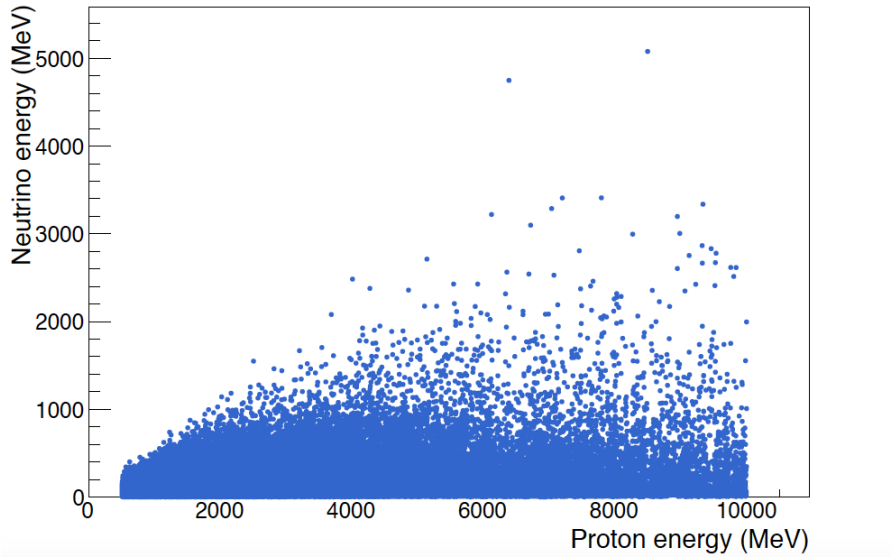

Figure 3.10: Energy of the neutrino as a function of the primary proton that produced it.

flavor to the total neutrino flux. The $\bar{\nu}_\mu$ mainly produced by the decay of muons, as seen in the next paragraph, slightly dominates over ν_e and ν_μ. $\bar{\nu}_e$ requiring the production of multiple pions, with therefore a higher production threshold, sparsely contributes to the total neutrino flux.

Secondary particles producing the neutrinos: Fig. 3.12 illustrates the neutrino flux expected for each neutrino flavor, split into the contribution from each parent. As seen in Fig. 3.12, ν_e and $\bar{\nu}_e$ are exclusively produced by μ decay as expected, with a small contribution from K and K_L. ν_μ and $\bar{\nu}_\mu$ are mostly produced through π and μ decay, with the dominant component coming from π (μ) for ν_μ ($\bar{\nu}_\mu$). This difference can be explained considering that we are close to the pion-production threshold. The accelerated proton spectrum therefore produces more likely π^+ (production threshold at 195 MeV for pp interaction) than π^- (production threshold at 600 MeV for pp interaction), leading to the observed difference of ν_μ and $\bar{\nu}_\mu$ production channel.

3.4.3 Impact of the spectral parameters on the neutrino fluence

In this section, we study the influence of the free parameters in our simulation. Since large neutrino telescopes, such as the IceCube Neutrino Observatory, may be sensitive to the upper part of the neutrino spectrum only, we focus on the influence at the relevant

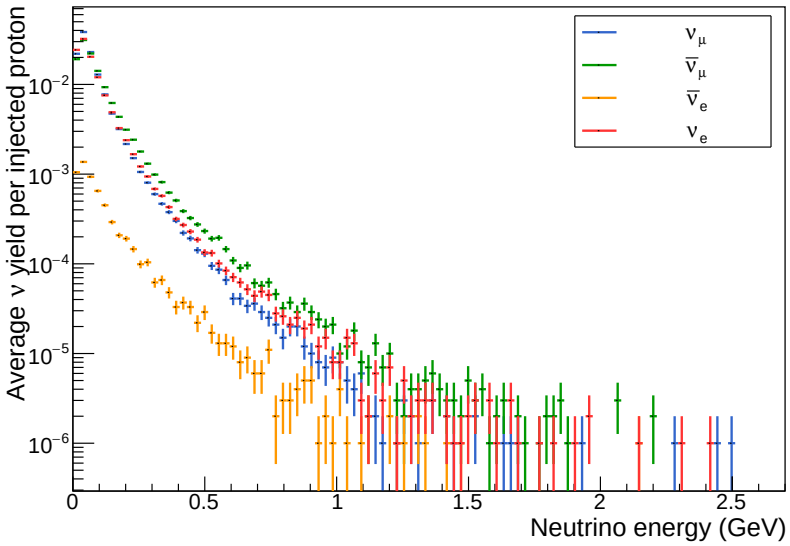

Figure 3.11: Energy distribution of each neutrino flavor produced in the solar atmosphere as a consequence of the solar flare.

energies.

Influence of the spectral index, δ: As detailed in Eq. 3.2, the accelerated proton spectrum is parametrized using a power law function with a spectral index δ. The resulting neutrino flux for different values of this spectral index is presented in Fig. 3.13. As expected, a harder proton spectrum (i.e. a lower value of the spectral index) leads to a higher neutrino yield per injected proton but also to an increase of the maximum neutrino energy produced during the interaction. These values are realistic values for the accelerated proton flux, as seen in Fig. 3.4. An exception is made for the spectral index $\delta = 2$, which is hard to produce in the solar flare environment assuming the acceleration mechanisms described in the previous Chapter. We however use it to fix an upper limit on the energy range one could expect for solar flare neutrinos. As seen on the different plots presented in this section, solar flare neutrinos seem to be produced up to energies < 5 GeV. This information will be of great importance when developing dedicated event selections in neutrino telescopes. It has to be noted that current gamma-ray observations allow to constrain the value of δ for different phases of the solar flare as seen in Fig. 3.4 and in the recent analysis of the bright flare of September 10th, 2017 [71].

Influence of the upper cutoff, E_{max}: A potential upper cutoff of the proton spectrum has been discussed in several studies (see e.g., [72]). The effect of this upper cutoff on the subsequent neutrino flux is illustrated in Fig. 3.14, where we show the average

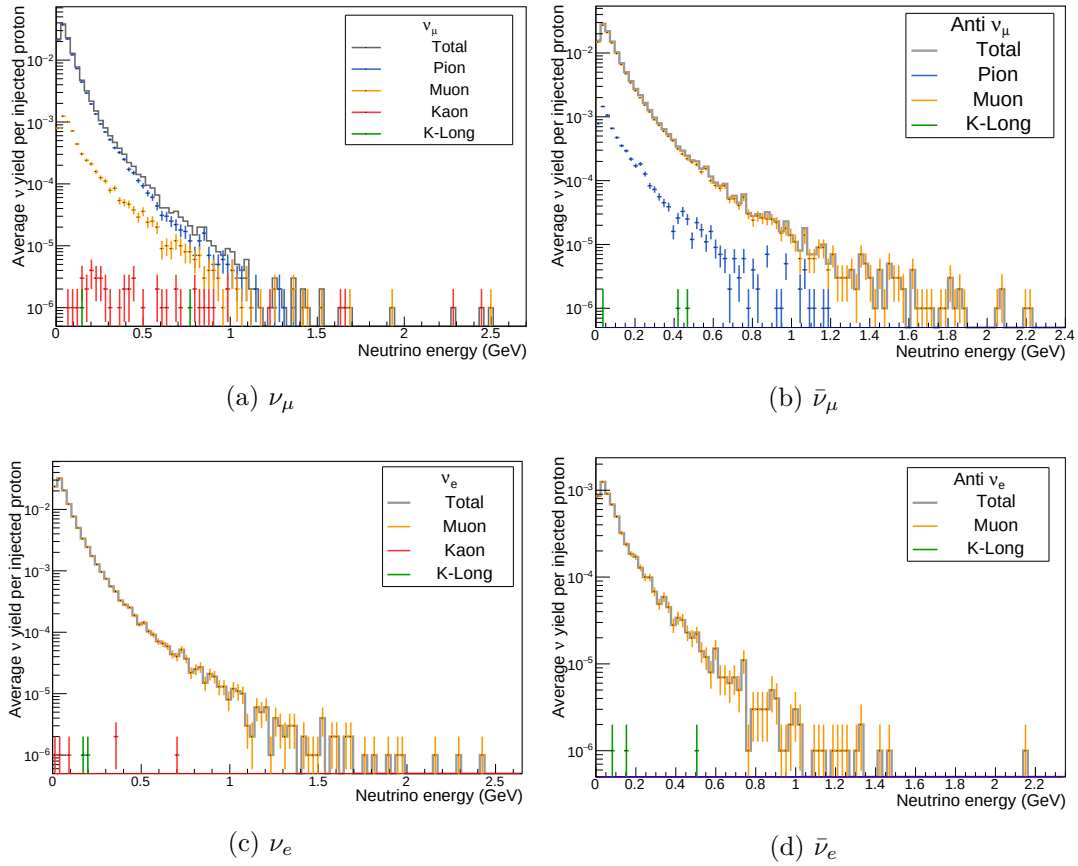

(a) ν_μ (b) $\bar{\nu}_\mu$

(c) ν_e (d) $\bar{\nu}_e$

Figure 3.12: Average neutrino yield per injected proton for each neutrino flavor produced in the solar atmosphere. Each panel shows the contribution of the different parent particles to the total neutrino flux.

neutrino yield per injected proton with $\delta = 3$ and $E_{max} = 10$ (red), 7 (green), 5 (blue) and 3 (orange) GeV. As seen in Fig. 3.14, an increase of the upper cutoff builds up the neutrino yield at lower energies. This comes from a wide spread in the energy loss distribution of the proton, or its daughter particle, before the neutrino production as illustrated in Fig. 3.10. A higher cutoff value also increases the maximum energy of the produced neutrinos. These two effects lead to a higher neutrino yield in the energy range targeted by the IceCube event selection described in Chapter 5. This means, as will be demonstrated later in the current Chapter, that the strength of the signal in large neutrino telescopes could be used to constrain this upper cutoff when assuming a value for the spectral index δ.

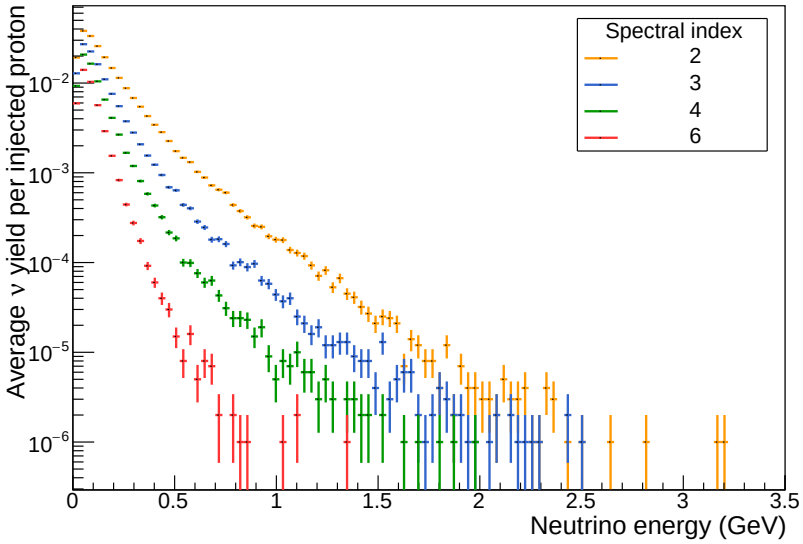

Figure 3.13: Influence of the spectral index of the proton spectrum on the resulting neutrino flux.

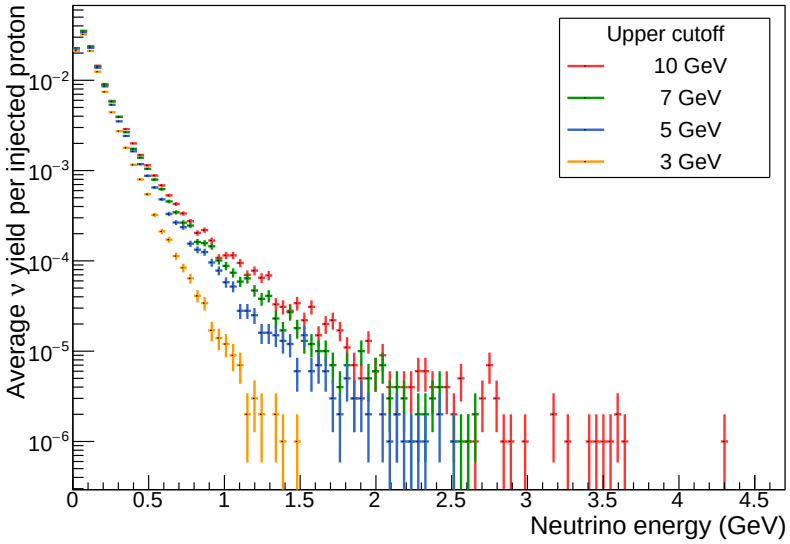

Figure 3.14: Energy distribution for neutrinos depending on the upper cutoff in the accelerated proton spectrum with a spectral index of 3.

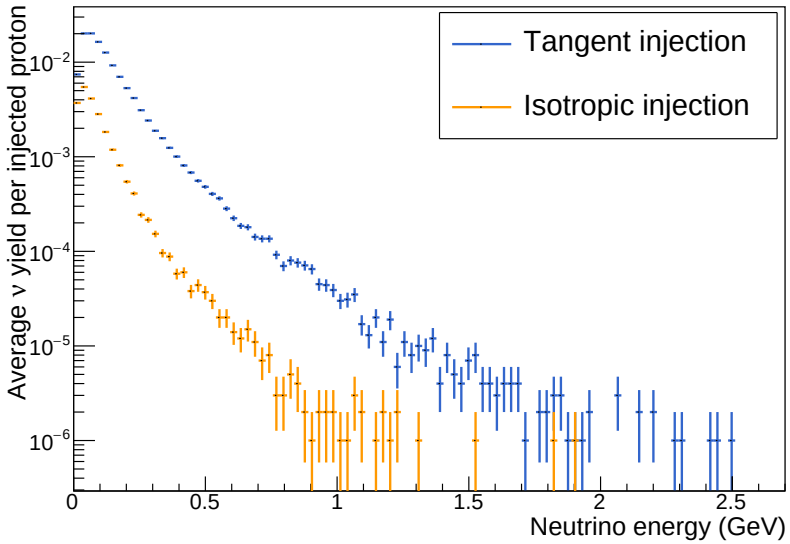

Figure 3.15: Neutrino energy distribution for two different directions of the primary proton flux.

Influence of the direction of the accelerated protons: Since the current simulation does not include any magnetic field effects, we attempt to estimate the potential influence these effects may have on the final neutrino flux by considering two extreme cases, i.e. a tangent emission emitted towards Earth and an isotropic emission. This parameter is related to the injection of particles onto a magnetic field line that we stressed out in the previous Chapter. Fig. 3.15 shows how the neutrino flux would be affected by these different assumptions on the accelerated flux. As seen in Fig. 3.15, an isotropic emission would lead to a fainter and softer neutrino flux. This dependency means that an incoming direction of the accelerated proton spectrum should be assumed when setting constraints on the upper cutoff.

Influence of the composition of the accelerated spectrum: As previously mentioned, we assume that the accelerated flux is only made of protons. Allowing alpha particles to be part of the accelerated flux would have the effect to decrease the threshold of pion production, and therefore also of neutrino production. The influence of the composition of the accelerated flux is shown in Fig. 3.16, where pure proton and pure alpha fluxes are assumed. As expected, a pure alpha flux would lead to a higher neutrino yield per injected particle. A composition of the accelerated beam should therefore be assumed when setting constraints on the upper cutoff. However, the effect of the composition is sub-dominant compared to the injection direction of the accelerated particles.

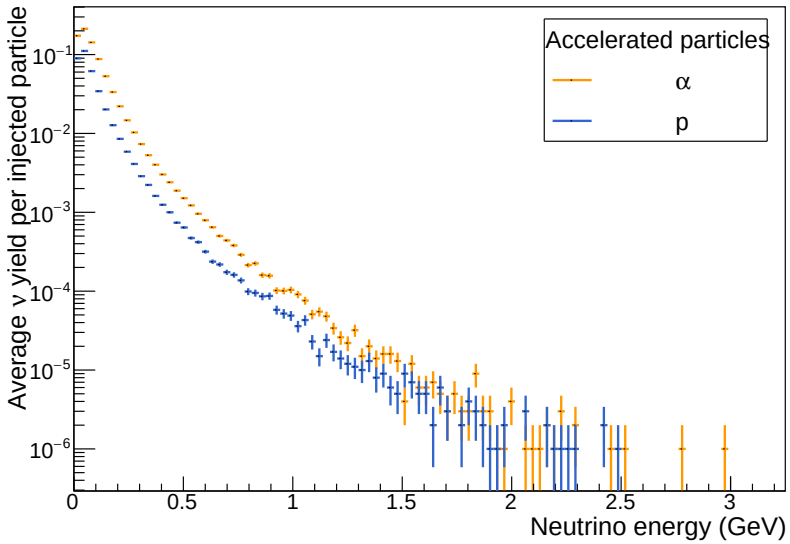

Figure 3.16: Neutrino energy distribution for a pure proton (blue) and a pure alpha (orange) accelerated flux.

3.4.4 Neutrino fluence at the solar and terrestrial surfaces

Solar flare neutrinos at the Sun

Before deriving the resulting neutrino flux at Earth, it is interesting to compare the neutrino yield to the gamma rays emitted from pion decays. This comparison can be seen in Fig. 3.17. As seen in Fig. 3.17, we expect a higher production of gamma rays at high energies but an overall higher neutrino production. This is consistent with the kinematics of the interactions presented in Eq. 3.1.

In view of evaluating the reliability of the simulation in producing a realistic estimate of the neutrino flux, we can compare the gamma ray flux predicted by our model with the solar flare flux observed by gamma ray detectors. Fig. 3.18 shows a comparison for the solar flare of June 3rd, 1982, as well as two events detected by Fermi-LAT. In view of determining the gamma-ray flux, we used the averaged proton spectral index derived from the gamma-ray observations for these three solar flare events. The following values have been used: $\delta = 3.1$ (June 3rd, 1982 [73]), $\delta = 4$ (March 7th, 2011 [50]) and $\delta = 3.5$ (March 7th, 2012 [50, 68]). Two upper cutoff values have been used, i.e. 1 and 5 GeV, as well as two different injection types of the accelerated proton spectrum: tangent directed towards Earth and isotropic. As seen in Fig. 3.18, the estimated gamma ray fluxes are either reproducing the observations or underestimating them. What we defined as *tangent* injection in our simulation seems to better reproduce the observations than

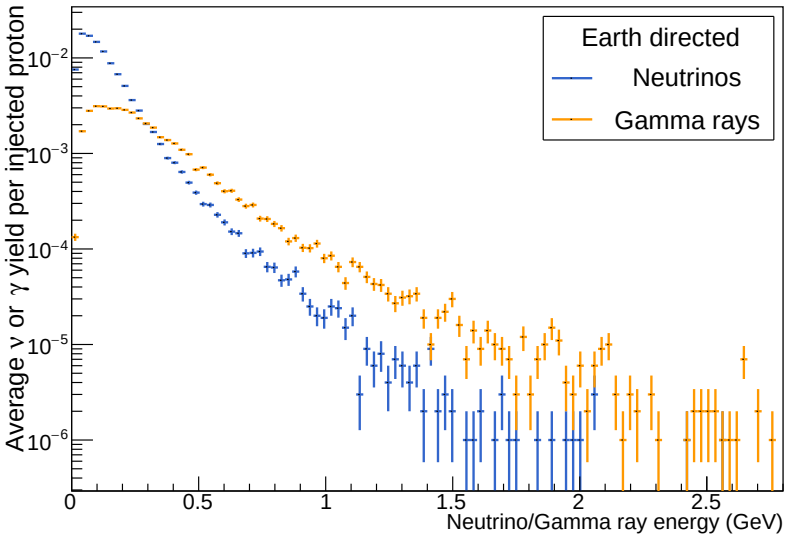

Figure 3.17: Comparison of the neutrino and gamma ray yield emitted towards Earth as a consequence of the proton acceleration by the solar flare.

the isotropic assumption. Estimating the gamma ray flux is not as straightforward as it can be for neutrinos, because the photon flux will suffer some attenuations when crossing the solar atmosphere. Some of these effects have however been taken into account in the presented bands. Our results, even if not perfectly matching the observations, are satisfactory and corroborate the reliability of the simulation presented in this Chapter.

We will use the following values for the different parameters in our simulation:

- $\delta = 3$. We have chosen this value since it is representative for the spectral index expected during the impulsive phase of the solar flare. As previously motivated, this phase is the most promising candidate for a neutrino search.
- a tangent injection since it seems to better reproduce the gamma-ray observations
- a pure proton flux to be more conservatice

The estimate of the neutrino flux will be given assuming these values. As will be shown later in this Chapter, neutrino telescopes could aim at constraining the upper cutoff of the proton spectrum. We therefore derive the neutrino flux for different values of this parameter. In order to establish the neutrino flux produced in the solar atmosphere, we need to assume a certain amount of accelerated protons. We use the total number of injected protons derived from observations of the June 3rd, 1982 event [49], i.e. 2.2 $\times 10^{33}$ protons with E $>$ 30 MeV, assuming that each solar flare radiates the same energy

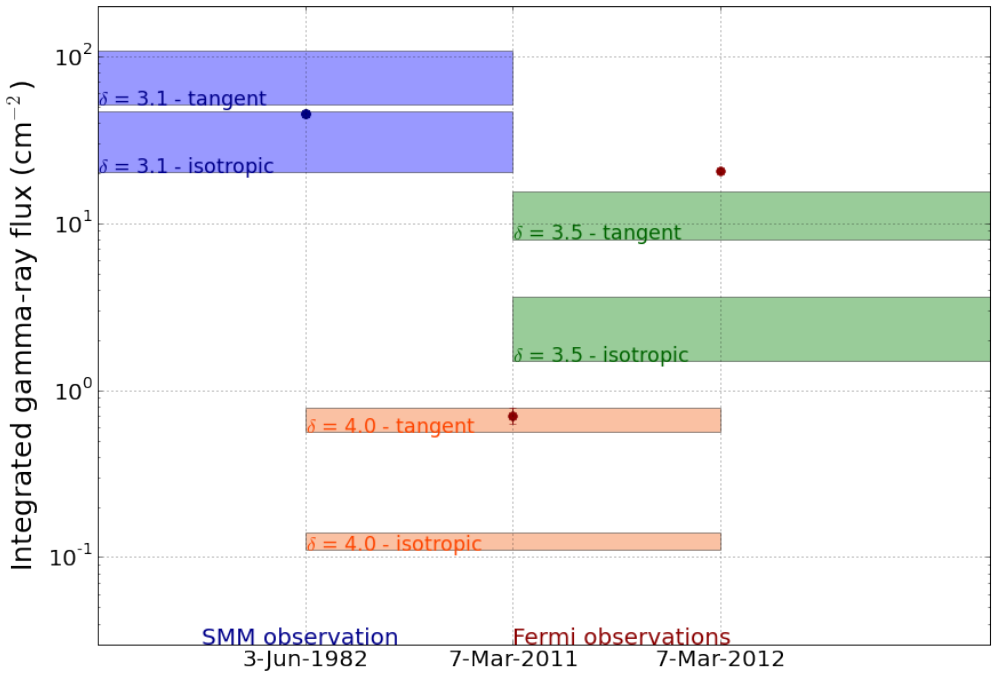

Figure 3.18: Comparison of the gamma-ray flux predicted for the considered models (color bands) and the SMM [73] and Fermi-LAT [50, 68] integrated flux (points). The upper(lower)-bound of the bands have been obtained assuming an upper cutoff at 5 GeV (1 GeV). We show the estimated gamma-ray flux for two different injections of the accelerated proton spectrum: tangent (upper band) and isotropic (bottom band).

in the accelerated proton flux. In case of the beam injection, all these protons have an initial momentum in the direction of the Earth, while for the isotropic case, the same number of protons has been injected isotropically. The two different injections therefore represent the most optimistic and pessimistic case, with a realistic value expected to lie somewhere between the two. This is a reasonable assumption considering that only specific solar flares, i.e. solar flares emitting pions and among the most significant ever detected, are considered in this study. Since we only simulate interactions of protons with a kinetic energy above 500 MeV, we renormalize the total amount of accelerated protons give in [49] taking into account the spectral index extrapolated from gamma-ray observations.

At the Earth

When propagating the neutrinos from a source to the Earth, one needs to take into account two effects:

- The solid angle of the neutrino emission: we consider solar flare neutrinos that may reach the Earth. In view of obtaining sufficient statistics, we consider the number of neutrinos emitted within $\cos\theta = 0.8$ and 1, where θ represents the angle between the directions of the injected proton flux and the produced neutrino. The distribution of this θ angle is shown in Fig. 3.19. We therefore consider a solid angle $d\Omega = 2\pi \times 0.2$ sr, centered at the Earth as seen from the Sun, but covering an area larger than the corresponding Earth disk. A conservative estimate of the fluence at Earth, expressed in cm^{-2}, is obtained from the particle number count produced at the Sun in the above solid angle by scaling it with a factor $\frac{1}{2\pi \times 0.2 \times d^2}$, where d is the distance between the Sun and the Earth.
- The neutrino oscillations: on their travel towards Earth, flavored neutrinos endure oscillations. The composition of the flux at the source - $\nu_e : \nu_\mu : \nu_\tau = 1 : 2 : 0$ - therefore changes to $\nu_e : \nu_\mu : \nu_\tau \simeq 1 : 1 : 1$ at Earth, with slightly more ν_e than other flavors.

The redshift of the emitting source compared to the Earth would also have an effect on the resulting flux at Earth. However, since we are considering a very nearby source in this work, this effect can be neglected. The involved gravitational red and blue shifts are negligible as well.
The resulting neutrino fluence above 500 MeV can be read in Table 3.3. These values have been obtained assuming a tangent injection of a proton spectrum with $\delta = 3$ and several realistic values of the upper cutoff, as mentioned above. The Table shows the *fluence*, i.e. the neutrino flux integrated over the total duration of the solar flare and over all flavors. As mentioned above, a higher value of the upper cutoff would lead to both more high-energy neutrinos and a higher neutrino yield in the flux above 500 MeV.

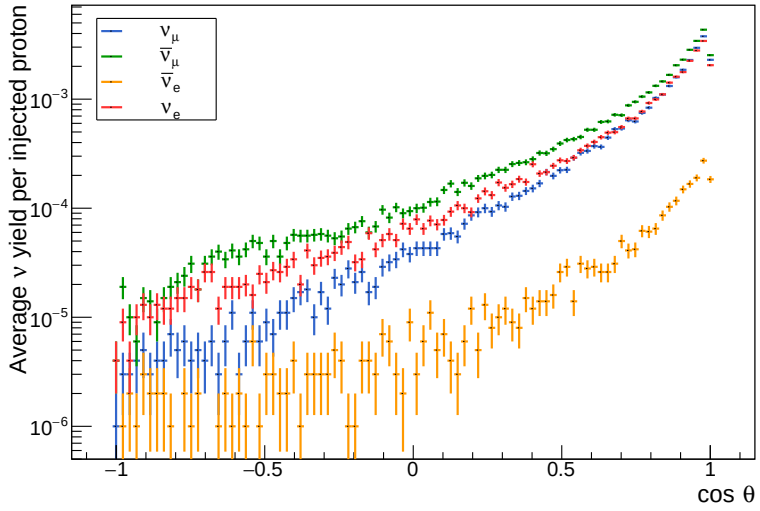

Figure 3.19: Angular distribution of the produced neutrino with respect to the injected proton flux, assuming a tangent injection directed towards the Earth. Neutrinos with energies above 100 MeV were used to obtain this plot.

Table 3.3: Estimated neutrino fluence at Earth between 0.5 and 5 GeV for different values of the upper cutoff, when assuming a $\delta = 3$ for the accelerated proton flux. The middle column shows the expected neutrino spectral index determined by fitting the output of the simulation.

Value of the upper cutoff (GeV)	Neutrino spectral index	Neutrino fluence at Earth (cm^{-2})
3	5.5	14 ± 1
5	4.5	33 ± 1
7	4	46 ± 1
10	3.6	58 ± 1

These two effects directly reflect a higher fluence for a higher value of the cutoff as seen in the Table.
This estimate can be compared with the prediction made by Daniele Fargion [42]. Considering Eq. 2.11 in [42], using $E_{fl} = 10^{32}$ erg and $< E_{\nu_e} >= 140$ MeV as well as an optimistic $< E_{\nu_e} >= 500$ MeV, we obtain 410×10^3 and 114×10^3 neutrinos cm^{-2} respectively, which is significantly larger than our estimate. While similar solar atmospheric models have been considered, an analytic approach is used, considering orthogonal upward protons with an energy >2 GeV. Moreover, the fraction of energy going from protons to pions producing neutrinos is estimated to be 0.27 by Fargion, compared to 0.16 in the work presented in this thesis. We note that these estimates should be consider as an upper limit on the neutrino flux, since, besides not mentioning the considered energy range, there is no consideration of the spectral index nor the upper cutoff in this prediction. We mention that, at the time of writing, these predictions are the only estimates of the solar flare neutrino flux in the GeV energy range.
According to both predictions, the solar flare neutrino fluence from the direction of the Sun is therefore expected to largely dominate the neutrino flux produced in the Earth atmosphere in the same energy range[3]. Atmospheric neutrinos will therefore not constitute a significant background for the search presented in Chapter 5.

3.4.5 Estimating the detection potential in large neutrino telescopes

More interesting than the absolute neutrino flux at Earth, is the resulting number of events in neutrino telescopes. In order to convert the flux into an expected number of events in neutrino telescopes, we use the following formula:

$$N_{events} = \int_{E_{min}}^{E_{max}} N_A \sigma(E) M_{eff}(E) \frac{d\Phi(E)}{dE} dE, \tag{3.3}$$

where

- N_A represents the Avogadro number, which converts the density into a number of targets for neutrinos
- σ is the cross section of neutrinos with the ice or water surrounding large neutrino telescopes described in Chapter 4. For this calculation, we use the cross sections derived in [18].
- M_{eff} is the effective mass of the neutrino telescope as seen by a neutrino in the considered energy range. We considered an effective mass of 0.4 10^{10} $\left(\frac{E}{MeV}\right)$ g.
- $\frac{d\Phi}{dE}$ is the solar flare neutrino fluence

[3]The atmospheric neutrino flux at 1 GeV is 0.2×10^{-2} and 0.4×10^{-2} cm^{-2} s^{-1} sr^{-1} for ν_e and ν_μ respectively.

Table 3.4: Estimated number of events due to solar flares in a neutrino telescope, for different values of the upper cutoff, when assuming a $\delta = 3$ for the accelerated proton flux.

Value of the upper cutoff (GeV)	Expected number of neutrino events
3	8.9 ± 0.1
5	26.7 ± 0.2
7	44.2 ± 0.3
10	66.2 ± 0.5

This calculation was performed in view of estimating the potential of solar flare detection in large neutrino telescopes, to decide whether a search would have the chance to be successful. The exact effective mass of the event selection presented in Chapter 5 was therefore not known yet. As we will see later, it turned out our first estimate of the effective mass was overestimating the real capabilities of IceCube for triggered interactions. In view of reaching the planned effective mass, expected from a specific data stream in IceCube[4], we have designed an alert system allowing us to save data when Fermi-LAT detects a significant solar flare. This alert system is presented in Chapter 7. We do not present the results of this search in this thesis, because no major solar flare happened when the alert system was running, except two very bright flares in September 2017. We managed to save several hours of HitSpool data for these two special events. However, the related IceCube data will arrive in the Northern Hemisphere in Spring 2018, so they could not be analyzed in this thesis.

The above calculation leads to a number of events in a neutrino telescope for different values of the upper cutoff presented in Table 3.4. The conclusion that can be drawn from this Table is that different values of the proton upper cutoff yield a different number of events in neutrino telescopes. The absolute number of events will evolve with the improvement of event selections and with the next generation of neutrino telescopes, but the relative amount of events for different values of the cutoff will remain, motivating the science case developed in the next section.

3.5 Potential Physics Reach for Large Neutrino Telescopes

Fig. 3.20 shows the results presented in Table 3.4 from a different perspective. In Fig. 3.20, we compare the expected number of events in neutrino telescopes due to solar flares with the expected background level after a dedicated neutrino event selection. Using this calculation, which was performed before obtaining the final rate of a

[4]Called *HitSpooling*, this data stream allows to save every neutrino interaction happening in the neighborhood of the detector. Both triggering and sub-threshold interactions are saved, which increases the effective volume for low energy neutrinos.

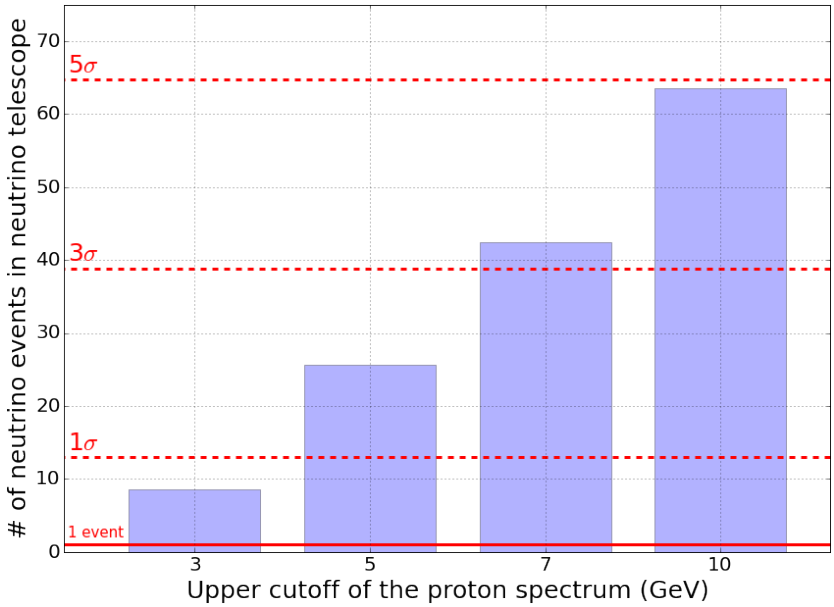

Figure 3.20: Predicted significance of a solar flare signal observed in a neutrino telescope, whose characteristics are described in the text. We have assumed a duration of 14 minutes, similar to Sep 1st, 2014 optimized time window, and performed a counting experiment. A proton spectral index of $\delta = 3$ and a tangent injection have been assumed.

dedicated event selection in IceCube presented in Chapter 5, we estimated a background level that could be reached when performing an event selection in neutrino telescopes. Our IceCube event selection turned out to show better results than what is estimated here, and the rate considered in this calculation is an order of magnitude above the final rate that will be presented in Chapter 5.

Even though some of the estimated values turn out to be different after performing the event selection, Fig. 3.20 highlights an important feature, already mentioned several times in this Chapter. Once a spectral index is assumed, the strength of the signal seen in neutrino telescopes, significant or not, would allow to constrain the upper cutoff of the proton spectrum and therefore to probe the efficiency of the acceleration mechanism(s) taking place in solar flares. Neutrino observations would indeed help to eliminate the degeneracy of spectral index and upper cutoff that gamma ray observations alone could not resolve.
Combining Fermi-LAT and neutrino observations, would therefore offer the potential to constrain both this upper cutoff and the spectral index by fitting the gamma-ray and neutrino spectra simultaneously. Practically, an iterative method could be developed, in which gamma rays would contribute more to the constraint of the spectral index, and neutrino observations would mainly limit the upper cutoff, but ensuring that both ob-

servations can be explained by the derived parameters. This multi-messenger analysis of the solar flare emissions would allow to get a more complete overview of the acceleration mechanism(s) in solar flares.
Once a constraint on the upper cutoff has been obtained, it will be of great interest to compare with similar constraints set by, e.g., *Pamela* and AMS. These particle detectors located in space are sensitive to the proton flux accelerated towards the interplanetary space [74, 59]. A disagreement between the constraints from gamma-ray and neutrino on the one hand, and SEP observations on the other hand would allow to conclude that these different fluxes arise from different acceleration mechanisms. As mentioned in Chapter 2, the exact mechanism(s) for accelerating solar matter in the flare environment is still an open question that the proposed approach would help solving.

We conclude this Chapter by mentioning that, in case of a neutrino detection, solar flares would be the first phenomenon in our Universe for which we are able to detect electromagnetic waves, charged particles and neutrinos. The Sun could therefore be turned into a laboratory to study particle acceleration that may also take place in the rest of our Universe.

J'inventai six moyens de violer l'azur vierge !

Cyrano de Bergerac, Troisième acte, scène XII,
Edmond Rostand

4

The IceCube Neutrino Observatory

This chapter reviews the main characteristics of neutrino detection through Cherenkov radiation produced by the secondary charged particles of a neutrino interaction. We first detail the detection principle and briefly describe the main experiments that have participated or still participate to the development of high-energy neutrino astronomy. We then focus on the IceCube Neutrino Observatory located at the geographic South Pole and describe its machinery. Finally we review the main achievements of this discovery machine that allowed, among others, to detect the first high-energy neutrinos with an astrophysical origin.

4.1 Very Large Neutrino Telescopes

During the sixties, while detectors such as Homestake [75], were already detecting low-energy neutrinos as previously mentioned, Mosey Markov published a groundbreaking idea that would lead to high-energy neutrino astronomy. He proposed to *install detectors deep in a lake or the sea and to determine the direction of charged particles with the help of Cherenkov radiation* [76]. As early as it was when this first step towards neutrino astronomy was taken, the proposal already contained all the important features of the current devices.

4.1.1 Detection principle

The main idea is to detect Cherenkov radiation emitted by a dielectric medium such as water or ice, when a charged particle propagates at sufficient speed through it. The medium polarizes as a consequence of the movement of the charged particle, and relaxes back emitting bursts of photons [77]. Constructive interferences can occur at an angle θ_c if the particle was travelling faster than the light in the medium. Therefore, a coherent electromagnetic shock wave propagates through the medium as illustrated in Fig. 4.1. This non-isotropic emission looks like a cone aligned with the direction of the charged

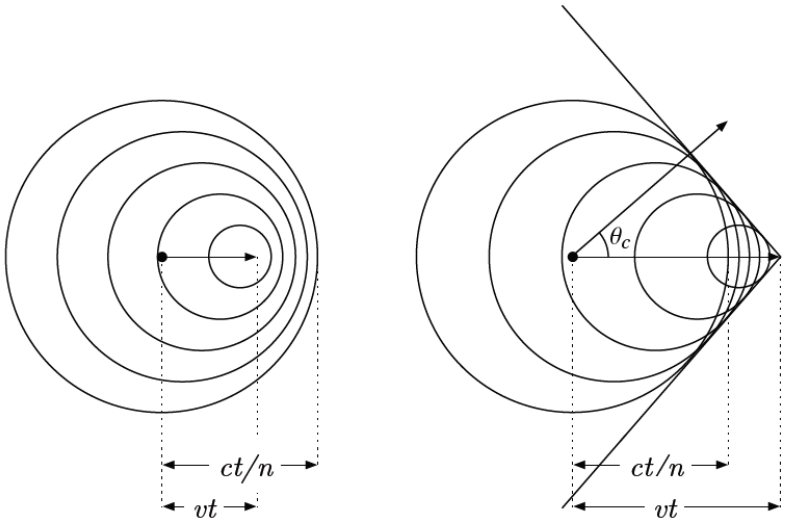

Figure 4.1: Illustration of the Cherenkov effect. The left figure shows the relaxation emission caused by a particle travelling at a speed $v < c/n$, with c being the speed of light in vacuum and n, the refractive index of the medium. The right part of the panel represents the Cherenkov effect created by a particle with a speed $v > c/n$. The emitted waves add constructively to create a coherent shock wave, called the Cherenkov cone. The light is emitted at an angle given by $\cos\theta_c = \frac{1}{\beta n}$. Figure from [78].

particle, allowing to reconstruct the direction of its propagation. It is then possible, using kinematics and conservation laws, to identify to some extent the direction of the incoming neutrino if the charged particle is the corresponding lepton produced in a charged current interaction.

As previously mentioned, the charged particle must travel faster than the light speed in the medium to force the medium to emit such radiation. One can calculate the minimal energy required for the different charged products of neutrino interactions.
The minimal value of the particle velocity v allowing the emission equals to the light speed in the medium, $c/n(\lambda)$ where n is the wavelength dependent refractive index of this particular medium. Considering $\beta = v/c$ and replacing it in the expression of the

total energy for a particle, we obtain the *Cherenkov threshold*, E_{th}

$$E_{th} = \frac{mc^2}{\sqrt{1 - n^{-2}}} \tag{4.1}$$

As we can see, this threshold value depends on the refractive index of the medium. As an example, we will consider ice. Assuming Cherenkov photons with a wavelength between 300 and 600 nm[1], the refractive index equals 1.33. This value leads to a threshold for the kinetic energy of about 0.3 MeV for electrons, 54.6 MeV for muons and 914.7 MeV for taus.

The photon yield also depends on the refractive index of the medium. The Frank-Tamm formula allows to estimate the number of Cherenkov photons with a wavelength λ emitted per unit length x [79]:

$$\frac{d^2N}{dxd\lambda} = \frac{2\pi\alpha}{\lambda^2}\left(1 - \frac{1}{\beta^2 n^2 \lambda}\right) \tag{4.2}$$

with α being the fine structure constant. The integral of this expression between 300 and 600 nm and using the refractive index of the ice, yields an emission of about 330 photons per cm for a relativistic charged-particle track. Detecting these photons and reconstructing the parent neutrino direction and energy is the goal for neutrino detectors. As such, these detectors can be considered as neutrino telescopes.

4.1.2 History and state of the art of neutrino telescopes

Another important word in Markov's proposal is the word *deep*. Placing neutrino detectors at a certain depth rather than at the surface indeed allows for a reduction of the large muon background coming from cosmic rays hitting the Earth atmosphere. Finally, it was noted that *a lake or the sea* would be needed in view of the large size of the device one has to build to detect neutrinos due to their small cross-sections with matter.
In summary, to detect neutrinos, one needs a large volume of dielectric medium located deep below the surface. The medium should also be transparent to Cherenkov photons and have a minimal light contamination in order to optimize the detection. Besides water as implied above, ice was also a potential candidate. All the ingredients were there to start building neutrino telescopes.

The history of cherenkov neutrino detectors started a few kilometers away from Big Island, Hawaii at a depth of 4.8 km [80]. The Deep Underwater Muon and Neutrino Detector, or *DUMAND* [81] was proposed at the 1973 International Cosmic Ray Conference in order to measure the muon depth-intensity curves. Unfortunately technical and financial reasons prevented the deployment of the originally conceived DUMAND

[1] As we will see later, this is the range where the IceCube sensors are sensitive.

and a smaller version was deployed. The most sustaining result from the DUMAND project has been to measure muon intensity as a function of depth as it was initially planned. For this measurement, the detection units were however deployed on a test string attached to a ship for some hours [82] rather than tied to the sea floor.

A few other places on Earth meet the above criteria for the location of a neutrino telescope while allowing hardware deployment and structure maintenance. Among those, three sites were chosen:

- Lake Baikal, Russia
- The Mediterranean sea
- The South Pole, Antarctica

Large neutrino detectors were installed in these locations. Nowadays, their successors operate (or are about to) with increased sensitivity compared to the initial design.

Lake Baikal The Southern part of the Lake Baikal contains the Baikal Neutrino Telescope. Located 3.6 km away from the shore and 1.1 km below the surface, the Baikal detector was the first, in 1993, to contain the three strings required to reconstruct the muon trajectories with full spatial resolution. The collaboration also reported the first atmospheric neutrino detected underwater [80]. The full configuration of the detector, an array of 192 optical modules, has been taking data since its completion in 1998.

An upgrade of the Baikal detector is currently under construction. The Gigaton Volume Detector, or *GVD*, will consist of 8 (and up to 18 in a second phase) clusters of 8 strings, each string carrying 24 optical modules spaced uniformly between 900 m and 1250 m below the surface. The clusters will have a lateral separation of 300 m. According to simulations, the threshold for muons would be of about 3-10 TeV [80]. In order to limit the contribution of accidental hits from dark noise and bioluminescence, the collaboration has to apply stringent cuts, reducing the effective area of the detector at lower energies. This detector therefore does not seem a promising candidate for low-energy neutrino searches, but may however lead to competitive results for neutrino signals from Gamma Ray Bursts or Active Galactic Nuclei jets in the 100 TeV region and beyond [80].

The Mediterranean sea The Mediterranean sea saw the deployment of three deep-sea detectors: NESTOR, ANTARES and NEMO, in this order. The "Astronomy with a Neutrino Telescope and Abyss environmental RESearch", or *ANTARES*, is the only detector with a successful installation. While the two others have performed technical R&D and deployed prototype devices, ANTARES has been operational since 2008. Located 2475 m below the sea surface in the region of Toulon, France, ANTARES consists

of 12 strings, installed 60 to 70 m away from each other, each carrying 25 *storeys* with a spacing of 14.5 m. Each storey is equipped with three optical modules as well as electronic and calibration devices. As for the Baikal detector, ANTARES has to deal with bioluminescence with a rate varying from a few 10 kHz to a few 100 kHz, in addition to generating "bursts" in the MHz region. The detector also records single photons from the decay of ^{40}K. While the raw data are transferred to the shore, an offline filtering selects event candidates based on multiple hit coincidences and/or multiple photo-electron hits in a single photomultiplier [80]. This results in an energy threshold for detected neutrino interactions of about 4 GeV [83].
The "NEutrino Mediterranean Observatory, or *NEMO*, project has Italian roots. The project started in 1998 and developed a new concept of *flexible towers* constructed of horizontal bars of a length up to 15 m. A first small version of the towers was deployed in 2007 and took data for a few months, providing the proof of concept for this technology. The same geometry has been selected for the *KM3NeT* detector, which is currently under construction.
Finally the *NESTOR* project started out in Greece in the early 90s. A first cable was installed at 4 km depth. A single floor with 12 optical modules was deployed and operated for more than a month.
In these two prototypes, the atmospheric muon flux appeared to be in good agreement with the expectations [80].

These three collaborations joined each other to form the *KM3NeT* project, a common deep-sea infrastructure coupling a neutrino telescope with measurement devices from marine biologists, oceanographers and environmental scientists. The detector will be divided into 2 sites: the *Arca* and the *Orca* detectors illustrated in Fig. 4.2 [84]. While the first one, under deployment close to Sicily at the Italian coast, is optimized for high-energy astrophysical neutrino searches, the second one near to Marseille, with a denser geometry, is designed for neutrino oscillation and mass hierarchy measurements. The KM3NeT optical modules have been designed to contain 31 photocathodes, allowing direction reconstruction based on single module detections as well as a better selection of physics over noise events, even at low energies. Once completed, both the Orca and Arca parts of KM3NeT may therefore be a good detector to search for GeV neutrinos from solar flares.

The South Pole Being the only location in the Southern Hemisphere, the South Pole offers ice, rather than water, as surrounding medium for the detector. Ice has several (dis-) advantages compared to water. The main advantage of ice is the stable, low noise rate of 560 Hz, compared to the 20-40 kHz due to ^{40}K decays and bioluminescence in deep water detectors. However the optical properties depend on the quality of the ice and therefore on the depth, which complicates the analysis of experimental data. On the one hand, the strong scattering causes a larger delay in photons, leading to a worse angular resolution in ice compared to water. On the other hand, larger absorption lengths result in better photon collection. These ice properties were tested, in 1993, in

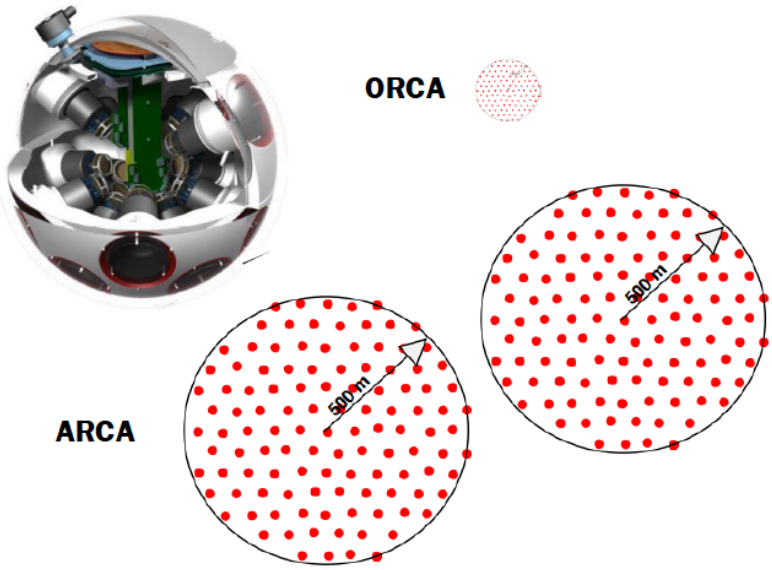

Figure 4.2: The two incarnations of KM3NeT. The two ARCA blocks (bottom) have diameters of 1 km and a height of about 600m and focus to high-energy neutrino astronomy. ORCA (top) is a shrunk version of ARCA with only 200 m diameter and 100 m height. Both ARCA and ORCA have 115 strings with 18 optical modules (OMs) per string. Top left, a drawing of an OMs is shown. Each OM houses 31 small photomultipliers. Figure and caption from [80].

a first test array with 80 optical modules distributed on four strings at depths between 800 and 1000 m. The full configuration of the Antarctic Muon And Neutrino Detector Array, or *AMANDA* was gradually deployed in the ice of the South Pole, a few hundred meters away from the Amundsen-Scott station and has been completed in January 2000. With 19 strings and 677 optical modules located between 1500 and 2000 m, the detector was the world's largest neutrino telescope and had a threshold of 50 GeV. The angular resolution was however worse than for ANTARES with 2 - 2.5 degrees compared to < 0.5 degrees for muon tracks and 25 degrees compared to 5 - 8 degrees in water for cascades [80].

Its successor, the *IceCube Neutrino Observatory* consists of a km^3 of instrumented ice located 1.5 km below the South Pole surface [85]. Completed in december 2010, the detector consists of 86 vertical strings, each connecting 60 digital optical modules, or *DOMs*. The strings have an averaged horizontal spacing of 125 m while the DOMs are located every 17 m along the string. A sub-detector, named *DeepCore*, is installed at the center of the array. Characterized by smaller spacings between strings (70 m) and DOMs (7 m), DeepCore presents a lower energy threshold, opening the neutrino detection down to 10 GeV. The low noise rate in the ice and the tremendous work achieved by

the Collaboration to understand the different noise sources and their patterns lead to a further reduction of the energy threshold. IceCube is therefore the first operational telescope that could allow the search described in this thesis.
Since this work focuses on the South Pole site and the ability of IceCube to detect solar flare neutrinos, we will continue discussing the detector characteristics for this specific detector.

4.2 Detecting Neutrinos at the South Pole

4.2.1 Properties of the ice

Absorption and scattering length Before the AMANDA detector, polar ice studies were made through the extraction of an ice core and the measurements of its optical properties in a laboratory. This technique does unfortunately not allow to resolve separately the absorption and the scattering of the light when travelling through the ice core. These two properties, however, were expected to produce a very different effect for reconstruction of neutrino events in the ice. The AMANDA Collaboration had therefore to develop a method allowing to study absorption and scattering lengths in situ. Initial measurements were performed using AMANDA optical modules deployed between 800 and 1000 m [86, 87, 88]. Absorption and scattering could be separated using the time dependencies of detected photons produced by monochromatic pulses of laser light with 4 ns duration. The collaboration measured absorption lengths of 200 m at visible wavelengths and this confirmed the superiority of ice over water for photon collection [86]. A wavelength dependency was observed, indicating the presence of absorbing impurities.
The scattering properties of the ice were also studied with the same technique [88]. It appeared that the scattering length was modified by a factor of two over 200 m of depth. This effect was attributed to the variation of air bubble density due to the formation of the ice by compression of compacted snow, trapping air in the process. However, in the deeper ice where IceCube was later installed, dust dominates the scattering effects over air bubbles as demonstrated by AMANDA-B, a 600 optical module version of the original detector located between 1500 and 2000 m below the surface.

A common study of the absorption and scattering profiles illustrated in Fig. 4.3, showed that, in the deep ice, the two effects are strongly correlated. This reflects the presence of dust grains, dominating both absorption and scattering. The sub-dominant contribution of air bubbles can be explained by the high-pressure at 1300 m or deeper. The air is under so high pressure that it diffuses into the surrounding ice and forms non-scattering hydrate crystals, or *clathrates* [89].

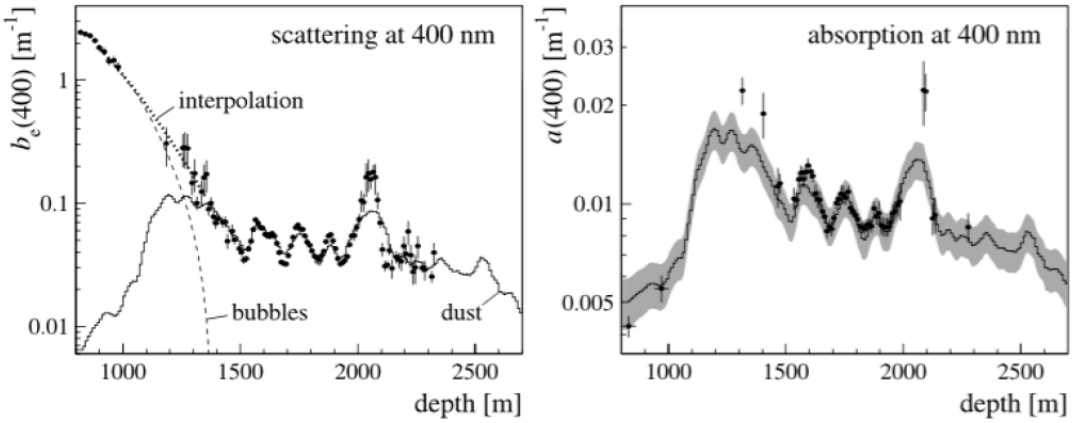

Figure 4.3: Correlation of dust concentration with (left) scattering ($b_e = \lambda_e^{-1}$) and (right) absorption ($a = \lambda_a^{-1}$) at 400 nm. The dust profile in the left part is derived from a 50-m running average of dust mass concentration measured in ice cores from Vostok [90] and Dome Fuji [91] and translated to South Pole depths. It has been linearly scaled to match the data points between 1600 and 1900 m. The dashed line is an estimate of the contribution to scattering by bubbles. The shaded band on the right figure contains the one-standard-deviation estimate of absorptivity calculated by applying the linear correlation to the dust contribution to scattering in the left picture. Figure and caption from [92].

Dust concentration Considering the measured effect of the dust on light propagation, it was important to measure the dust concentration as a function of depth. A *dust logger*, i.e. a combination of cameras and lasers, was lowered in the ice holes, prior to AMANDA-B string deployments. This dust logger allowed to establish several facts, as mentioned in [93]:

- The features identified by the logger could be matched with known features at other locations, allowing to date the moment where the ice surrounding the current IceCube detector was created. Ice at 2 km depth is 65,000 years old.
- A large dust concentration was discovered around depths of 1300 m, corresponding to the last glacial maximum.
- The logger allowed to identify several layers of a few centimeters where the dust concentration increases. These correspond to known volcanic eruptions.
- Independently of volcanic eruptions, a steadily varying dust concentration of atmospheric origin has been observed.
- A dust layer has been localized 2000 m below the surface.

The same exercise was realized in IceCube holes, and the results can be seen in Fig. 4.4. As seen in this figure, there is a difference in the peaks depending on the depths. The layers of constant time properties have the same deposition time. However, these isochrones are no longer coplanar due to the flow and the shearing of the ice. This resulted in a tilt, creating the effects seen by the dust logger [93].

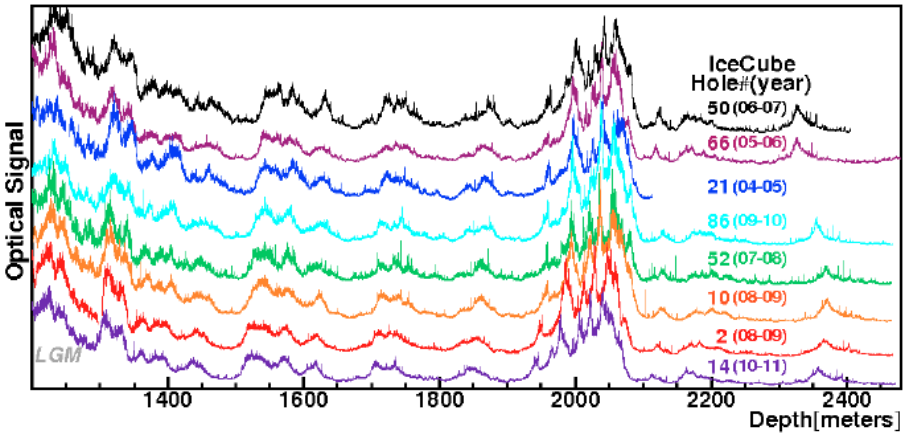

Figure 4.4: Results of the dust logger operation in IceCube, prior to deployment. Figure from [94].

Hole Ice A *Sweden Camera* has been installed in the IceCube version of the detector, at the bottom of string 80 at a depth of 2455 m. This camera allowed to identify ice structures due to the deployment of the strings. The system is still used nowadays to monitor the evolution of the hole ice and to observe features, not considered so far, that could improve the understanding of light propagation around the optical modules. An example of such features are air bubbles present in the hole due to the refreezing of the ice around the optical modules. These bubbles create an artificial isotropization of the signal due to shorter scattering lengths. Fig. 4.5 illustrates the operation run of the camera during the South Pole summer season 2016-2017.

All these effects are compiled in ice models developed by the IceCube Collaboration and taken into account in the reconstruction of the events. The uncertainty on each parameter constitutes systematic errors that will be discussed in Chapter 5.

4.2.2 Geometry and optical modules

In order to install the optical modules in the ice as described above, holes were made using a hot-water drill. Once the hole was formed, a string holding 60 digital optical modules, or *DOMs*, was lowered into the ice. 86 of these strings were deployed between January

Figure 4.5: Operation of the Sweden Camera during summer season 2016-2017. Filaments and air bubbles can be seen on the last figure.

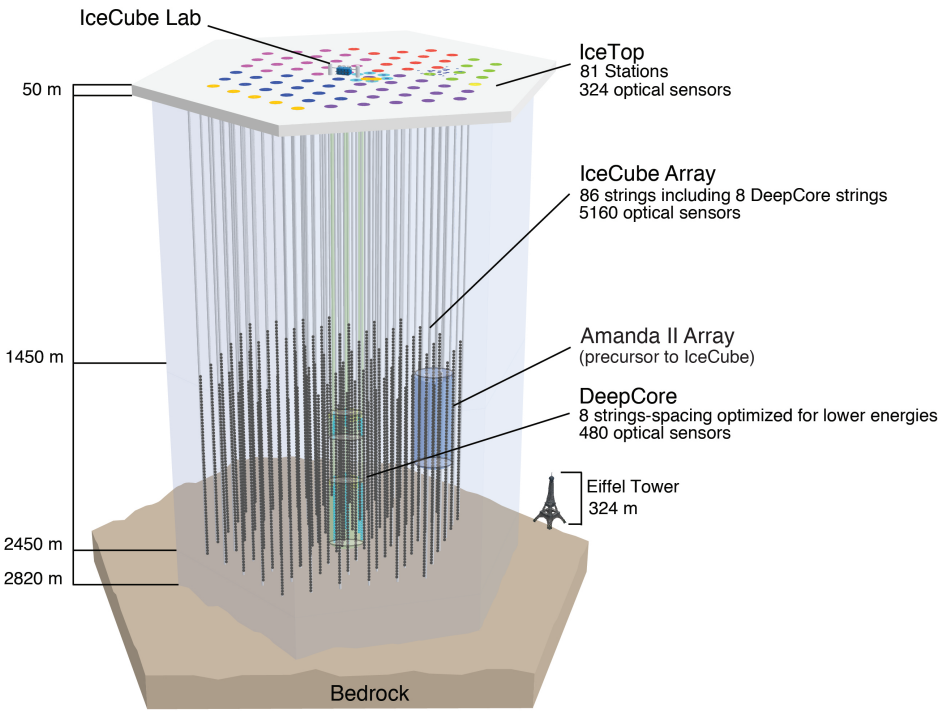

Figure 4.6: Schematic view of the IceCube Neutrino Observatory with the IceTop array and the DeepCore. For comparison, the AMANDA detector is illustrated. Credits: the IceCube Collaboration.

2005 and December 2010[2]. In total, 5160 DOMs were frozen into the ice at depths of 1450 to 2450 m. Additional DOMs, 320 in total, were installed at the surface to form the IceTop array used both to veto atmospheric muons and for cosmic ray studies. The inner core of IceCube has been filled with extra strings to form the DeepCore sub-array, allowing to lower the threshold to 10 GeV. A schematic view is presented in Fig. 4.6.

Geometry The environmental studies performed during the AMANDA time allowed to reoptimize the spacing between the DOMs and the strings. It resulted in an average horizontal spacing of 125 m between the strings and 17 m between the DOMs on the same string [85].
The DeepCore part consists of 7 standard IceCube strings plus 6 additional special strings. It results into a smaller spacing between each element: 7 m vertical separation between two DOMs and strings are on average 72 m apart. The DOMs on the additional strings are equipped with photomultiplier tubes (PMTs) with an enhanced

[2]Due to the extreme conditions at the South Pole, the deployment was only feasible during Austral summer seasons, i.e. from November to February.

quantum efficiency. This denser layout allows to reach a threshold of 10 GeV for track reconstruction. In addition of the smaller spacing between its elements and the 30% higher quantum efficiency of the PMTs, DeepCore benefits from the clearer surrounding ice located below 1750 m providing optimal optical properties. One can also use the rest of the IceCube detector to veto atmospheric events. Details about the IceTop array as well as the acquisition system allowing IceCube to be sensitive to supernova bursts can be found in [85].

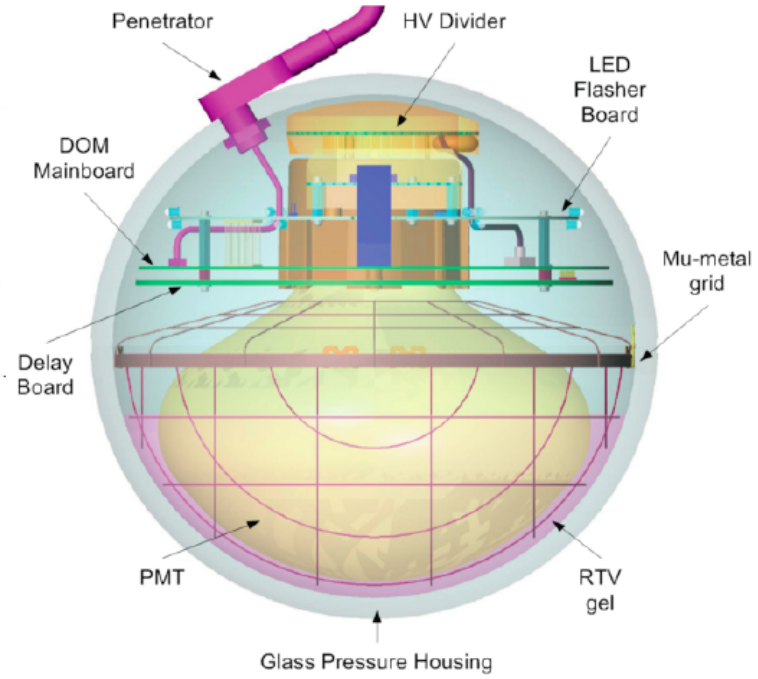

Figure 4.7: Schematic view of a Digital Optical Module, or *DOM*. The different components are detailed in the text. Credits: The IceCube Collaboration.

Optical Modules As previously mentioned, IceCube consists of 5160 Digital Optical Modules, or *DOMs*. Each of them consists of a Hamamatsu R7081-02 10-inch photomultiplier tube, oriented downward, embedded in a 13-inch glass sphere. The average gain of the PMT is set to 10^7. The sphere, sealed with dry nitrogen at 0.5 atm, also contains [85]:

- a mu-metal grid to reduce the influence of the Earth magnetic field
- silicon gel to mechanically and optically couple the glass sphere to the PMT
- a high-voltage generator providing power for the different elements of the DOM

- a main board where the signal is digitized by a fast Analog-to-Digital Converter (fADC) and two Analog Transient Waveform Digitizers (ATWDs) operating in a *ping-pong* mode to avoid dead-time. The ATWDs operate at 300 mega samples per second and each of them has 3 input channels at different amplification levels to obtain a large dynamic range and cope with saturation effects. The readout of the ATWD signal has a maximum duration of 426 ns and a bin size of about 3.3 ns. Meanwhile, the fADC operates at 40 mega samples per second for a maximum duration of readout of the order of 6 μs with a bin size of 25 ns. The digital section of this main board is based on a field-programmable gate array (FPGA). This allows the communication with the electronics located at the surface.

- a LED flasher board emitting pulses used for calibration purposes

- a precise quartz oscillator to provide local clock signals. All the clocks are synchronized every few seconds with a central GPS clock.

The material is optimized for Cherenkov radiation detected by the PMTs and is therefore transparent between 300 and 650 nm with a maximum of transparency at 410 nm. Finally a penetrator is connecting the inside of the DOM with a single twisted-pair of 1 mm copper conductor going up to the surface. This cable allows for power and communication between the DOM and the surface. At the surface, power, communication and calibration are provided by 8 custom PCI cards per string. A schematic view of a DOM is visible in Fig. 4.7. More details can be found in [85].

4.2.3 Triggering and filtering

The time resolution allowed by this architecture is around 2 ns and it can operate without any dead-time. The digitization of the signal is performed if the analog output of the PMT is above a discriminator threshold equal to 25% of the average signal from one photoelectron. The full array records about 800 GB/day of raw data written on tape. Different flags are attributed to qualify the signal [85]:

- Hard Local Coincidence, or *HLC*, when two neighbor or next-to-neighbor DOMs on the same string have recorded a signal above threshold within a 1 μs time window. The full fADC and ATWD waveforms are then available.

- Soft Local Coincidence, or *SLC*, if the hit does not qualify for the above criteria. In this case, only reduced fADC information is available, i.e. the highest bin and two neighboring bins with a timestamp. Due to the lower clock frequency of the fADC compared to the ATWDs, the time resolution for these hits is less accurate.

The resulting data sample is at this stage still dominated by noise[3]. In order to reduce this noise rate, trigger conditions based on coincidence are applied. The main trigger for IceCube events is the Simple Majority Trigger, or *SMT-8*, which required at least 8 DOMs with HLC pulses within a 5 μs time window. Other geometrical triggers, as for example the StringTrigger, have also been implemented to save a specific morphology of events, i.e. almost vertical events in the chosen example [85]. A softer trigger condition has been implemented for DeepCore events in order to lower the energy threshold. The *SMT-3* requires, similarly to its counterpart in IceCube, 3 DOMs with HLC pulses within 2.5 μs. Considering the low energy expected for solar flare neutrinos, we will focus on events that have fulfilled the SMT-3 condition.
Once an event has passed one or several trigger conditions, it is submitted to filters. Several filters have been designed to select specific physics cases. Among them, we encounter the *Cascade Filter* aiming at selecting cascade-like events or the *EHE filter* selecting events that reflect the signal from extremely high energy neutrino interactions. We will use the features and experience with each of the existing filters in order to select GeV neutrinos. We indeed do not expect GeV scale events to pass directly any of the developed filters but we will exploit the *DeepCore filter* to act as a veto against some atmospheric muons[4].
Once the event has passed at least one filter, it qualifies to be sent north via satellite. About 90 GB/day are sent daily to the Northern Hemisphere and used in offline processing to search for interesting physics signals [85]. A more detailed description of the online and offline processing can be found in [85]. Fig. 5.3 shows examples of events detected by IceCube.

[3]Since the study presented in this thesis required a detailed understanding of the noise, the different contributions of the noise will be described in the Chapter 5.

[4]We will allow the events to pass two additional filters, i.e. the *Full-Sky-Starting* and the *Low-Up* filters. Details on the chosen filters will be presented in Chapter 5.

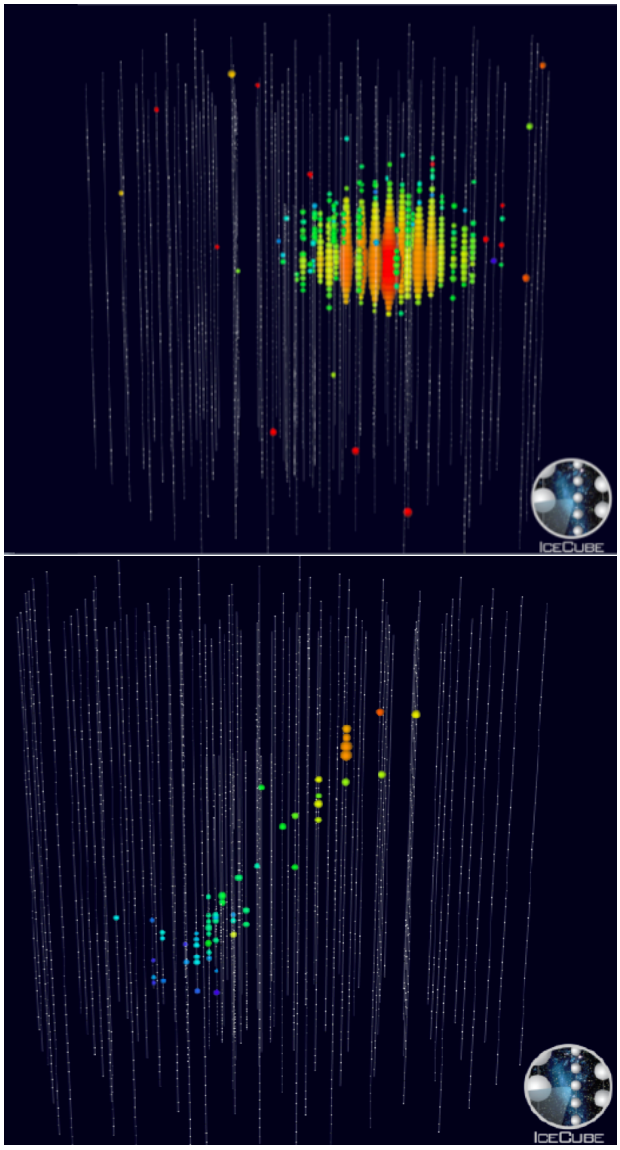

Figure 4.8: Examples of events as seen in IceCube. The top part of the panel shows one of the famous astrophysical events (for details see later in this Chapter), being a CC interaction of a ν_e or a NC interaction creating a cascade-like event. The bottom part represents a typical down-going atmospheric muon crossing the detector. The morphology of this event is called a *track*. A third morphology, not represented here because it has not yet been observed, is expected - the so called *double-bang*. A first cascade would come from a ν_τ interaction in IceCube followed shortly by a second one produced by the decay of the subsequent τ lepton. Credits: The IceCube Collaboration.

4.3 Breakthrough and other Noteworthy Achievements

The machinery described in the previous sections has proven itself through a breakthrough discovery and several remarkable contributions in (astro-)particle physics. We will outline the main achievements of the IceCube detector and the goals for the near future.
On top of the astrophysical searches briefly described below, the IceCube Collaboration is also active in particle physics research. By the use of DeepCore, measurements of the neutrino oscillation parameters are realized through the study of the (dis-)appearance of flavors in the atmospheric neutrino flux. Sterile neutrinos and non standard interactions are also studied using DeepCore [95, 96].

The astrophysical neutrino flux In 2013, the IceCube Collaboration has announced the first observations of neutrinos with an astrophysical origin. From the two events accidentally discovered at that time, a dedicated analysis running over the 6 year data sample has allowed to extract 82 events shown in Fig. 4.9 [97]. The so-called High-Energy Starting Event, or *HESE*, analysis searches for a diffuse neutrino flux by selecting events with high charge deposit in the detector (at least 6000 photoelectrons) and a *starting event*, i.e. events that have started inside of the detector without producing hits in the veto layer surrounding the array. These starting events can only be induced by neutrinos and consequently the atmospheric muon background is eliminated. However, at the highest energies this analysis is limited to the Southern hemisphere, since the Earth becomes opaque, even for neutrinos, due to the increasing cross section with increasing energy. Unfortunately the events do not statistically point toward a precise location of the Universe and no neutrino source has been identified yet. The HESE analysis was joined by several other analyses optimized for different energy scales [97] or different topology of events[5] [97]. A joint analysis of the different event selections leads to a measured astrophysical flux whose parameters are $\phi_{astro} = 1.01\ 10^{-18}$ GeV^{-1} cm^{-2} s^{-1} sr^{-1} and a spectral index $\gamma_{astro} = 2.19$ [97]. We note that future observations will have to assess whether the single power law hypothesis is viable or not.

IceCube as a point source detector Another approach to identify neutrino sources is to search for a neutrino counterpart from known astrophysical objects, such as, among others, Blazars or Active Galactic Nuclei. Focusing on existing catalogs established through detection of X-rays or gamma rays, one can select neutrino candidates arriving from the reported direction and search for an excess in comparison with the rest of the

[5]The HESE analysis by construction favored cascades over tracks. The more recently developed analyses target starting or through going tracks. The probability for the event to be of neutrino origin has therefore to be evaluated taken into account a potential atmospheric muon counterpart. However these event selections allow for a better angular reconstruction, limiting the area of the sky where the neutrino could have been produced.

sky. The sky map resulting from such searches is presented in Fig. 4.10. This approach, as the previous one, did not lead yet to the identification of a neutrino source.

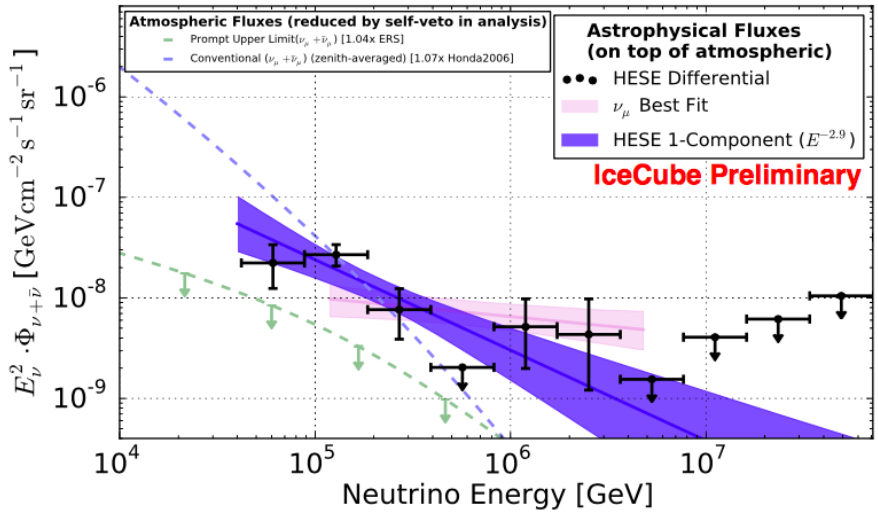

Figure 4.9: Best-fit per-flavor neutrino flux results (combined neutrino and anti-neutrino) as a function of energy. The black points with 1σ uncertainties are extracted from a combined likelihood fit of all background components together with an astrophysical flux component with an independent normalization in each energy band (assuming an E^{-2} spectrum within each band). The atmospheric neutrino and muon fluxes are already subtracted. The best-fit conventional flux and the best-fit upper limit on 'prompt' neutrinos are shown separately, not taking into account the effect of the atmospheric self-veto, which will significantly reduce their contribution. The blue band shows the 1σ uncertainties on the result of a single power-law fit to the HESE data. The pink band shows the $\nu_{\mu,up}$ best fit with 1σ uncertainties. Its length indicates the approximate sensitive energy range of the $\nu_{\mu,up}$ analysis. Figure and caption from [97].

The same method can be applied to localize neutrino production from dark matter. High-density objects as the Sun, the Earth, dwarf galaxies or the galactic center, are expected to accrete a potentially large amount of dark matter. As described in Chapter 1, scattering of dark matter particles with the ambient nuclei slows them down and provokes the gravitational trapping of such particles inside of the objects. This higher concentration of dark matter is therefore an ideal ground to search for neutrinos coming from the annihilation of these particles. As already mentioned, such searches targeting neutrino signal from the center of the Sun led to the best limit on the spin-dependent cross-section for dark matter-proton interactions [38].

Search for transients It is also possible to focus on astrophysical objects for which a transient neutrino signal is expected. In addition to focusing on a small part of the

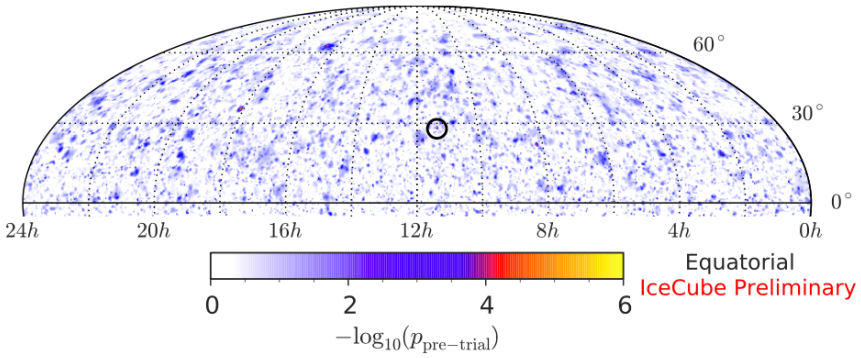

Figure 4.10: Pre-trial p-value sky map of the Northern hemisphere scan in equatorial coordinates down to -5 degrees declination. The pre-trial p-value is given as -log10 (pre-trial). The position of the hottest spot is indicated by a black circle, with a post-trial corrected p-value of 90.5%, thus compatible with background only. Figure and caption from [98].

sky, the short time window where the emission is expected according to theoretical predictions allows for a further reduction of the atmospheric background. Among the objects studied by the collaboration, we can mention the Gamma Ray Bursts, or *GRBs*, considered as one of the most promising sources of the ultra high energy cosmic rays observed at Earth [99]. The latest limits on the flux are shown in Fig. 4.11, where we can see that the cosmic ray escape via neutron production [100] is disfavored while the escape via proton [99] is in tension with the current limits. Fast radio bursts and novae are also topic of dedicated searches.

It is important to note that the event selection presented in this work allows IceCube to be sensitive to a GeV neutrino transient flux. Therefore, any of the objects studied in the high energy range could potentially be also studied using the innovative event selection outlined later on.

IceCube in the multi-messenger era A few years ago, the IceCube Collaboration joined the worldwide effort for multi-messenger astronomy. The participation of IceCube is twofold. On one hand, the collaboration sends alerts for high-energy events that are likely from astrophysical origin. Two different streams, *HESE* and *EHE* (see [102] for details), trigger searches for electromagnetic counterparts by observatory partners following the alerts.
On the other hand, the collaboration has set up a fast response analysis, allowing to give a realtime detection or limit on the neutrino flux coming from observed astrophysical objects. Follow-up searches for Cygnus X-3, GRB 170405A and AGL J0523+0646 among others, were already performed [98]. No coincident neutrinos were detected yet through this method.

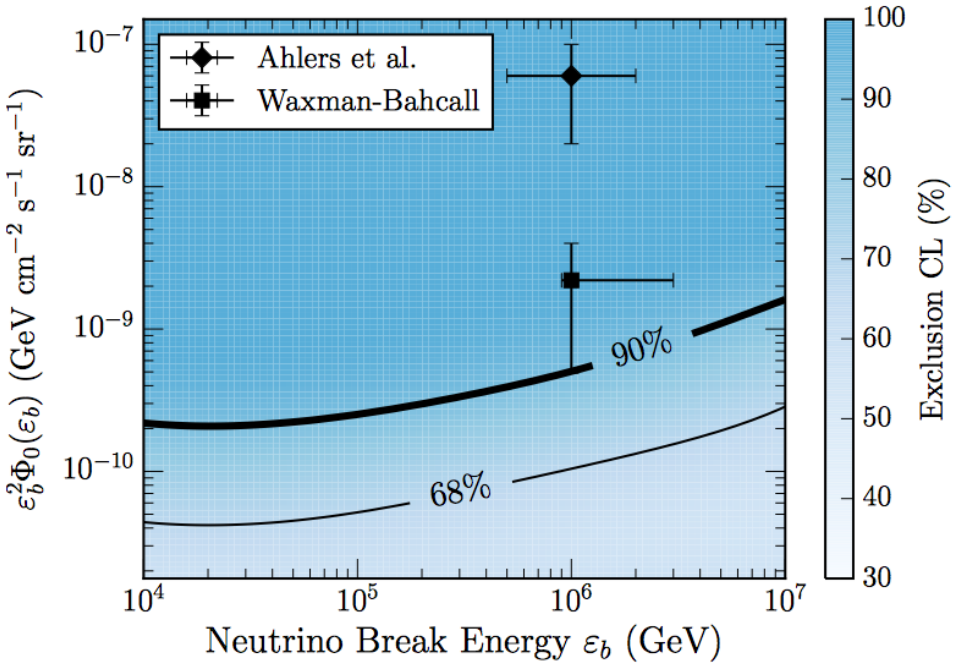

Figure 4.11: Exclusion contours, calculated from the combined three-year all-sky ν_e, ν_τ, $\nu_\mu$shower-like event search and four-year Northern Hemisphere ν_μ track-like event search results, of a per-flavor double broken power law GRB neutrino flux of a given flux normalization ϕ_0 at first break energy ϵ_b. Figure and caption from [101].

Finally, it has to be noted that IceCube is a partner of the gravitational wave interferometers, LIGO and Virgo. The collaboration has successfully received the alerts sent for, among others, the historical event of August 17th, 2017 [103]. On this date, the first observation of a binary neutron star (BNS) merger was followed about 1.7 s later by the observation of a gamma ray signal consistent with a short GRB [104]. The event was then detected in other wavelengths through the observation of a kilonova as illustrated in Fig. 4.12. This joint observation confirmed *inter alia* BNS mergers to be the possible progenitors of short GRBs as predicted. Unfortunately no neutrinos were observed, but the machinery proves its proper function and the collaboration will continue to follow gravitational wave alerts during the next observational run of the interferometers planned for Fall 2018.

The different searches briefly described here prove that the IceCube Collaboration continuously pushes the limits of the detector in order to obtain always better scientific results. The search presented in this thesis is along the same line. The next chapter will describe how combining transient and low-energy techniques, we can manage to lower the energy threshold of IceCube down to the single GeV level.

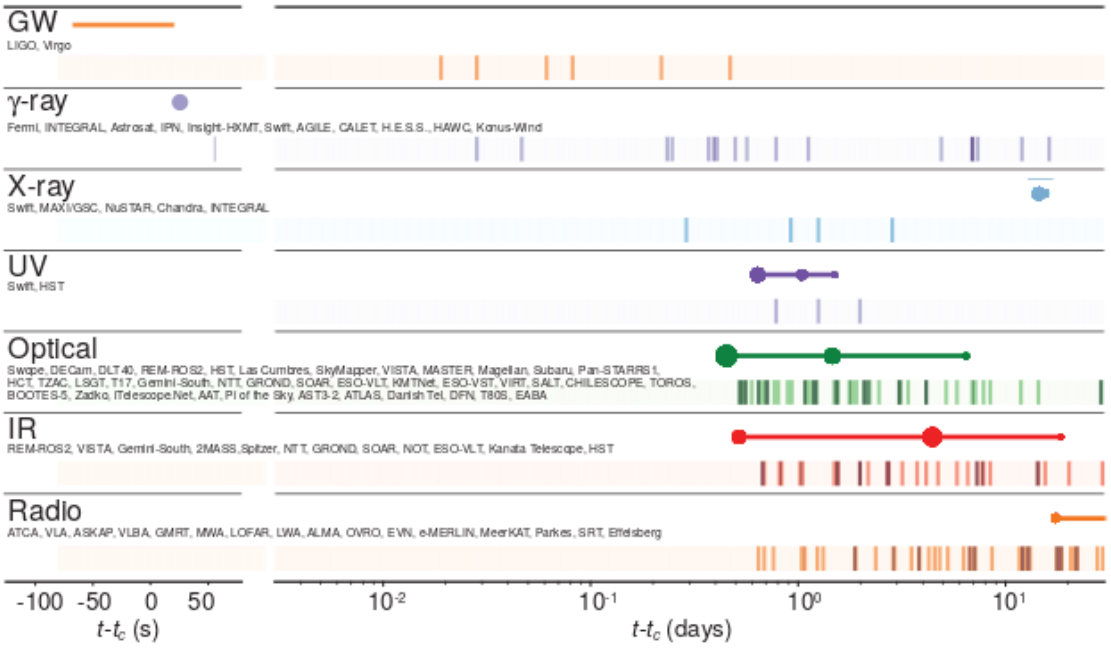

Figure 4.12: Timeline of the discovery of GW170817, GRB 170817A, SSS17a/AT 2017gfo, and the follow-up observations are shown by messenger and wavelength relative to the time t_c of the gravitational-wave event. Two types of information are shown for each band/messenger. First, the shaded dashes represent the times when information was reported in a GCN Circular. The names of the relevant instruments, facilities, or observing teams are collected at the beginning of the row. Second, representative observations in each band are shown as solid circles with their areas approximately scaled by brightness; the solid lines indicate when the source was detectable by at least one telescope. Figure and caption adapted from [104].

De Guiche: – *Mais voilà six moyens excellents!... Quel système*
Choisîtes-vous des six, Monsieur ?
Cyrano: *Un septième !*

Cyrano de Bergerac, Troisième acte, scène XII,
Edmond Rostand

5

Detecting Low Energy Transient Events with IceCube

This Chapter describes a new approach in using the IceCube Neutrino Observatory. It presents an innovative analysis method developed to study low-energy interactions happening in the neighborhood of IceCube. As will be shown in Section 5.5.1, the event selection is optimized for GeV neutrinos and is therefore ideal to search for solar flare neutrinos. After presenting the main characteristics of GeV interactions as seen in IceCube, we will review the different steps of the selection procedure and conclude with the effective area for such a low-energy signal.

5.1 Searching for Low Energy Neutrinos with IceCube

5.1.1 General idea

While IceCube was originally designed to observe TeV neutrinos as mentioned in the previous Chapter, the collaboration has demonstrated the ability to extend the sensitivity to a larger energy range by the use of DeepCore. Up to now, neutrino searches in IceCube were possible in the MeV range for large fluxes by the use of the Supernova Data Acquisition system [85] and starting at around 10 GeV for neutrino oscillation and atmospheric studies in DeepCore [85]. We present a novel selection procedure which enables us to cover the gap between these two energy ranges. The general idea of the

analysis described in this chapter is to monitor the rate of GeV-like events in IceCube and to search for an increase in this rate during an astrophysical transient, as for example a solar flare.

5.1.2 Event samples

The new event selection has been developed in a data-driven way. We have used several hours of off-time data, i.e. IceCube data recorded when no solar flare was happening on either side of the solar disk. In order to determine the time period when such data were available, we compared the observations of GOES [48], detecting X-ray emission from solar flares and Fermi-LAT [105], which is sensitive to gamma rays. We also used the observations from satellites observing the back side of the Sun, i.e. the Stereo-A and B satellites [106], which detect, among others, solar energetic particles. In order to prevent bias in future searches for neutrino emission from, e.g., Novae, FRBs, or flaring blazars, using the same event selection, the absolute time of the data will be omitted on purpose. A day of data has been used in the following periods:

- July 2011
- December 2012
- February 2013
- June 2014
- May 2015
- March 2017

We also used simulated events in order to understand the behavior of the selection to the different types of events present in the data. The following simulation data sets have been used:

- CORSIKA [107]: the Cosmic Ray Simulations for Kascade is a Monte Carlo simulation program simulating extensive air shower events initiated by high-energy cosmic particles hitting the Earth's atmosphere. We used here a version specific to IceCube, propagating the produced muons in the ice and generating hits in the detector. These simulation data sets are used to study atmospheric muons (as background or signal) traveling in the neighborhood of IceCube.
- GENIE [108]: The GENIE Neutrino Monte Carlo Generator generates neutrino interactions between 100 MeV and a few hundred GeV. It is generally used by the IceCube Collaboration to study interactions of atmospheric/astrophysical neutrinos. This generator is coupled to PROPOSAL [109] to propagate the muons as well as GEANT4 [69] for the direct propagation of:

  - Taus and muons
  - Hadrons with an energy below 30 GeV
  - Electrons and photons with an energy below 100 MeV

  An OpenCL-based photon-tracking simulation and a noise generator are also used to generate the events as seen in IceCube.

- Pure Noise simulation: We use events created by random hits in the detector. These events are produced by a noise event generator based on an empirical model consisting of three noise components inherent to IceCube DOMs : uncorrelated thermal noise, uncorrelated radioactive noise and correlated scintillation noise. More details will be presented later in this Chapter. This simulation set will be called *Vuvuzela* in this Chapter.

- Signal-like events: We used GENIE simulation data to create signal-like events. We selected generated interactions of neutrinos with an energy < 5 GeV arriving from a solar direction, i.e. -23 degrees $<$ declination $<$ 23 degrees. Two different simulation sets have been used. The first one targets neutrinos with an energy above 1 GeV while the second one generates interactions from neutrinos with an energy between 500 MeV and 1 GeV. The consistency between these two different simulation sets has been checked and is presented in the next sections. The following terms will be used to mention the different simulation sets:

  - *Elowen*: for neutrinos between 500 MeV and 1 GeV
  - *Lowen*: for neutrinos between 1 GeV and 5 GeV

5.1.3 Neutrino interactions for energies below 5 GeV

The following interaction processes, represented in Fig. 5.1, can happen in the energy range concerned in this search [22]:

- Deep inelastic scattering (DIS): Above a few GeV, the neutrino - matter cross section is dominated by deep inelastic scattering. The interaction can be written as $\nu_l + \text{nucleon} \rightarrow l^- + X$ for neutrinos and $\bar{\nu}_l + \text{nucleon} \rightarrow l^+ + X$ for antineutrino where l represents the flavor of the neutrino and the produced charged lepton. Similar reactions are expected for neutral current interactions of neutrinos with matter.

- Quasi-elastic scattering (QE): At lower energies (< 1 GeV), the quasi-elastic scattering and resonance production processes dominate. The quasi-elastic scattering refers to $\nu_l + n \rightarrow l^- + p$ for neutrino and $\bar{\nu}_l + p \rightarrow l^+ + n$ for antineutrino as well as $\nu_l + p \rightarrow \nu_l + p$ and $\nu_l + n \rightarrow \nu_l + n$. A charged lepton and a single nucleon are ejected during this interaction of a neutrino with a nucleon of the target material.

- Resonant production (RES): Neutrinos can also inelastically scatter at nuclear matter producing a nucleon excited state, such as Δ or N*. The process is therefore $\nu_l + N \rightarrow \nu_l + N^*$ with a later relaxation $N^* \rightarrow N + \pi^0$

- Coherent scattering (COH): In the same line of the RES production, a neutrino can scatter off the entire nucleus and produce pions through both CC and NC interactions $\nu_l + A \rightarrow l^- + A + \pi^0$ or $\nu_l + A \rightarrow \nu_l + A + \pi^0$ for neutrino

The contribution of each of the different interaction processes described above is illustrated in Fig. 5.2 for ν_e and ν_μ. As can be seen in the figure, the two different simulation sets give a consistent contribution of each process around 1 GeV.

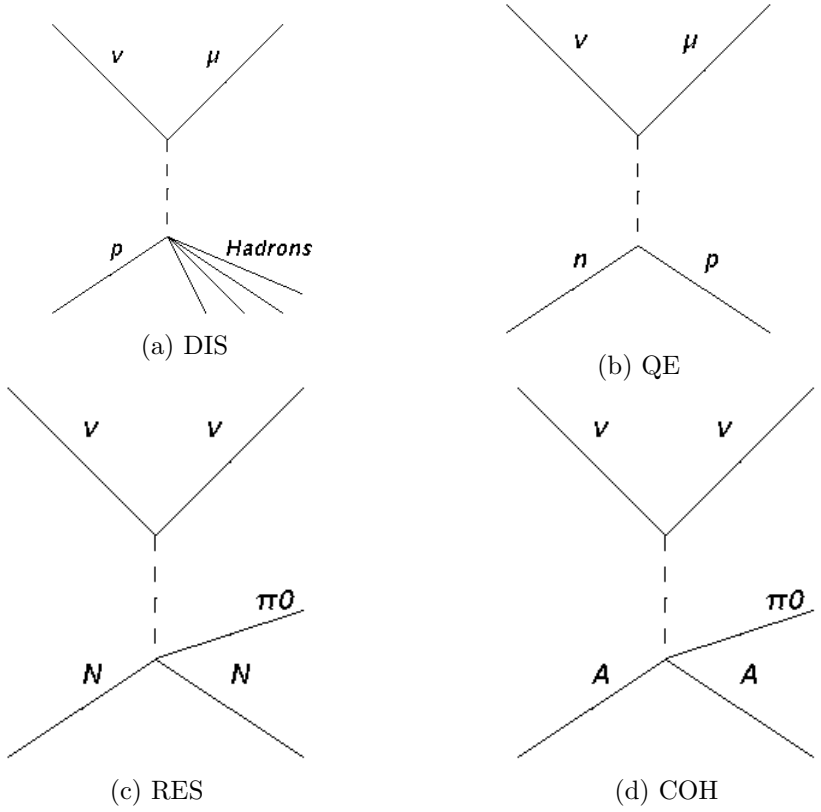

(a) DIS (b) QE

(c) RES (d) COH

Figure 5.1: Feynman diagrams of the different interactions presented in the text.

Fig. 5.3a and 5.3b show examples of < 5 GeV neutrino interactions as seen in IceCube. More events are presented in Appendix B. They are all characterized by low light yield in the detector and a small number of DOMs able to record the interaction. The main difficulty in this event selection is to differentiate these extremely low-energy interactions from pure noise events that are due to detector effects. For comparison, Fig. 5.3c shows a pure noise event.

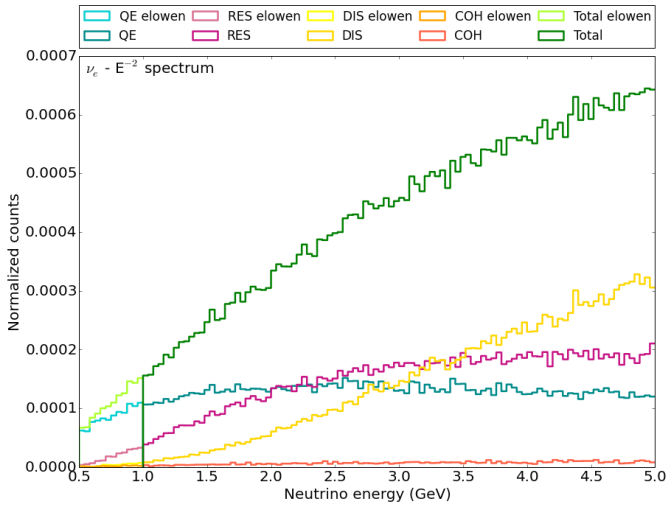

(a)

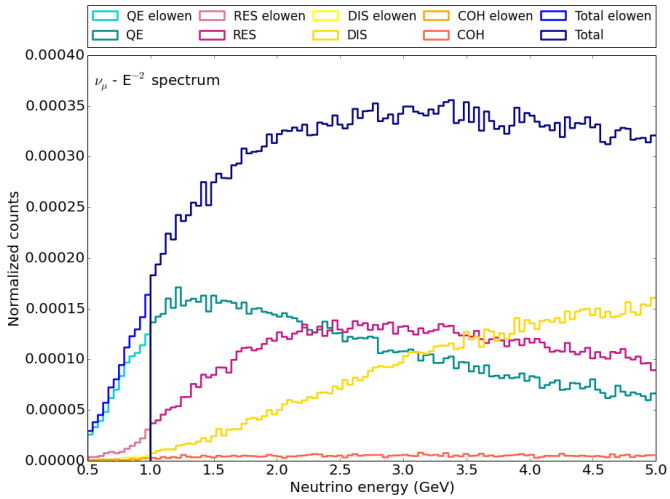

(b)

Figure 5.2: Contribution of the different interaction processes for GeV neutrinos as explained in the text. The top (bottom) part of the figure is for $\nu_e(\nu_\mu)$.

Produced Charged Leptons It is interesting to look at the estimated energy obtained by the charged lepton after the interaction process. The results are visible in Fig. 5.4. Once again, there is a good agreement in the prediction given by the two simulation sets. Fig. 5.4 also shows the expected track length of the charged muon produced in CC interaction of ν_μ. A relativistic muon produced by a 1 GeV neutrino will travel less than 5 m.

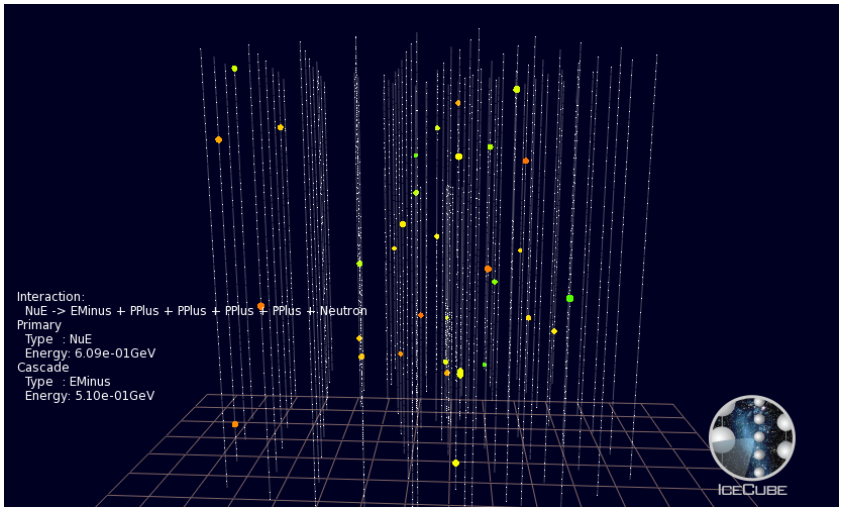

(a)

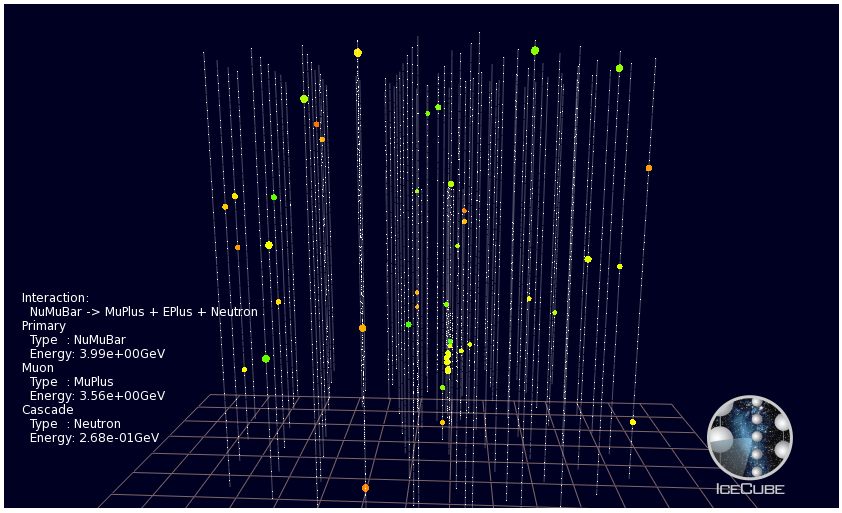

(b)

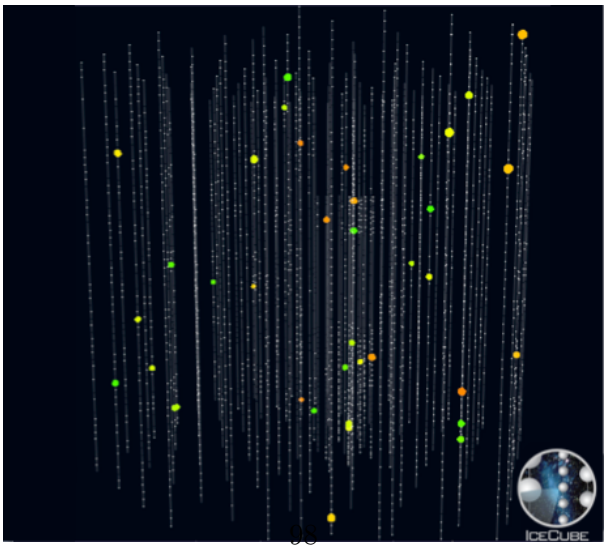

(c)

Figure 5.3: The first two pictures represent GeV neutrino interactions as seen in IceCube. The bottom part of the figure illustrates a typical noise event arising from detector effects.

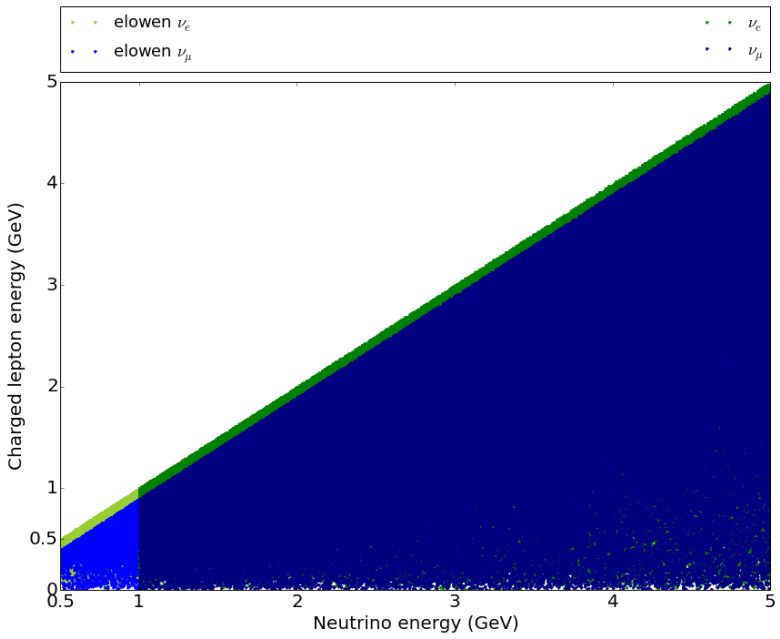

(a)

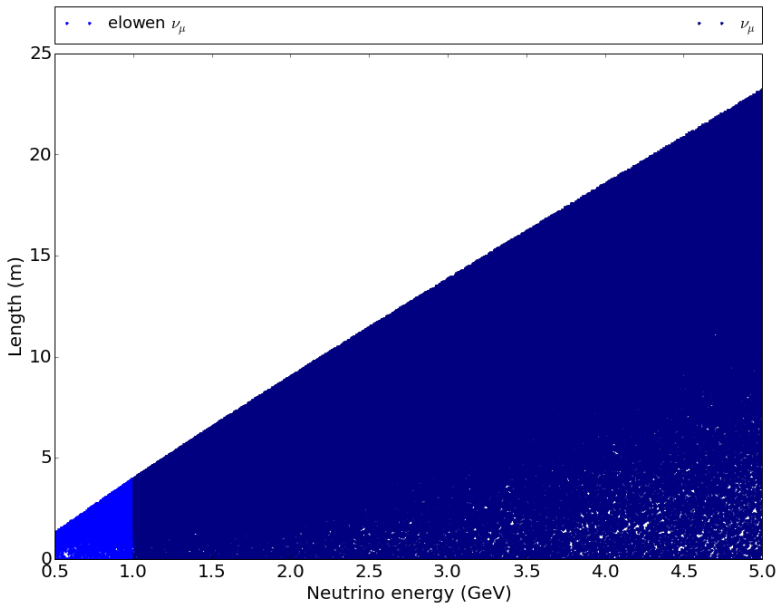

(b)

Figure 5.4: Top: Energy obtained by the charged lepton in CC neutrino interactions. Bottom: Track length of the muon produced in CC interactions of ν_μ. The two simulation sets mentioned in the text give consistent values for the two parameters around 1 GeV.

Table 5.1: Combinations of passed filters that allow an event to be kept in the sample.

Variable	Passing conditions
Passing filters	DeepCore
	DeepCore + LowUp
	DeepCore + FSS

5.2 Removing High-Energy Events

This part of the event selection aims at reducing the amount of *high-energy* events, i.e. neutrinos with an energy > 5 GeV, from the data sample. This is motivated by the energy range in which we expect solar flare neutrinos. This energy range extends up to maximum 5 GeV for optimistic assumptions on the initial proton spectrum, as demonstrated in Chapter 3. The main difference between an event with arbitrarily high energy and a GeV neutrino interaction is the amount of light emitted in the ice. A dedicated filter selection, as outlined below, removes high-energy events from the sample. Furthermore, imposing strong constraints on the number of optical modules that provide a signal due to the interaction eliminates neutrinos and remaining muons with an energy exceeding 5 GeV.

5.2.1 Filter selection

As mentioned earlier, this event selection aims at extracting a GeV signal from IceCube data. The first step is therefore to select the appropriate trigger and filters to identify these events. Considering the low energy of the neutrino interactions we try to extract from our data, we focus on *SMT-3* triggered events that pass the *DeepCore filter*. We also make use of the numerous filters that have been developed to tag specific kind of events or physics such as high energy muons or cascades. As it can be seen in Fig. 5.3, our events activate a small amount of DOMs. We thus do not expect them to pass any of the filters designed to tag high-energy interactions (see Chapter 4 and [85] for details about these filters). To be part of our event sample, an event has therefore to pass the *DeepCore filter* and fail all other filter conditions. An exception is made for the *Low-up* (LowUp) and *Full Sky Starting* (FSS) filters if the event fulfills as well the DeepCore filter conditions. This specific selection of the filters will be called *DC sel.* The *Low-up filter* has been designed to target low-energy neutrinos coming from the Northern sky and the *Full Sky Starting* filter uses parts of the detector as veto against incoming muon events, allowing to search for low-energy neutrinos from all directions. Table 5.1 summarizes the combinations of passed filters that allow an event to be kept in the selection. One can see in Fig. 5.5 how this combination (*DC sel.*) improves both background and noise rejection compared to the *DeepCore filter*.

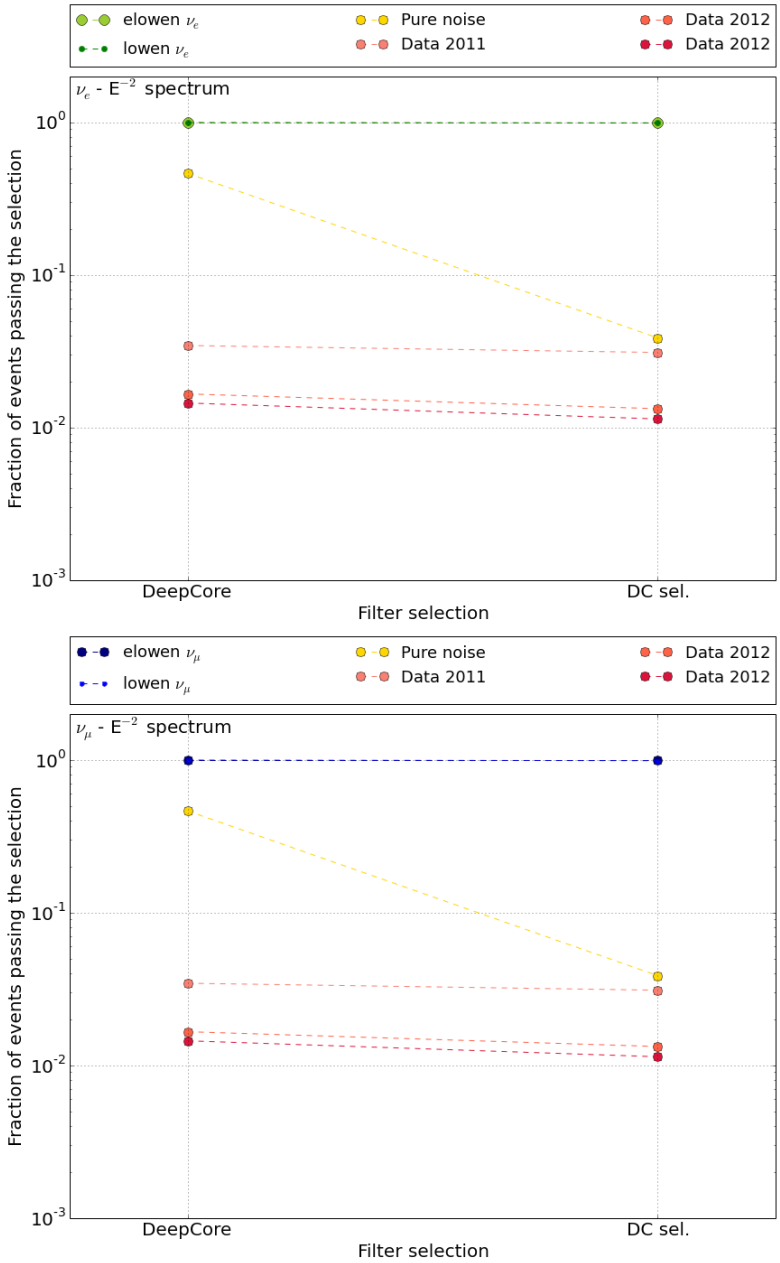

Figure 5.5: Comparison of the *DeepCore filter* and the new filter selection (*DC sel.*) efficiencies in background rejection and ν_e (top) or ν_μ (bottom) selection.

The *DC sel.* combination of filters results in a significant reduction of the number of atmospheric muons. The data rate after applying this filter selection is of the order of 15 Hz while the original rate was around 1400 Hz. More than 98% of the signal events, both for the *lowen* and *elowen* simulations, pass this filter selection.

5.2.2 Minimizing the luminosity in the detector

Number of HLC hits The number of HLC hits in IceCube and DeepCore strings is strongly limited for simulated low energy signal events, as can be seen in Fig. 5.6. On the contrary, data events are showing a large amount of HLC hits in the detector. We can therefore impose a constraint on the maximum amount of HLC hits allowed in DeepCore and IceCube-without-DeepCore to remove high-energy events from our sample.

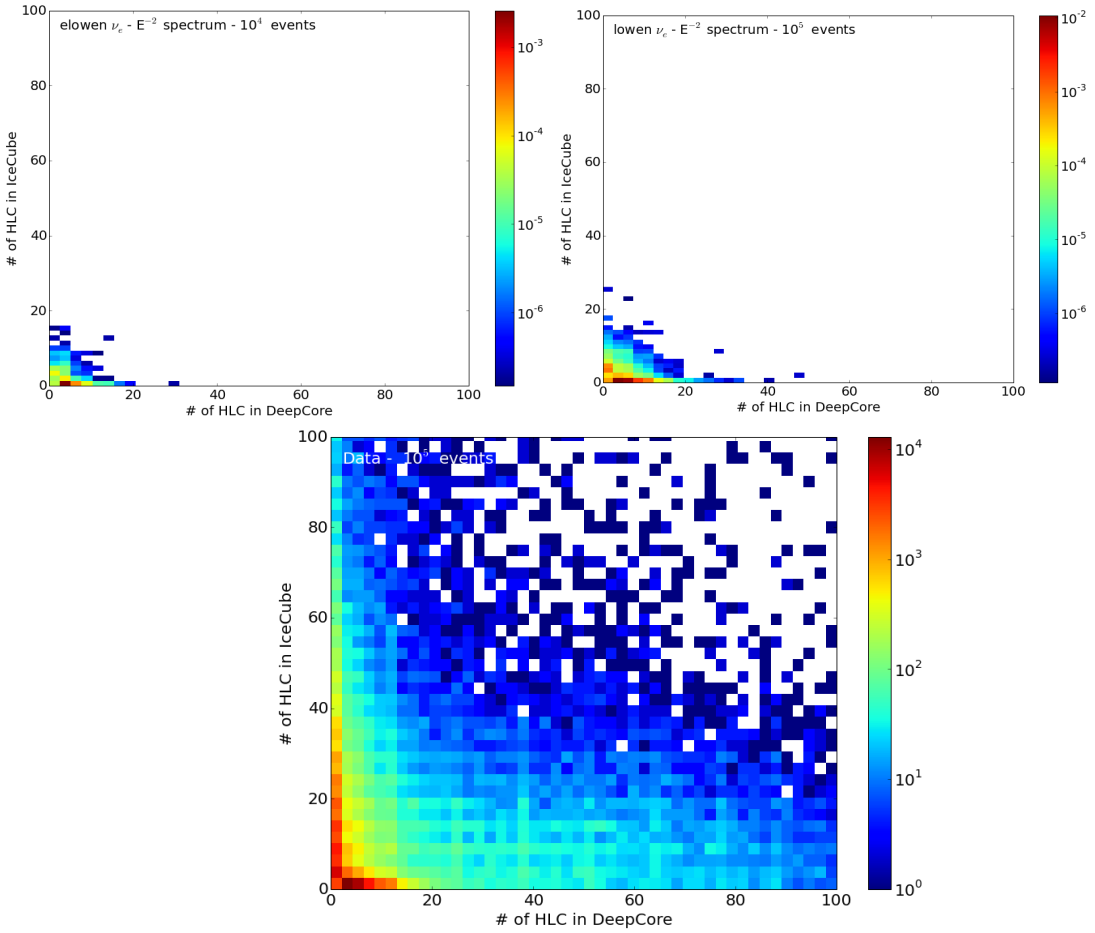

Figure 5.6: Number of HLC hits in DeepCore (x-axis) and IceCube-without-DeepCore (y-axis) for ν_e (first line, left: *elowen*, right: *lowen*), and data (bottom). Similar plots are obtained for ν_μ and ν_e.

For the moment, we want to keep the events that are fully contained in DeepCore, i.e. the events that have 0 HLC hits in IceCube-without-DeepCore. If they are too energetic, these events will be removed from the sample at a later stage. The constraints shown in Table 5.2 allow to reduce the data rate down to a bit more than 6 Hz and to keep 99% and 97% of *elowen* and *lowen* simulation samples respectively. In order to

guide the eye of the reader, Fig. 5.7 shows the performed selection. The shaded area represents the parameter space that does not pass the selection. Similar plots have been produced for the following selection criteria. They are presented in Appendix C.

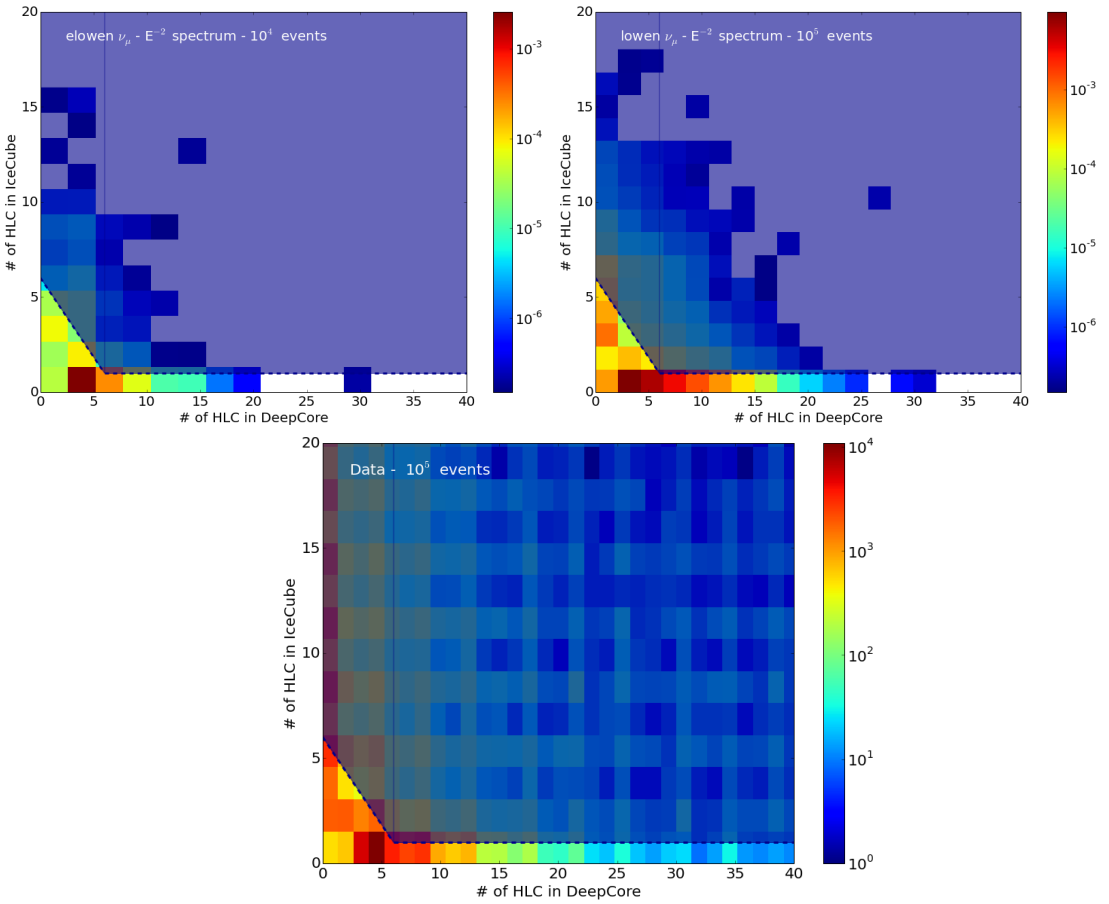

Figure 5.7: Number of HLC hits in DeepCore (x-axis) and IceCube-without-DeepCore (y-axis) for ν_e (first line, left: *elowen*, right: *lowen*) and data (bottom). The shaded area represents the parameter space that does not pass the selection.

Causal connection The number of causally connected hits present in the event can also be used as a parameter for the amount of light emitted in the detector as a consequence of the neutrino interaction. We use the *SRTInIce* [1] pulses and simply put a limit on the corresponding number of hits contained in the event. Fig. 5.8 shows the distribution of the number of SRT pulses for data and GENIE simulation. This constraint

[1] "SeededRTCleaning": this algorithm has been designed to select sets of hits most likely connected to the same physical interaction, and therefore unrelated with dark noise. The algorithm selects hits that have another hit within a sphere of radius R and within a dT time window. We used the default values, i.e. R = 150 m and dT = 1000 ns.

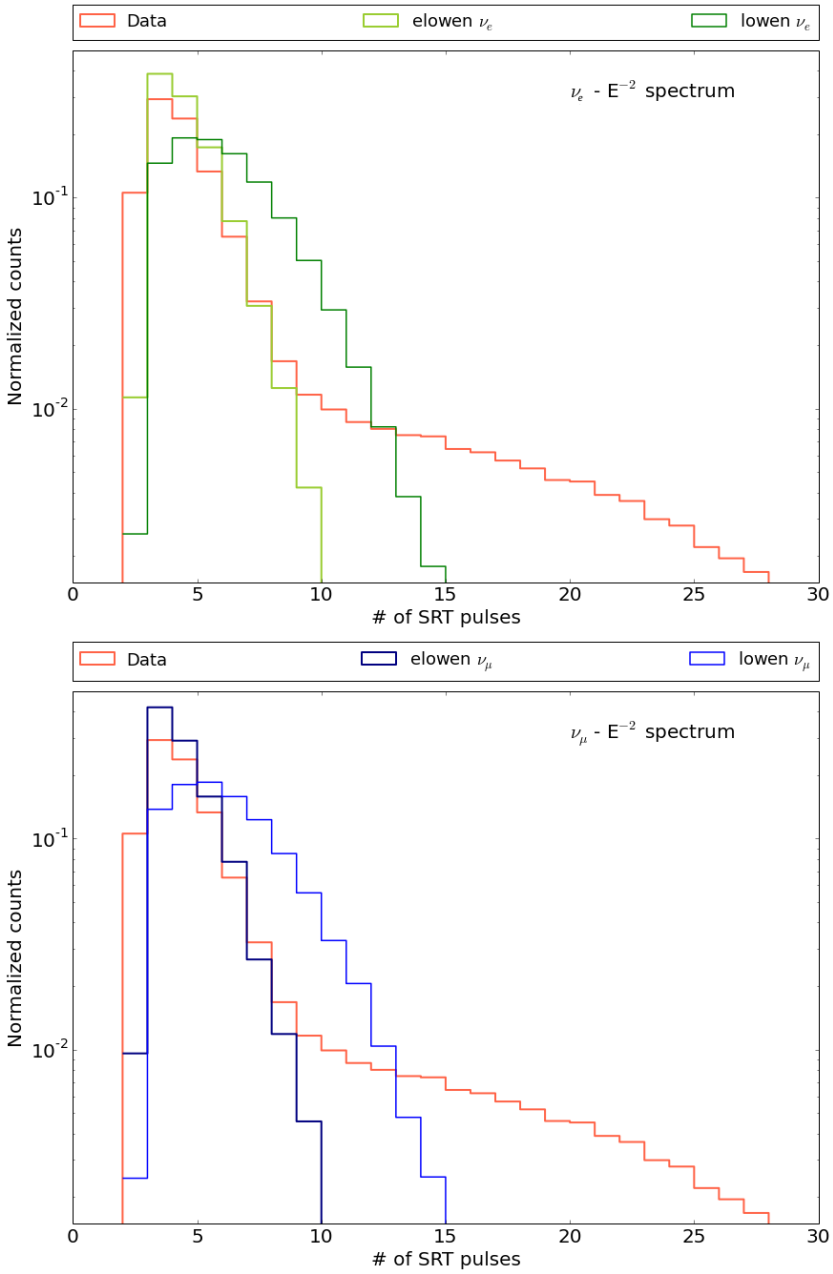

Figure 5.8: Number of SRT pulses for ν_e (top) and ν_μ (bottom) and data. The part of the parameter space excluded by the selection criterion is shown in Appendix C.

allows to reduce the data rate down to about 5.5 Hz and keeps 99% and more than 93% of *elowen* and *lowen* simulation events respectively. Table 5.2 summarizes the numbers of HLC hits in DeepCore and in IceCube-without-DeepCore and SRT pulses needed for an event to remain in the sample.

Table 5.2: Conditions for the cuts described in the text that allow an event to be kept in the sample. If the event has no HLC hits in IceCube-without-DeepCore DOMs, the even is kept, independently of the number of HLC hits in DeepCore.

Variable	Passing conditions
Number of HLC hits in IceCube-without-DeepCore	$= 0$ ≤ 6
Number of HLC hits in DeepCore	≤ 7
Number of SRT hits	≤ 10

5.3 Minimizing the Contribution of Pure Noise

It turns out that, once the above cuts are applied, the resulting data rate is similar to the noise rate when evaluated using pure noise simulation. The next step of the event selection is therefore to differentiate low-energy neutrino interactions from detector noise. Understanding this noise in details is essential to achieve this goal.

5.3.1 Noise sources in IceCube

Most of the background hits occurring in IceCube are due to *dark noise*. This name reflects the emission of an electron from the cathode of the PMT in absence of a Cherenkov photon. This effect can arise from numerous sources including, as mentioned in [85], thermionic emission, electronic noise, field emission within the PMT, Cherenkov light from radioactive decays, and scintillation/luminescence in the glass of the PMT and pressure sphere. All these contributions add together to reach a rate of 560 Hz for IceCube DOMs and 780 Hz for the DeepCore DOMs with high quantum efficiency. In addition, cosmic-ray muons are expected to create a rate from 25 Hz to 5 Hz, decreasing with depth. In order to understand the different contributions, the IceCube Collaboration has used the data stream previously mentioned, called *HitSpool data*. The contributions can be divided in three different groups [85]:

- Afterpulses: This contribution, following a Gaussian distribution, arises from the PMT itself. It is attributed to ionization of residual gases by electrons accelerated between the dynodes.
- Uncorrelated: These Poissonian noise pulses occur with a rate between 230 and 250 Hz. The hits can be explained by thermal noise and radioactive decay. In view of minimizing this noise contribution, the potassium component in the glass sphere has been limited to reduce the ^{40}K decay contamination.

- Correlated: The origin of this contribution is not fully understood yet. Hits with a short-time interval happen with an increased rate compared to what would be expected from a Poissonian process. These hits are clustered in bursts. A temperature-dependence has been observed and leads to an average number of hits per burst from 3.3 at -10°C and 3.8 at -30°C. An empirical approach allowed to successfully simulate this noise component but the exact physical explanation is still to be confirmed. A possible source is the luminescence of the glass triggered by radioactive decay of, among others, ^{40}K. These effects contribute in the total rate as high as 280 Hz to 340 Hz.

The sum of these effects is not constant over time. While the environmental noise due to the drilling process dominated the fluctuations of the mean rate at first; the seasonal variations of atmospheric muons took over as the dominant source of fluctuations. More details about the different noise contributions can be found in [85]. Fig. 5.9 compares the detector noise with fits of the different contributions briefly described above. The

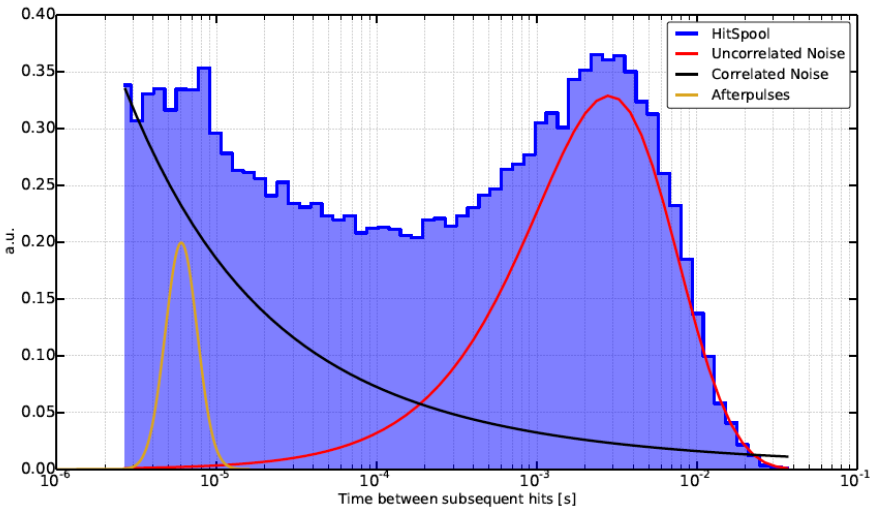

Figure 5.9: Histogram of time differences between successive hits from HitSpool data of DOM 15 on string 27 (blue) on a logarithmic scale in order to visualize the different noise components. A fourth subdominant component centered at 100 μs is not parameterized and is still under study. Figure and caption from [85].

noise model used to elaborate this event selection incorporates these sources [110]. The bottom part of Fig. 5.3 represents a typical noise event satisfying the SMT-3 trigger condition and passing the DeepCore filter. The accidental triggers by pure noise are not problematic for bright events but constitute a significant background for low-energy interactions such as the ones illustrated in Fig. 5.3. The study of the behavior of these pure noise events allowed to develop an algorithm able to identify them.

5.3.2 *NoiseEngine*, the noise filter

As detailed in [110], noise triggers occur with relatively few hits and no preferred direction. The algorithm to identify and eliminate noise signals has therefore been developed based on these two characteristics. Using the different parameters listed in Table 5.3, the algorithm searches for a preferential direction in pairs of hits to classify the event as *physics*. In practice, an event is classified as *physics* if it contains, during a certain time window (W), a minimum of X pairs of hits with an effective speed contained in a [Y,Z] interval pointing in excess towards a certain direction. If this is not the case, the event is classified as *noise*.

Table 5.3: List of the parameters used in the NoiseEngine algorithm in order to determine if an event is most likely detector noise or a physics interaction.

Parameter	Range	Signification
Start velocity Y (m/ns) End velocity Z (m/ns)	[0.,1.] [starting velocity,1.]	Apparent velocity interval (distance between the DOMs divided by the time between the hits)
Time window W (ns)	[0.,1000]	Time window used to select the pairs of hits
Threshold X	[0,10]	Number of pairs in the defined time window with an apparent velocity included in [Y,Z]

A default set of these four parameters ([W, X, Y, Z] = [500, 7, 0.05, 0.5]) is implemented in the IceCube software. The processor has a boolean output. In this standard configuration, *True* is attributed to physics-like events and a noise event is likely producing a *False*.

5.3.3 Upgrading NoiseEngine

The algorithm has been originally optimized to differentiate noise from 10-100 GeV neutrino interactions. In order to be effective for our low-energy events, we have therefore re-optimized the method. We have applied the algorithm for each possible parameter set in the range defined in Table 5.3. The passing fraction, i.e. # of True outputs/Total

number of events, obtained for each set of parameters for noise (x-axis) and *lowen* simulation (y-axis) is shown in Fig. 5.10. For comparison, we also show the same plot using actual data instead of noise events. As one can see, the two plots show the same trend, confirming the noise to be the dominant component in data at this stage. Fig. 5.10 also shows the similar plots for *elowen* events.

Instead of considering a unique set of values for the variables presented in Table 5.3, we have considered a combination of sets. A possible combination is to require an event to pass the criteria of either NoiseEngine(100, 2, 0.20, 0.90), or NoiseEngine(100, 0, 0.20, 0.90) when failing NoiseEngine(1000, 0, 0.00, 0.10), where NoiseEngine(100, 2, 0.20, 0.90) contains the output of the NoiseEngine set of parameters:

- W = 100 ns
- X = 2 pairs of hits
- Y = 0.2 m/ns
- Z = 0.9 m/ns

As seen in Fig. 5.10, the combination (light blue point) leads to a higher passing fraction for the signal while minimizing the passing fraction of the noise. Two different combinations of NoiseEngine were applied to the sample. The first one is the example previously mentioned. The second condition asks an event to:

- either pass NoiseEngine(300, 2, 0.20, 0.40)
- either pass NoiseEngine(300, 2, 0.10, 0.90) and fail NoiseEngine(800, 0, 0.00, 0.10)
- or to pass NoiseEngine(500, 2, 0.20, 0.30).

The passing fraction for each possible set of parameters of NoiseEngine, after the first combination was applied, can be seen in Fig. 5.11. The result of the second combination is shown in this figure with a light blue point, proving that the combination leads to a maximized(minimized) passing fraction for signal(noise).

These combinations were found and optimized by maximizing the signal to noise ratio. While it may seem arbitrary, the output *True* and *False* are requested for different types of events. We request an output *False* for sets of variables specifically targeting small apparent speed in a long time window. These parameters correspond to scattered hits. On the contrary, the sets for which a *True* output is required to pass the selection select high apparent speed in a short time window, i.e. direct hits.
The data rate is about 0.2 Hz after applying these two combinations using NoiseEngine. For comparison the noise rate is of the order of 0.12 Hz. More than 55% of *lowen* c.q. *elowen* simulation events survive these cuts.

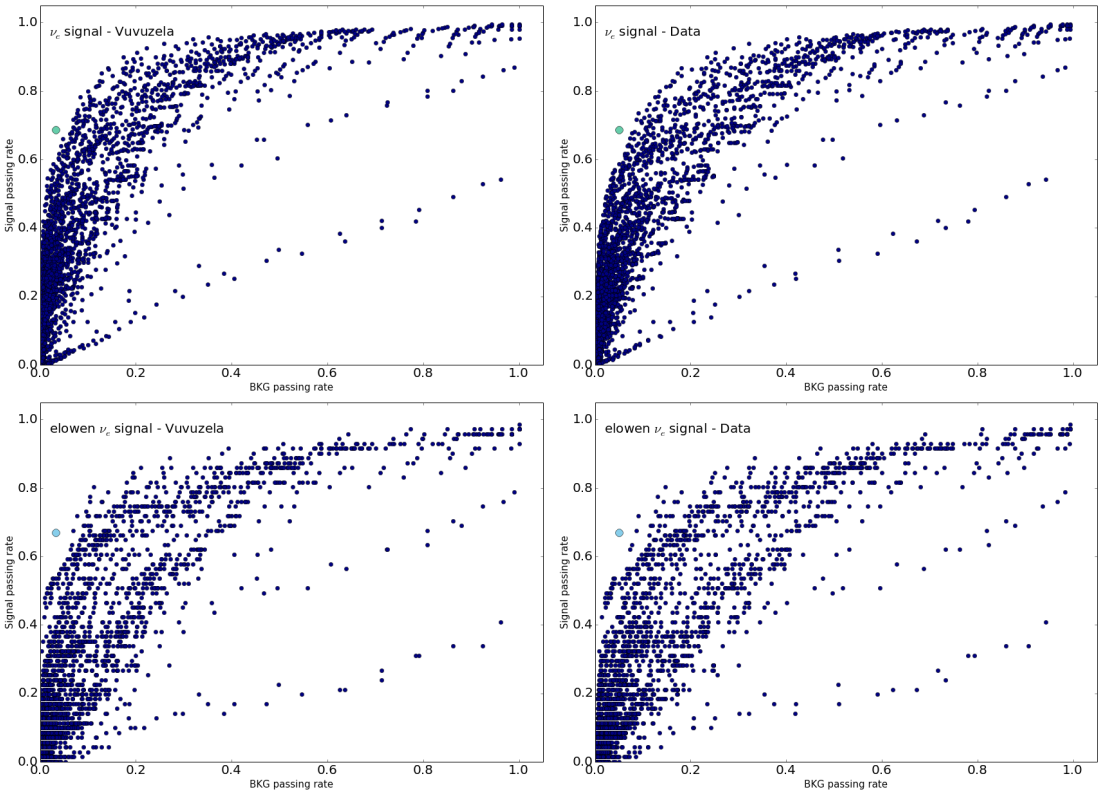

Figure 5.10: ROC curve comparing the different NoiseEngine sets. The dark blue points represent the passing fraction for background (x-axis) and ν_e signal (y-axis) for all possible combinations of NoiseEngine parameters. The light blue point shows the passing fractions when applying the chosen combination. The top(bottom) plots use a lowen(elowen), and the left(right) plots assume background is pure noise(real data). The ν_μ events show a similar behavior as ν_e.

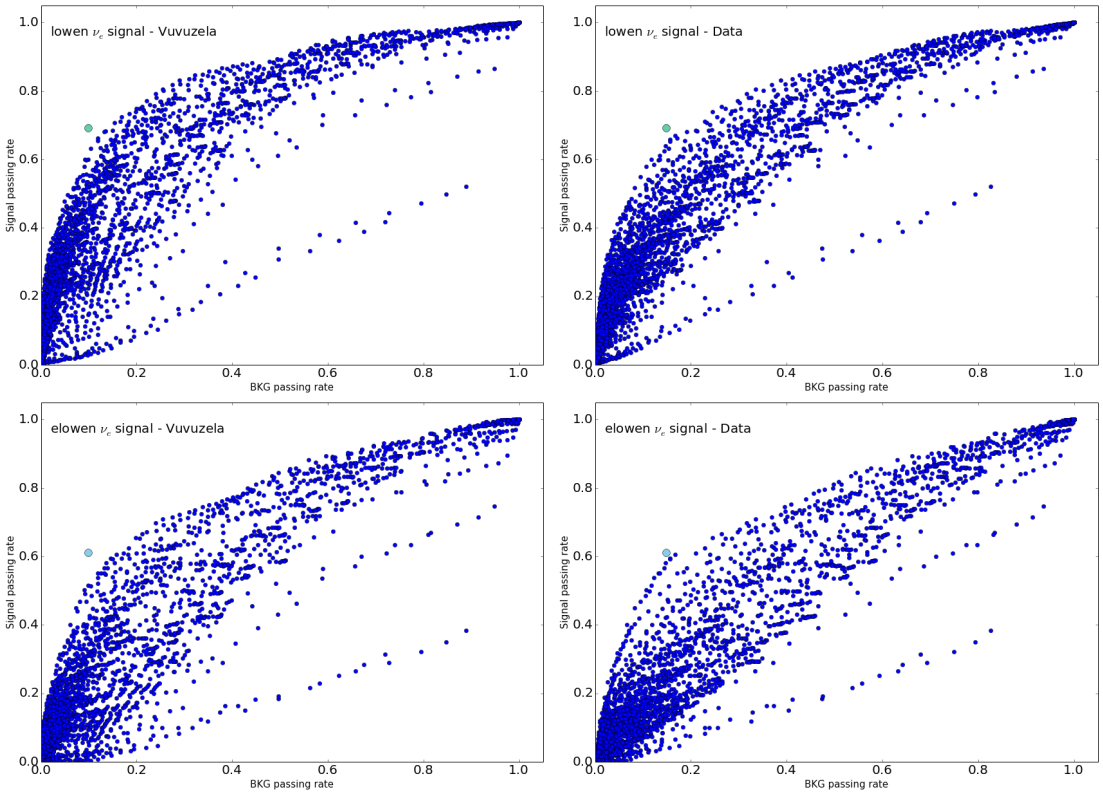

Figure 5.11: ROC curve comparing the different NoiseEngine sets after the first combination was applied. The blue points represent the passing fraction for background (x-axis) and ν_e signal (y-axis) for all possible combinations of NoiseEngine parameters. The light blue point shows the passing fractions when applying the chosen combination. The top(bottom) plots use a lowen(elowen), and the left(right) plots assume background is pure noise(real data).The ν_μ events show a similar behavior as ν_e.

5.4 Increasing the Purity

With most of the pure noise events being removed from the sample, we can now work on removing the remaining high-energy events and trying to increase the purity of our sample. Several selections are used for this purpose as outlined in details in the following sections:

- Charge distribution: cut on the ratio of the charge deposited in DeepCore during the first 600 ns after the first HLC hit in DeepCore and the total charge in the event
- Depth: cut on the depth of the first HLC hit in DeepCore
- Centroid of the event: cut on the distance and the delay between the first and the second HLC hit in DeepCore
- Total charge: cut on the total charge
- HLC hits: cut on the number of HLC hits in DeepCore

The three first selections target the morphology of the events while the two last ones aim at normalizing the data and signal distributions.

5.4.1 Morphology of the event

Charge distribution As mentioned above, the aim of these final selections is to increase the purity and remove remaining high-energy events from the sample. This first cut targets especially remaining muons. We can witness the energy loss of the muon as soon as it enters the detector. A neutrino interaction on the other hand deposits most of its energy close (in time and distance) to the interaction point. We consider the first 600 ns [2] after the first HLC hit in DeepCore and we integrate the charge in DeepCore DOMs. We compare this integrated charge with the total charge in the event and we call this fraction *Q-ratio*. Fig. 5.12 shows the behavior of data and signal events for this variable. To be kept in the sample, an event is requested to have a Q-ratio superior to 0.26. This selection allows to reduce the data rate down to 0.095 Hz (2011) and 0.08 Hz (2012) while keeping at this stage more than 53% and 50% of *lowen* and *elowen* respectively.

[2] This time window has been optimized through the maximization of the signal to background ($\frac{S}{\sqrt{B}}$) ratio.

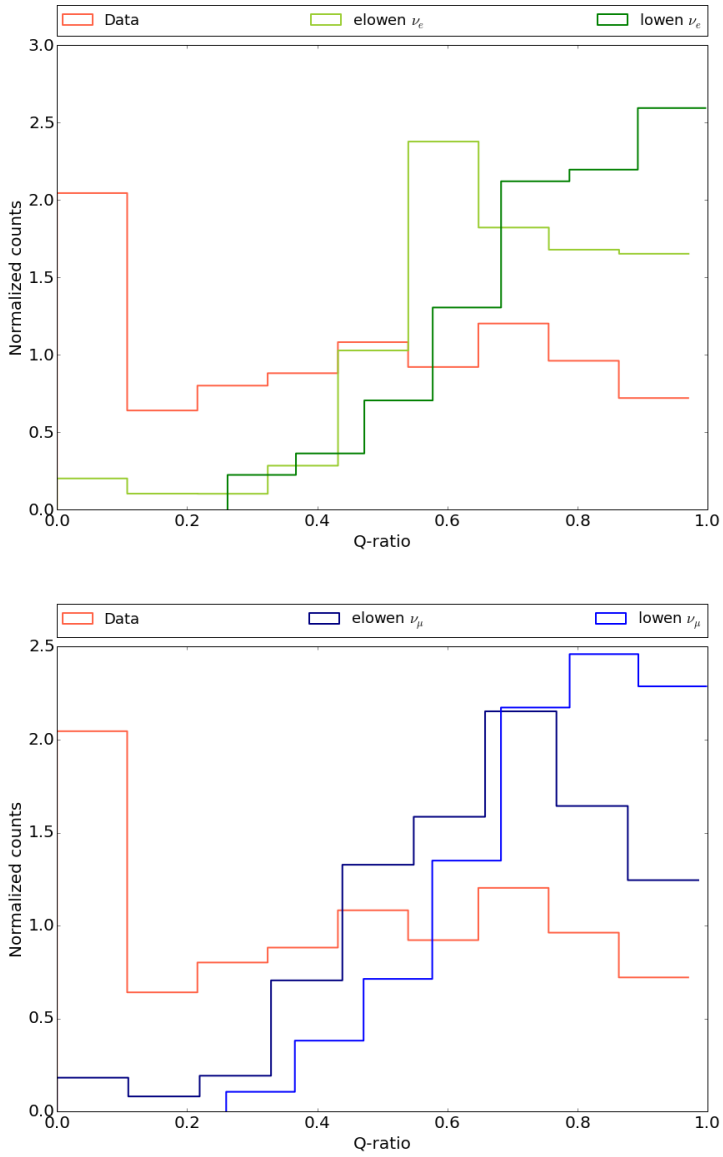

Figure 5.12: Distribution of Q-ratio for *elowen*, *lowen* ν_e (top) and ν_μ (bottom) events and data. The part of the parameter space excluded by the selection criterion is shown in Appendix C.

Depth of the interaction We now want to reduce the contamination of low-energy down-going muons. Fig. 5.13 shows the depth of the first HLC hit in DeepCore. We expect most of our low energy signal events to start in the dense core of the detector while the atmospheric particles have their first HLC high in DeepCore or IceCube. While we could have used the distribution of the first HLC of the event, we decide to focus

on DeepCore. Since our events are expected to be very localized and we want to take benefits of the higher DOMs density to maximize the number of hits due to the neutrino interaction. Selecting events with a first DeepCore HLC hit between [-2453, -2158]m

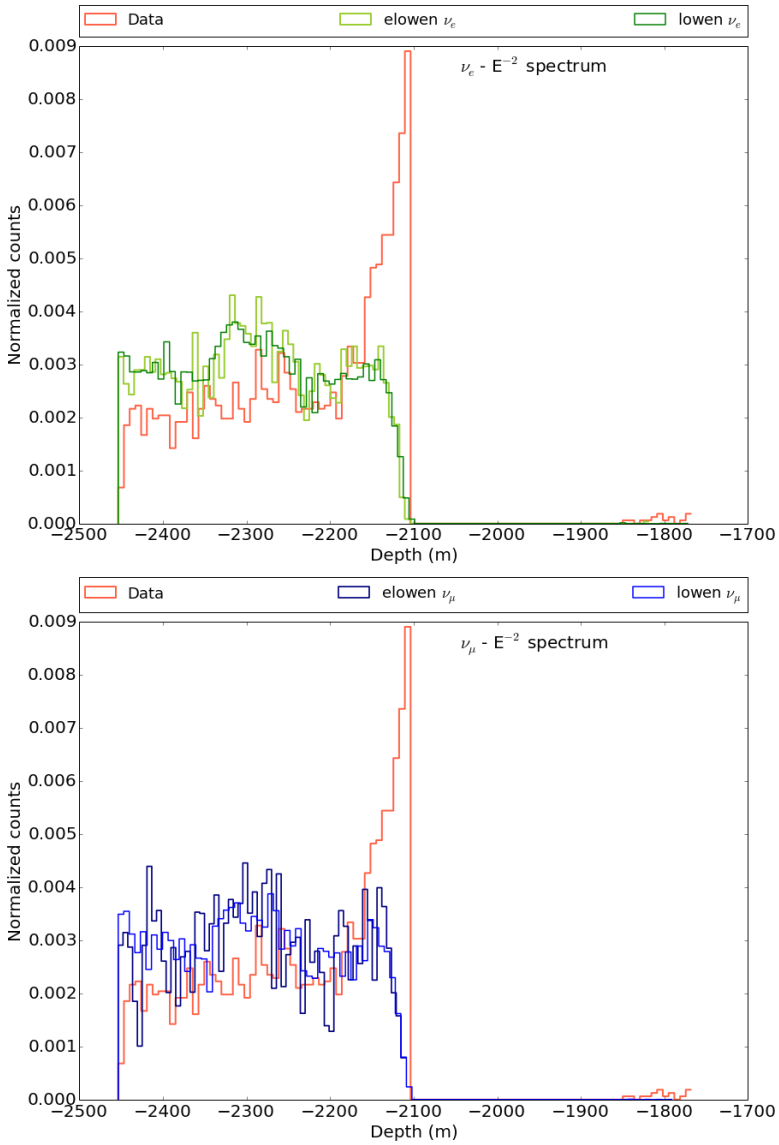

Figure 5.13: Distribution of the depth of the first HLC in DeepCore for *elowen*, *lowen* ν_e (top) and ν_μ (bottom) events and data. The presence of data events around -1800 m is due to the upper part of DeepCore located above the dust layer. The part of the parameter space excluded by the selection criterion is shown in Appendix C.

allows to reduce the data rate to 0.064 Hz (2011) and 0.055 Hz (2012) while keeping more than 40% and 45% for *elowen* and *lowen* respectively, compared to the initial

Table 5.4: Conditions for the cuts based on the morphology of the event that allow an event to be kept in the sample.

Variable	Passing conditions
Charge ratio	> 0.26
Depth of the first HLC in DeepCore	$>$ -2453 m $<$ -2158 m
Distance and delay between 1st and 2nd HLC in DeepCore	$<$ 70 m and $<$ 50 ns

number of events.

Centroid of the event We used one more time the causality between hits within the same event. Since our events are of low energy, the DOMs able to record the events are close to each other, both in distance and time. On the contrary, if the particles produced in the neutrino interaction are able to travel a long distance, it increases the chance to observe scattered hits. Fig. 5.14 shows the time and distance between the first and the second HLC hit in DeepCore for *elowen* and *lowen* events as well as data.

Requesting the distance between these two hits to be smaller than 70 m and the delay not more than 50 ns, we manage to reach a data rate of 0.035 Hz (2011) and 0.030 Hz (2012). About 40% and 45% of *elowen* and *lowen* events pass, respectively, the selection so far. Table 5.4 summarizes the three cuts based on the morphology of the events.

5.4.2 Normalizing the data and signal distributions

Total Charge We now remove the remaining events that have a too high deposited charge to be created by low-energy neutrino interactions. As seen in Fig. 5.15, the total charge distribution is slightly different for data compared to *lowen* and *elowen* simulation events. We keep the events that have a charge inferior to 60 photoelectrons. This results in a data rate of 0.027 Hz (2011) and 0.022 Hz (2012). More than 40% and 35% of the *lowen* and *elowen* events survive the selection so far.

HLC Hits Finally we remove the events that still have a relatively high number of HLC hits in DeepCore compared to the expectations for GeV neutrino interactions. This may seem paradoxal since an upper limit on the number of HLC hits in DeepCore has already been used as a selection criterion. However, events with an arbitrarily high number of HLC hits in DeepCore may still be present in the sample at this stage if they did not have any single HLC hit on IceCube strings (see Section 5.2.2). Fig. 5.16 shows

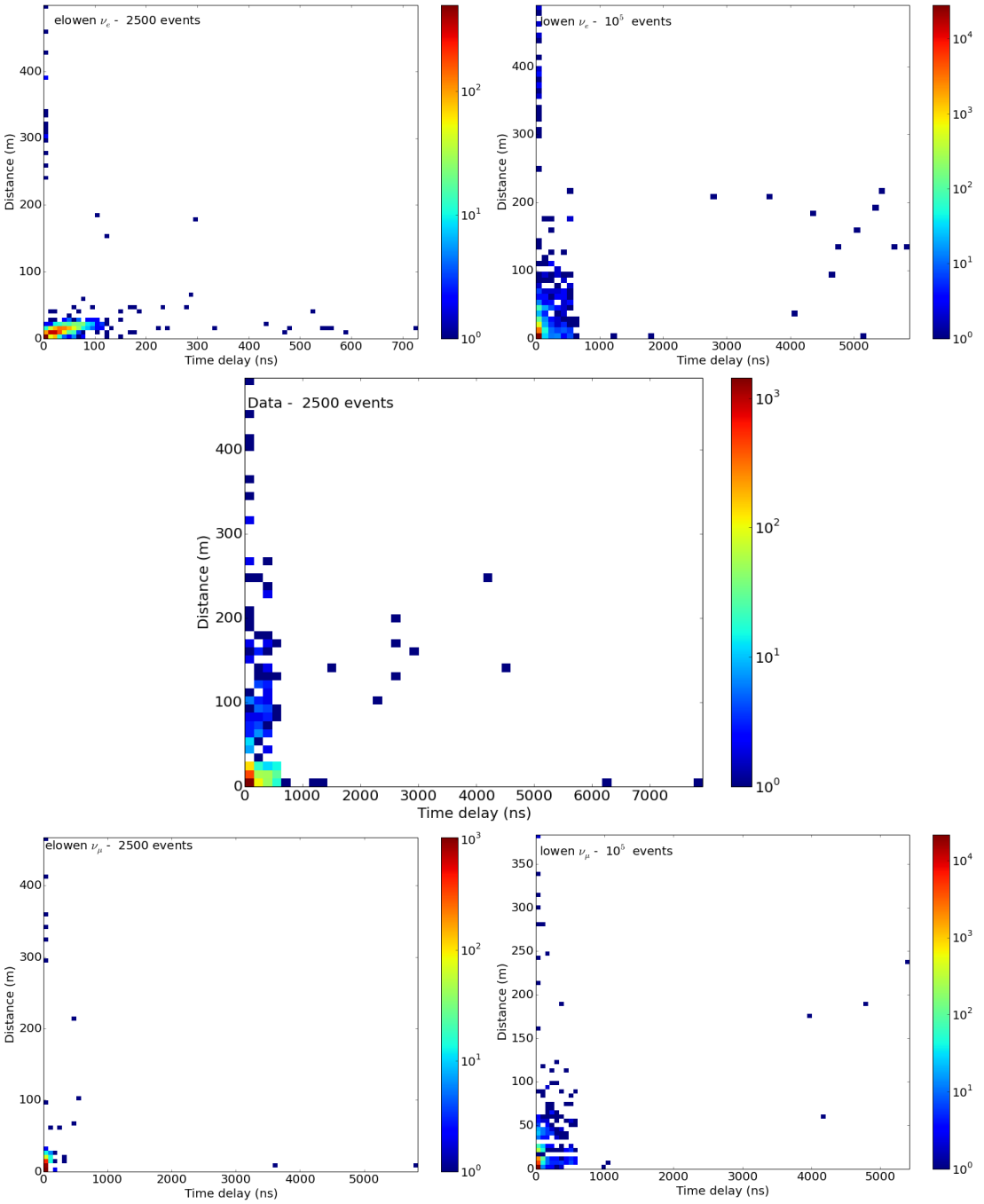

Figure 5.14: Time and distance between the first and the second HLC in DeepCore for *elowen* (left), *lowen* (right) ν_e (top) and ν_μ (bottom) events and data (middle).

Table 5.5: Conditions for the cuts normalizing the distributions of the data and signal events that allow an event to be kept in the sample.

Variable	**Passing conditions**
Total charge	< 60 photoelectrons
Number of HLC in DeepCore	< 10

the distribution for data and signal events. We kept the events that have less than 10 HLC hits in DeepCore. This results in a data rate of 0.025 Hz (2011) and 0.018 Hz (2012). More than 35% of the *elowen* c.q. *lowen* events survive this event selection. Table 5.5 summarizes the two last cuts applied to the sample.

5.4.3 Summary of the selection

Table 5.6 summarizes all the selections applied to IceCube data in order to constitute a GeV-like sample.

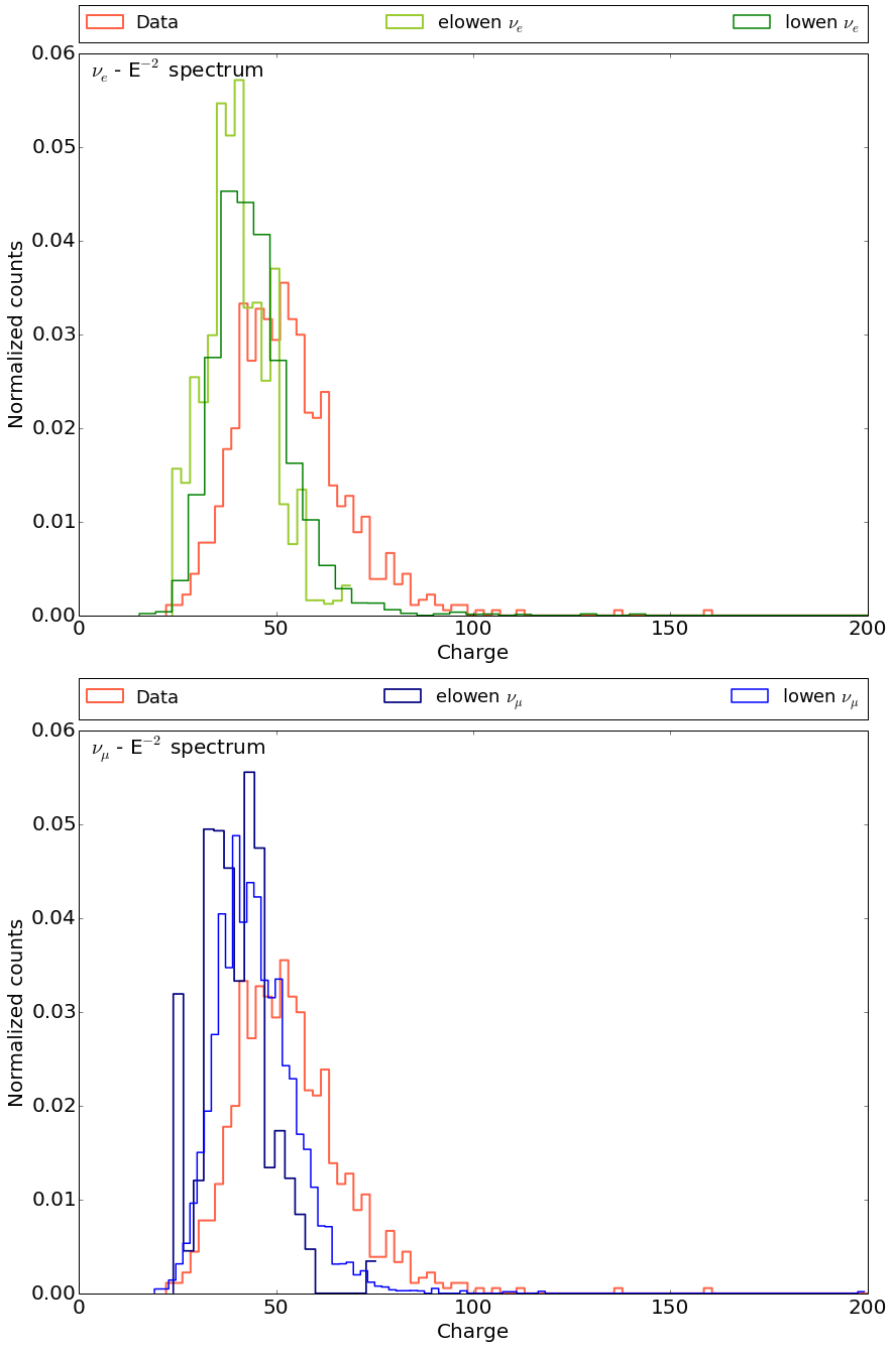

Figure 5.15: Total charge (in photo electrons) distribution for data, *elowen*, *lowen* ν_e (top) and ν_μ (bottom) events. The part of the parameter space excluded by the selection criterion is shown in Appendix C.

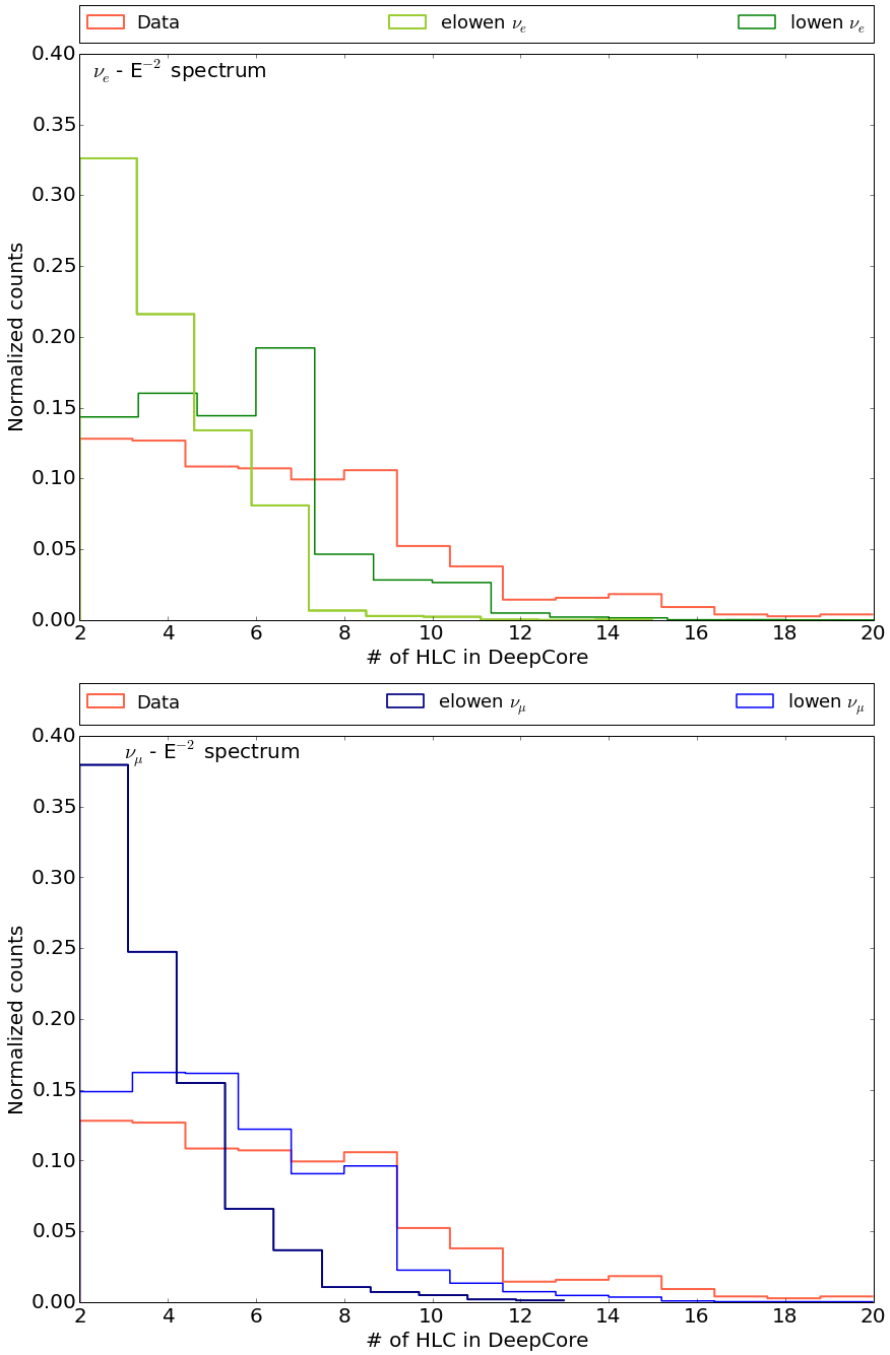

Figure 5.16: Distribution of HLC hits for data, *elowen*, *lowen* ν_e (top) and ν_μ (bottom) events. The part of the parameter space excluded by the selection criterion is shown in Appendix C.

Table 5.6: Summary of the cuts applied in the event selection.

Variable	**Passing conditions**
Passing filters	DeepCore **OR** DeepCore + LowUp **OR** DeepCore + FSS
Number of HLC in IceCube w/o DeepCore (X) Number of HLC in DeepCore (Y)	X = 0 **OR** X = $\leq$ 6 **AND** Y $\leq$ 7
Number of SRT hits	$\leq$ 10
NoiseEngine combination I	NoiseEngine(100, 2, 0.20, 0.90) = True **OR** NoiseEngine(100, 0, 0.20, 0.90) = True **AND** NoiseEngine(1000, 0, 0.00, 0.10) = False
NoiseEngine combination II	NoiseEngine(300, 2, 0.20, 0.40) = True **OR** NoiseEngine(300, 2, 0.10, 0.90) = True **AND** NoiseEngine(800, 0, 0.00, 0.10) = False **OR** NoiseEngine(500, 2, 0.20, 0.30) = True
Charge ratio	> 0.26
Depth of the first HLC in DeepCore (Z)	Z > -2453m **AND** Z < -2158 m
Distance (D) and delay (Δt) between 1st and 2nd HLC in DeepCore	D < 70 m **AND** Δt < 50 ns
Total charge	< 60 photoelectrons
Number of HLC in DeepCore (Y)	Y < 10 (with X = 0)

Table 5.7: Rate of different simulation and data sets at final level of the event selection presented in this work.

Sets		**Rate**
Data	2011	0.025 ± 0.003 Hz
	2012	0.021 ± 0.003 Hz
	2013	0.020 ± 0.003 Hz
	2014	0.022 ± 0.003 Hz
	2015	0.021 ± 0.003 Hz
	2017	0.019 ± 0.003 Hz
Pure noise		0.018 Hz
Corsika		$<$ 0.005 Hz (Hoerandel)
GENIE	ν_e	0.0003 Hz
	ν_μ	0.0008 Hz

5.5 Event Characteristics at Final Level

5.5.1 Event rates

Table 5.7 summarizes the rate of the different sets at final level. Corsika and GENIE rates (see Section 5.1.2 for details) are shown for comparison. Table 5.8 shows the passing fraction of the simulated signal events. In addition of showing the results for events arriving from a solar direction, we present the fraction of events from all sky ending up in the final sample. Since the passing fractions for the solar and all-sky direction turn out to be very similar, there is only a small zenith dependency created by the selection as will be shown later. Therefore, the event selection could be used to search for transient events at an arbitrary position in the sky.

Fig. 5.17 represents the passing fraction of *elowen* and *lowen* as as function of the energy. As seen in the plots, the event selection seems to be optimized for 1 to 2.5 GeV neutrinos. This event selection presents therefore an ideal tool to search for solar flare neutrinos.

5.5.2 Composition at final level

It is interesting to perform a qualitative estimation of the data composition at final level. There are potentially two dominant components: atmospheric muons and events due to pure noise trigger.

Fig. 5.18 shows the distribution of the number of hits recorded by the DOM that

Table 5.8: Passing fraction of different signal simulation sets at final level of the event selection presented in this work. We assume the signal events follow a E^{-2} spectrum. Assuming a softer spectrum leads to similar passing fractions.

Sets	Particle type	Energy	Direction	Passing fraction
Signal	ν_e ($\bar{\nu}_e$)	1-5 GeV	Solar	45%
			All sky	46%
		0.5-1 GeV	Solar	41%
			All sky	42%
	ν_μ ($\bar{\nu}_\mu$)	1-5 GeV	Solar	43%
			All sky	44%
		0.5-1 GeV	Solar	36%
			All sky	37%
	ν_τ ($\bar{\nu}_\tau$)	1-5 GeV	Solar	40%
			All sky	40%

recorded the 1st HLC hit in the event. The distribution for pure noise shows a peak at 4 hits, representative of the 'burst' discussed earlier. This peak is not present, or is at least not the dominant contribution, in the data distribution. This implies that correlated noise does not dominate the data events at the end of the event selection.

Another way of testing the composition at final level is to calculate the ratio of the number of hits in different parts of the detector. The results allow to confirm that atmospheric muons do not largely dominate the final sample, as confirmed by the low rate of Corsika presented in Table 5.7. We define DeepCore in three regions:

- TOP = [-2158 m, -2248 m]
- MIDDLE = [-2248 m, -2348 m]
- BOTTOM = [-2348 m, -2453 m]

Table 5.9 presents the values of the different ratios for each data/simulation event samples.
The precise composition of the final sample would require further investigations, but is not needed for the study of transient events presented in this thesis, where only variations of the rate are relevant.

5.5.3 Purity

Fig. 5.19 shows the evolution of the purity, defined as $\frac{Signal}{Signal+Background}$. We have used an arbitrary normalization of an E^{-2} spectrum between 1 and 5 GeV for the signal events

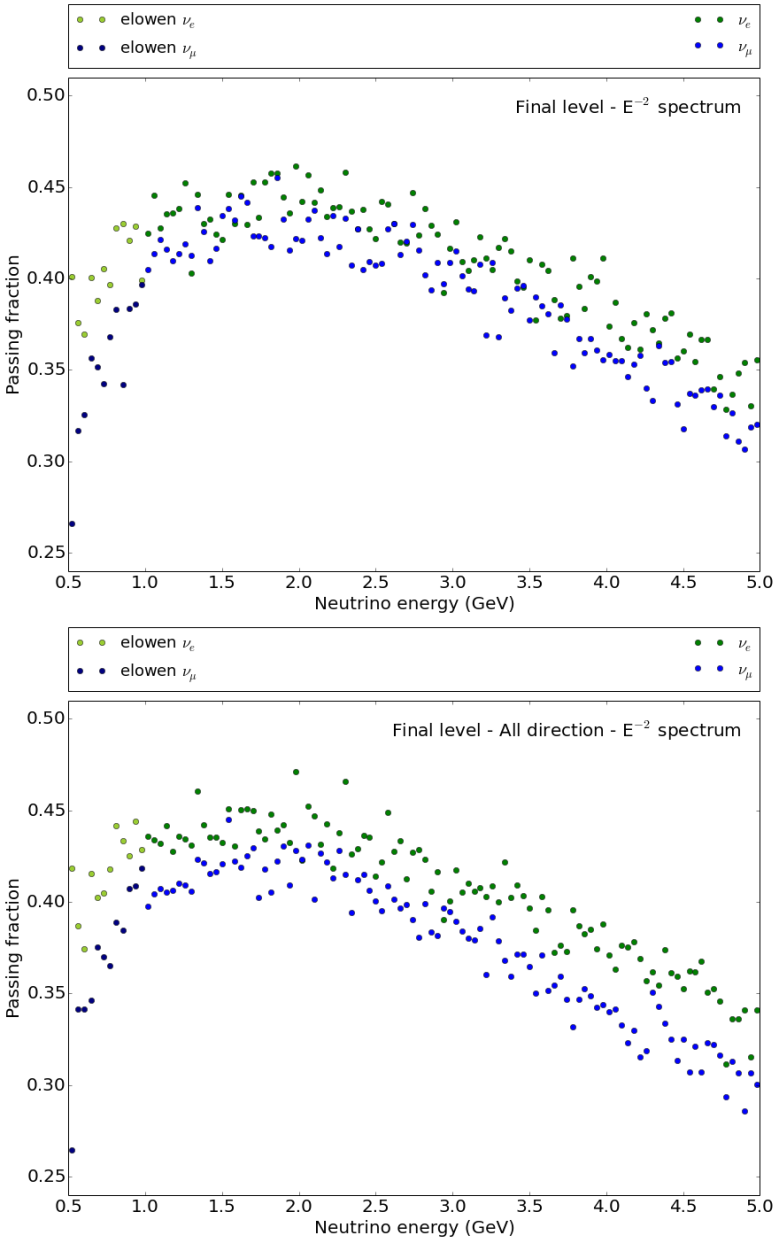

Figure 5.17: Passing fraction - # events at final level/# events after triggering - for ν_e (green) and ν_μ (blue) from solar direction (top) and all sky (bottom).

and off-time data events have been used to evaluate the background. We note that using a softer signal spectrum, i.e. a larger spectral index, does not affect the results as the passing fractions for different signal spectra are similar to each other. As shown in the figure, the purity increases after each cut, with a maximum increase due to the Noise Engine cuts.

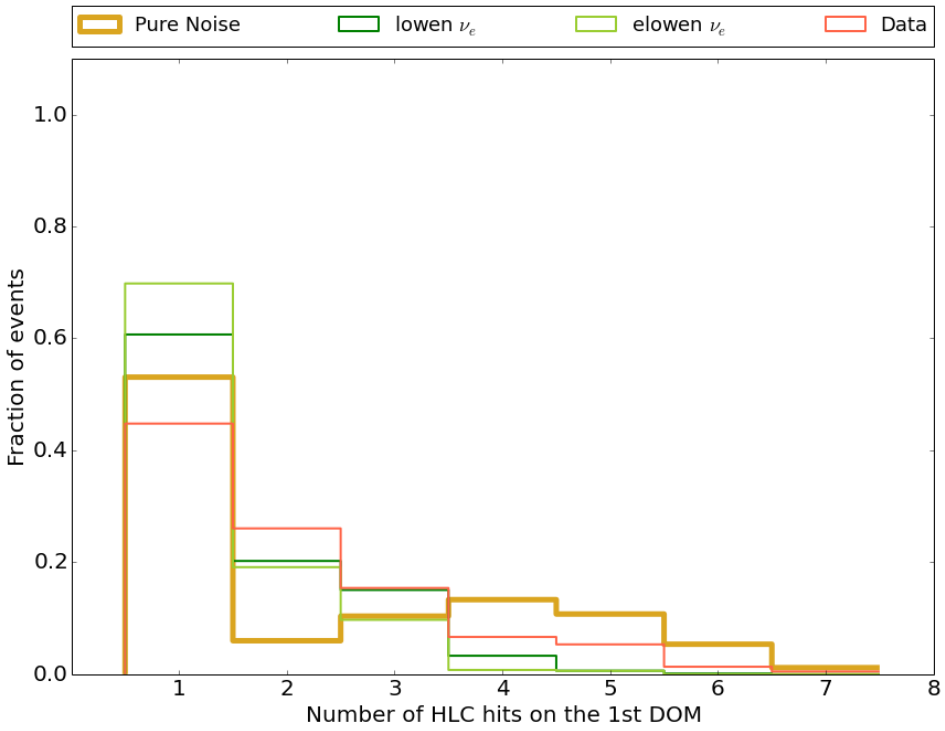

Figure 5.18: Distribution of the number of hits recorded by the DOM that shows the 1st HLC hit in the event. The bump centered at 4 hits in the pure noise distribution does not appear in the distribution of data events, meaning correlated noise does not dominate the final sample.

5.5.4 Testing the data-signal consistency

Several tests have been performed in order to check the consistency between the simulation and data samples at final level. It is possible to visually compare the events to search for obvious different features in the data and the simulated signal. We also performed more quantitative tests, such as the charge asymmetry distribution.

Visual properties A first test consists of comparing by eye simulated signal events and actual data. As seen in Fig. 5.20, the two different samples share the same features. Both data and signal events have been randomly picked. More events are presented in Appendix B.

Table 5.9: Ratios of number of hits in different parts of DeepCore for different data/simulation event samples. The disagreement between the values of data and Corsika seems to indicate that atmospheric muons do not dominate the final sample.

	Data	**GeV neutrinos**	**Corsika**	**Pure Noise**
TOP/MIDDLE	1.05 ± 0.07	0.66 ± 0.04	2.45 ± 0.16	0.82 ± 0.05
TOP/BOTTOM	1.33 ± 0.09	0.82 ± 0.06	3.02 ± 0.22	1.29 ± 0.09
(TOP+MIDDLE)/BOTTOM	2.59 ± 0.16	2.05 ± 0.12	4.25 ± 0.29	2.87 ± 0.18

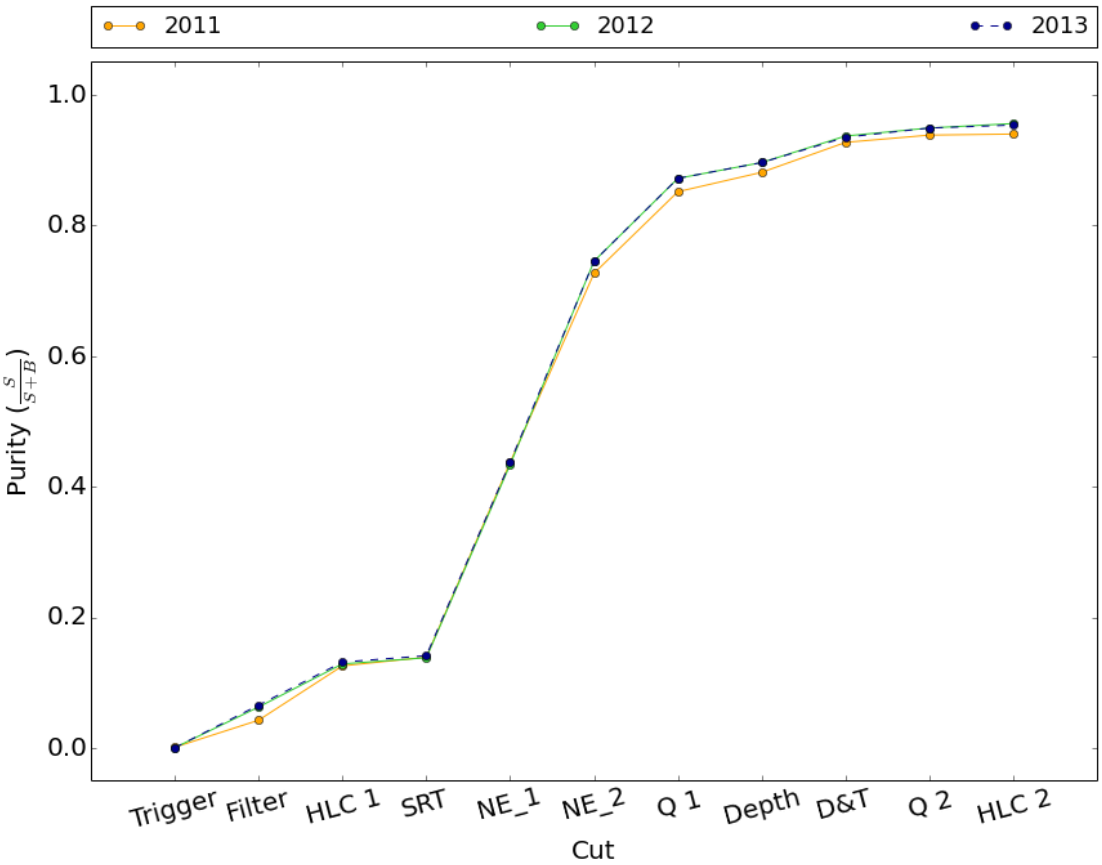

Figure 5.19: Purity (S/(S+B)) assuming a random normalisation of an E^{-2} flux between 1 GeV and 5 GeV. The x-axis represents the different steps of the event selection presented in this Chapter, considered in the same order.

Charge asymmetry It has been recently observed that some events may be influenced by flaring DOMs [3]. The exact origin of this sporadic emission of light is still

[3]This observation was made inside of the IceCube Collaboration, and the issue has been solved by developing a filter that removes the small number of pathological events from low energy data samples.

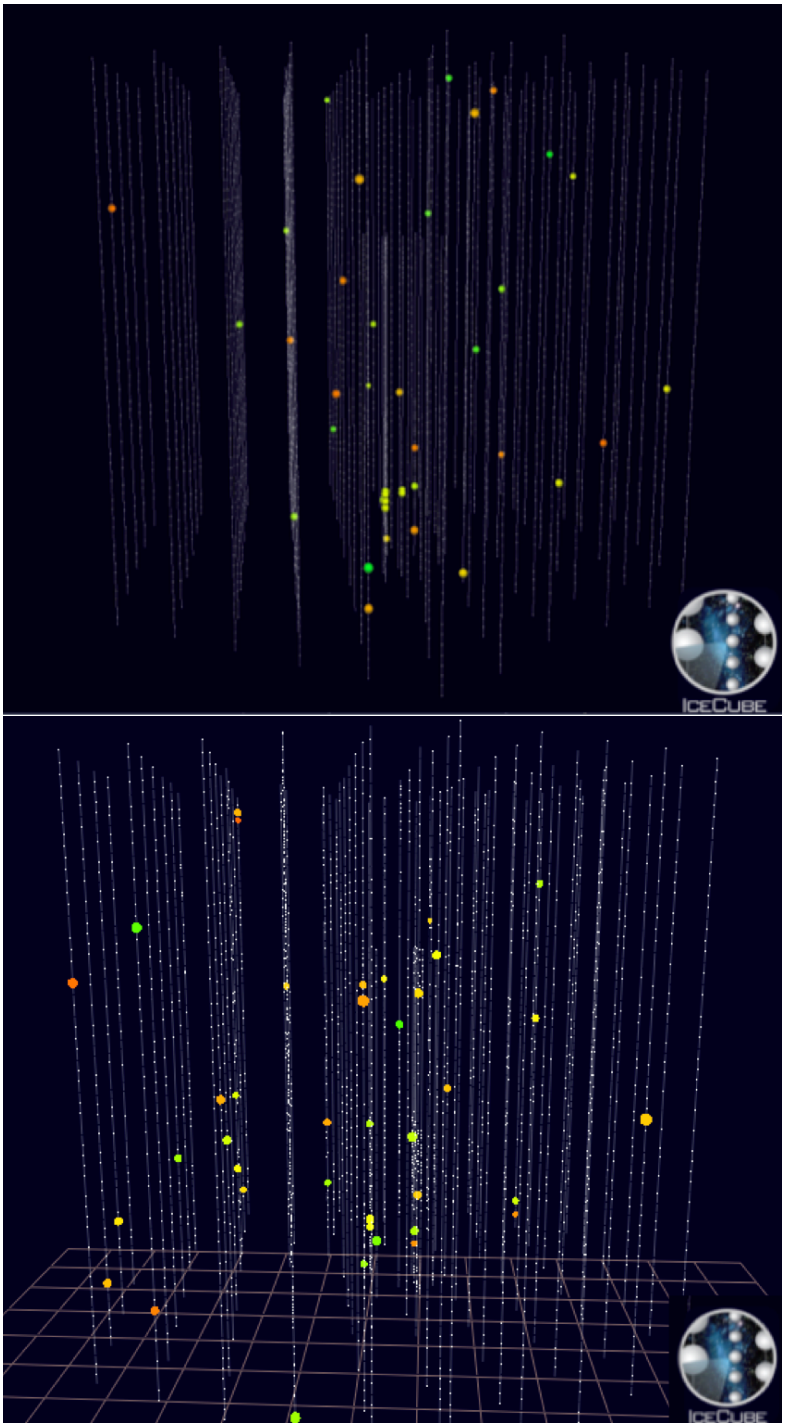

Figure 5.20: Two randomly picked events from simulated signal (top) and data (bottom). The two events share the same features.

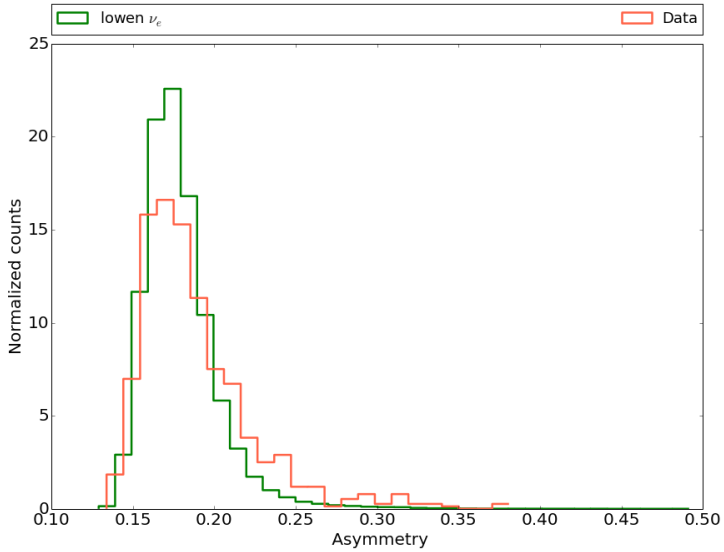

Figure 5.21: Asymmetry distribution for data (obtained using the event selection previously described, i.e. selecting neutrino interactions between 0.5 and 5 GeV) ν_e signal events.

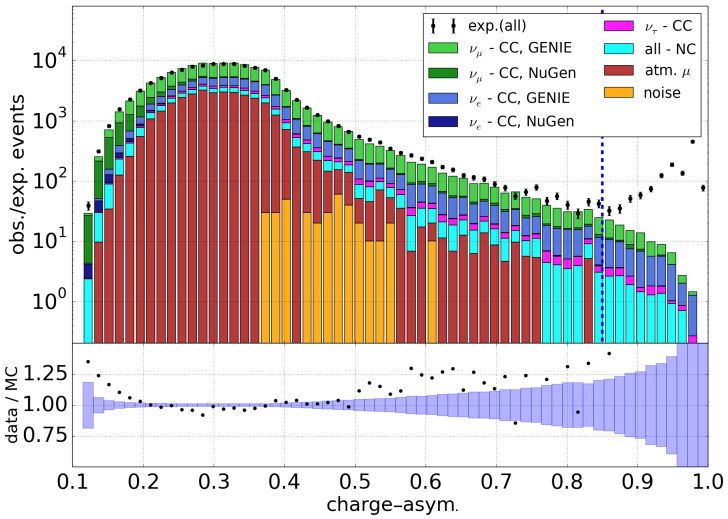

Figure 5.22: Illustration of a pathological asymmetry distribution. The black points (data, obtained using an event selection targeting neutrino interactions between 5 and 50 GeV) deviate from the expected distribution given by the simulated events (colored bands). The bottom part of the plot represents the deviation of data over simulation, the blue bands showing the statistical uncertainties. Plot with the courtesy of Martin Leuermann.

under investigation at the time of writing. In order to ensure that these DOMs do not contaminate our sample, we compared the charge asymmetry distribution of data and signal-like events. The asymmetry is defined as $\frac{\sqrt{\Sigma Q_i^2}}{\Sigma Q}$. If a DOM shows an abnormal behavior compared to the average DOM, the asymmetry would present a higher tail compared to the normal distribution. The results can be seen in Fig. 5.21. For comparison, a pathological asymmetry distribution is presented in Fig. 5.22. No major difference is observed in Fig. 5.21 between the two distributions and we therefore conclude that the flaring DOMs do not play an important role in the final sample.

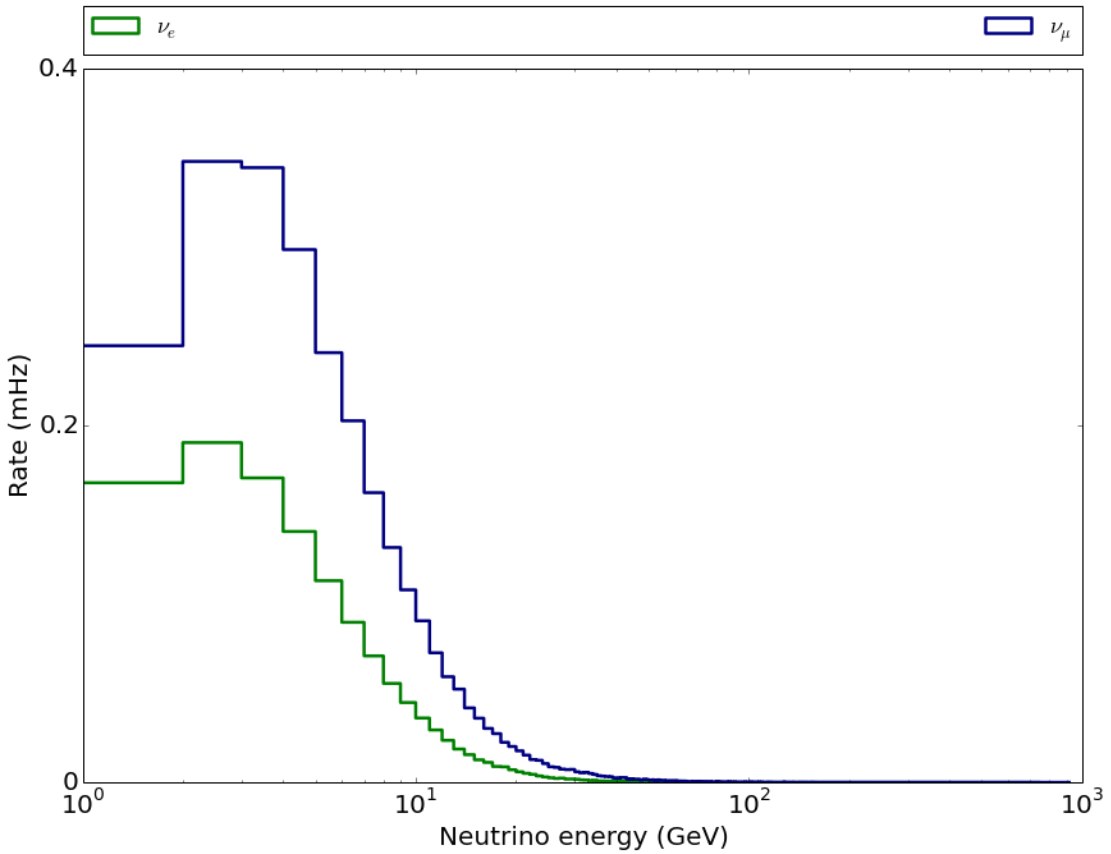

Figure 5.23: Energy distribution at final level for atmospheric ν_e and ν_μ based on Honda flux [111].

Energy distribution Finally, we can estimate the fraction of high-energy neutrinos remaining in the event sample by studying the energy distribution of simulated atmospheric neutrinos. The results can be seen in Fig. 5.23. As seen in the figure, the contribution of these high-energy events is small compared to < 5 GeV neutrinos. Fig. 5.24 shows some high-energy events passing the event selection. We investigated on the reasons why these events, expected to be bright according to the energy of the

primary neutrino, were seen as GeV-like events by the event selection. It turned out that more than 75% of the remaining events > 700 GeV are NC interactions. The average energy of the most energetic cascade produced by these interactions in the detector is around 20 GeV. Among the 25% of the remaining CC interactions, 85% happen below the minimal depth of the detector (i.e. outside) and therefore create a small amount of hits in DeepCore.

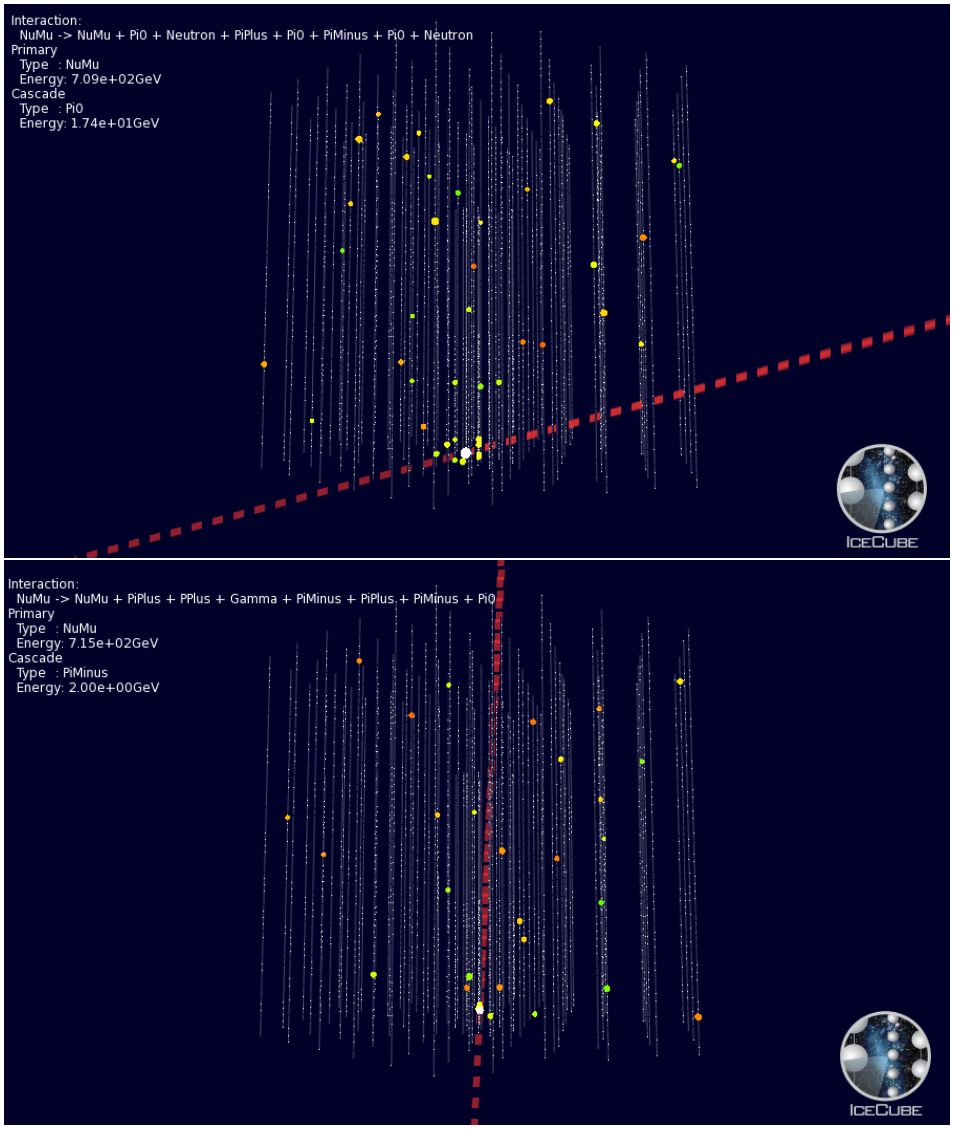

Figure 5.24: Examples of high-energy events surviving the selections described above. More events are presented in Appendix B.

5.6 Study of the Systematic errors

As mentioned in the previous Chapter, systematic errors arise from our limited understanding of the optical properties of the surrounding ice. By stretching several parameters in the simulation within realistic limits, the effect of the following parameters has been investigated: the DOM efficiency and the hole ice. Considering the low energy of the neutrinos studied in this thesis, we expect a detected interaction to happen very close to the optical modules, preventing otherwise the modules to see light from it. Therefore the uncertainties on the light absorption and scattering in the ice will have a negligible effect compared to the two other systematics effects described here.

5.6.1 DOM efficiency

As described in Chapter 4, the optical modules use a photocathode to detect the Cherenkov light emitted as a consequence of the neutrino interaction. The quantum efficiency of these photocathodes is thus a source of systematic uncertainties. Assuming a default efficiency of 1, and using a conservative variation of $\pm$ 10%, we obtained an estimate of the systematic errors due to this hardware component. Fig. 5.25 (top) shows the expected effect as a function of the energy. Since, at the time of writing, we are not able to reconstruct the energy of the detected GeV-like events, we will not be able to take into account the variation of this effect with energy. We therefore, in view of being conservative, consider the largest uncertainty, which is at low energy. The uncertainty is therefore estimated to be within 20% (for energies $>$ 1GeV) of the nominal value.

5.6.2 Hole ice

Chapter 4 describes the property of the ice used as a dielectric medium by the IceCube Collaboration. However, the properties of this ice have been altered in the close neighborhood of the optical modules due to the deployment process. The ice directly surrounding the modules has therefore different optical properties than the bulk of the detector. These effects are studied together by varying the so-called *Hole ice* (H) effect shown in Fig. 5.25 (bottom). Different scattering lengths are assumed in the model H_1 (100 cm) and in H_2 (50 cm), and therefore constitute one of the differences between the two models. Similarly to what we did for the DOM efficiency, we followed a conservative approach, considering the highest uncertainty at low energy. This one is also estimated to be within 20% of the nominal value.
These two systematics uncertainties, added in quadrature, will be used when deriving the upper limit on the solar flare neutrino flux presented in Chapter 6.

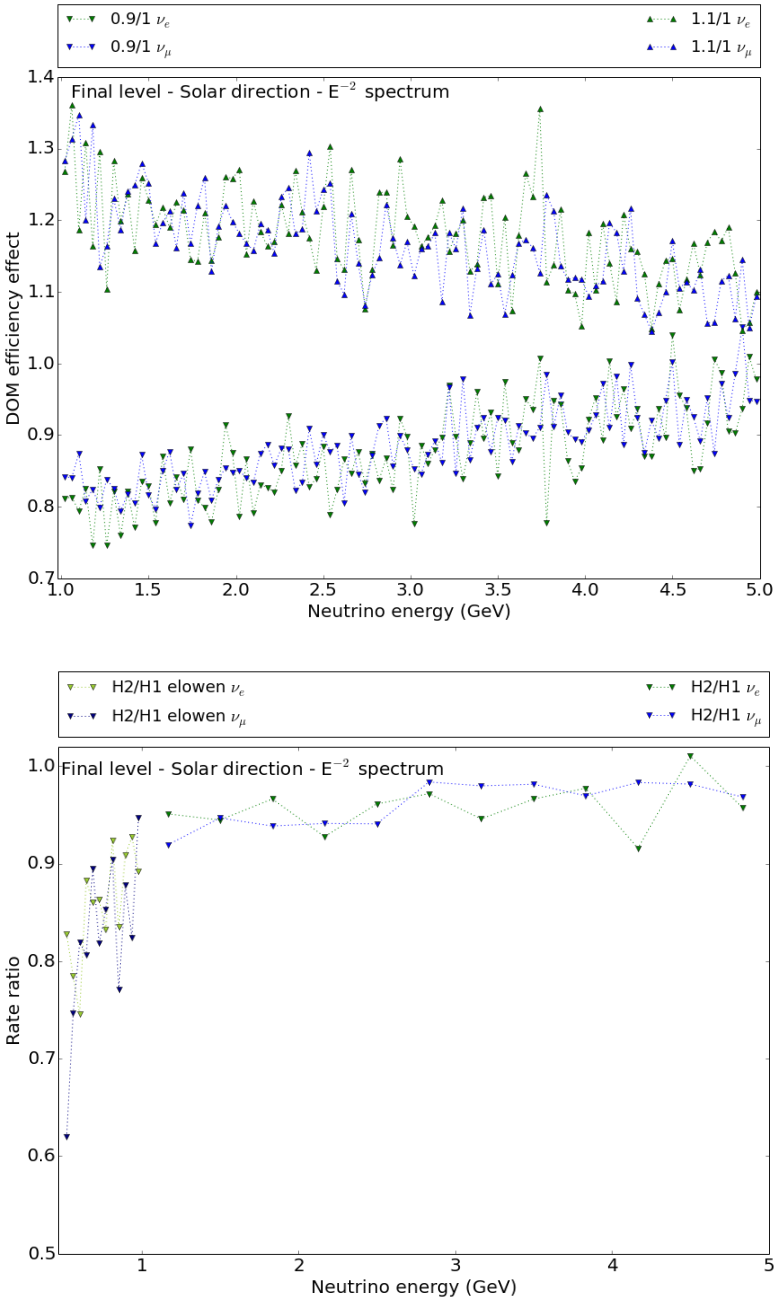

Figure 5.25: Study of two systematic effects: the estimation of the DOM efficiency (top) and the so-called hole ice effect (bottom). The y-axis represents the effect of the systematic parameter on the event rate seen in IceCube.

5.7 Effective Area for GeV Neutrino Interactions

The sensitivity of our analysis method and the ability of the event selection to lead to a neutrino detection depends on its effective area. In general, the effective area A_{eff} can be defined as

$$A_{\text{eff}} = \frac{\text{Observed event rate}}{\text{Incoming flux}}, \tag{5.1}$$

reflecting the area of the detector, scaled down by the fraction of events triggering the detector over the total number of events incident on the detector. Obviously this effective area can only be determined by means of simulation studies. It should also be noted that in case of no significant detection, the effective area allows us to impose a flux upper limit. Fig. 5.26 shows the effective areas for events arriving from a solar direction. In addition, the effective area for all sky searches as function of the energy as well as the zenith dependency of this variable are also presented in Fig. 5.26. It is observed that the zenith dependency of this event selection is very small, allowing it to be used for all-sky searches in the future. The next Chapter will combine the solar flare selection and time profile analysis described in Chapter 3 with the event selection presented here. This combination will be applied to solar flares in order to search for a neutrino signal.

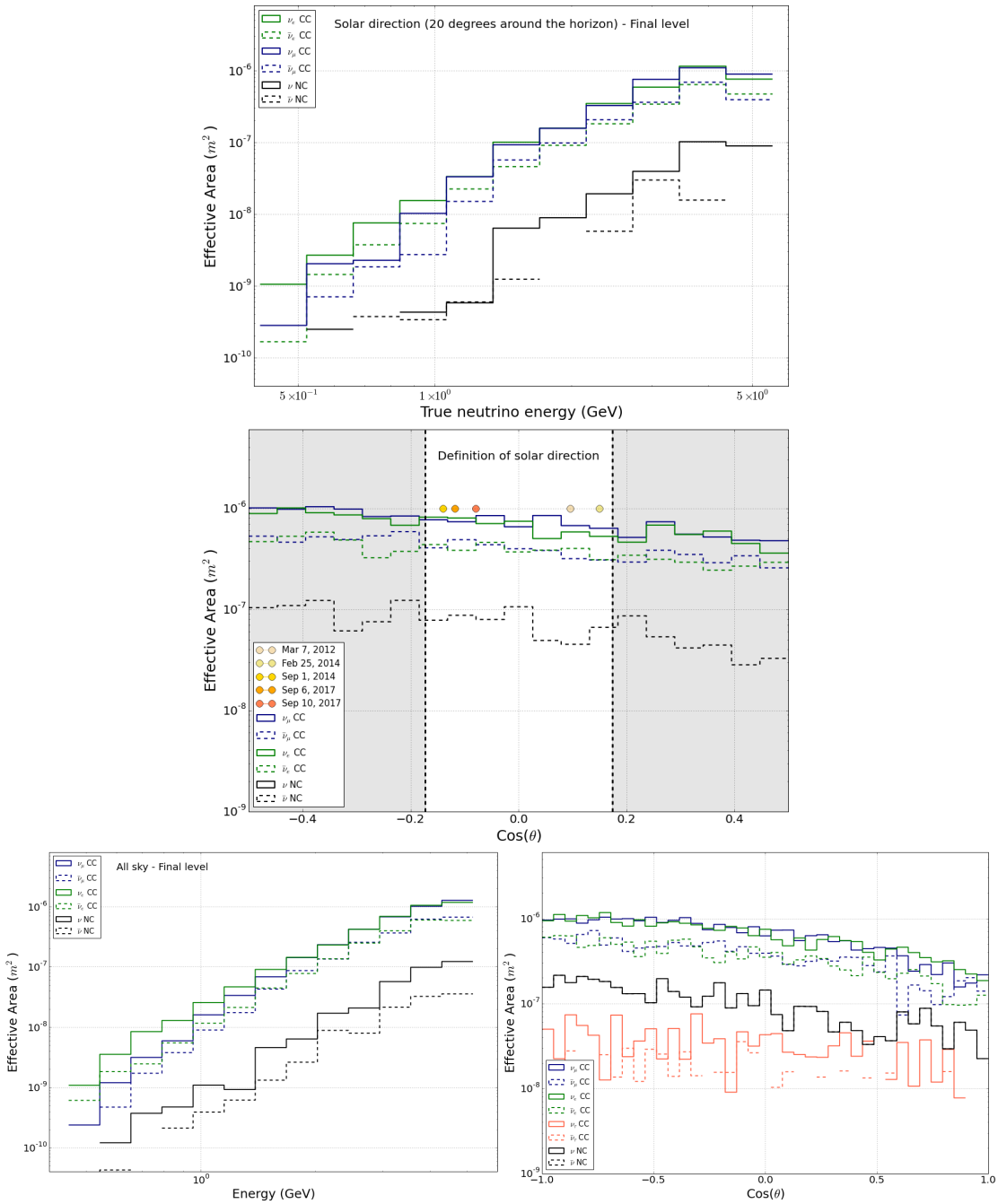

Figure 5.26: Effective area for ν_e and ν_μ at the final level of the event selection. The top plot shows the effective area for events arriving $\pm$ 10 degrees around the horizon. The middle plot shows that the effective area is constant in the zenith band considered on the top plot. For illustration, we have added the position of the studied solar flares on the Figure. The colored dots illustrate the zenith angle of the solar flares studied in this work. As one can see, they are all localized between $\pm$ 10 degrees. The bottom plots show the effective area for all sky searches (left) as well as its zenith dependency (right).

Mais on ne se bat pas dans l'espoir de succès !
Non ! non ! c'est bien plus beau lorsque c'est inutile.

Cyrano de Bergerac, Cinquième acte, scène VI,
Edmond Rostand

6

Investigating Solar Flare Neutrino Emission

This Chapter combines the solar flare selection described in Chapter 3 and the neutrino event selection described in the previous Chapter. We first present the statistical analysis we have carried out, before showing the sensitivity and discovery potential for solar flare neutrino searches with this event selection. Finally, we present the results, which have been obtained after a complete review and approval of this analysis by the IceCube Collaboration.

6.1 Description of the Statistical Analysis

In the previous Chapter, we have studied the properties of the final event sample. What is more interesting in the framework of a statistical analysis, is the stability and fluctuations of its rate with time. As previously described, we applied the event selection on several sets of data, each of them having a duration of 8 hours. These data were taken between 2011 and 2017 when no solar flares were observed [1].

6.1.1 Characterizing the background fluctuations

The main idea behind this analysis is to search for an increase in the rate recorded in IceCube during an astrophysical transient. In order to evaluate the background level

[1] See Chapter 5 for more details about the choice of the data.

and its natural fluctuations, we integrate 8 hours of data prior to the solar flare of interest [2]. This integration time allows us to define a rate level of about 0.02 Hz with ± 13% of uncertainty [3]. Fig 6.1 shows the evolution of the rate with time, for the 6 years that have been studied. The various panels illustrate the results of pseudo-experiments, where no solar flares happened during the selected data run. For illustration, the total duration has been divided into 20 minute control regions. In each region, the total number of events has been obtained and compared to the expected value of a Poisson distribution based on the overall rate estimation. The resulting p-values are indicated in each panel of Fig. 6.1. These indicate that the rate at final level is consistent with a Poisson distribution. We do not use the time region directly before the solar flare to make sure we do not include potential precursor neutrino emission in the background level determination.

6.1.2 Estimating the signal significance

In view of the rather large statistical uncertainties, we use the statistical test proposed by Li and Ma [112]. This method has been developed to estimate the significance of events in a certain time region, with a null-hypothesis being that no extra source exists. Three parameters are used and their description in the framework of our analysis is:

- N_{on}: number of events in the solar flare region.
- N_{off}: number of events in the control region, i.e. the time region prior to the solar flare onset.
- $\alpha = \frac{t_{\rm on}}{t_{\rm off}}$, where $t_{\rm off}$ is the duration of the control region, i.e. 8 hours, and t_{on}, the selected time window during the solar flare [4].

The derivation of the significance S of the observed results can be read in [112], where the final results is:

$$S = \sqrt{2}\left(N_{\rm on}\ \ln\left[\frac{1+\alpha}{\alpha}\left(\frac{N_{\rm on}}{N_{\rm on}+N_{\rm off}}\right)\right] + N_{\rm off}\ \ln\left[(1+\alpha)\left(\frac{N_{\rm off}}{N_{\rm on}+N_{\rm off}}\right)\right]\right)^{1/2} \quad (6.1)$$

This estimation of the significance can be used under the conditions that an event (N_{on}, N_{off}) was obtained by a single observation, where N_{on} and N_{off} are not too few. If these conditions are fulfilled, S refers to the number of standard deviation of the event (N_{on}, N_{off}) [112]. This approach is particularly interesting when, as it is the case in this analysis, there are two unknown parameters:

[2] Details about the time window selection have been presented in Chapter 3
[3] See Table 5.7 in Chapter 5.
[4] The definition of the time window for solar flare neutrino search is detailed in Chapter 3.

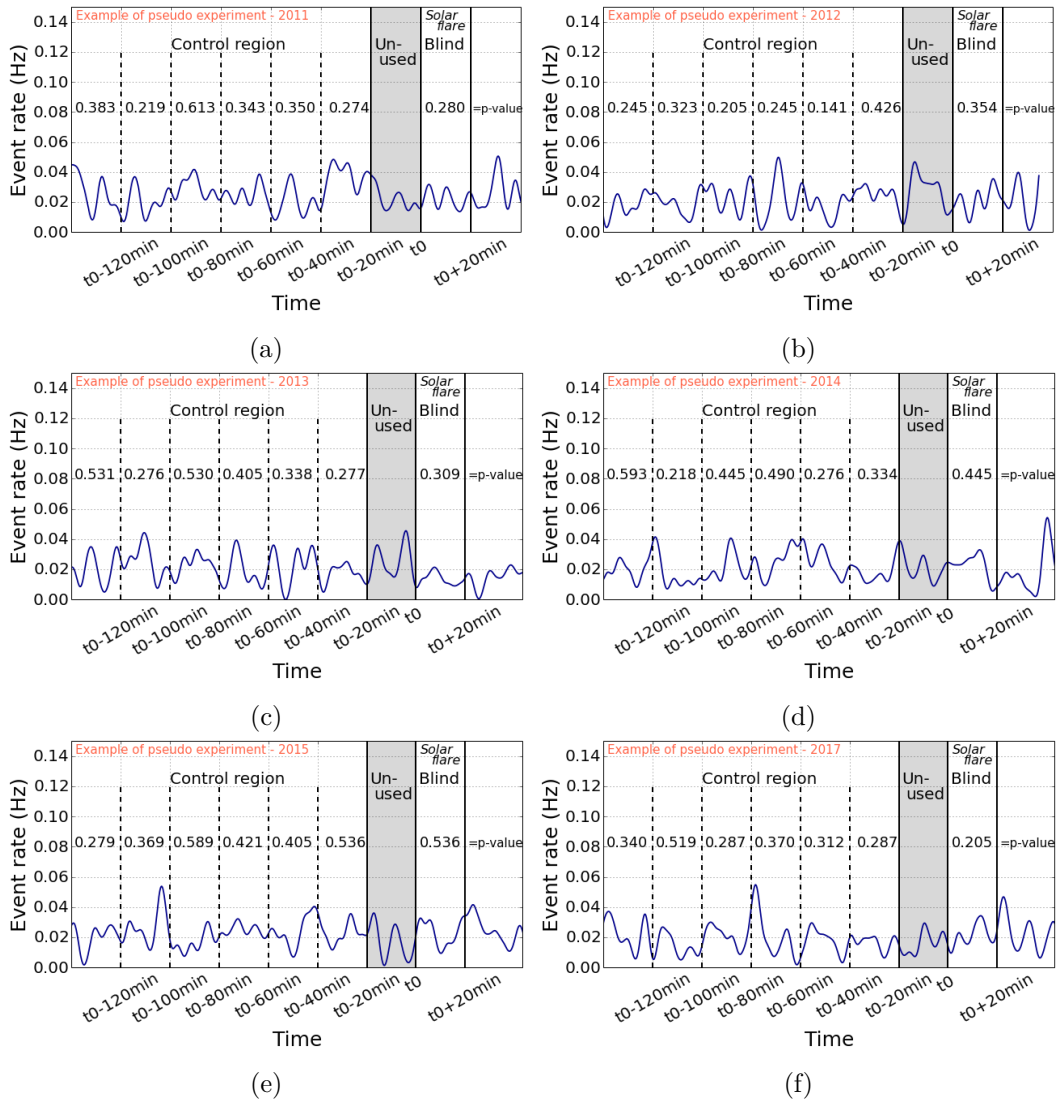

Figure 6.1: Evolution of the rate with time for 6 different years. No solar flare happened during the time windows presented in this Figure. Each time region shows a rate consistent with the Poisson distribution derived from the rate averaged during 8 hours. The p-values displayed in the plots confirm that the events in each time region are consistent with this Poisson distribution. The plots have been obtained using a 10 s smoothing. The grey shaded area represents the period before the solar flare that we do not consider in the analysis to avoid potential signal contamination in the estimation of the background.

- N_s: the number of signal events, equivalent to N_{on} - α N_{off}
- N_B: the number of background events, during the time window of the search.

Using Eq. 6.1 for a 6-minute off-source time window [5] should lead to a S compatible with the null-hypothesis. If we indeed replace N_{on} by 7, being an observed value during one of the 6-minute off-source time windows, and N_{off} by 550 events during a 8 hours control region, we obtain that S equals to 0.1 σ.

Deriving the Discovery Potential Let us now determine what would be the required number of signal events N_s, to obtain a significance $S = 5\sigma$ in 50 % of the cases. Solving Eq. 6.1 for N_{on} with S = 5, we obtain that N_{on} has to be at least 26 events for the example case mentioned above. Using the definition of N_s presented above, we directly get that a minimum of 19 events is required to make a 5-sigma observation.

In view of establishing what is the potential flux that could be probed with such a significance, we need to convert the number of events. The following formula links the number of observed events and the neutrino fluence Φ:

$$N_s = \int A_{eff}(E)\ \Phi(E)\ dE, \tag{6.2}$$

where A_{eff} is the effective area. We can express the different parts as follows:

- $A_{eff} = A \left(\frac{E}{1\ MeV}\right)^b\ cm^2$, where for ν_e, A = 1.31×10^{-9} cm^2 and b = 2 extracted from fitting the effective area presented in Fig. 5.26.
- $\Phi = C \left(\frac{E}{1\ MeV}\right)^{-\delta_\nu}\ cm^{-2}$, where both C and δ_ν have to be determined.

In view of converting N_s into a flux, we have considered the flavor ratio after vacuum oscillations between the Sun and the Earth. As previously mentioned, we expect a flavor ratio of $\nu_e : \nu_\mu : \nu_\tau \simeq 1 : 1 : 1$ at Earth. We can therefore estimate the fraction of each flavor in the total number of signal events, using the effective areas for each flavor and each interaction type. For ν_e and ν_μ both CC and NC interactions may induce an event in IceCube, while ν_τ only produces NC interactions in this energy range. The obtained values are presented in Table 6.1. These fractions will be relevant when deriving the upper limit from the observed number of signal events, since the conversion uses the effective areas that are different for each flavor and interaction type.

From our simulation of proton interactions with the solar atmosphere presented in Chapter 3, we know that the neutrino spectral index δ is expected to be between 4 and 7. We can therefore establish the discovery potential for the flux with different values of C and δ converting the required fluence Φ using the relation $\Phi = C\ E^{-\delta}$. Table 6.2 shows some examples of the obtained flux. In this Table, we present the fluence, i.e. the flux integrated over 6 minutes and over all flavors. Since we do not consider always the same duration for the different solar flares, the discovery potential slightly changes from

[5] Similar to the selected duration for Sep 10th, 2017 flare.

Table 6.1: Flavor composition of the signal events when assuming a flavor ratio at Earth $\nu_e : \nu_\mu : \nu_\tau = 1 : 1 : 1$.

Flavor	Interaction type	Fraction
ν_e	CC and NC	0.56
$\bar{\nu}_e$	CC and NC	0.05
ν_μ	CC and NC	0.11
$\bar{\nu}_\mu$	CC and NC	0.26
$\nu_\tau + \bar{\nu}_\tau$	NC	0.02

Table 6.2: Discovery potential of the analysis described in this thesis for different values of the normalization constant C of the solar flare neutrino flux, and its spectral index δ.

δ_ν	**C** (cm^{-2})	Fluence (ν cm^{-2})
4	1.07×10^{14}	285×10^{3}
6	6.52×10^{19}	417×10^{3}

one flare to another. Discovery potentials, sensitivities and comparison with theoretical predictions are presented in Appendix D. Fig. 6.2 represents these different discovery potentials together with the sensitivities in the (δ, C) parameter space.

Deriving the Sensitivity Similarly, we can derive the fluence needed to obtain a distribution of the S parameter that would be in 90% of the cases above the expected mean value under the null-hypothesis. Since S follows a gaussian distribution, we use the inverse error function to get the required mean of a S-distribution that would behave as needed. Using the example case mentioned above, we obtain that the required mean of the S-distribution leading to the sensitivity level is 1.64. Solving for this value, we obtain a N_{on} equals to 12, and therefore a N_s of 5 events. Repeating the procedure described above, we obtain the values of δ, C and Φ presented in Table 6.3. Fig. 6.2 illustrates the sensitivity in the (δ, C) parameter space. For comparison, we have added our theoretical estimates described in Chapter 3. We also compare with D. Fargion's prediction [42]. Using Eq. 2.11 in the cited paper, with the values $E_{fl} = 10^{32}$ erg and $< E_{\nu_e} > = 140$ MeV and 500 MeV, we obtained respectively the orange dashed and dotted lines presented in Fig. 6.2. As seen in the Figure, the current effective area of IceCube does not allow to probe the solar flare neutrino emission according to the estimations presented in Chapter 3. However, the sensitivity of this analysis would allow testing the estimate of [42]. However, we note that the orange lines constitute an optimistic estimate, since there is no consideration of the spectral index nor the upper cutoff of the proton flux. Furthermore, the neutrino energy range for this estimated flux is not specified.

Fig. 6.3 shows that similar results are obtained for the sensitivity when using a Poisson test.

Table 6.3: Sensitivity of the analysis described in this thesis for different values of the normalization constant C of the solar flare neutrino flux, and its spectral index δ.

δ_ν	**C** (cm^{-2})	Fluence (ν cm^{-2})
4	2.57×10^{13}	68×10^{3}
6	1.57×10^{19}	100×10^{3}

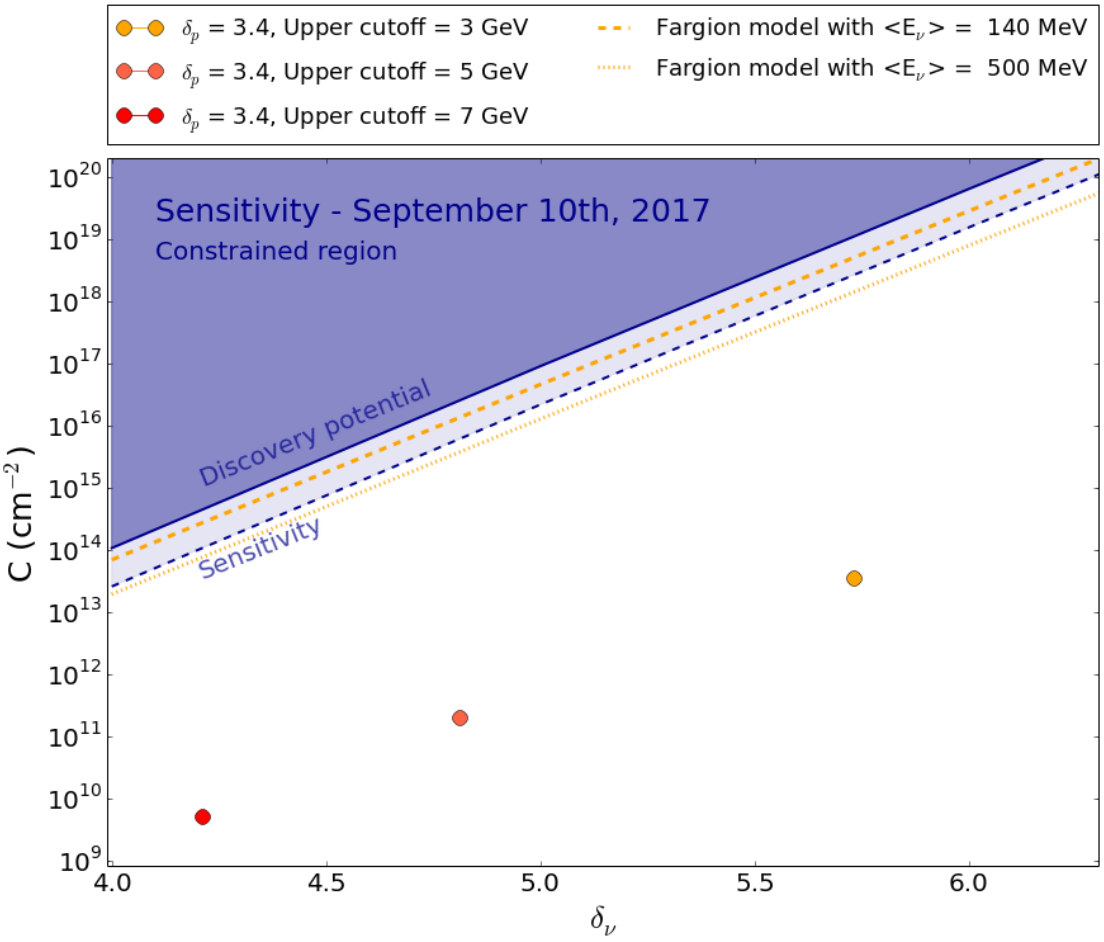

Figure 6.2: Discovery potential and sensitivity for a solar flare time window of 6 minutes. For comparison, the orange points show the estimations presented in Chapter 3. The orange line shows the predictions from [42], with E_{fl}=10^{32} erg and $< E_{\nu_e} >$=140 MeV (dashed) and 500 MeV (dotted).

6.2 Applying the Statistical Analysis to Solar Flare Data

In this section, we show the results of the analysis described in the last chapters. As announced in Chapter 3, we analyze 5 solar flares, selected based on their significance

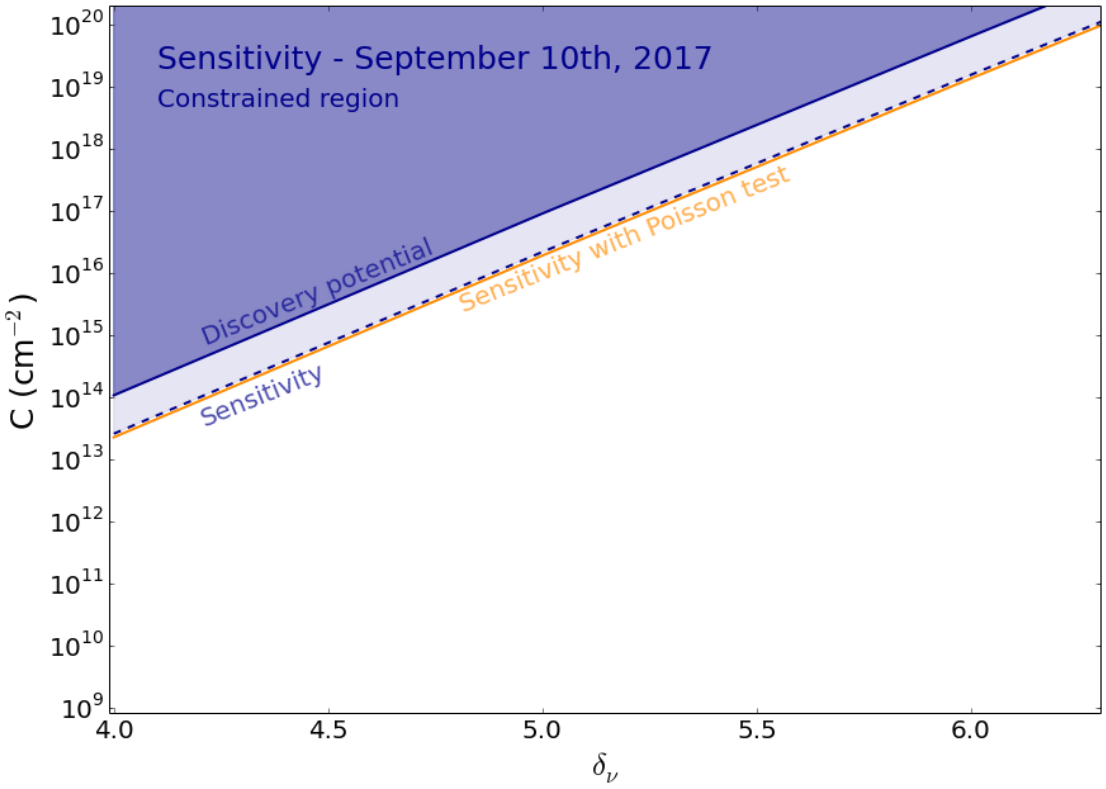

Figure 6.3: Li and Ma discovery potential and sensitivity as outlined in the text for a solar flare time window of 6 minutes. For comparison, the orange full line shows the sensitivity obtained with a Poisson test.

level in gamma ray observations. A time window for neutrino search has also been defined in Chapter 3, and the corresponding Discovery Potential and Sensitivity are presented in Appendix D.

6.2.1 Estimating the background level

Table 6.4 shows the rate in IceCube averaged over the 8 hours prior to each solar flare. As seen in the Table, the rate is constant over the years as already shown in Chapter 5. The $\pm 13\%$ of uncertainty on the rate constitute an additional source of systematic uncertainty. In the calculation of the upper limit, we therefore quadratically combine this uncertainty on the rate level with the systematic errors due to the modeling of the detector, presented in Chapter 5. Similarly to Fig. 6.1, we performed a Poisson test on the 10 last time regions prior to the solar flare. The 10-s smoothed rate and the p-values for each time region are shown in Fig. 6.4. The p-values show that all time regions are consistent with the expected Poisson distribution derived from the 8-hour prior to

Table 6.4: 8-hour averaged rate in IceCube prior to the studied solar flares.

Event	Rate (Hz)
Mar 7th, 2012	0.026 ± 0.003
Feb 25th, 2014	0.021 ± 0.003
Sep 1st, 2014	0.022 ± 0.003
Sep 6th, 2017	0.020 ± 0.003
Sep 10th, 2017	0.018 ± 0.003

Table 6.5: Number of off-source and on-source IceCube events as well as the corresponding significance obtained for each solar flare. For comparison, we add the expected amount of events ($N_{\text{on-expected}}$) based on the rates presented in Table 6.4 and the considered duration for each solar flare.

Event	t_{on} (min)	N_{off}	N_{on}	$N_{on\text{-}expected}$	Significance S
Mar 7th, 2012	40	761	67	62	0.43 σ
Feb 25th, 2014	25	611	27	32	0.86 σ
Sep 1st, 2014	14	621	21	18	0.65 σ
Sep 6th, 2017	517	569	639	620	0.79 σ
Sep 10th, 2017	5.96	529	5	6	0.64 σ

the onset of the solar flare. The Li and Ma test presented earlier in the Chapter can therefore be applied to estimate the significance of a potential neutrino signal emitted by the solar flare.

6.2.2 Calculating the number of potential signal events

We applied the statistical test described in Eq. 6.1. Table 6.5 shows the number of off-source and on-source IceCube events as well as the corresponding significance S. As a reminder we also include the durations of the different time windows, which have been optimized in Chapter 3. The off-time duration is 8 hours for every solar flare.

None of the studied solar flares led to a significant signal when using the analysis presented in this work. We can therefore derive upper limit on the neutrino flux based on the potential number of signal events obtained solving N_{on} - α N_{off} and the effective areas presented in Chapter 5.

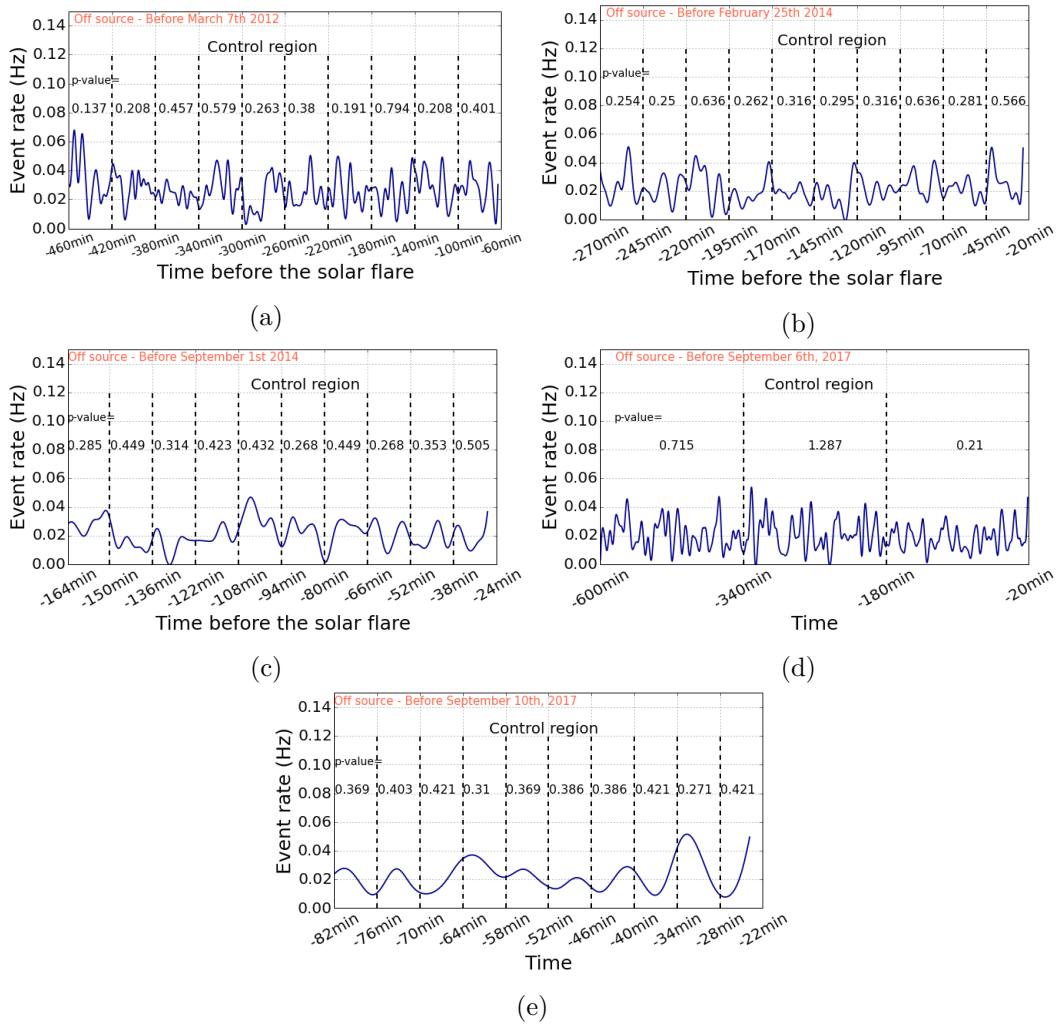

Figure 6.4: Evolution of the rate with time for the 10 time regions prior to the 5 solar flares of interest. An exception is made for the background region prior to the Sep 6th, 2017 solar flare, for which only 3 time regions are shown in view of getting as close as possible from the optimized duration for this event, i.e. 515 minutes. Each region has the same duration than the optimized time window of the studied solar flare. Each time region shows a rate consistent with the Poisson distribution derived from the rate averaged during 8 hours. The p-value displayed in the plots indicates that the events in each time region are consistent with this Poisson distribution. The plots have been obtained using a 10 s smoothing. Since we do not apply a Poisson test to estimate the significance of our signal, as described below, we did not calculate the p-value for the solar flare time region.

6.2.3 Deriving upper limit on the neutrino flux

In view of converting the number of signal events into an upper limit, we use the flavor composition presented in the previous section. The final upper limits presented in Table 6.6 therefore takes into account the flavor ratio and the effective area expected for each interaction type.
As mentioned in Table 3.2, the optimized time window for our neutrino search only contains a fraction of the observed gamma-ray light curve. Since this analysis assumes that the neutrinos are emitted jointly with the gamma rays, we can assume our time windows contain the same fractions of the total neutrino emission. We therefore take these fractions into account when comparing with theoretical predictions. The limits presented in Table 6.6 thus constrain the integrated neutrino flux emitted during the considered time window. We note that similar fractions of the light curves are observed for the events of March 7th, February 25th and September 1st. This is reflected in the similar upper limits set for these events. Approximatively half of this fraction is contained in the flare of September 10th, which explains the apparent lower upper limit. Finally, the September 6th flare targets the long duration emission that lasted for several hours, as previously mentioned. The origin of a such temporally extended emission is still under investigation, and therefore cannot, at the moment, be compared with the neutrino upper limits set for the other solar flares.

We can compare the values obtained with theoretical predictions as done in Fig. 6.2. We estimated the solar flare flux using the simulation described in Chapter 3 using the proton spectral index derived from Fermi-LAT observations when this one was available. Fig. 6.5, 6.7 and 6.8 illustrate the upper limit obtained for the March 7th, 2012, Sep 1st, 2014 and Sep 10th, 2017 solar flares in the (δ, C) parameter space. We note that all the upper limits are located, as expected, between the sensitivity and the discovery potential previously set for each solar flare and presented in this Chapter or in Appendix D.
As previously, the expectations derived from the simulation are shown by the colored circles. For one of the two remaining flares presented in Fig. 6.6, there was no spectral index of the accelerated proton flux available and we could not compare with our simulation output, we therefore only compared with D. Fargion's prediction.

For all the solar flares, except September 6th time window, which targets a different part of the solar flare and therefore cannot be compared with the models, the experimental upper limit constrains Fargion's prediction when assuming an average energy of 140 MeV. The optimistic 500 MeV line is slightly below the reach of the current sensitivity. Our prediction however stands far below the current reach of IceCube and cannot be tested at the moment of writing. In the next Chapter, we propose some possible improvements that would directly increase the sensitivity of very large neutrino telescopes in the GeV energy range, and could therefore lead to stronger constraints or a detection of the solar flare neutrino flux.

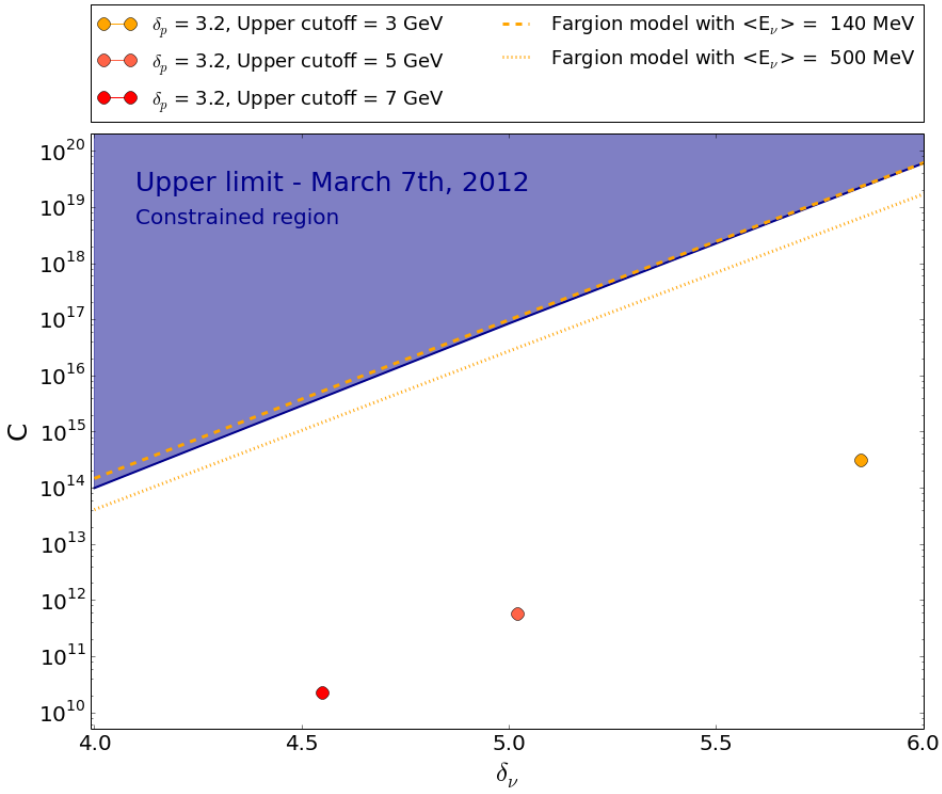

Figure 6.5: Comparison of the experimental upper limit derived for March 7th, 2012 and the corresponding theoretical predictions. The orange points show the output of our simulation when assuming a proton spectral index of 3.2, derived from gamma-ray observations. The orange line shows the predictions from [42], with E_{fl}=10^{32} erg and $< E_{\nu_e} >$=140 MeV (dashed) and 500 MeV (dotted).

Table 6.6: Upper limit on the solar flare neutrino fluence for each solar flare studied in this work.

Event	Duration (minutes)	Assumed spectral index δ_ν	**Upper limit** (90% C.L.) (cm^{-2})	**Upper limit** (90% C.L.) (cm^{-2}, including systematic uncertainty)
Mar 7th, 2012	40	4	263×10^3	456×10^3
		6	385×10^3	668×10^3
Feb 25th, 2014	25	4	228×10^3	273×10^3
		6	334×10^3	400×10^3
Sep 1st, 2014	14	4	157×10^3	204×10^3
		6	230×10^3	299×10^3
Sep 6th, 2017	515	4	1310×10^3	3480×10^3
		6	1920×10^3	5100×10^3
Sep 10th, 2017	5.96	4	98×10^3	116×10^3
		6	144×10^3	170×10^3

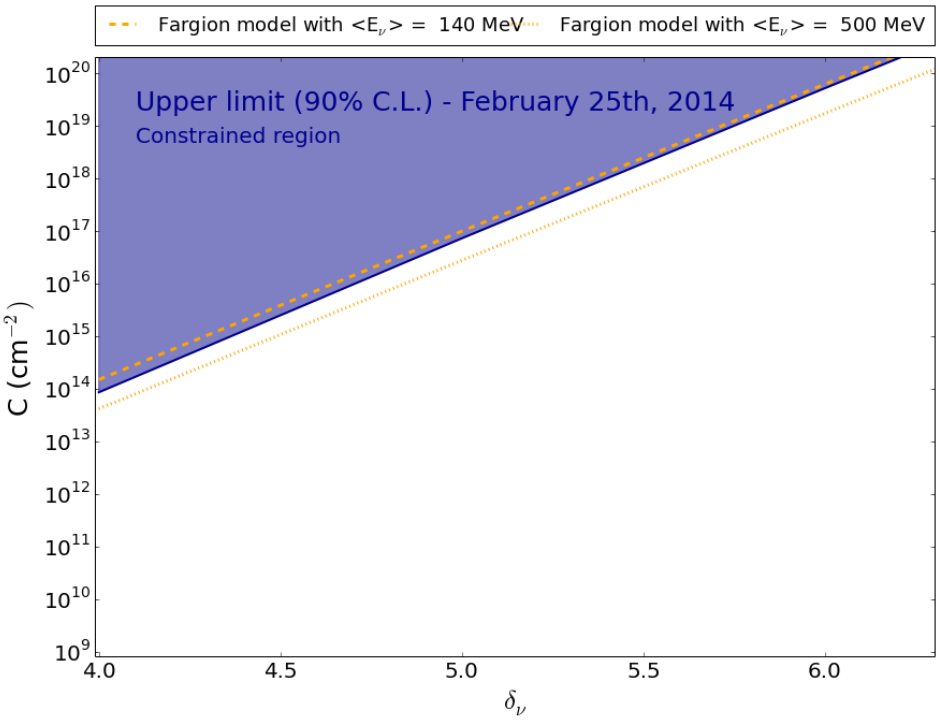

Figure 6.6: Comparison of the experimental upper limit derived for February 25th, 2014 and the corresponding theoretical predictions. The orange line shows the predictions from [42], with E_{fl}=10^{32} erg and $< E_{\nu_e} >$=140 MeV (dashed) and 500 MeV (dotted).

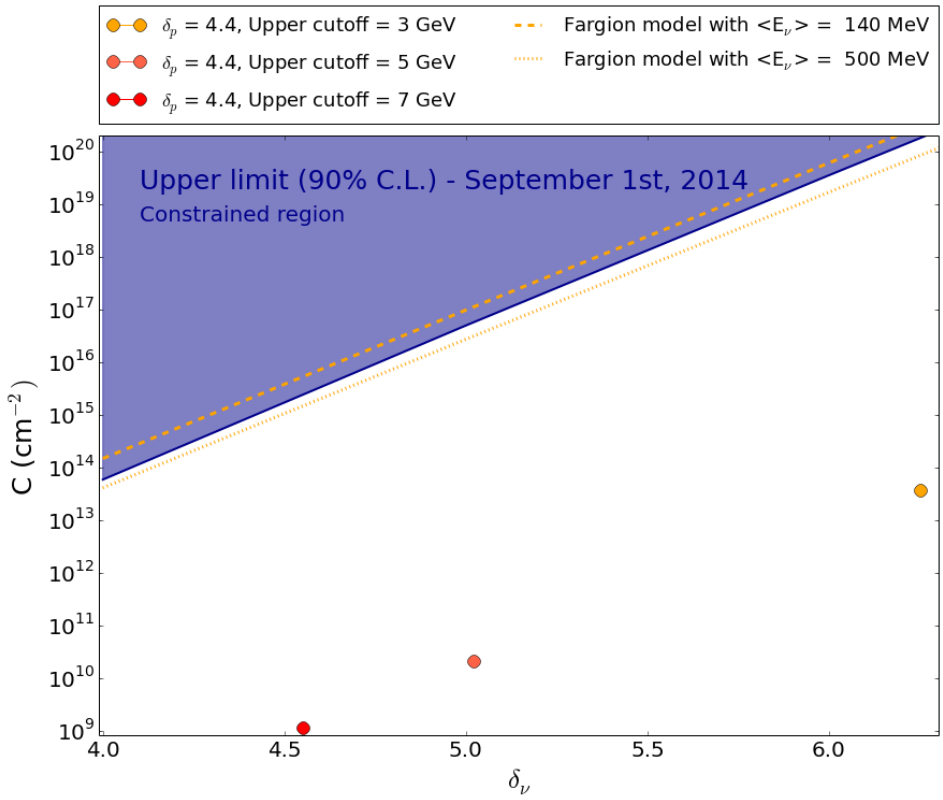

Figure 6.7: Comparison of the experimental upper limit derived for September 1st, 2014 and the corresponding theoretical predictions. The orange points show the output of our simulation when assuming a proton spectral index of 4.4, derived from gamma-ray observations. The orange line shows the predictions from [42], with E_{fl}=10^{32} erg and $< E_{\nu_e} >$=140 MeV (dashed) and 500 MeV (dotted).

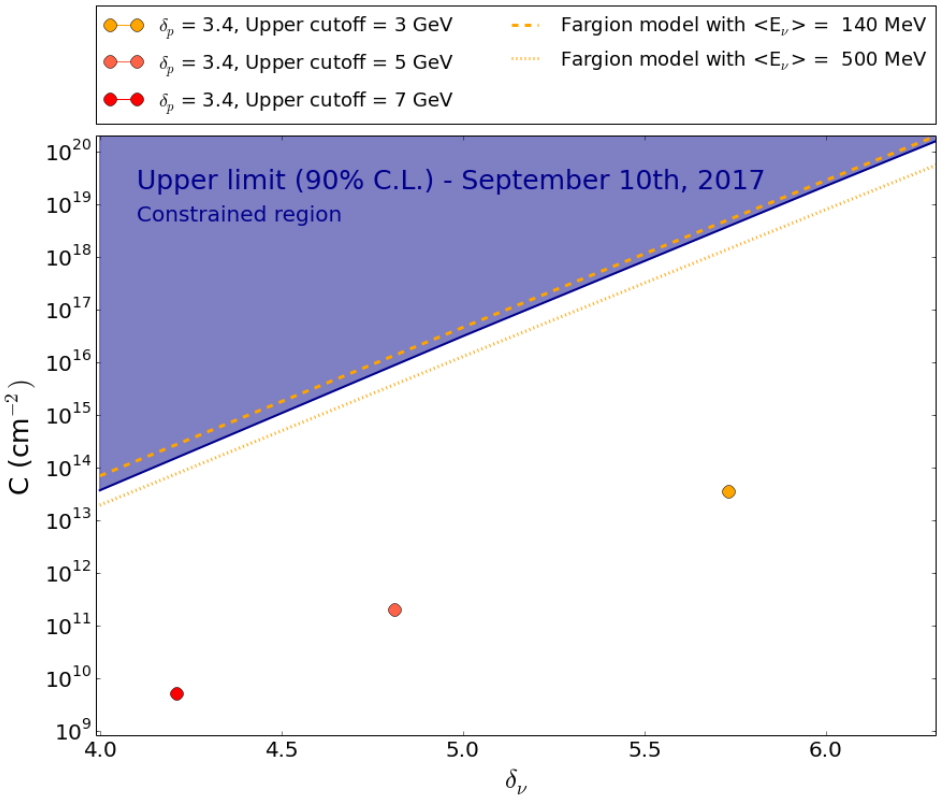

Figure 6.8: Comparison of the experimental upper limit derived for September 10th, 2017 and the corresponding theoretical predictions. The orange points show the output of our simulation when assuming a proton spectral index of 3.4, derived from gamma-ray observations. The orange line shows the predictions from [42], with E_{fl}=10^{32} erg and $< E_{\nu_e} >$=140 MeV (dashed) and 500 MeV (dotted).

Cuigy: – *Mais cent hommes !...*
Cyrano: *Ce soir, il ne m'en faut pas moins !*

Cyrano de Bergerac, Premier acte, scène VII,
Edmond Rostand

7

Short and Long Term Prospects

In this Chapter, we present some possible prospects for the work presented in this thesis. The proposed improvements would be beneficial for solar flare neutrino searches as well as any other GeV neutrino searches that could be performed. Some of them have already been implemented or may be in the coming months. The others should be considered as goals in view of developing GeV neutrino astronomy in the next generation of neutrino telescopes presented in Chapter 4.

7.1 Short Term Prospects

7.1.1 Searching for GeV neutrinos from gravitational wave events.

The event selection presented in Chapter 5 may be used to search for neutrino emission from other astrophysical transient events, such as, among others, Novae, Fast Radio Bursts, or Gamma Ray Bursts. Considering the recent observations of gravitational waves, short Gamma Ray Bursts [104], which are believed to be produced by binary neutron star mergers as has recently been witnessed, constitute preferred candidates. We have applied the event selection to all the mergers observed by the LIGO and Virgo interferometers so far. Among them are six binary black hole mergers (BBH), see e.g. [113], and one binary neutron star merger (BNS) [104]. This last event, which happened on August 17th, 2017, was the first ever observed through gravitational and electromagnetic waves. Unfortunately, the search for high-energy neutrinos did not lead

to a significant detection, similarly to the searches performed for the BBH events.

We have carried out two different searches targeting the precursor, prompt and afterglow phases of a GRB-like emission.

Searching for a prompt signal While TeV neutrinos are predicted as a consequence of the internal shocks in the prompt phase of the GRBs, GeV neutrinos should be produced by n,p collisions following decoupling [114, 115]. A neutrino search in the GeV energy range would therefore be complementary to the existing limits that have been set by neutrino telescopes in the TeV range as explained in Chapter 4.
We considered the 3 s following the merger detection by the LIGO and Virgo interferometers. Similarly to the solar flare analysis previously described, we have performed a Li and Ma test comparing the number of events passing our event selection during these 3 s and during 8 hours before the merger. The current IceCube layout and the analysis presented in this thesis lead to a sensitivity of 3.2×10^3 neutrinos cm^{-2} s^{-1}, if we assume a E^{-2} neutrino spectrum and a constant emission in the three seconds following the merger.
The same procedure has been applied to the BBH and BNS data. No extra events were observed during the studied time windows. The corresponding upper limit on the flux is therefore similar to the sensitivity, i.e. 3.2×10^3 neutrinos cm^{-2} s^{-1}, when assuming a E^{-2} neutrino spectrum and a constant emission in the three seconds following the merger. The BNS analysis led to a similar constraint on the flux assuming a E^{-2} neutrino spectral index. This constitutes the first constraint on BBH and BNS neutrino flux in the GeV energy range, for the 3 s following the merger.

Probing all the potential neutrino emissions in a GRB-like event Some models, also predict neutrino emission before - called *precursor* - or after, called *afterglow*, the prompt phase where the gamma ray peak is observed during the GRB [116]. It has been shown that considering a time window of 1000 s around the merger allows to contain all the potential neutrino emissions (see e.g. [117]).
We proposed to study the time distribution of the IceCube events during the 1000 s around the merger time. If we consider that the distribution of noise events is consistent with a Poisson distribution, meaning we expect n events in a certain time interval Δt when assuming a data rate r, one can invert the problem and consider the time interval expected to contain exactly n events consistent with a Poisson distribution of a rate r. The Erlang distribution, a special case of the Gamma distribution, can therefore be interpreted as the Δt needed to observe n events. The expression of the distribution can therefore be written as:

$$p(\Delta t|n, r) = \frac{(r\Delta t)^{n-1} r}{(n-1)!} e^{-r\Delta t}, \tag{7.1}$$

with n being the shape parameter and r the mean rate of a Poisson distribution.

For this analysis, we stack all the BBH merger data together. The stacking is eased by the fact that we consider a fixed time window of 1000 s centered around the merger time. In case of a neutrino emission happening always at the same moment with respect to the merger time, some neutrino interactions would be added to the background and therefore lead to a shorter duration between two GeV-like events, creating a clustering of events in time. We have chosen to use a shape parameter $n = 2$ for this analysis. A $n = 1$ being similar to the negative exponential distribution, would exhibit a maximum at 0. It would therefore be difficult to see small deviations in the rate of low Δt. A shape parameter of 2 means that we consider the duration between next-to-neighbor events. We use as background level the background averaged during the 8 hours prior to the (merger time - 500 s). In order to obtain the discovery potential and the sensitivity, we performed a Kolmogorov-Smirnov test [118] and a Bayesian Psi test [119]. We note that the Super-Kamiokande Collaboration had set a limit on the fluence of 14 - 37 (19 - 50) cm^{-2} for muon neutrinos (muon antineutrinos) between 1.6 GeV and 100 PeV from GW150914 [120].
Unfortunately when stacking the background regions, prior to each merger, we found a deviation from the expected Erlang distribution. In view of understanding this deviation, we performed the same test on individual mergers, applying the KS test during the background and the merger time windows. While all the time regions showed a p-value consistent with the pure background hypothesis, one significantly deviates with a p-value of 9.33×10^{-5}. The corresponding gravitational wave event was labeled GW170608 by the LIGO Collaboration. Interestingly, during the follow-up campaign triggered last June by the LIGO observation, Fermi-LAT has observed gamma rays inside the LIGO Bayestar probability map, 1200 s after the merger time [1]. The first checks performed in our analysis show that IceCube was stable at the moment of the merger. However, more detailed investigations are required, and currently ongoing, to understand the origin of the potential extra events observed in IceCube.

7.1.2 Selecting GeV neutrino events in IceCube

As pointed out above, the event selection presented in this thesis may be used to search for neutrino emission from any astrophysical transient. In order to allow the Collaboration to efficiently perform these searches, we have designed a filter based on this event selection and a proposal has been submitted and recently approved by the IceCube Collaboration. As of the 2018 data run, a filter flag will be added during the processing of the IceCube events that pass the trigger and filter conditions described in Chapter 4. One will therefore only have to select events that pass this selection to obtain a sample of GeV-like events during the time of interest.

[1] The observations made for this event are summarized in https://gcn.gsfc.nasa.gov/other/G288732.gcn3.

7.1.3 Reconstructing the direction in the GeV range

In order to move towards neutrino astronomy in the GeV range, one would need to be able to reconstruct the incoming direction of these low energy interactions. Unfortunately, GeV neutrino interactions generate very few hits in the current layout of the IceCube detector, leading to a reduced amount of information that can be used in a reconstruction algorithm. We propose here two different approaches that may lead, if worked out, to the possibility of reconstructing the direction of the interacting neutrino.

Using the delay between HLC hits on the same string As seen in Chapter 4, GeV-like events are characterized by several hits along the same string. This is due to a closer distance between DOMs on the same string compared to neighbor strings. One can therefore use the delay between the hits to give a rough approximation of the direction of the event. Let us consider the first HLC hit in the event, probably the closest one from the interaction point. We can calculate the delay between this first HLC hit and the ones recorded on the same DOM or the close neighbors, as illustrated in Fig. 7.1. The three different curves show the delay for hits happening on the same DOM, on the top neighbor (-1) or bottom neighbor (+1). Two different incoming directions have been considered: up-going and down-going events. As seen in the figure, we expect similar delays on the top and bottom DOMs for down-going events, while the two delay distributions are different for up-going events. Fig. 7.2 is similar to Fig. 7.1, illustrating the delay between HLC hits on the second neighbor DOMs. The same conclusion can be drawn. Both Fig. 7.1 and 7.2 use simulated neutrino events between 1 and 5 GeV. These differences, partially due to the geometry of the downward looking DOM, could be used to reconstruct, to some extent, the direction of the charged lepton, and therefore to get an approximate direction of the neutrino. We note that a precise reconstruction of the incoming neutrino will never be achieved because of the rather large uncertainty of the angle between the charged lepton emission with respect to the incoming neutrino due to kinematic considerations.

Using SANTA The IceCube Collaboration has a dedicated tool to reconstruct the direction of low-energy neutrino events. Called *Single string ANTares-inspired Analysis* (SANTA) [121], this algorithm first applies a strong definition of 'direct hits' to select events with a good reconstruction potential. It then tries to reconstruct the direction by studying the signature of the projection of the Cherenkov cone on a single string. 3 % (0.03 %) of the signal events between 1 and 5 GeV (0.5 and 1 GeV) pass the SANTA selection. This is a small amount, but it has to be compared with the 0.08 % of data events at final level passing the same selection. This algorithm could therefore be used to obtain a clean sample of GeV neutrinos with a reconstructible direction. Considering the stringent selection, this may be more useful for longer integration time where we could afford to cut more on the expected signal and still have some events in the sample.

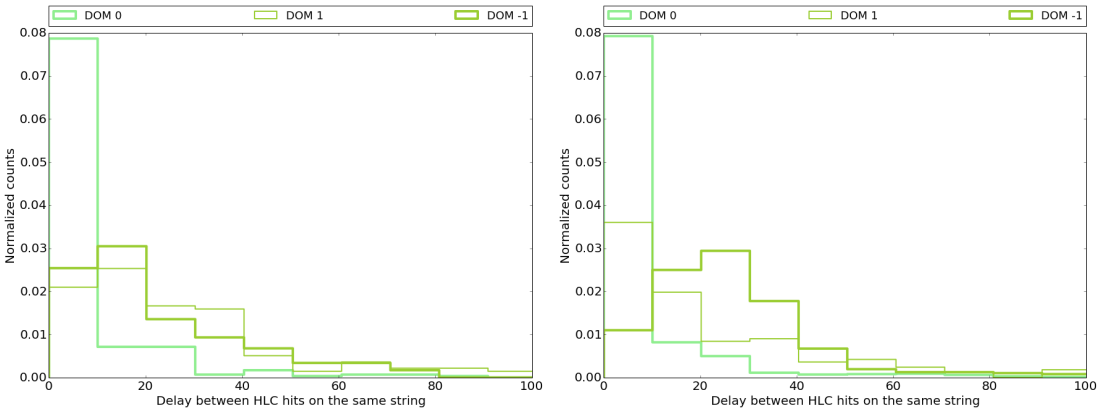

(a) Down-going neutrino (b) Up-going neutrino

Figure 7.1: Delay between the first HLC hit and the others recorded on the same, or direct neighbor DOMs. The left (right) plot shows the distributions for down (up) going neutrinos. More explanations are given in the text.

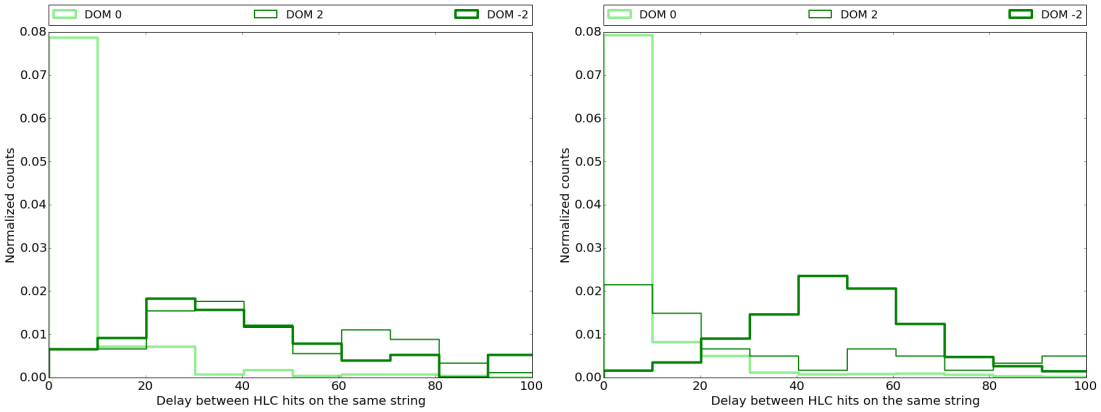

(a) Down-going neutrino (b) Up-going neutrino

Figure 7.2: Delay between the first HLC hits and the others recorded on the same, or next-to-neighbor DOMs. The left (right) plot shows the distributions for down (up) going neutrinos. More explanations are given in the text.

Once these techniques are established and combined with the filter described in the previous section, one would be able to perform a larger range of analyses, searching for e.g., neutrino point sources or dark matter in this energy range.

7.1.4 Increasing the sensitivity

The limitation of this analysis is determined by the current effective area of the IceCube detector for GeV neutrinos. Besides the small cross section of GeV neutrinos with the surrounding matter that limits the amount of interactions, each of these interactions needs to trigger the detector to be recorded. As described in Chapter 4, the minimal requirement to be considered as an event is 3 DOMs with HLC pulses within 2.5 μs. A few years ago, a new data stream was developed in IceCube. Called *HitSpooling*, this stream allows to save every single hit happening in the detector, independently of the trigger condition [85]. This means that sub-threshold neutrino interactions, lost in regular IceCube data, can be saved and studied. It directly results in an increase of the sensitivity. It was originally designed for Supernova searches, being triggered by the IceCube SNDAQ [85].
HitSpool data structures have a significantly larger size than regular IceCube data, and cannot therefore be continuously saved. However, it guarantees a 100% uptime of IceCube during an interesting event. In view of taking advantage of this new data stream and its increased sensitivity, we have collaborated with Fermi-LAT scientists, especially Melissa Pesce-Rollins and Nicola Omodei, to create an alert system and a database called *SFNews*. Based on the solar flare selection described above, the system is continuously searching for significant solar flare events in Fermi-LAT data in view of triggering the IceCube HitSpool data stream. This system, supported by the IceCube Collaboration, is running since September 2015 and successfully saved data for the bright solar flares of September 2017. A dedicated analysis is currently ongoing.
Another alert system, *GW-HS* has been developed in view of saving HitSpool data coincident with the detections of BBH or BNS mergers by the Ligo and Virgo interferometers. This alert system will be fully automated for the next run of LIGO expected for Fall 2018.

7.2 Long Term Prospects

On a longer time scale, we propose three directions that would help to increase the discovery potential of neutrino telescopes in the GeV range, both for solar flare and other transient searches.

7.2.1 Using the hit multiplicity

As shown in Fig. 7.3, GeV neutrino interactions leave more than one hit on the same DOM. The next generation of neutrino telescopes, currently under construction such as KM3NeT, or planned as the IceCube upgrade, will be an asset for GeV neutrino astronomy. These new detectors will be equipped with optical modules with multi

PMTs, as illustrated in Fig. 7.4. A GeV neutrino interaction may therefore be detected by several PMTs on the same DOM, instead of creating several hits on the same single photocathode. The PMTs where the hits were recorded and the delay between these hits would allow us, taking into account scattering in the ice or water, to reconstruct the direction of the charged lepton.

It is therefore important to study the physics potential for GeV neutrino detection of the next generation of neutrino telescopes. The design, if not fully fixed yet, as well as the triggering and filtering system may be adapted to add GeV astronomy to the science case of these detectors.

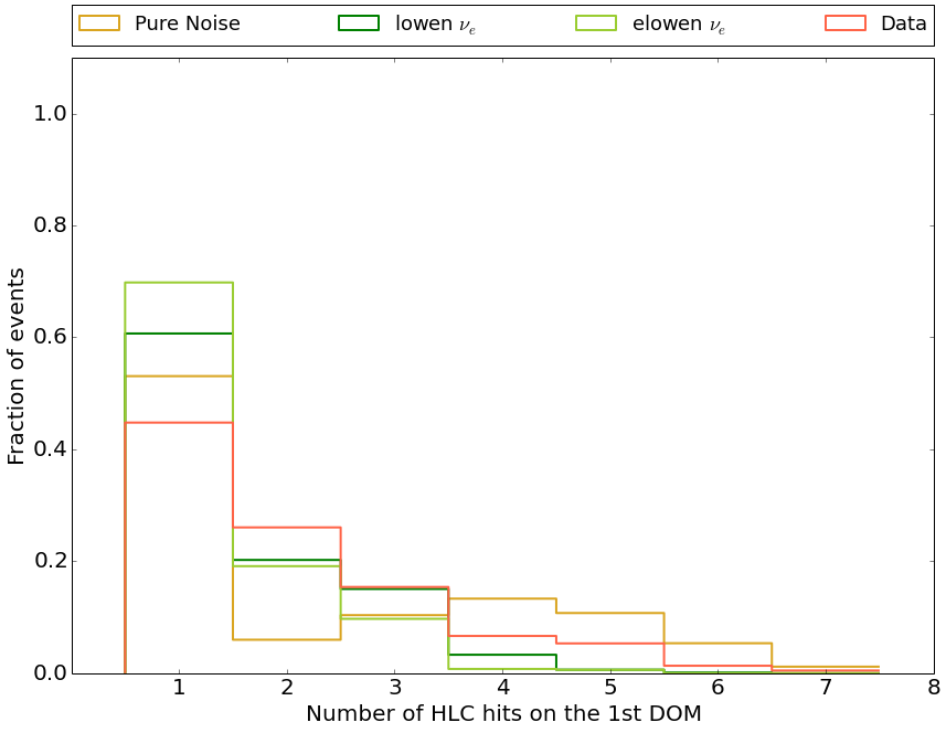

Figure 7.3: Distribution of the number of hits on the DOM where the 1st HLC hit was recorded.

7.2.2 Potential new searches with increased sensitivity

Once a sufficient sensitivity will be reached, a new window on the study of transient events may be opened. Instead of triggering GeV neutrino searches based on electromagnetic or gravitational wave observations as described above, we could use neutrino telescopes to trigger sub-threshold searches in gravitational or electromagnetic wave detectors. By continuously monitoring the rate of GeV neutrino events, one could send

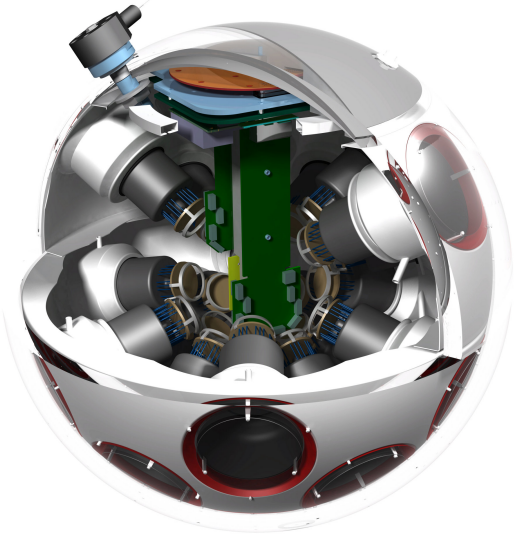

Figure 7.4: Illustration of an optical module equipped with multi PMTs. This figure shows the KM3NeT modules, which have 31 PMTs distributed around the sphere. Credits: The KM3NeT Collaboration.

alerts to partners when this rate becomes significant. It would allow to perform sub-threshold searches with e.g., the LIGO and Virgo interferometers. Such searches may allow to observe new classes of sources, such as *failed GRBs* or *obscured sources* that do not lead to significant detection in electromagnetic waves. LIGO and Virgo scientists have already shown interest for these kind of searches.

In the solar flare framework, this increased sensitivity will open the possibility of new searches. Solar flares happening on the back side of the Sun, far behind the limb, may not be detected by Fermi-LAT. As previously mentioned, the STEREO mission monitors the solar activity happening on the far side of the Sun, but the mission does not have any instrument dedicated to the study of gamma rays. The increased sensitivity would therefore allow us to search for solar flare neutrinos without the prior on the starting time based on gamma-ray observations. This is particularly interesting considering that these back-side flares are expected to yield a higher neutrino flux compared to the front face, due to geometrical effects. They therefore constitute preferred candidates to constrain solar flare physics via neutrino observations.

7.2.3 GeV neutrinos in a Global Neutrino Observatory

A Global Neutrino Observatory, whose first step has been the creation of the Global Neutrino Network in 2013, would be especially interesting for the development of GeV

astronomy. Combining simultaneous observations in different neutrino telescopes would have several advantages. We could indeed use the three KM3NeT sites together with the IceCube/IceCube-Gen2 detector in order to increase the effective volume for low-energy neutrino interactions. Besides, while the detector noise is the dominant background source in the analysis presented in this thesis, using the approaches proposed in this Chapter and combining the observations would have the benefit to reduce this noise contribution. Since only a physical signal would produce an increase in the rate of all detectors at the same time, we could remove random fluctuations and decrease the final off-source rate of the analysis.

Travailler sans soucis de gloire ou de fortune,
A tel voyage, auquel on pense, dans la lune !

Cyrano de Bergerac, Deuxième acte, scène VIII,
Edmond Rostand

Epilogue

Solar flare neutrinos were the main topic of this thesis. Along the chapters we studied their production, characteristics and potential signature in very large neutrino telescopes. We started by presenting a review of the different processes that take place in the solar environment and could lead to a neutrino production and a potential detection in neutrino telescopes. We concluded that a very specific signature, i.e. transient and in the few MeV-GeV energy range, was expected from solar flare neutrinos, preventing these ones to be mistaken with others.

Chapter 2 was dedicated to the physics involved in the solar environment with a special attention on the particle acceleration and interaction sites, especially relevant for neutrino production. An original study of the neutrino production was then presented in Chapter 3: we first briefly summarized the state of the art before showing an approach based on multi-messenger astronomy that allows to optimize solar flare neutrino searches. The Chapter ended with an original simulation aiming at estimating the amount of neutrinos one could expect from solar flares, and concluded that neutrino telescopes could contribute to constrain particle acceleration when combining their observations with gamma-ray detection. In particular, different values of the high-energy cutoff of the proton spectrum would produce, when assuming a spectral index, different amounts of detected events.

We then presented a review of very large neutrino telescopes, which current generation devices are the GVD Baikal detector, ANTARES and the IceCube Neutrino Observatory. We concluded the latter was the only detector that is capable to search for solar flare neutrinos at the moment. A detailed description of IceCube and its surrounding ice has therefore been presented and we concluded with a summary of the achievements and discovery in neutrino astronomy made so far. Considering the expected energy range for solar flare neutrinos, we have developed an innovative analysis in a so far unexplored energy range with IceCube. After detailing every step of this selection, we presented the expected effective area for GeV neutrinos.

In the last part of this thesis, we combined solar flares and the neutrino analysis to evaluate the sensitivity of our statistical approach. We presented the results of this search and compared with the existing theoretical predictions. While none of the studied solar flares have created a significant signal in IceCube, the upper limits we have set could

strongly constrain one of the existing predictions. Improvements in hardware, software and statistical analysis may lead to stronger constraints or detections of the solar flare neutrinos in a near future. We therefore concluded this thesis with a presentation of short and long-term prospects for GeV neutrino astronomy.

In addition to the work presented in this manuscript, I have been contributing to different other projects. I participated to a phenomenological study, combining the recently observed gravitational waves and the non-detection of correlated high-energy neutrinos [122]. This approach allowed to constrain the amount of matter surrounding the binary merger.
I also had the opportunity to work on instrumentation: I installed a system monitoring the snow coverage above IceTop, the surface array of IceCube, and integrated it to the existing software environment of IceCube. The system, monitored for more than a year, led to very stable measurements and constitutes a promising solution for long-term automated snow monitoring for the future extension of the IceCube surface array.
Finally I have also been active in science communication through the organization of several activities, projects and the writing of articles, press releases or papers. Some of these activities are summarized in [123] and in 2017 I was awarded the Science Communication Prize of the Royal Flemish Academy of Belgium for Science and the Arts.

Mettre, quand il vous plaît, son feutre de travers,
Pour un oui, pour un non, se battre,- ou faire un vers !

Cyrano de Bergerac, Deuxième acte, scène VIII,
Edmond Rostand

Achievements and Additional Contributions

Instrumentation and Contribution within the IceCube Collaboration

In addition to the SFNews alert system developed in view of saving HitSpool data for promising solar flare events, I have developed a similar data base for gravitational wave events detected by the interferometers LIGO and Virgo. This system, running since the second observational run of LIGO, allowed to save HitSpool data for several binary black hole mergers. The automation of the system, coupled with a realtime analysis of the HitSpool data, will allow to obtain, in a near future, detections or constraints of the GeV neutrino flux emitted in correlation with events observed by LIGO and Virgo.
I also had the opportunity to work on instrumentation: I installed a system to monitor the snow coverage above IceTop, the surface array of IceCube, and integrated it to the existing software environment of IceCube. The system, running for more than a year, has led to very stable measurements and constitutes a promising solution for long-term automated snow monitoring for the future extension of the IceCube surface array.

Phenomenological studies

As mentioned in Chapter 1 and 3, I have studied two neutrino fluxes produced in the solar environment: solar atmospheric neutrinos [39] and solar flare neutrinos [41]. I also participated to a study of the combination of the recently observed gravitational waves and the non-detection of correlated high-energy neutrinos [122]. This approach allowed to constrain the amount of matter surrounding the binary merger.

Dissemination and Communication

Along my PhD studies, I had the opportunity to communicate and disseminate the results of the various projects previously mentioned. I presented several talks in parallel

or plenary sessions of international conferences as well as several posters. Earlier in 2018, I have received a Young Speaker award from the Belgian Physical Society.

Vulgarization and Outreach

Finally I have also been active in science communication through the organization of several activities, projects and the writing of articles, press releases or papers. Some of these activities are summarized in [123]. In 2017 I was awarded the Science Communication Prize of the Royal Flemish Academy of Belgium for Science and the Arts.

A

Optimization of Time Window for Solar Flare Neutrino Searches

In this Appendix, we present the time window optimization for neutrino searches based on the light curves observed by Fermi-LAT. Details about the optimization method are presented in Chapter 3 together with a summary of the time window selected for each event.

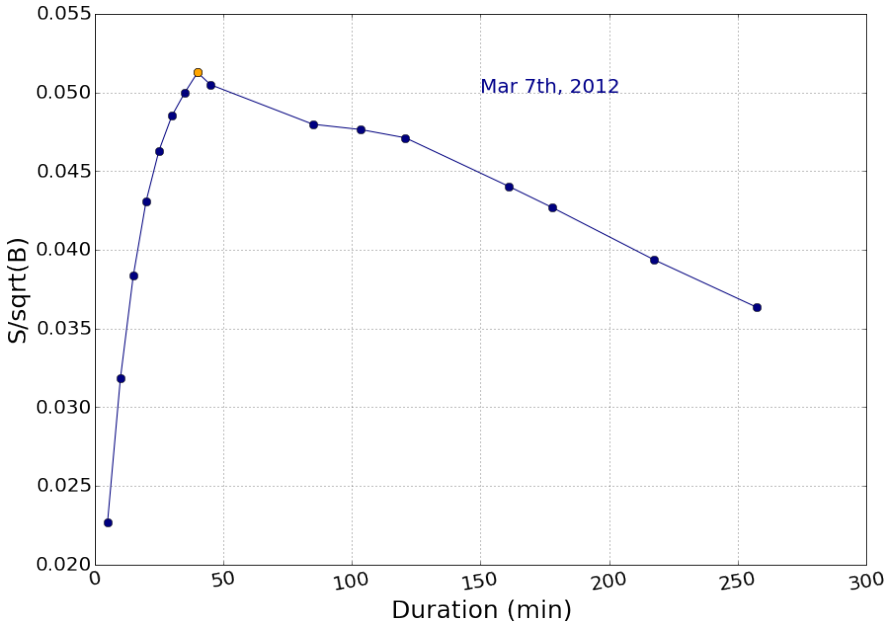

(a) Ratio of signal over background for the Mar 7th, 2012 event. This curve has been obtained via the procedure outlined in Chapter 3. The maximum of the curve is highlighted with an orange point.

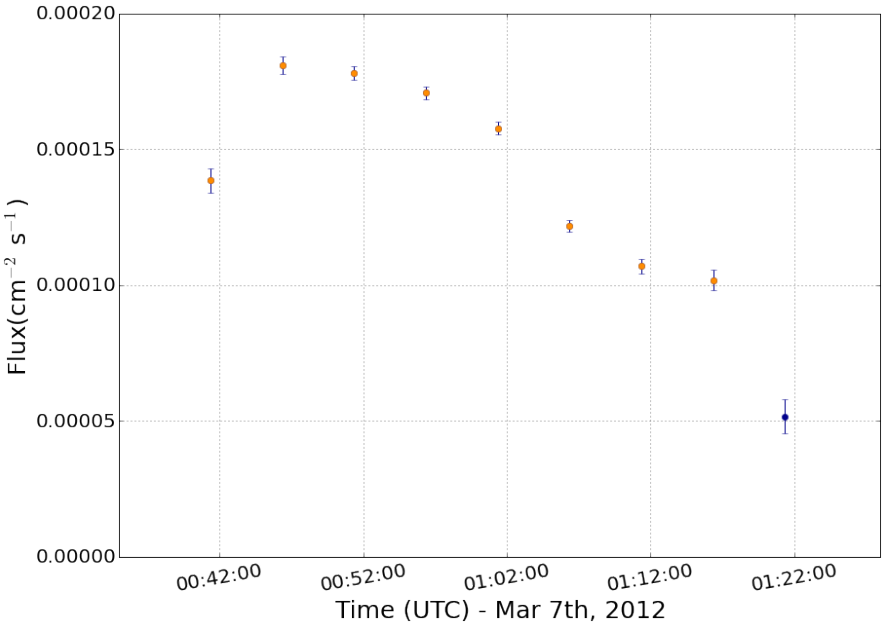

(b) Selected time window (orange points) compared to the initial gamma-ray light curve for the Mar 7th, 2012 solar flare event.

Figure A.1: Optimized time window for the March 7th, 2012 solar flare.

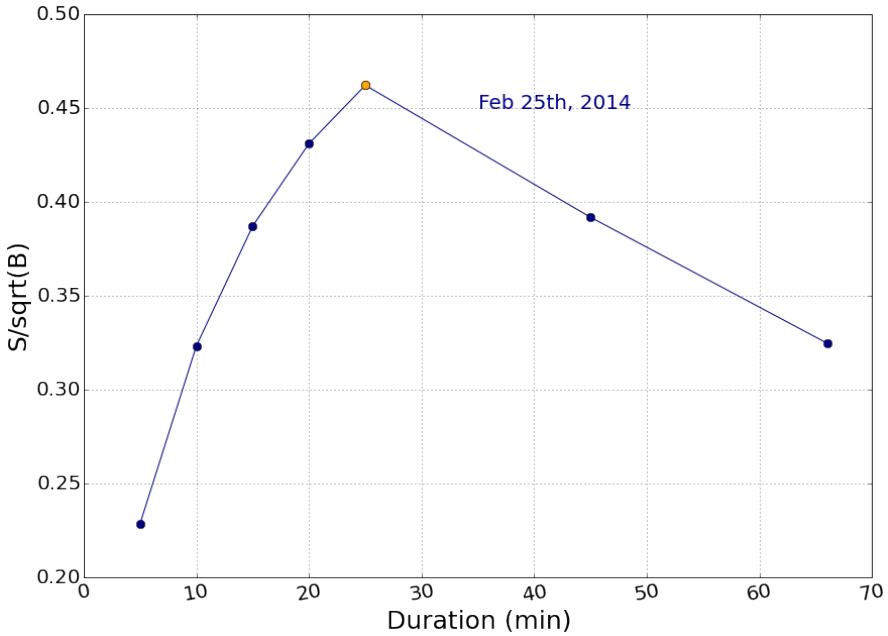

(a) Ratio of signal over background for the Feb 25th, 2014 event. This curve has been obtained via the procedure outlined in Chapter 3. The maximum of the curve is highlighted with an orange point.

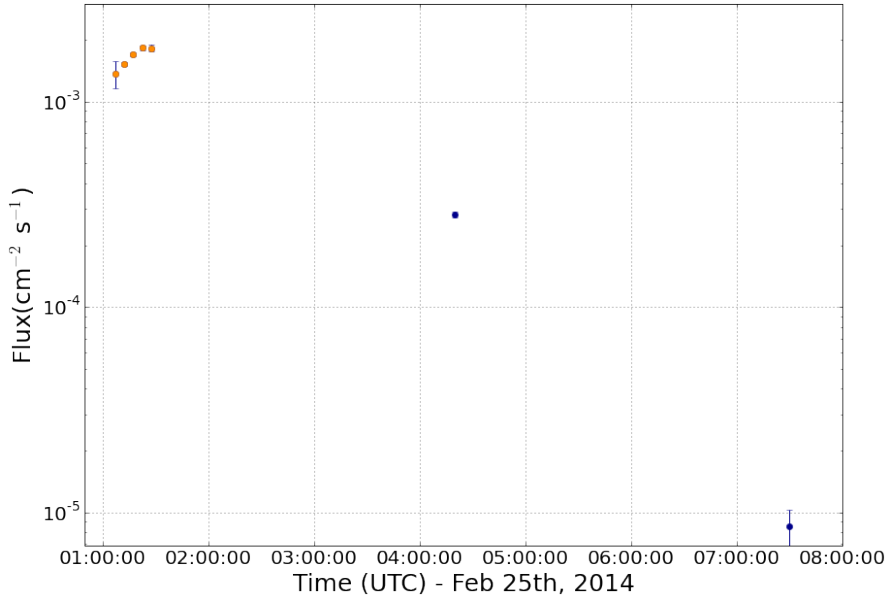

(b) Selected time window (orange points) compared to the initial gamma-ray light curve for the Feb 25th, 2014 solar flare event.

Figure A.2: Optimized time window for the February 25th, 2014 solar flare.

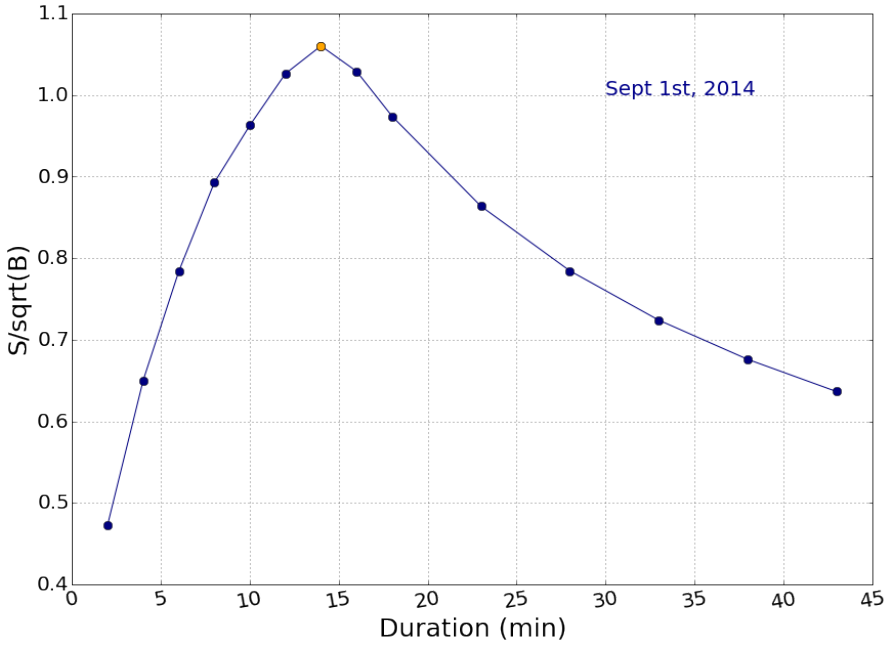

(a) Ratio of signal over background for the Sep 1st, 2014 event. This curve has been obtained via the procedure outlined in Chapter 3. The maximum of the curve is highlighted with an orange point.

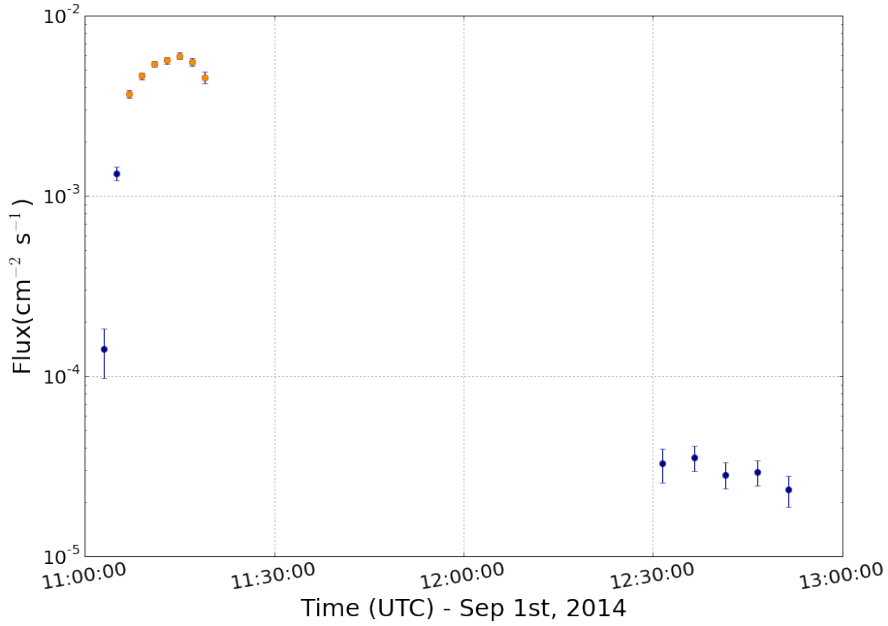

(b) Selected time window (orange points) compared to the initial gamma-ray light curve for the Sep 1st, 2014 solar flare event.

Figure A.3: Optimized time window for the September 1st, 2014 solar flare.

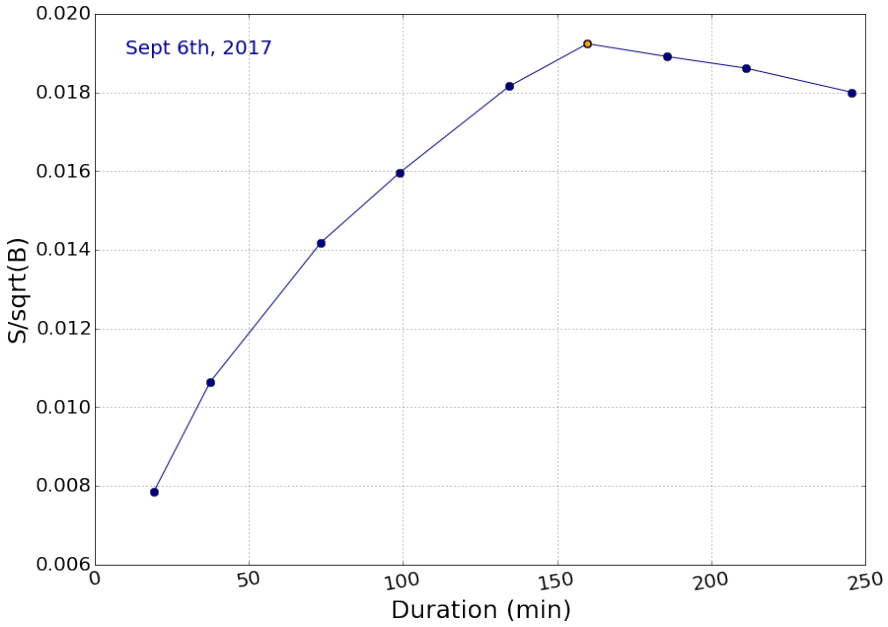

(a) Ratio of signal over background for the Sep 6th, 2017 event. This curve has been obtained via the procedure outlined in Chapter 3. The maximum of the curve is highlighted with an orange point.

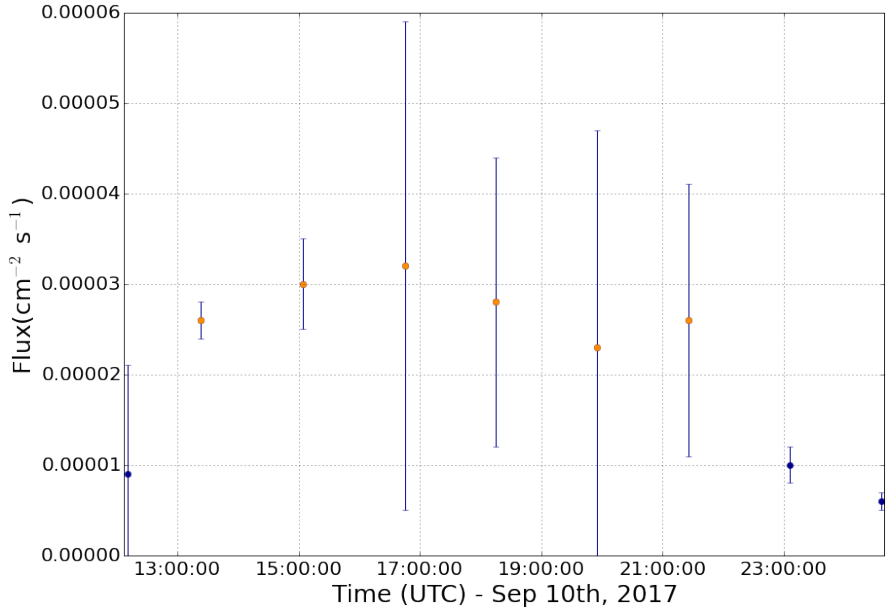

(b) Selected time window (orange points) compared to the initial gamma-ray light curve for the Sep 6th, 2017 solar flare event.

Figure A.4: Optimized time window for the September 6th, 2017 solar flare.

B

Examples of GeV Neutrino Events

This Appendix presents additional simulated events. The first section shows GeV events as seen in IceCube, while the second section contains some of the high-energy neutrino events passing the event selection.

B.1 Simulated GeV Neutrino Events

As described in Chapter 5, GeV neutrino interactions leave only a few hits in the detector. Fig. B.1, B.2, B.3, B.4 and B.5 confirm this statement.

B.2 Simulated High-Energy Neutrino Events Surviving the Event Selection

Fig. B.6 shows a few additional examples of high-energy neutrino interactions passing the event selection described in Chapter 5. The reasons why these events are seen as GeV-like events by the event selection is explained in Chapter 5.

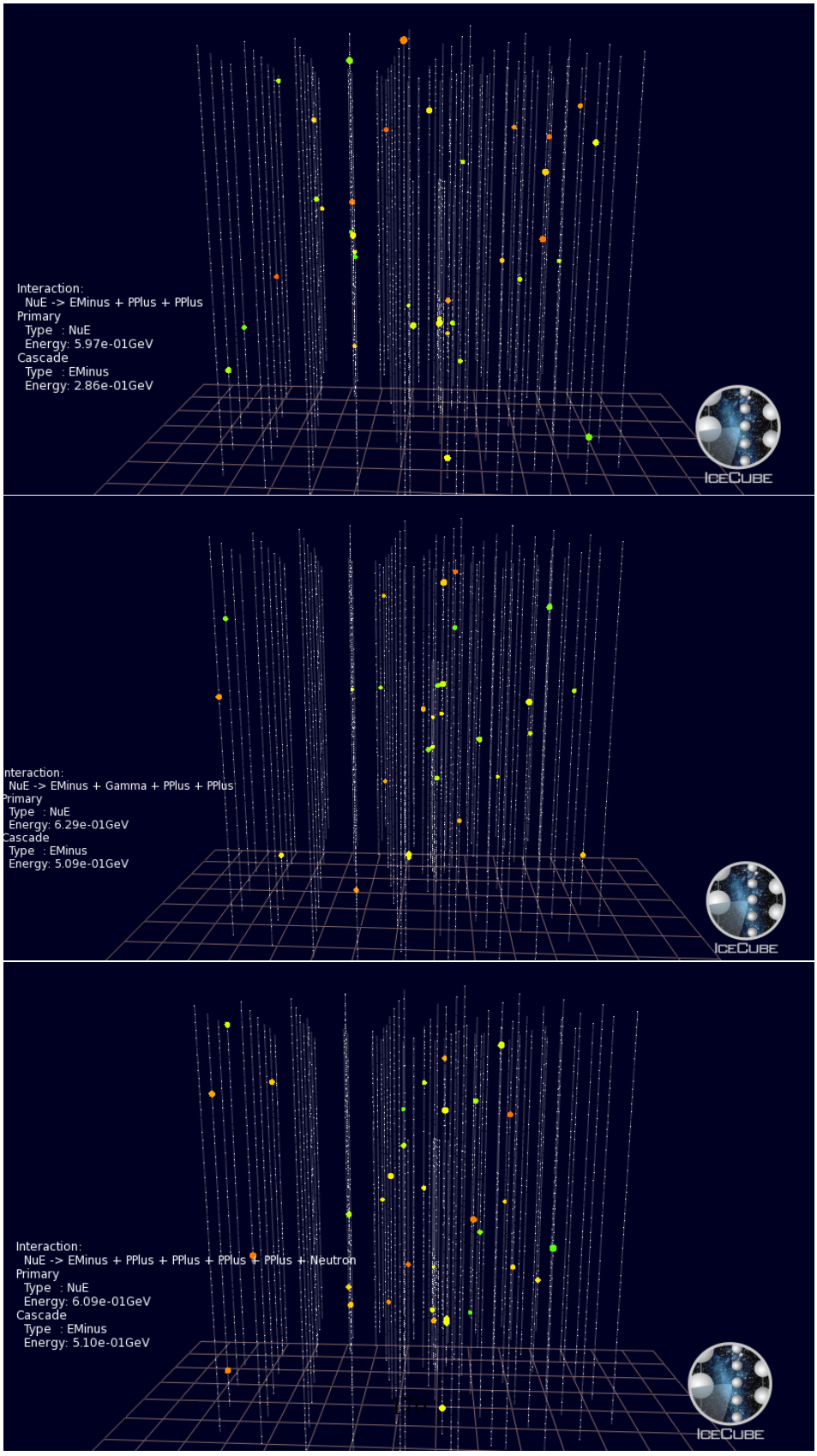

Figure B.1: Additional examples of simulated GeV electron neutrino interactions as seen in IceCube. All these interactions were generated by neutrinos with energies below 1 GeV.

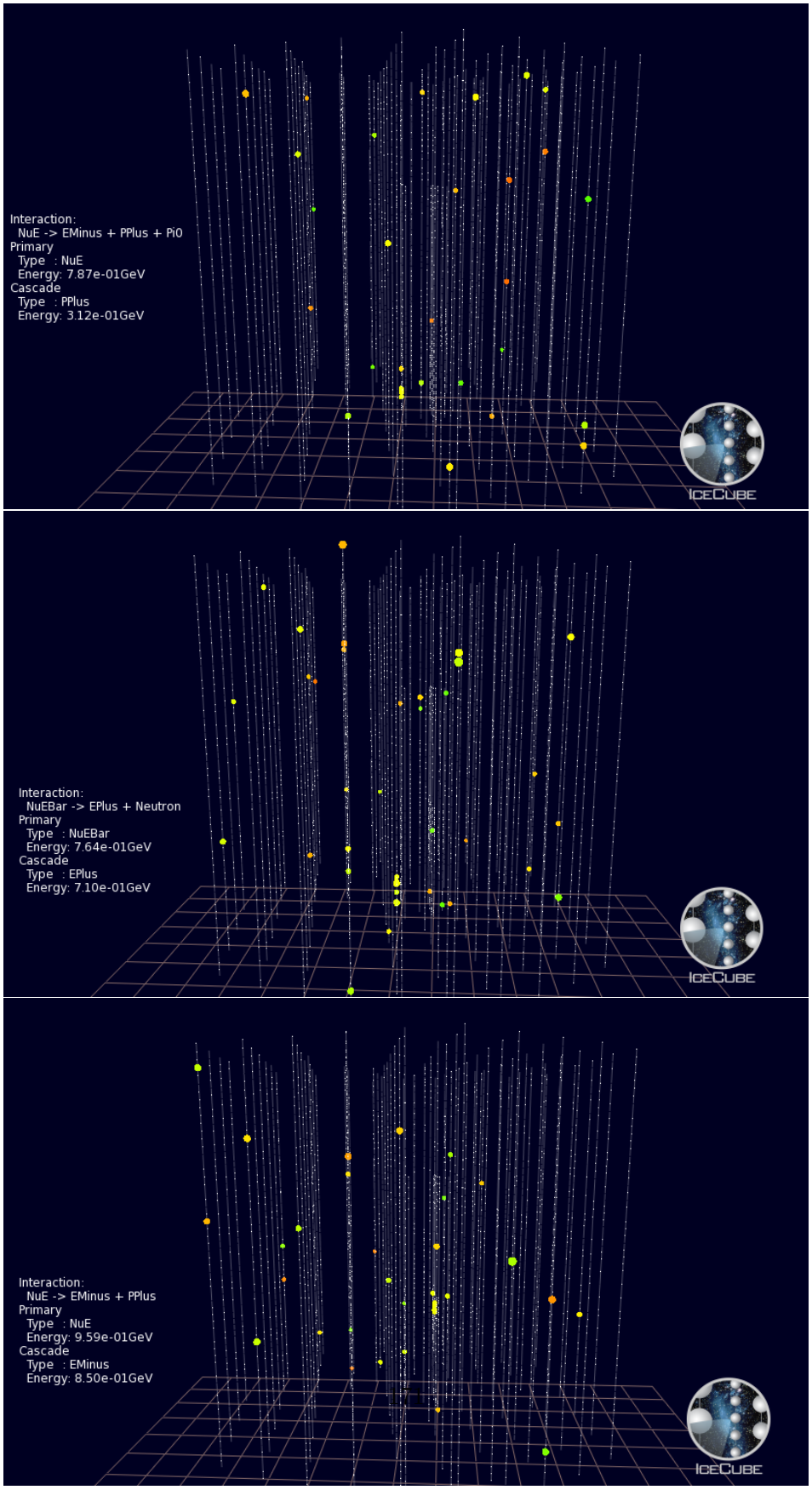

Figure B.2: Additional examples of simulated GeV electron neutrino interactions as seen in IceCube. All these interactions were generated by neutrinos with energies below 1 GeV.

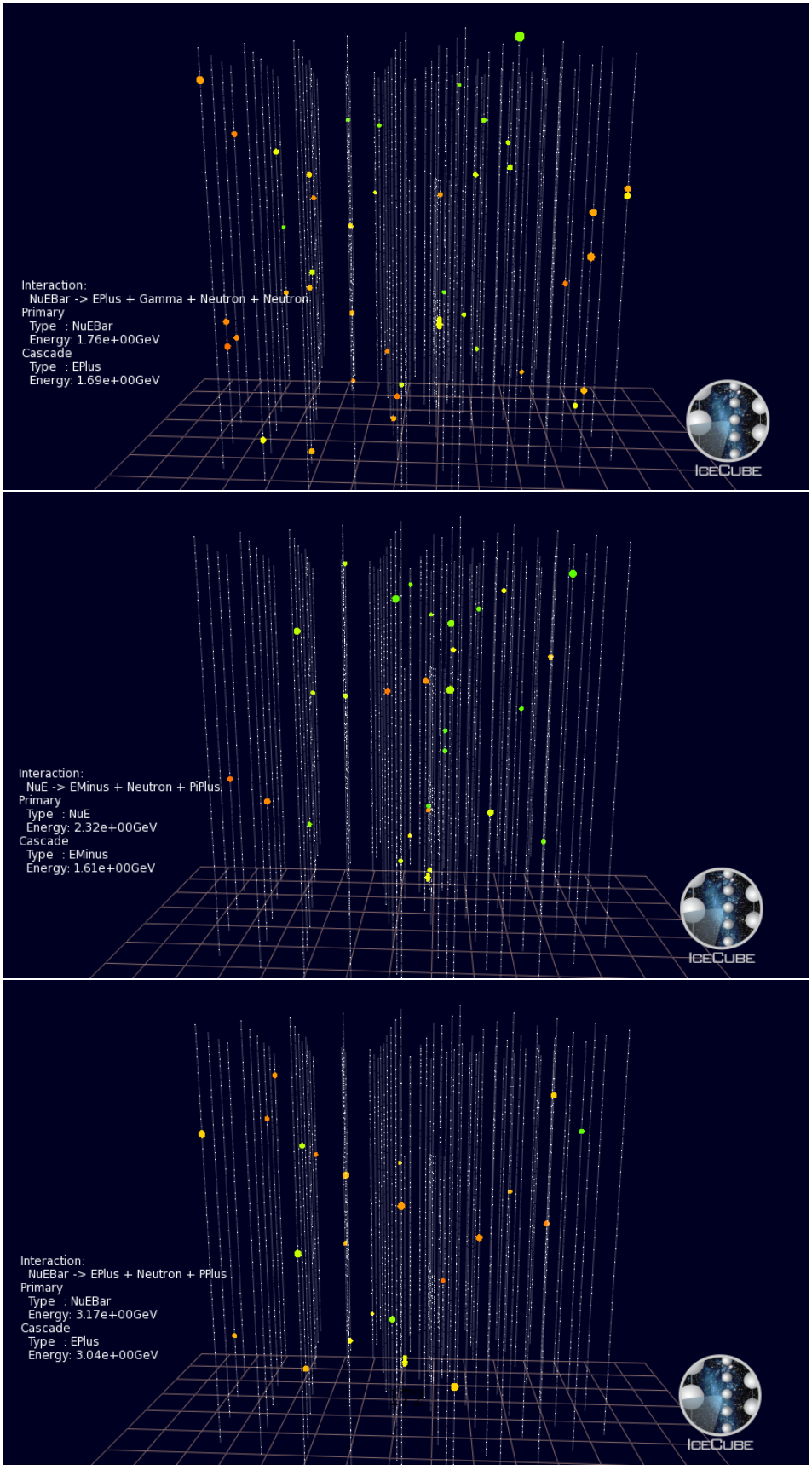

Figure B.3: Additional examples of simulated GeV electron neutrino interactions as seen in IceCube. All these interactions were generated by neutrinos with energies between 1 and 5 GeV.

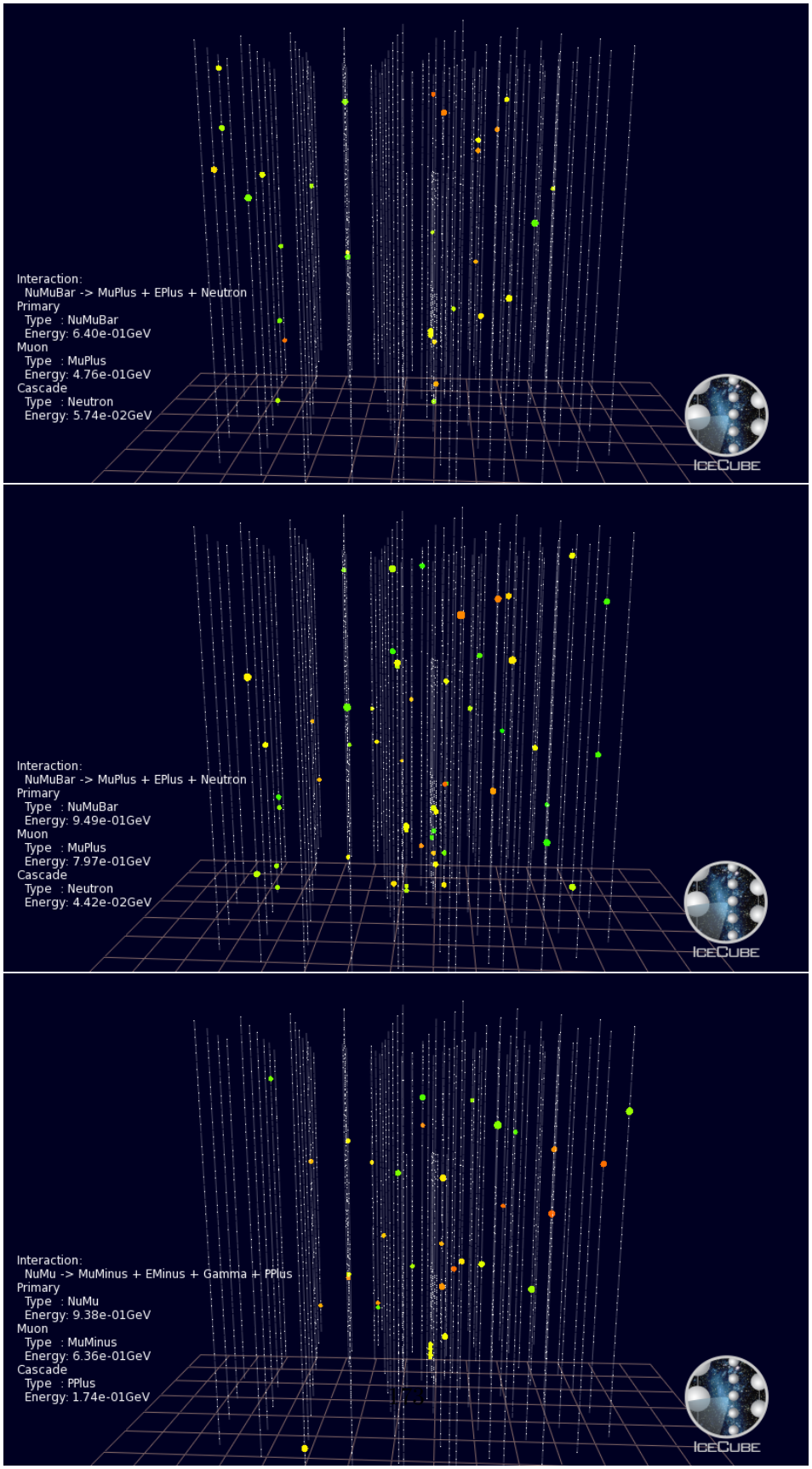

Figure B.4: Additional examples of simulated GeV muon neutrino interactions as seen in IceCube. All these interactions were generated by neutrinos with energies below 1 GeV.

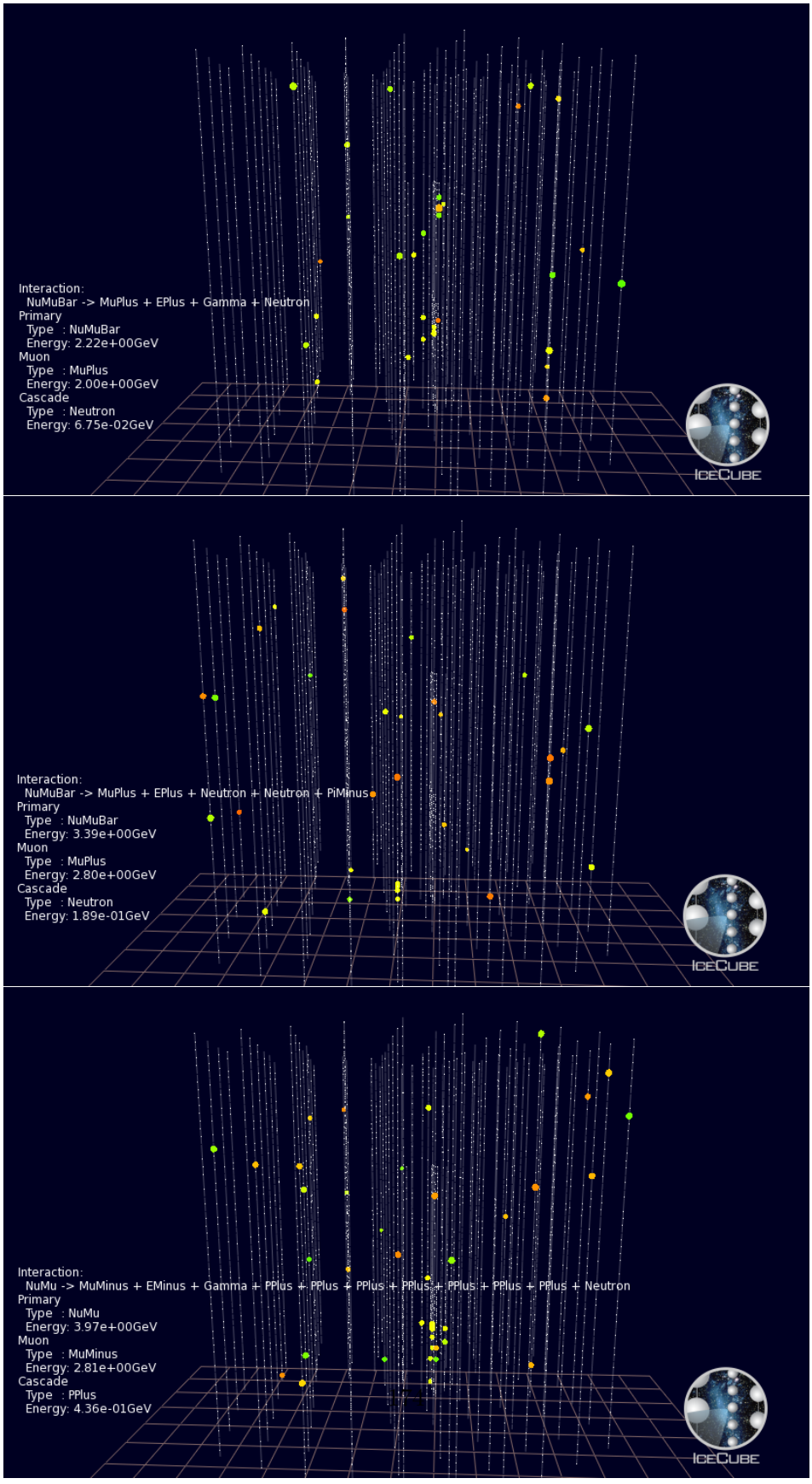

Figure B.5: Additional examples of simulated GeV muon neutrino interactions as seen in IceCube. All these interactions were generated by neutrinos with energies between 1 and 5 GeV.

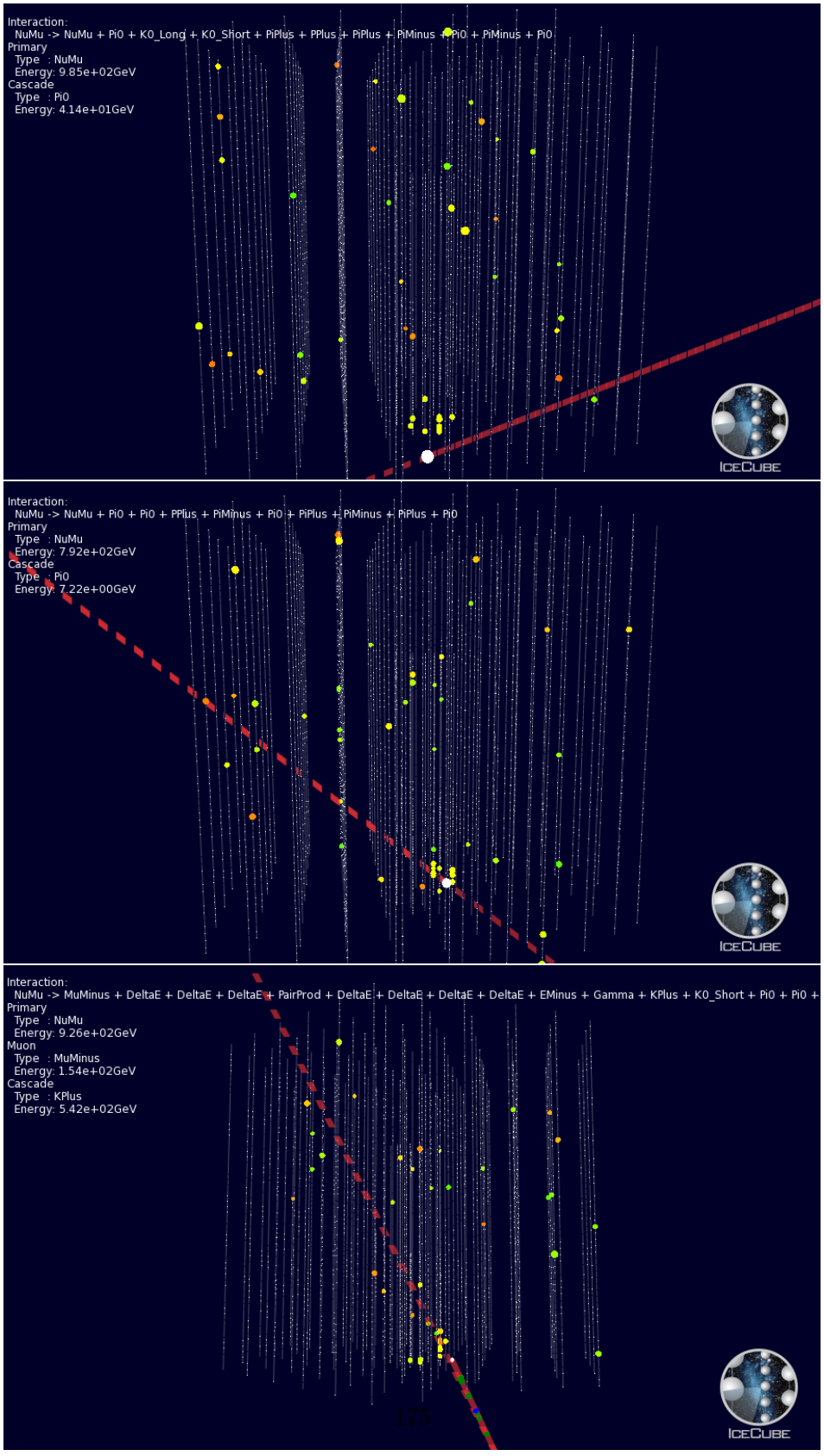

Figure B.6: Additional examples of simulated high-energy neutrino interactions surviving the event selection. All these interactions were generated by neutrinos with energies above 700 GeV.

C

Illustration of the Event Selection

This Appendix contains the distribution of some of the variables used in the event selection presented in Chapter 5. The shaded areas in each distribution represent the part of the parameter space rejected by the selection criteria described in Chapter 5.

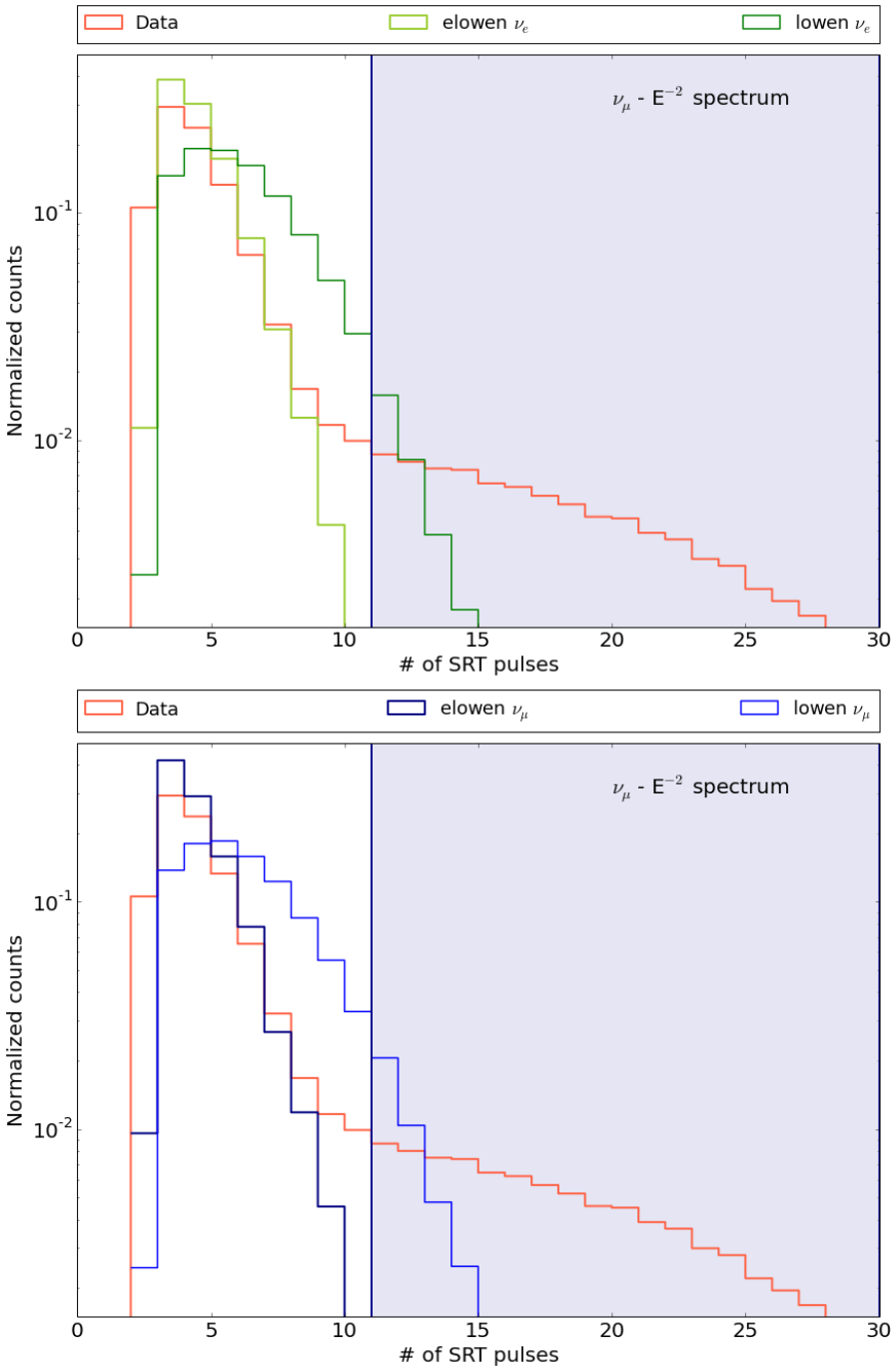

Figure C.1: Number of SRT pulses for ν_e (top) and ν_μ (bottom) and data. The part of the parameter space excluded by the selection criterion is illustrated with the shaded area.

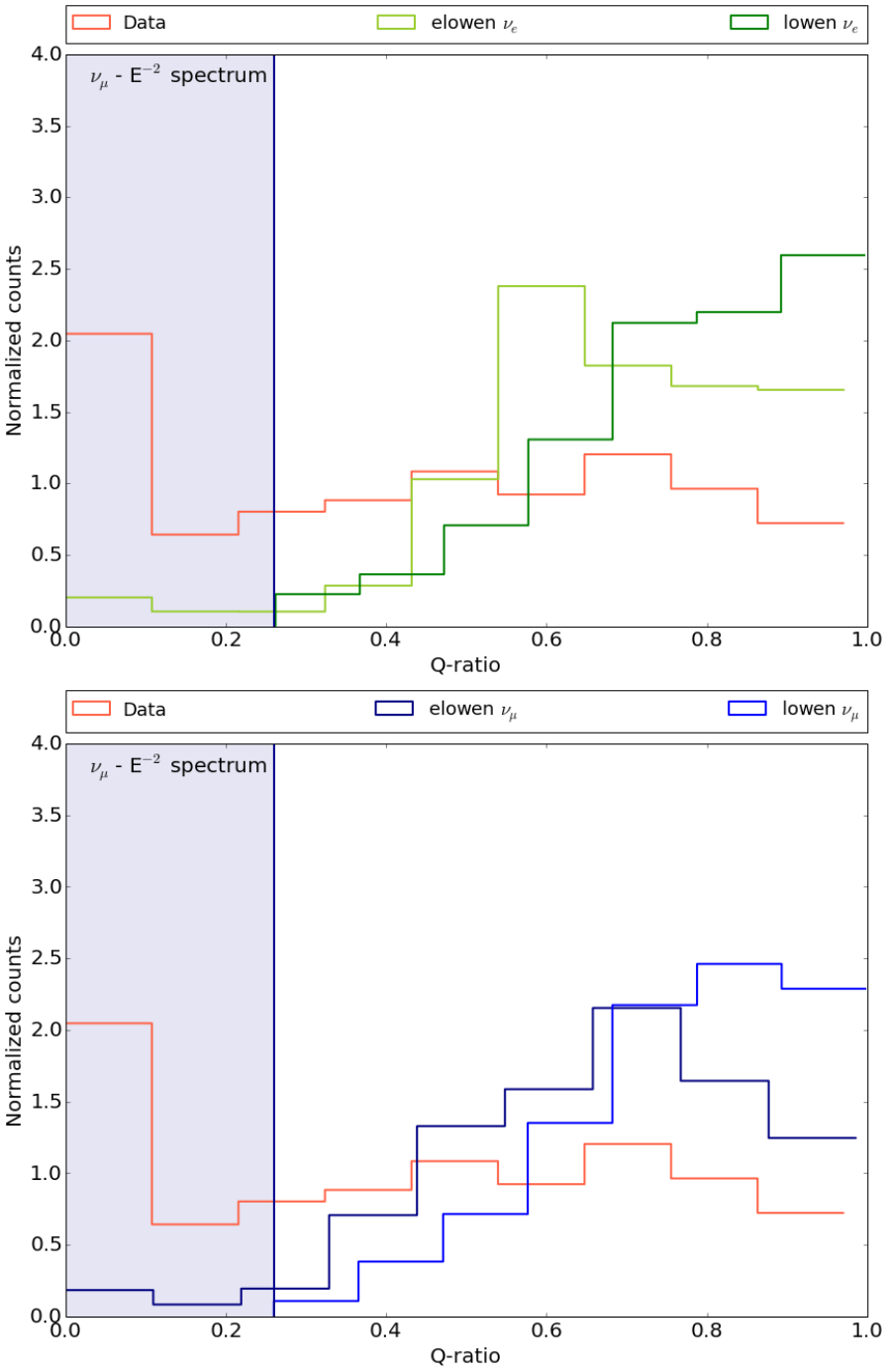

Figure C.2: Distribution of Q-ratio for *elowen*, *lowen* ν_e (top) and ν_μ (bottom) events and data. The part of the parameter space excluded by the selection criterion is illustrated with the shaded area.

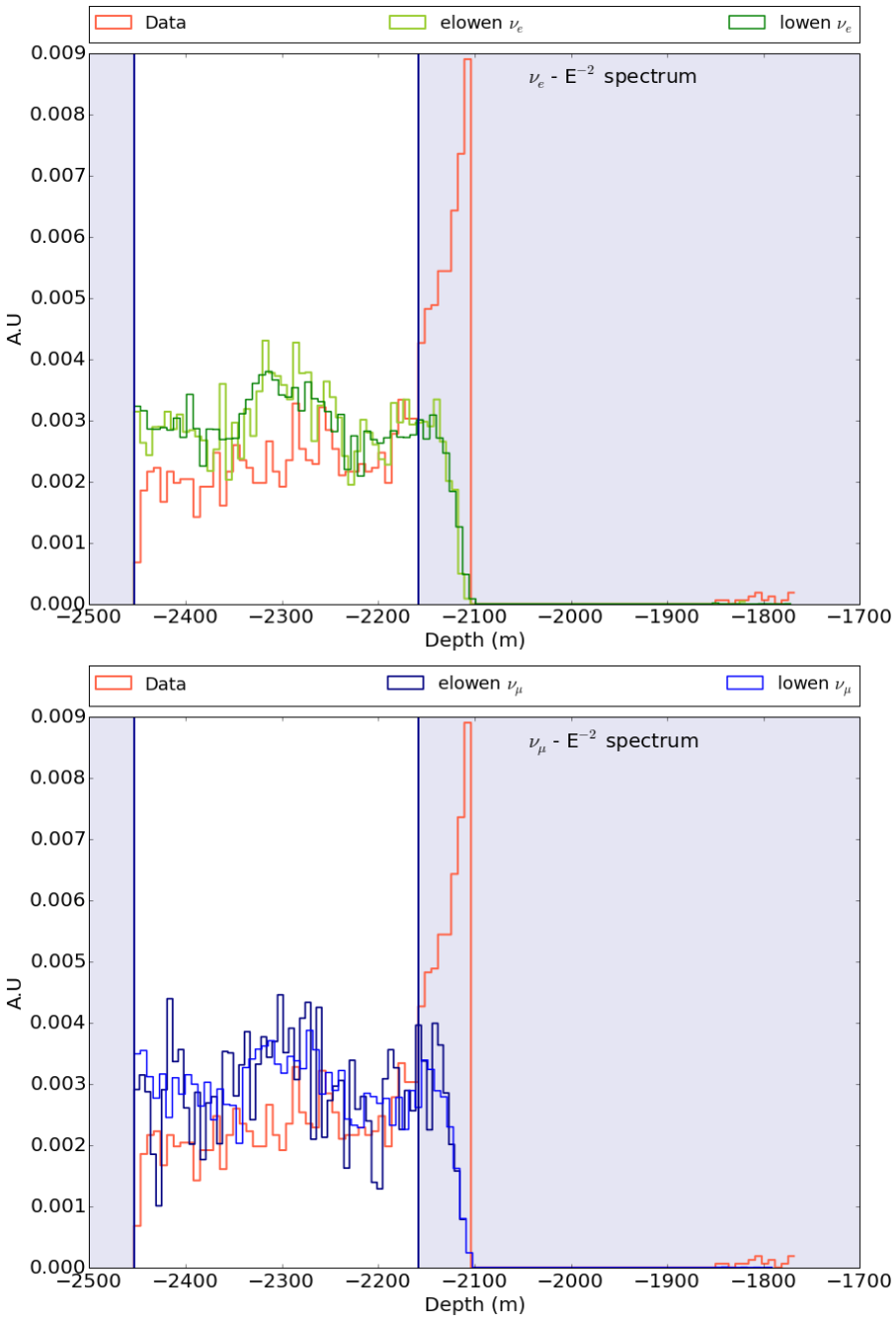

Figure C.3: Distribution of the depth of the first HLC in DeepCore for *elowen*, *lowen* ν_e (top) and ν_μ (bottom) events and data. The presence of data events around -1800 m is due to the upper part of DeepCore located above the dust layer. The part of the parameter space excluded by the selection criterion is illustrated with the shaded area.

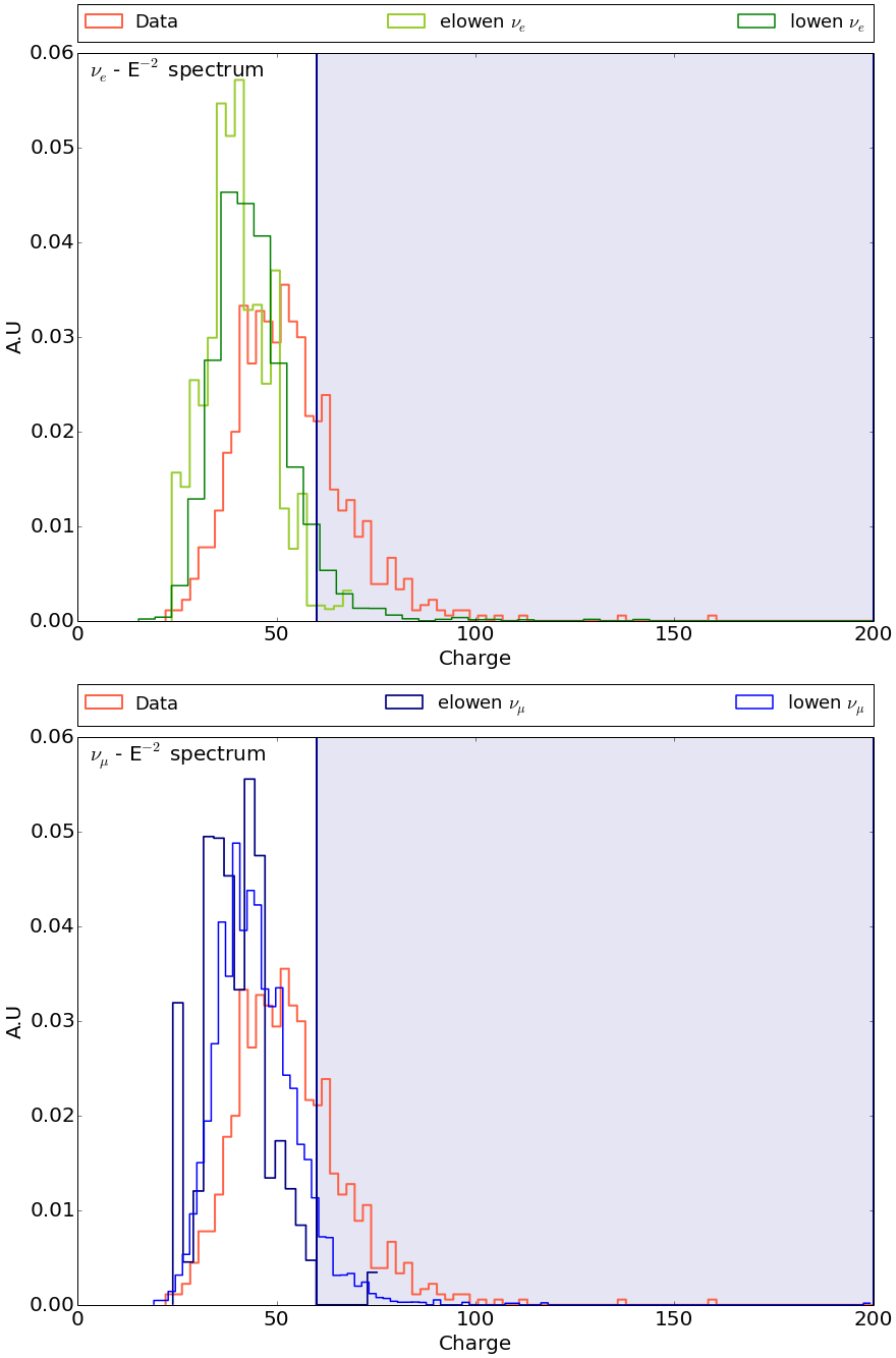

Figure C.4: Total charge (in photo electrons) distribution for data, *elowen*, *lowen* ν_e (top) and ν_μ (bottom) events. The part of the parameter space excluded by the selection criterion is illustrated with the shaded area.

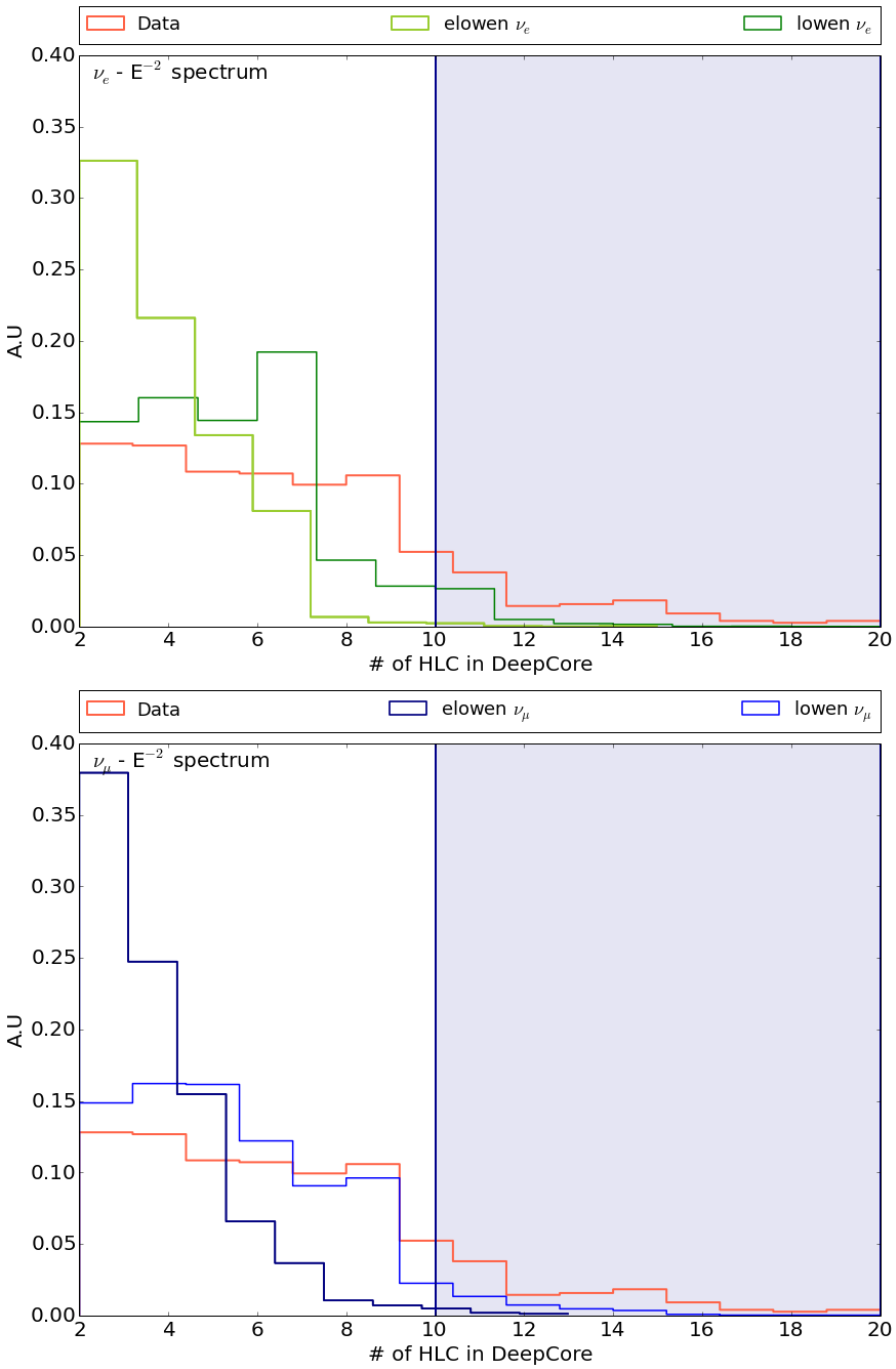

Figure C.5: HLC distribution for data, *elowen*, *lowen* ν_e (top) and ν_μ (bottom) events. The part of the parameter space excluded by the selection criterion is illustrated with the shaded area.

D

Discovery Potentials, Sensitivities and Upper limits

We illustrate in this Appendix the discovery potentials and sensitivities derived for each of the studied solar flares. More details on the performed calculation can be read in Chapter 6.

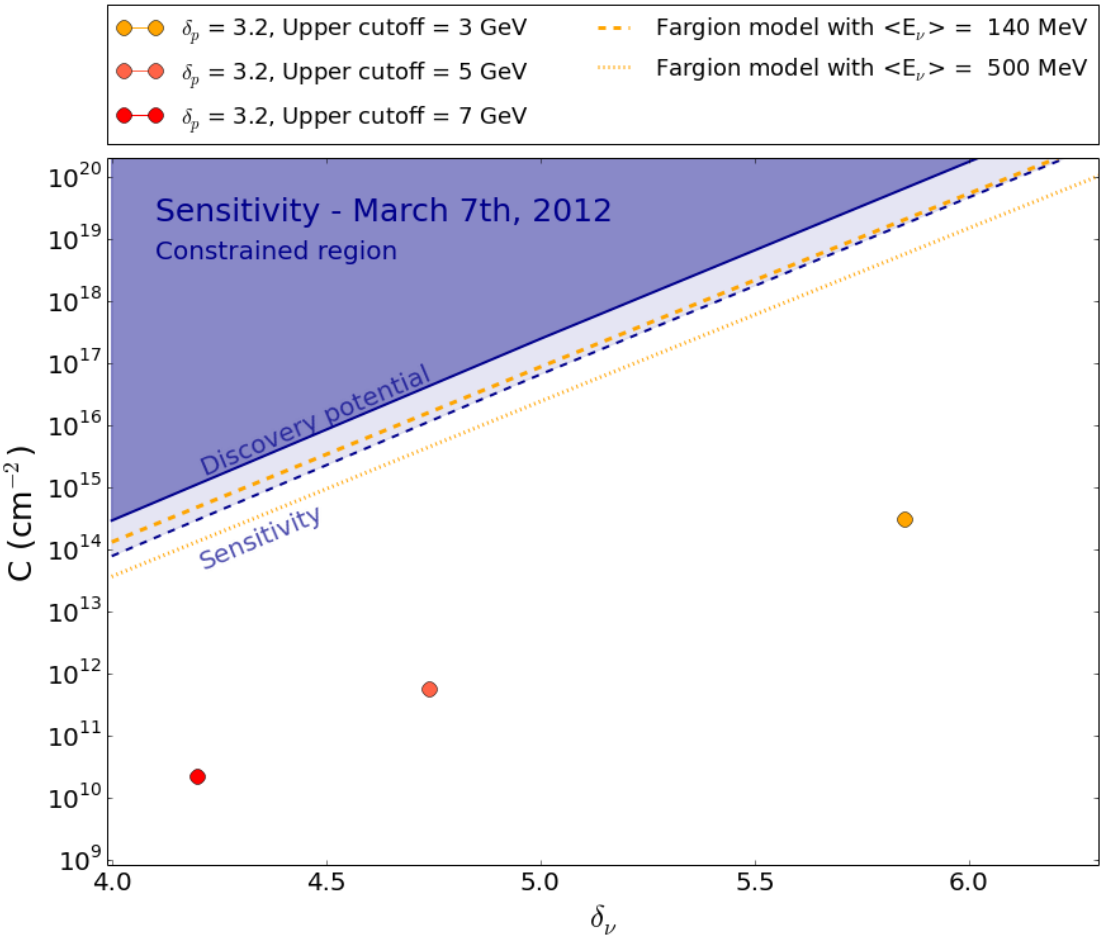

Figure D.1: Discovery potential and sensitivity for a solar flare time window of 40 minutes. For comparison, the orange points show the estimations presented in Chapter 3. The dashed (dotted) orange line shows the predictions from [42], with E_{fl}=10^{32} erg and $< E_{\nu_e} >$=140 MeV (dashed) and 500 MeV (dotted).

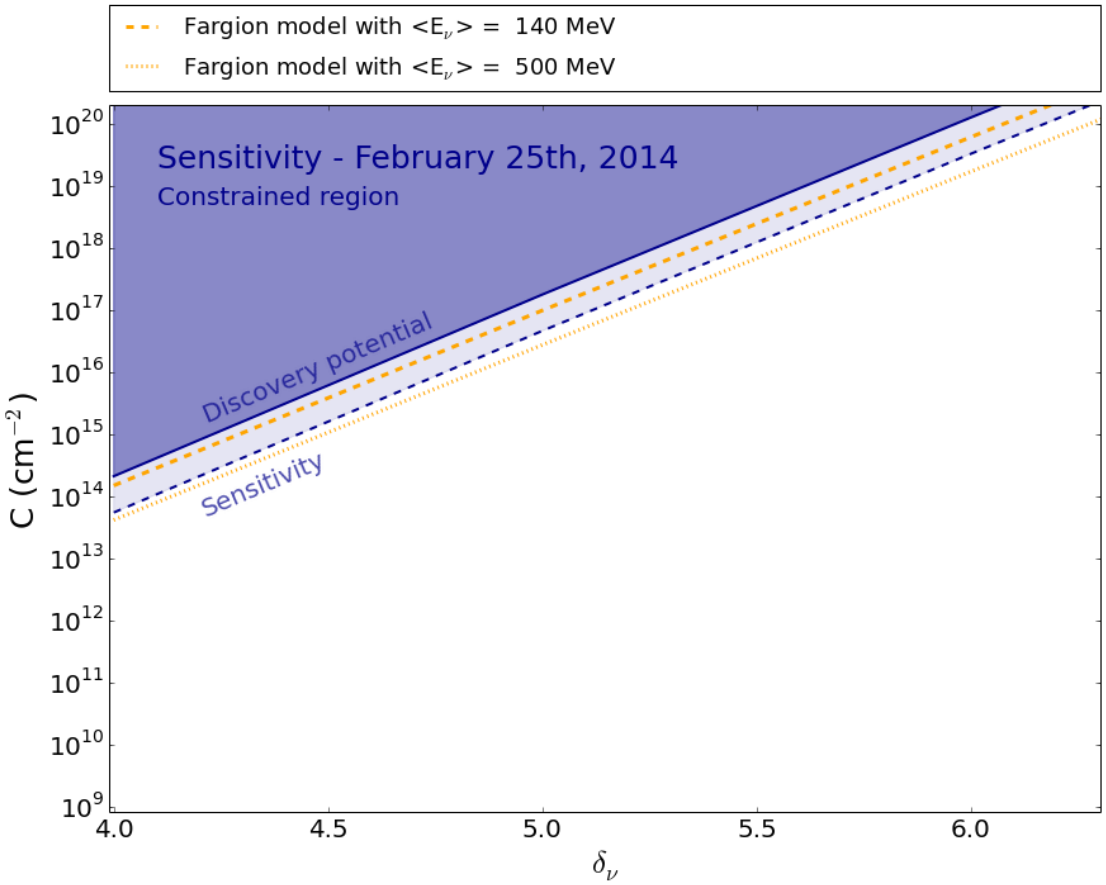

Figure D.2: Discovery potential and sensitivity for a solar flare time window of 25 minutes. The dashed (dotted) orange line shows the predictions from [42], with E_{fl}=10^{32} erg and $< E_{\nu_e} >$=140 MeV (dashed) and 500 MeV (dotted).

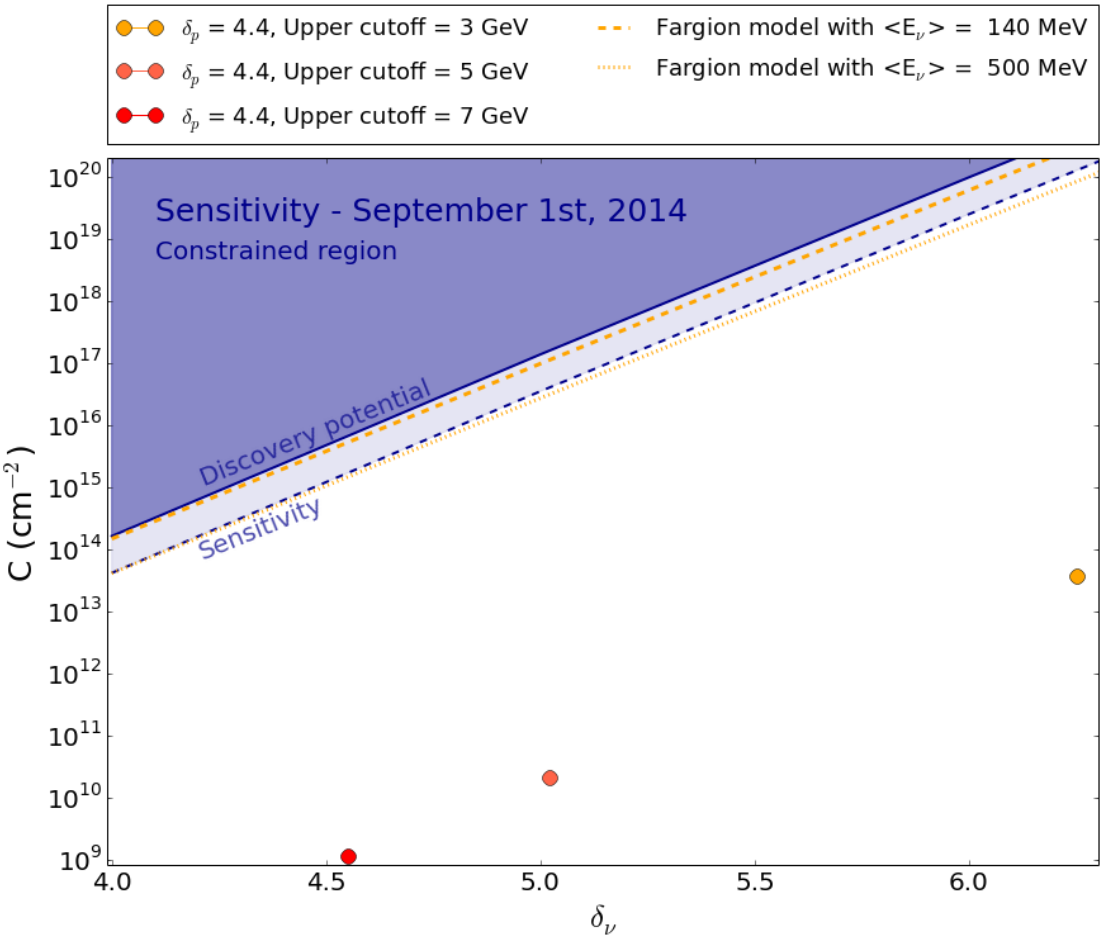

Figure D.3: Discovery potential and sensitivity for a solar flare time window of 14 minutes. For comparison, the orange points show the estimations presented in Chapter 3. The dashed (dotted) orange line shows the predictions from [42], with E_{fl}=10^{32} erg and $< E_{\nu_e} >$=140 MeV (dashed) and 500 MeV (dotted).

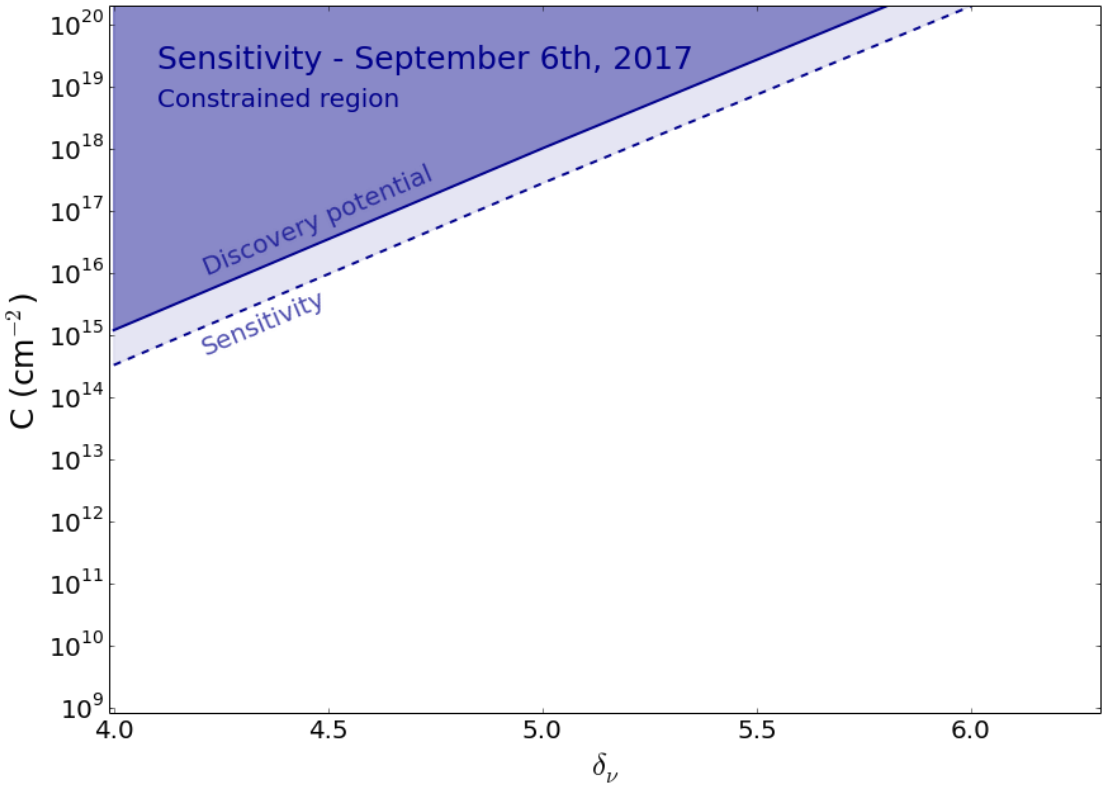

Figure D.4: Discovery potential and sensitivity for a solar flare time window of 515 minutes.

List of Figures

List of Tables

Bibliography

[1] R. J. M. Olson and J. M. Pasachoff. Moon-Struck: Artists Rediscover Nature and Observe. In *Earth-Moon Relationships Proceedings of the Conference held in Padova, Italy at the Accademia Galileiana di Scienze Lettere ed Arti*, 2000.

[2] Resolution B2. RESOLUTION B2 on the re-definition of the astronomical unit of length. *Beijing, Kina: International Astronomical Union*, 31 August 2012, retrieved 2012-09-19.

[3] NASA. *Sun*. World Book at NASA.

[4] M. Ossendrijver. Solar Dynamo. *The Astron. Astrophys. Rev.*, 11:287, 2003.

[5] T. K. Friedli. Sunspot observations of Rudolf Wolf from 1849–1893. *Sol. Phys.*, 291:2505, 2016.

[6] W. Pauli. Letter to gauverein wien meeting in tubingen. From the CERN Pauli Archives.

[7] J. Chadwick. Possible Existence of a Neutron. *Nature*, 129:312, 1932.

[8] E. Fermi. An attempt of a theory of beta radiation. *Zeitschrift für Physik*, 88:161–177, 1934.

[9] C.L. Cowan, F. Reines, F.B. Harrison, H.W. Kruse and A.D. McGuire. Detection of the free neutrino: A Confirmation. *Science*, 124:103–104, 1956.

[10] G. Danby *et al.* Observation of High-Energy Neutrino Reactions and the Existence of Two Kinds of Neutrinos. *Phys. Rev. Lett.*, 9:36–44, 1962.

[11] K. Hoshino. Result from DONUT: First direct evidence for tau-neutrino. In *APPC2000 Conf. Proc.*, pages 58–63, 2000.

[12] S. Schael *et al.* Precision electroweak measurements on the Z resonance. *Phys. Rept.*, 427, 2006.

[13] P. Lipari. Introduction to neutrino physics. In *2001 CERN-CLAF School of high-energy physics, Itacuruca, Brazil, 6-19 May, 2001: Proceedings*, pages 115–199, 2001.

[14] D. Griffiths. *Introduction to elementary particles*. 2008.

[15] The IceCube Collaboration (M.G. Aartsen and others). Evidence for High-Energy Extraterrestrial Neutrinos at the IceCube Detector. *Science*, 342:1242856, 2013.

[16] D. H. Perkins. *Particle astrophysics*. 2003.

[17] R. Davis. Solar neutrinos. II: Experimental. *Phys. Rev. Lett.*, 12:303–305, 1964.

[18] J. A. Formaggio and G. P. Zeller. From eV to EeV: Neutrino Cross Sections Across Energy Scales. *Rev. Mod. Phys.*, 84:1307, 2012.

[19] Y. Fukuda and others. Evidence for oscillation of atmospheric neutrinos. *Phys. Rev. Lett.*, 81:1562–1567, 1998.

[20] F. P. An *et al.* Observation of Electron-Antineutrino Disappearance at Daya Bay. *Phys. Rev. Lett.*, 108:171803, Apr 2012.

[21] J. K. Ahn *et al.* Observation of Reactor Electron Antineutrinos Disappearance in the RENO Experiment. *Phys. Rev. Lett.*, 108:191802, May 2012.

[22] C. Patrignani and others. Review of Particle Physics. *Chin. Phys.*, C40(10):100001, 2016.

[23] M. Thomson. *Modern particle physics.* Cambridge University Press, 2013.

[24] W. N. Cottingham and D. A. Greenwood. *An introduction to the standard model of particle physics.* Cambridge Univ. Press, Cambridge, 1998.

[25] I. Esteban, M. C. Gonzalez-Garcia, M. Maltoni, I. Martinez-Soler and T. Schwetz. Updated fit to three neutrino mixing: exploring the accelerator-reactor complementarity. *Journal of High Energy Physics*, 2017(1):87, Jan 2017.

[26] The IceCube Collaboration (M.G. Aartsen and others). PINGU: A Vision for Neutrino and Particle Physics at the South Pole. *J. Phys.*, G44(5):054006, 2017.

[27] M. Jongen. Sensitivity to the Neutrino Mass Hierarchy of KM3NeT/ORCA. *PoS*, ICRC2015:1092, 2016.

[28] R. Acciarri and others. Long-Baseline Neutrino Facility (LBNF) and Deep Underground Neutrino Experiment (DUNE). *FERMILAB-DESIGN-2016-02*, 2015.

[29] F. An and others. Neutrino Physics with JUNO. *J. Phys.*, G43(3):030401, 2016.

[30] E. Vitagliano, J. Redondo and G. Raffelt. Solar neutrinos at keV energies: thermal flux. 2017.

[31] E. Vitagliano, J. Redondo and G. Raffelt. Solar neutrino flux at keV energies. 2017.

[32] L. Bergstrom. Dark Matter Evidence, Particle Physics Candidates and Detection Methods. *Annalen Phys.*, 524:479–496, 2012.

[33] Rameez Mohamed. *IceCube searches for neutrinos from dark matter annihilations in the Sun and cosmic accelerators.* PhD thesis, University of Geneva, 04/27 2016. ID: unige:83851.

[34] K. Choi, C. Rott and Y. Itow. Impact of the dark matter velocity distribution on capture rates in the Sun. *JCAP*, 1405:049, 2014.

[35] R. Catena and B. Schwabe. Form factors for dark matter capture by the Sun in effective theories. *JCAP*, 1504(04):042, 2015.

[36] G. Jungman, M. Kamionkowski and K. Griest. Supersymmetric dark matter. *Phys. Rept.*, 267:195–373, 1996.

[37] K. C. Y. Ng, J. F. Beacom, A. H. G. Peter and C. Rott. Solar Atmospheric Neutrinos: A New Neutrino Floor for Dark Matter Searches. *Phys. Rev. D*, D96(10):103006, 2017.

[38] The IceCube Collaboration (M.G. Aartsen and others). Search for annihilating dark matter in the Sun with 3 years of IceCube data. *Eur. Phys. J.*, C77(3):146, 2017.

[39] C. A. Arguelles, G. de Wasseige, A. Fedynitch and B. J. P. Jones. Solar Atmospheric Neutrinos and the Sensitivity Floor for Solar Dark Matter Annihilation Searches. *JCAP*, 1707(07):024, 2017.

[40] K. Edsjo, J. Elevant, R. Enberg and C. Niblaeus. Neutrinos from cosmic ray interactions in the Sun. *JCAP*, 1706(06):033, 2017.

[41] G. de Wasseige. On the Study of Solar Flares with Neutrino Observatories. In *Proceedings, 51st Rencontres de Moriond on Electroweak Interactions and Unified Theories: La Thuile, Italy, March 12-19, 2016*, pages 573–576, 2016.

[42] D. Fargion. Detecting solar neutrino flares and flavors. *JHEP*, 06:045, 2004.

[43] G. E. Kocharov, G. A. Kovaltsov and I.G. Usoskin. Solar Flare Neutrinos. *Il Nuovo Cimento C*, 14(417), 1991.

[44] R. Davis. Search for Neutrinos from the Sun. In *Meeting on Neutrino Physics, Moscow, USSR*, 1968.

[45] Super-Kamiokande Collaboration (K. Abe and others). Solar Neutrino Measurements in Super-Kamiokande-IV. *Phys. Rev. D*, D94(052010), 2016.

[46] K. Shibata and T. Magara. Solar Flares: Magnetohydrodynamic Processes. *Living Reviews in Solar Physics*, 8(1):6, Dec 2011.

[47] M. J. Aschwanden. Particle acceleration and kinematics in solar flares – A Synthesis of Recent Observations and Theoretical Concepts (Invited Review). *Space Science Reviews*, 101(1):1–227, Jan 2002.

[48] J. R. Lemen and others. The solar x-ray imager for GOES, 2004.

[49] R. Murphy and R. Ramaty. Solar-flare neutrons and gamma rays. *Advances in Space Research*, 4:127–136, 02 1984.

[50] Fermi-LAT Collaboration (M. Ackermann and others). High-energy Gamma-Ray Emission from Solar Flares: Summary of Fermi Large Area Telescope Detections and Analysis of Two M-class Flares. *Astrophys. J.*, 787:15, 2014.

[51] M. J. Aschwanden. Particle Acceleration and Kinematics in Solar Flares and the Solar Corona. In Wilson, A. and et al., editor, *Magnetic Fields and Solar Processes*, volume 448 of *ESA Special Publication*, page 1015, 1999.

[52] R. J. Murphy, C. D. Dermer and R. Ramaty. High-energy processes in solar flares. *Astrophys. J. Supplement Series*, 63(721), 1987.

[53] M. S. Longair. *High Energy Astrophysics*. Cambridge University Press, 2011.

[54] N. Vilmer, A. L. MacKinnon and G. J. Hurford. Properties of Energetic Ions in the Solar Atmosphere from γ-Ray and Neutron Observations. *Space Science Reviews*, 159:167, 2011.

[55] N. Vilmer. Solar flares and energetic particles. *Philosophical Transactions of the Royal Society of London A: Mathematical, Physical and Engineering Sciences*, 370(1970):3241–3268, 2012.

[56] C. Meegan *et al.* The Fermi Gamma-ray Burst Monitor. *Astrophys. J.*, 702:791, 2009.

[57] W. B. Atwood *et al.* The Large Area Telescope on the Fermi Gamma-Ray Space Telescope Mission. *Astrophys. J.*, 497(2):1071, 2009.

[58] M. Pesce-Rollins, N. Omodei, A. Allafort, V. Petrosian, S. Raino and W. Liu. Fermi Large Area Telescope observations of the Sun: The first ten years. In Proceedings of Science, editor, *7th International Fermi Symposium (IFS2017)* , volume 7, 2017.

[59] V. Bindi. Solar Energetic Particles measured by AMS-02. In *Proceedings, 34th International Cosmic Ray Conference (ICRC 2015): The Hague, The Netherlands, July 30-August 6, 2015*, volume ICRC2015, 2015.

[60] J. M. Ryan, J. A. Lockwood and H. Debrunner. Solar Energetic Particles. *Space Science Reviews*, 93(1):35–53, Jul 2000.

[61] The IceCube Collaboration (R. Abbasi and others). Solar Energetic Particle Spectrum on 13 December 2006 Determined by IceTop. *Astrophys. J.*, 689:L65–L68, 2008.

[62] R. Davis. A review of measurements of the solar neutrino flux and their variation. *Nuclear Physics B - Proceedings Supplements*, 48(1):284 – 298, 1996. Proceedings of the Fourth International Workshop on Theoretical and Phenomenological Aspects of Underground Physics.

[63] J. N. Bahcall. Solar flares and neutrino detectors. *Phys. Rev. Lett.*, 61(23):2650, 1988.

[64] K. S. Hirata *et al.* Search for correlation of neutrino events with solar flares in Kamiokande. *Phys. Rev. Lett.*, 61(23):2653, 1988.

[65] B. Aharmim and others. A Search for Astrophysical Burst Signals at the Sudbury Neutrino Observatory. *Astropart. Phys.*, 55:1, 2014.

[66] Fermi-LAT Collaboration (Ackermann, M. and others). Fermi-LAT Observations of High-energy Behind-the-limb Solar Flares. *Astrophys. J.*, 835(2):219, 2017.

[67] M. Pesce-Rollins, N. Omodei, V. Petrosian, W. Liu, F. Rubio da Costa, A. Allafort and Fermi-LAT Collaboration. Fermi Large Area Telescope observations of high-energy gamma-ray emission from behind-the-limb solar flares. In *34th International Cosmic Ray Conference (ICRC2015)*, volume 34 of *International Cosmic Ray Conference*, page 128, 2015.

[68] Fermi-LAT Collaboration (Ajello, M. and others). Impulsive and Long Duration High-Energy Gamma-ray Emission From the Very Bright 2012 March 7 Solar Flares. *Astrophys. J.*, 789(1):20, 2014.

[69] S. Agostinelli *et al*. Geant4—a simulation toolkit. *Nucl. Instrum. Meth.*, 506(3):250 – 303, 2003.

[70] M.E. Machado, E. H. Avrett, J. E. Vernazza and R. W. Noyes. Semiempirical models of chromospheric flare regions. *Astrophys. J.*, 242:336, 1980.

[71] N. Omodei, M. Pesce-Rollins, F. Longo, A. Allafort and S. Krucker. Fermi-LAT observations of the 2017 September 10^{th} solar flare. *arXiv - astro-ph.HE 1803.07654*, 2018.

[72] Dj. Heristchi, G. Trottet and J. Perez-Peraza. Upper cutoff of high energy solar protons. *Sol. Phys.*, 49(1):151–175, Jul 1976.

[73] D. J. Forrest, W. T. Vestrand, E. L. Chupp, E. Rieger, J. F. Cooper and G. H. Share. Neutral pion production in solar flares. In *International Cosmic Ray Conference*, volume 4, 1985.

[74] G. A. Bazilevskaya *et al.* Solar energetic particle events in 2006-2012 in the PAMELA experiment data. In *Proceedings, 23rd European Cosmic Ray Symposium (ECRS 2012): Moscow, Russia, July 3-7, 2012*, volume 409, page 012188, 2013.

[75] J. K. Rowley and B. T. Cleveland and R. Davis. The Chlorine Solar Neutrino Experiment. *AIP Conf. Proc.*, 126:1–21, 1985.

[76] M. Spurio. *Particles and astrophysics : a multi-messenger approach.* Cham, Switzerland : Springer, [2015], [2015].

[77] J. D. Jackson. *Classical Electrodynamics.* Wiley, 1998.

[78] J. van Santen. *Neutrino Interactions in IceCube above 1 TeV: Constraints on Atmospheric Charmed-Meson Production and Investigation of the Astrophysical Neutrino Flux with 2 years of IceCube Data Taken 2010-2012.* PhD thesis, University of Wisconsin-Madison, 2014.

[79] I. Tamm. *Radiation Emitted by Uniformly Moving Electrons.* Springer, 1991.

[80] U. F. Katz and Ch. Spiering. High-Energy Neutrino Astrophysics: Status and Perspectives. *Prog. Part. Nucl. Phys.*, 67:651–704, 2012.

[81] P. K. F. Grieder. DUMAND II: String 1 deployment, initial operation, results and system retrieval. *Nuclear Physics B - Proceedings Supplements*, 43(1):145 – 148, 1995.

[82] J. Babson and others. Cosmic Ray Muons in the Deep Ocean. *Phys. Rev.*, D42:3613–3620, 1990.

[83] J. A. Aguilar and others. Measurement of the atmospheric muon flux with a 4 GeV threshold in the ANTARES neutrino telescope. *Astropart. Phys.*, 33:86–90, 2010. [Erratum: Astropart. Phys.34,185(2010)].

[84] S. Adrian-Martinez and others. Letter of intent for KM3NeT 2.0. *J. Phys.*, G43(8):084001, 2016.

[85] The IceCube Collaboration (M.G. Aartsen and others). The IceCube Neutrino Observatory: Instrumentation and Online Systems. *JINST*, 12(03):P03012, 2017.

[86] P. Askebjer and others. Optical properties of the South Pole ice at depths between 0.8-km and 1-km. *Science*, 267:1147–1150, 1995.

[87] P. B. Price and L. Bergström. Optical properties of deep ice at the South Pole: scattering. *Appl. Opt.*, 36(18):4181–4194, Jun 1997.

[88] P. Askebjer and others. Optical properties of deep ice at the South Pole: Absorption. *Appl. Opt.*, 36:4168–4180, 1997.

[89] B. Halvarsson. *Interaction Analysis in Multivariable Control Systems?: Applications to Bioreactors for Nitrogen Removal.* PhD thesis, 2010.

[90] J. R. Petit *et al.* Climate and atmospheric history of the past 420,000 years from the Vostok ice core, Antarctica. *Nature*, 399:429, 1999.

[91] O. Watanabe, K. Kamiyama, H. Motoyama, Y. Fujii, H. Shoji and K. Satow. The paleoclimate record in the ice core from Dome Fuji station, Antarctica. *Ann. Glaciol.*, 29:176, 1999.

[92] M. Ackermann *et al.* Optical properties of deep glacial ice at the South Pole. *Journal of Geophysical Research: Atmospheres*, 111(D13):n/a–n/a, 2006. D13203.

[93] B. J. P. Jones. *Sterile Neutrinos in Cold Climates*. PhD thesis, MIT, 2015.
[94] R. Bay. IceCube dust map.
[95] The IceCube Collaboration (M.G. Aartsen and others). Searches for Sterile Neutrinos with the IceCube Detector. *Phys. Rev. Lett.*, 117(7):071801, 2016.
[96] The IceCube Collaboration (M.G. Aartsen and others). Search for Nonstandard Neutrino Interactions with IceCube DeepCore. 2017.
[97] The IceCube Collaboration (M.G. Aartsen and others). The IceCube Neutrino Observatory - Contributions to ICRC 2017 Part II: Properties of the Atmospheric and Astrophysical Neutrino Flux. 2017.
[98] The IceCube Collaboration (M.G. Aartsen and others). The IceCube Neutrino Observatory - Contributions to ICRC 2017 Part I: Searches for the Sources of Astrophysical Neutrinos. 2017.
[99] E. Waxman. High-Energy Cosmic Rays from Gamma-Ray Burst Sources: A Stronger Case. *Astrophys. J.*, 606(2):988, 2004.
[100] M. Ahlers, M. C. Gonzalez-Garcia and F. Halzen. GRBs on probation: testing the UHE CR paradigm with IceCube. *Astropart. Phys.*, 35:87, 2011.
[101] The IceCube Collaboration (M.G. Aartsen and others). An All-Sky Search for Three Flavors of Neutrinos from Gamma-Ray Bursts with the IceCube Neutrino Observatory. *Astrophys. J.*, 824(2):115, 2016.
[102] The IceCube Collaboration (M.G. Aartsen and others). The IceCube Realtime Alert System. *Astropart. Phys.*, 92:30–41, 2017.
[103] A. Albert and others. Search for High-energy Neutrinos from Binary Neutron Star Merger GW170817 with ANTARES, IceCube, and the Pierre Auger Observatory. *Astrophys. J.*, 850(2):L35, 2017.
[104] B. P. Abbott and others. Multi-messenger Observations of a Binary Neutron Star Merger. *Astrophys. J.*, 848(2):L12, 2017.
[105] N. Giglietto, A. Allafort, M. Brigida, F. Longo, N. Omodei, H. Takahashi and Y. Tanaka. Fermi LAT observation of quiet gamma-ray emission from the Sun and first solar flares detection. *Nuclear Instruments and Methods in Physics Research Section A: Accelerators, Spectrometers, Detectors and Associated Equipment*, 692(Supplement C):262 – 264, 2012. 3rd Roma International Conference on Astroparticle Physics.
[106] M.L. Kaiser. The STEREO mission: an overview. *Advances in Space Research*, 36(8):1483 – 1488, 2005. Solar Encounter, Solar-B and STEREO.
[107] D. Heck and others. CORSIKA: A Monte Carlo code to simulate extensive air showers. 1998.
[108] C. Andreopoulos and others. The GENIE Neutrino Monte Carlo Generator. *Nucl. Instrum. Meth.*, A614:87–104, 2010.
[109] J. H. Koehne *et al.* PROPOSAL: A tool for propagation of charged leptons. *Comput. Phys. Commun.*, 184:2070–2090, 2013.
[110] M. Larson. Simulation and identification of non-poissonian noise triggers in the IceCube neutrino detector. Master's thesis, University of Alabama, Tuscaloosa, 2013.

[111] M. Honda, T. Kajita, K. Kasahara, S. Midorikawa and T. Sanuki. Calculation of atmospheric neutrino flux using the interaction model calibrated with atmospheric muon data. *Phys. Rev. D*, 75(4):043006, 2007.

[112] T. P. Li and Y. Q. Ma. Analysis methods for results in gamma-ray astronomy. *Astrophys. J.*, 272:317, 1983.

[113] Virgo, LIGO Scientific (B. P. Abbott and others). Observation of Gravitational Waves from a Binary Black Hole Merger. *Phys. Rev. Lett.*, 116(6):061102, 2016.

[114] K. Asano and K. Murase. Gamma-Ray Bursts as Multienergy Neutrino Sources. *Adv. Astron.*, 2015(568516), 2015.

[115] J. N. Bahcall and P. Meszaros. 5-GeV to 10-GeV neutrinos from gamma-ray burst fireballs. *Phys. Rev. Lett.*, 85:1362, 2000.

[116] P. D'Avanzo. Short gamma-ray bursts: A review. *Journal of High Energy Astrophysics*, 7:73 – 80, 2015. Swift 10 Years of Discovery, a novel approach to Time Domain Astronomy.

[117] B. Baret *et al.* Bounding the Time Delay between High-energy Neutrinos and Gravitational-wave Transients from Gamma-ray Bursts. *Astropart. Phys.*, 35:1, 2011.

[118] R. Wilcox. *Kolmogorov-Smirnov Test: Basic.* American Cancer Society, 2014.

[119] D. Bose, L. Brayeur, M. Casier, K. D. de Vries, G. Golup and N. van Eijndhoven. Bayesian approach for counting experiment statistics applied to a neutrino point source analysis. *Astropart. Phys.*, 50:57, 2013.

[120] Super-Kamiokande Collaboration (K. Abe and others). Search for Neutrinos in Super-Kamiokande associated with Gravitational Wave Events GW150914 and GW151226. *Astrophys. J.*, 830(1):L11, 2016.

[121] The IceCube Collaboration (M.G. Aartsen and others). Measurement of neutrino oscillations with the full IceCube detector. In *33th International Cosmic Ray Conference (ICRC2013)*, 2013.

[122] K. D. de Vries, G. de Wasseige, J.-M. Frère and M. Vereecken. Constraints and prospects on gravitational-wave and neutrino emissions using GW150914. *Phys. Rev. D*, D96(8):083003, 2017.

[123] C. De Clercq, J. De Schauwers, G. de Wasseige and J. van Laer. A better communicator is always a better scientist, or the reason why every PhD student should engage in science outreach. In *ICRC2017*, 2017.